

KAMEL DEMMOUCHE

$\mathcal{N} = 1$   $SU(2)$  **Supersymmetric**  
**Yang-Mills theory on the lattice with**  
**light dynamical Wilson gluinos**



““This version of the thesis differs slightly from the official document submitted to the faculty. Typos are corrected while results and conclusions are unchanged.””



THEORETISCHE PHYSIK

$\mathcal{N} = 1$   $SU(2)$  SUPERSYMMETRIC YANG-MILLS  
THEORY ON THE LATTICE WITH LIGHT  
DYNAMICAL WILSON GLUINOS

Inaugural-Dissertation  
zur Erlangung des Doktorgrades  
der Naturwissenschaften im Fachbereich Physik  
der Mathematisch-Naturwissenschaftlichen Fakultät  
der Westfälischen Wilhelms-Universität Münster

vorgelegt von  
KAMEL DEMMOUCHE  
aus Oran  
-2009-

---

Dekan:	Prof. Dr. Johannes Peter Wessels
Erster Gutachter:	Prof. Dr. Gernot Münster
Zweiter Gutachter:	Prof. Dr. Owe Philipsen
Tag der mündlichen Prüfungen:	27.03.2009
Tag der Promotion:	.....

# Abstract

The supersymmetric Yang-Mills (SYM) theory with one supercharge ( $\mathcal{N} = 1$ ) and one additional Majorana matter-field represents the simplest model of supersymmetric gauge theory. Similarly to QCD, this model includes gauge fields, gluons, with color gauge group  $SU(N_c)$  and fermion fields, describing the gluinos. The non-perturbative dynamical features of strongly coupled supersymmetric theories are of great physical interest. For this reason, many efforts are dedicated to their formulation on the lattice. The lattice regularization provides a powerful tool to investigate non-perturbatively the phenomena occurring in SYM such as confinement and chiral symmetry breaking.

In this work we perform numerical simulations of the pure  $SU(2)$  SYM theory on large lattices with small Majorana gluino masses down to about  $m_{\tilde{g}} \sim 115$  MeV with lattice spacing up to  $a \simeq 0.1$  fm. The gluino dynamics is simulated by the Two-Step Multi-Boson (TSMB) and the Two-Step Polynomial Hybrid Monte Carlo (TS-PHMC) algorithms. Supersymmetry (SUSY) is broken explicitly by the lattice and the Wilson term and softly by the presence of a non-vanishing gluino mass  $m_{\tilde{g}} \neq 0$ . However, the recovery of SUSY is expected in the infinite volume continuum limit by tuning the bare parameters to the SUSY point in the parameter space. This scenario is studied by the determination of the low-energy mass spectrum and by means of lattice SUSY Ward-Identities (WIs).

# Zusammenfassung

Die supersymmetrische Yang-Mills (SYM) Theorie mit einer Super-Ladung ( $\mathcal{N} = 1$ ) und einer zusätzlichen Majorana Fermion Feld stellt das einfachste Modell von Super-Yang-Mills Theorien dar. Ähnlich wie bei QCD enthält dieses Modell Eichfelder, die Gluonen, mit der Farb-Eichgruppe  $SU(N_c)$  und fermionische Felder, die Gluinos. Von großem physikalischen Interesse ist die Untersuchung der nichtperturbativen Effekte wie Confinement und chirale Symmetriebrechung in der stark gekoppelten supersymmetrischen Theorie. Aus diesem Grund wurden Formulierungen vorgeschlagen, um Supersymmetrie auf dem Gitter einzusetzen. Die Gitterregularisierung stellt ein mächtiges Werkzeug für die Untersuchung der SYM Eigenschaften durch numerische Simulationen dar.

In dieser Arbeit führen wir numerische Simulationen der reinen  $SU(2)$  SYM Theorie auf großem Gitter mit kleinen Gluinomassen von etwa  $m_{\tilde{g}} \sim 115$  MeV und Gitter-Abstand bis zu  $a \sim 0.1$  fm durch. Die dynamischen Gluinos werden mit den “Two-Step Multi-Boson” und “Two-Step Polynomial Hybrid Monte Carlo” Algorithmen simuliert. Supersymmetrie ist explizit von der Diskretisierung und der Wilson Formulierung gebrochen und ist weich durch die nicht verschwunden Gluinomasse gebrochen. Allerdings wird SUSY im Kontinuumlimes durch die Feineinstellung der nackten Parameter wiederhergestellt. Diese Szenario wird durch die Bestimmung des Massenspektrums und die supersymmetrischen Ward-Identitäten untersucht.



## Acknowledgements

I am grateful to my PhD supervisor Prof. Dr. Gernot Münster for having introduced me to the world of Lattice Gauge Theory. I am very indebted to the Deutscher Akademischer Austausch Dienst (DAAD) for the scholarship in the program Research Grants for Doctoral Candidates under the matriculation: A/05/06300.

I would like to thank all my collaborators in our research group DESY-Münster collaboration: F. Farchioni, A. Ferling, I. Montvay, E.E. Scholz, T. Sudmann and J. Wuilloud for many fruitful discussions.

A special thank goes to Federico Farchioni for his patience, suggestions and the stimulating discussions we had.

The numerical simulations presented here have been performed on Blue Gene L/P and JuMP systems at JSC Jülich, Opteron PC-cluster at RWTH Aachen and the ZIV PC-cluster of the university of Münster. I thank all the staffs for their kind support.

# Contents

<b>Introduction</b>	<b>1</b>
<b>1 The Supersymmetry formalism and continuum <math>\mathcal{N} = 1</math> SYM model</b>	<b>8</b>
1.1 Poincaré algebra and its irreducible representations . . . . .	8
1.2 All possible (super-)symmetries of the S-matrix . . . . .	11
1.3 Supersymmetry multiplets . . . . .	14
1.4 $\mathcal{N} = 1$ Super Yang-Mills theory . . . . .	18
1.5 Low energy effective actions . . . . .	20
<b>2 Simulation of <math>\mathcal{N} = 1</math> SYM on the lattice and measurement methods</b>	<b>22</b>
2.1 Lattice action . . . . .	22
2.2 Improved actions and stout smearing . . . . .	25
2.3 Algorithms for numerical simulations . . . . .	25
2.3.1 Two-Step Multi-Boson algorithm (TSMB) . . . . .	26
2.3.2 Two-Step Polynomial Hybrid Monte Carlo algorithm (TS-PHMC) . . . . .	27
2.4 Monte Carlo measurements and Autocorrelation times . . . . .	30
2.5 Reweighting method . . . . .	33
2.6 Matrix inversion . . . . .	34
2.7 Correlators and mass determination . . . . .	36
2.7.1 Adjoint mesons . . . . .	38
2.7.2 Gluino-glueballs . . . . .	39
2.7.3 Glueballs . . . . .	41
2.8 Methods to compute all-to-all propagators . . . . .	42
2.8.1 Improved Volume Source Technique (IVST) . . . . .	43
2.8.2 Stochastic Estimators Technique (SET) . . . . .	44
2.9 Lattice SUSY Ward Identities (WIs) . . . . .	45
2.10 Smearing methods . . . . .	47
2.10.1 APE smearing . . . . .	47
2.10.2 Jacobi smearing . . . . .	48
2.11 Variational method . . . . .	50
2.12 Confinement potential and Sommer scale $r_0/a$ . . . . .	52
2.12.1 Two-fit procedure potential method . . . . .	52

2.12.2	Force method and Creutz ratios . . . . .	54
2.13	Jackknifing and Blocking . . . . .	56
2.14	Linearization method . . . . .	57
2.14.1	Linearization error for effective mass . . . . .	58
2.14.2	linearization error for effective mass with variational methods . . . . .	59
<b>3</b>	<b>Numerical Analysis and Spectrum Results: TSMB</b>	<b>62</b>
3.1	Simulation details . . . . .	62
3.1.1	Simulation parameters . . . . .	63
3.1.2	Smallest eigenvalues . . . . .	65
3.1.3	Autocorrelation-time . . . . .	67
3.2	Confinement and physical scale . . . . .	69
3.2.1	Static potential . . . . .	69
3.2.2	Physical scale . . . . .	70
3.3	The low-lying spectrum . . . . .	73
3.3.1	The adjoint pion $a\text{-}\pi$ . . . . .	75
3.3.2	The pseudo-scalar $0^{-+}$ adjoint meson $a\text{-}\eta'$ . . . . .	80
3.3.3	The $a\text{-}a_0$ adjoint meson . . . . .	89
3.3.4	The scalar $0^{++}$ $a\text{-}f_0$ adjoint meson . . . . .	91
3.3.5	The $1^{++}$ $a\text{-}f_1$ adjoint meson . . . . .	92
3.3.6	The Glueball $0^{++}$ . . . . .	93
3.3.7	The Gluino-glueballs . . . . .	96
3.4	Lattice SUSY Ward-Identities . . . . .	103
3.5	The massless gluino limit . . . . .	105
3.5.1	OZI arguments . . . . .	106
3.5.2	Ward-Identities . . . . .	107
3.6	Masses from ratios of correlators . . . . .	109
3.6.1	The $a\text{-}\eta'$ adjoint meson from ratio of correlators . . . . .	110
3.6.2	The $a\text{-}f_0$ adjoint meson from ratio of correlators . . . . .	113
3.7	Summary of the spectrum analysis . . . . .	115
3.8	Further spin-1 states in the $\mathcal{N} = 1$ $SU(2)$ SYM theory . . . . .	118
3.8.1	Introduction . . . . .	118
3.8.2	Majorana-Link-Majorana Operator . . . . .	119
3.8.3	Parity and Charge Conjugation transformations . . . . .	121
3.8.4	Construction of the representation . . . . .	122
3.8.5	Correlation functions of Majorana-Link-Majorana (M-L-M) operator	126
3.8.6	Axial vector-like correlator . . . . .	129
3.9	Spin-1 states from splitting point operator . . . . .	130
<b>4</b>	<b>Numerical Analysis and Spectrum Results: TS-PHMC</b>	<b>132</b>

4.1	Simulation details . . . . .	133
4.1.1	Simulation parameters . . . . .	134
4.1.2	Smallest eigenvalues . . . . .	136
4.1.3	Autocorrelation-time . . . . .	138
4.2	Confinement and physical scale . . . . .	140
4.2.1	Static potential . . . . .	140
4.2.2	Physical scale . . . . .	141
4.3	Tuning the simulations towards massless gluino . . . . .	145
4.4	Masses of the low-lying spectrum . . . . .	149
4.4.1	The adjoint pion $a$ - $\pi$ . . . . .	150
4.4.2	The adjoint pseudo-scalar meson $a$ - $\eta'$ ( $J^{PC} = 0^{-+}$ ) . . . . .	151
4.4.3	The adjoint scalar meson $a - f_0$ ( $J^{PC} = 0^{++}$ ) . . . . .	168
4.4.4	The Glueball $J^{PC} = 0^{++}$ . . . . .	177
4.4.5	The Gluino-gluonballs . . . . .	183
4.5	Lattice SUSY Ward-Identities . . . . .	193
4.6	The massless gluino limit . . . . .	197
4.6.1	Gluino condensate . . . . .	200
4.7	Summary and discussion . . . . .	204
<b>Conclusions and Outlook</b>		<b>210</b>
<b>A Dirac matrices, Majorana fermions and fermion matrix</b>		<b>213</b>
<b>B Preconditioning</b>		<b>215</b>
<b>C Spin <math>J^{PC}</math> on the lattice</b>		<b>216</b>
C.1	Irreps of the cubic group $O_h$ . . . . .	216
C.2	Orthonormal basis ONB . . . . .	218
<b>D Scaling and <math>\beta</math>-function</b>		<b>220</b>
<b>E Majorana-Link-Majorana correlators</b>		<b>222</b>
<b>Bibliography</b>		<b>224</b>

# Introduction

Supersymmetry (SUSY) is one of the most beautiful recent ideas in physics. It enables fermions to transform into bosons and vice versa. Thus generically the supercharge acts as

$$Q|\text{boson, fermion}\rangle = |\text{fermion, boson}\rangle . \quad (0.1)$$

This symmetry admits particles of integer and half-integer spin in common symmetry multiplets (supermultiplets). This leads to a doubling of the particle spectrum of the Standard Model (SM) in Physics, the theory of electroweak and strong interactions. Each particle in SM acquires a superpartner with similar properties and differing by one-half in spin. Even if not yet observed, SUSY is still one of the most fascinating theories and attractive field of research in contemporary physics. SUSY is believed to be relevant in the physics beyond the SM, it offers the most compelling solution to stabilize the *hierarchy problem* in the SM. There is unfortunately no direct evidence for SUSY, as no superpartner has yet been observed. For example, the bosonic partner of the electron, the "*Selectron*" which should have identical mass as the electron, is lying yet undiscovered. Therefore, if SUSY is a symmetry of the real world, at all it must be broken: The masses of supermultiplet members are split by SUSY breaking effects being of order  $M_{SUSY} \sim 10^2 - 10^3$  GeV. The superpartners are then expected at higher energy range of  $\mathcal{O}(\text{TeV})$ , and possibly discovered in forthcoming high energy accelerator experiments probing these energies. This is one of the major goals of the Large Hadron Collider (LHC) [1]; discovering the supersymmetric particles. At the moment, there is just an indirect evidence for SUSY: in the supersymmetric extended standard model, known as the Minimal Supersymmetric Standard Model (MSSM) the matching of the running gauge couplings occurs around Grand Unification Theory (GUT) scale  $m_{GUT} \approx 2 \cdot 10^{16}$  GeV (see Fig. 0.1).

The SM of particle physics, the most successful model of particle physics, predicts with high accuracy the outcome of experiments. In SM, matter consists of quarks and leptons (and associated anti-particles), which are described by quantum field theories possessing local gauge symmetry. The gauge symmetry group of SM is  $SU(3)_C \times SU(2)_L \times U(1)_Y$ . The subscripts  $C, L, Y$  refer respectively to color, left chirality (or weak isospin) and weak hypercharge. The gauge group  $SU(3)_C$  is associated to the Quantum Chromo Dynamics (QCD), the theory of strong interaction, while this symmetry group involved in the electroweak (EW) theory ( $SU(2)_L \times U(1)_Y$ ). All fermion fields (quarks and leptons) of

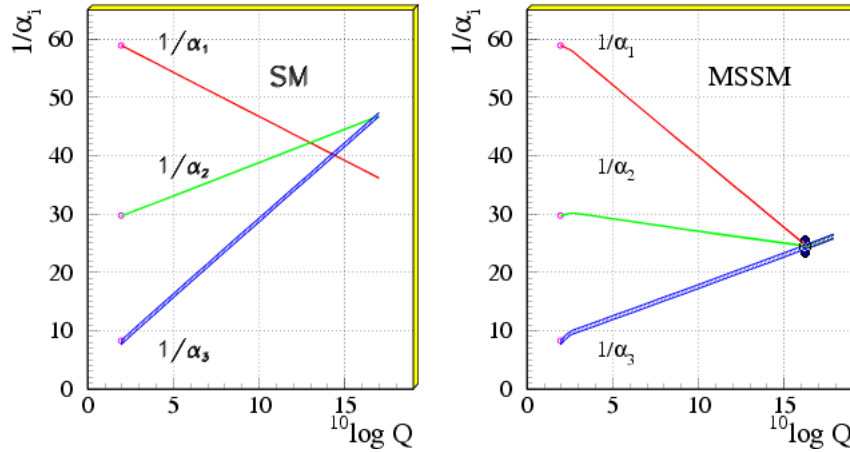


Figure 0.1: Gauge running coupling unification in non-SUSY GUTs on the left vs. SUSY GUTs on the right using the LEP data as of 1991. [2]

SM are fields with left-handed ones transforming as doublets and right-handed ones as singlets of  $SU(2)_L$ . The SM describes how quarks and leptons interact with each other through the exchange of *gauge bosons*: gluons for strong force,  $W^\pm$  and  $Z$  bosons for weak force and photons for electromagnetic interactions. The Higgs mechanism is an essential ingredient of the SM, because it explains how the fundamental particles obtain their mass through the electroweak (EW) symmetry breaking which occurs at a scale  $m_W \approx 10^2$  GeV. In fact, the vacuum in SM is not empty, but is instead filled with a condensate of Higgs particles. The particles derive their masses by their continuously interacting with the Higgs condensate. The Higgs particle is expected not to be much heavier than the top quark with a mass  $\approx 175$  GeV.

However, in spite of all success of SM, it is unlikely to be the complete theory of fundamental interactions and many questions are left unanswered. For example, it fails to cleanly integrate gravity with the other forces, and also because new observed phenomena such as *neutrino oscillations*. This phenomenon implies a non vanishing mass for the neutrino. This cannot be explained within the scope of SM where neutrinos are massless. The matter fields acquire their masses from their left and right handed couplings to the Higgs field. However, while there are only left-handed neutrinos in SM. A right-handed version of the neutrino field is added by the popular *seesaw mechanism* resulting in a heavy right-handed neutrino mass close to the GUT scale. Thus, this is a first jump to physics beyond SM. Furthermore, right-handed neutrinos can help to explain the origin of the matter through *leptogenesis* (process of lepton creation after the Big Bang). Therefore, there are good reasons to expect that SM is only an approximation to some, more global, theory of leptons and quarks. The underlying theory could be either based on larger gauge group of all interactions, including strong

interactions and gravitation, or a theory of more elementary particles which would, in some sense, constitute the known leptons and quarks.

There are also some lacks related to the missing piece of SM; the Higgs particle. The Higgs derives its mass from coupling to the Higgs condensate, in addition, it gains mass from radiative corrections where virtual fermion loops contribute to the Higgs mass. As arbitrary large energies for virtual loops are allowed, this makes the Higgs mass arbitrary large. This is known as the *gauge hierarchy problem*. The solution would be to find a symmetry which protects the Higgs mass from diverging quantum corrections. When computing the quantum correction in SUSY, each SM particle and its superpartner contributes equally to the Higgs mass but with opposite sign, so each other cancels. This is known as the *stabilization* of the hierarchy problem.

SUSY first appeared in the early seventies as a symmetry of the two dimensional world sheet in the context of string theory. The string theory is a unification candidate of gravity with SM. Furthermore, when a local supersymmetric theory is considered, supersymmetric gauge theory can be constructed and gauge and gravitational interactions can be connected. This is realized by supersymmetric Yang-Mills theories (SYM). The gravity can be enlarged to a supersymmetric theory of matter and gravitation, also known as the theory of supergravity (SUGRA).

In the last three decades, together with the theoretical and experimental particle physics a third tool appeared, the simulations of QFTs on computers. Numerical simulations also offer methods and approaches to explore energies which still not accessible within the today available experiments or due to high costs. This allowed successfully investigations of many properties of strongly coupled gauge theories like QCD at large distances non-perturbatively. At first, a well-defined mathematical formulation of the theory is required at the non-perturbative level. A viable work which led to these achievement was provided by K.G. Wilson in 1974 [3], who first provided the lattice formulation of QCD or the lattice gauge theory (LGT). Besides the possibility of evaluating the path integral non-perturbatively, this formulation reduces the infinite number of degrees of freedom of QFT to a finite number number by introducing a finite space-time lattice. Hence the quantum field theory can be put on a computer. This was the starting point for beginning the interesting perspective to solve QCD by applying numerical simulations. The use of Monte Carlo (MC) methods for studying LGT was carried out few years after Wilson formulation. Creutz *et al.* adapted MC techniques to study of LGT [4]. The first computer simulations involving fermions began two years later. Moreover, nowadays LGT has established itself as an integral part of theoretical elementary particle physics and has become a multidisciplinary science: it is a mixture of quantum field theory, statistical physics, numerical analysis and high performance computer science. The development in computer algorithm and the exponential rise of the nowadays available computer capacity made the LGT a powerful an robust predictive tool. There are many questions that have been approached either numerically

or analytically through the framework of lattice regulator. These cover for example the computation of the hadron spectrum, hadronic matrix elements, exploring the electroweak sector of SM, properties of QCD and the vacuum structure. The most recent results and the present status of the whole subject come every year in the *Proceeding of the International Symposium on Lattice Field Theory*.

Since Wilson succeeded in formulating gauge theories on the lattice, it was of interest to ask whether there exists a lattice version of SUSY [5]. There were many attempts to formulate supersymmetric theories on the lattice and study the non-perturbative mechanism of supersymmetric gauge theories. However, difficulty immediately arises because the Poincaré algebra, which takes part in the supersymmetry algebra, is broken by space-time discretization. Thus, the supersymmetry requires the existing of a complex Grassmannian generator which satisfies

$$\{Q, \bar{Q}\} \sim P, \quad (0.2)$$

where  $P$  is the generator of infinitesimal translations. But on the lattice, there are no symmetries corresponding to infinitesimal translations, and the above relation cannot be fulfilled. On the euclidean space, the Lorentz invariance becomes simply the rotation invariance. The rotation group is then broken on the lattice to a finite set of rotation group elements which is the discrete cubic group  $O_h$  [6, 7]. The preserved discrete symmetry will serve to a restoration of the full Lorentz group in the continuum limit. In the case of SUSY no discrete subgroup is preserved and SUSY theory is only recovered in the continuum. One approach to deal with this problem is to construct lattice structures which directly display at least a subset of exact supersymmetry. This would be enough to guarantee that the full SUSY is restored in the continuum limit without fine tuning (see for example [8]). Early works achieved constructions of low dimensional lattice theories with explicit SUSY, however, the lattice actions were non-local which is not suitable for MC simulations. Another strategy is to use a (nonlinear) deformation of the continuum transformations on the lattice [9]. It remains then to show such lattice SUSY transformations resemble the SUSY transformations in the continuum limit even in the presence of quantum corrections to all orders in perturbation theory. Recently, there were new ideas for implementing SUSY on the lattice for a variety of  $4d$  SYM theories including  $\mathcal{N} = 4$ . The motivation is based on the (De)construction approach [10]<sup>1</sup>. However, a notable exception is the model considered in this work: the  $4d$   $\mathcal{N} = 1$  SYM theory which is treated separately. This case has a chiral symmetry, and the only relevant SUSY-violating operator, the mass term, is forbidden by chirality in the continuum limit when the bare gluino mass is set to zero. By fine tuning the bare parameters to the SUSY point, supersymmetry can only be recovered in the continuum limit. In this approach, the effective action suitable for MC simulations was formulated

---

<sup>1</sup>For a recent summary of the actual status of the subject see ref. [11]



by Curci and Veneziano (CV) in the form of Wilson fermions [12]. Therefore, in the last decade first steps have been taken to investigate SYM numerically using the CV effective action on the lattice with Wilson fermions. Besides the spectrum calculations, an independent way to study the SUSY restoration is through SUSY Ward-Identities (WIs). If SUSY is exact the supercurrent is conserved, so the WIs are fulfilled in the continuum limit up to  $\mathcal{O}(a)$  correction. This property is used to measure whether the SUSY point in parameter space is achieved, and therefore to tune bare parameters to find the SUSY point. A lot of effort to investigate numerically the spectrum, WIs and chiral phase transition of this system was pursued for several years by the DESY-Münster-Roma Collaboration (DMRC) (for a review see [13] and references therein.) There were also other studies based on chiral formulations. Domain Wall Fermions (DWF) exhibit explicit chiral symmetry and yield a chiral formulation in the limit of an infinite 5th dimension. In ref. [14], MC simulations of  $4d \mathcal{N} = 1$  SYM have been performed using DWF. The cost of such simulations is, however, high due to the residual mass parameter, so only limited results on the gluino condensate have been obtained.

The  $4d \mathcal{N} = 1$  supersymmetric-Yang-Mills theory is nothing but  $4d$  Yang-Mills with single, "one flavour", massless adjoint Majorana fermion field  $\lambda$  (the gluino  $\tilde{g}$ ). SYM is also characterized by rich low energy dynamics with interesting aspects as confinement and spontaneous chiral symmetry breaking. This is the basis of a strong theoretical interest to investigate supersymmetry non-perturbatively. Besides SUSY, the continuum  $4d \mathcal{N} = 1$  SYM is invariant under the anomalous  $U(1)_A$  chiral symmetry which coincides with the  $R$ -symmetry in supersymmetry. Due to the axial anomaly, in the case of  $SU(N_c)$  SYM, only a  $Z_{2N_c}$  subgroup of  $U(1)_A$  survives at the quantum level. This is spontaneously broken to  $Z_2$  by the condensation of the gluino bilinear,  $\langle \lambda\lambda \rangle \neq 0$ . The consequence of this spontaneous (discrete) chiral symmetry breaking pattern is the coexistence of  $N_c$  vacua with different orientation of the gluino condensate, and hence the existence of first order phase transition at zero gluino mass  $m_{\tilde{g}} = 0$ .

For the description of the low energy features of  $\mathcal{N} = 1$  SYM a low energy effective action has been proposed by Veneziano and Yankielowicz (VY) [15]. The action is built up from gauge invariant and colorless bound states. In analogy to QCD, these bound states are composite fields of gluons, gluinos or a mixing of them. At the SUSY point  $m_{\tilde{g}} = 0$ , these states are mass degenerate ( $M_H$ ) and can be combined to form a Wess-Zumino chiral supermultiplet. The VY supermultiplet consists of three composite states: a  $0^+$  scalar meson  $\bar{\lambda}^a \lambda^a$ , a  $0^-$  pseudoscalar meson  $\bar{\lambda}^a \gamma_5 \lambda^a$ , (the  $a$  refers to the adjoint representation.) and a spin- $\frac{1}{2}$  mixed gluino-gluon state  $\chi_H \equiv F_{\mu\nu}^a \sigma_{\mu\nu} \lambda^a$ . The later which is denoted with  $\chi_H$  has no analogy in QCD. However, in analogy to flavour singlet QCD the pseudoscalar meson is denoted with  $a - \eta'$ , and the scalar with  $a - f_0$ . Glueballs are absent in VY formulation.

The question of including dynamical degrees of freedom built up from gluons was solved several years later by Farrar *et al.* (FGS) [16, 17] by introducing an extra term.

At SUSY point, the low lying spectrum predicted by FGS low energy effective action predicts two supermultiplets with different masses where the VY supermultiplet is in fact the heavier one. The lighter one is consisting of: a  $0^+$  scalar glueball  $F_{\mu\nu}F_{\mu\nu}$ , a  $0^-$  pseudoscalar glueball  $\epsilon_{\mu\nu\rho\sigma}F_{\mu\nu}F_{\rho\sigma}$  and a lighter gluino-gluon bound state  $\chi_L$ . Moreover, in this FGS picture a non-zero mixing of  $a - f_0$  and  $0^+$  glueball can occur. In the case of mixing the bound states are arranged into two massive supermultiplets having mass  $M_-$  and  $M_+$  at the SUSY point (Fig. 0.2).

One of the interesting features is how the low energy spectrum is influenced by the *soft* supersymmetry breaking. The introduction of a non-zero small gluino mass  $m_{\tilde{g}} \neq 0$  leads to a mass splitting within each supermultiplet and the degeneracy is lifted. A qualitative behavior of the soft supersymmetry breaking pattern is represented in Fig. 0.2.

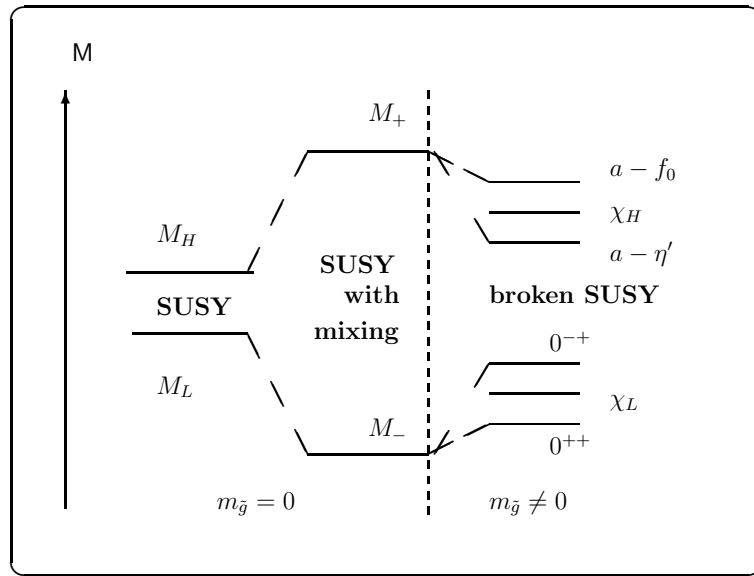


Figure 0.2: SUSY soft breaking scenario.

The SUSY soft breaking scenario and the SUSY point of  $\mathcal{N} = 1$  SYM can be investigated numerically within the lattice approach in the same way that is used in QCD. The Monte Carlo simulations are based on the CV effective gauge action with Wilson fermions. The discretized CV action is no longer SUSY where Wilson and mass terms are also added. The restoration of SUSY is only expected in the (infinite volume) continuum limit. This can be achieved by fine-tuning the only relevant parameter, the bare gluino mass, to its critical value corresponding to vanishing gluino mass. Both the mass spectrum and the WTIs calculations are used to find the SUSY point where the masses are expected to be reorganized in two supermultiplets.

The present work was carried out within the DESY-Münster collaboration (DMC). It

represents a continuation of the long-standing project of the collaboration, the recently obtained results are summarized in [18, 19, 20]. Previous collaboration investigations were carried out on quite fine lattices, but in small volume; this was suitable for the study of lattice SUSY WTIs [21], valid also in a finite volume. However, due to the smallness of the physical volume the mass spectrum can have significant finite volume effects. The gluino dynamics were included in the simulation by the Two-Step Multi Boson (TSMB) algorithm [22] which was developed as part of the collaboration. This algorithm, however, becomes less efficient when simulating at too light gluino mass values. Thus, the development of new dynamical algorithms was also stressed. Recently, new dynamical algorithms were developed. In the present simulations, the analyzed ensembles were prepared by the Two-Step Polynomial Hybrid Monte Carlo (TS-PHMC) algorithm [23], which is based on the Two-Step polynomial approximation [22]. Besides the new algorithmic implementation, improved actions are used in this work, mainly tree-level Symanzik improved gauge action and stout smearing. The goals of the present study are:

- Implementing the TS-PHMC algorithm.
- Performing tests to check the new algorithmic implementations by comparing to previous DESY-Münster results.
- Generate new coarser lattice with larger physical volume and perform fine-tuning toward sufficiently light gluino mass.
- Mass spectrum determination and lattice SUSY WTIs calculations<sup>2</sup>.
- Investigate new methods used in QCD to compute the disconnected propagators of the adjoint mesons correlators with more efficiency.

The SYM theory is also related to the one flavor QCD ( $N_f = 1$  QCD) which is also subject for investigations by the DESY-Münster collaboration [24].

The thesis is organized as follows: in Chapter 1 we give a review on the supersymmetric formalism and the low energy content of  $\mathcal{N} = 1$  SYM in the continuum in the sense of low energy effective models. Chapter 2 is devoted to the formulation of  $\mathcal{N} = 1$  SYM on the lattice and to the relevant techniques of analysis in numerical simulation of SYM. The simulation parameters, results and the analysis of the TSMB and the TS-PHMC ensembles are discussed in Chapter 3 and Chapter 4 respectively. Finally, we discuss, summarize the results and give prospects for the future investigations in the conclusion. Convention, notations and some technical aspects used throughout this work are, however, described in the appendices.

---

<sup>2</sup>We also analyzed TSMB ensembles which were available at the beginning stage of this work.

# 1 The Supersymmetry formalism and continuum $\mathcal{N} = 1$ SYM model

This chapter is devoted to the basic concepts of supersymmetry where a brief pedagogical overview of supersymmetry is given and the basic ideas are introduced. This symmetry enables fermions to transform into bosons and vice versa by means of transformations generated by spin- $\frac{1}{2}$  operators. We begin by reviewing the continuous symmetry of particle interactions observed so far, namely that of the Poincaré group and its irreducible representations (irreps). Then, we give a brief mathematical definition of the so-called  $\mathcal{Z}_n$  graded Lie algebra. In this sense, the Lie (super) algebra is defined as a  $\mathcal{Z}_2$  graded Lie algebra which has the first grading the Poincaré generators and the second grading spinorial generators. After that, the derivation of irreps of the superalgebra (super-Poincaré algebra) is presented. Then, we turn to the description of SUSY in the superfield formalism and the formulation of  $\mathcal{N} = 1$  SYM is given. Before writing the WTIs, the non-perturbative effects predicted by effective models are reviewed.

## 1.1 Poincaré algebra and its irreducible representations

The Lorentz group  $SO(3,1)$  is an invariance group of the Minkowski space  $\mathcal{M}$  in four dimension which differs from the Euclidean space by a non-trivial metric  $\eta_{\mu\nu} = \text{diag}(+, -, -, -)$ . The Lie algebra of the Lorentz group  $\mathfrak{so}(3,1)$  generated by the Lorentz generators  $M^{\mu\nu} = -M^{\nu\mu}$  ( $\mu, \nu = 0, \dots, 3$ ) can be written as a direct sum of two distinct copies of angular momentum algebra  $\mathfrak{su}(2)$ . Hence, each representation of the Lorentz algebra can be labeled by two half-integers:  $(j_1, j_2)$  where the dimension of the representation is  $(2j_1 + 1)(2j_2 + 1)$  and the sum  $j = j_1 + j_2$  is the spin of the representation. Thus, the irreducible representations in terms of fields introduce scalars, spinors and vector fields, ... etc. These objects are used to construct Lorentz-invariant Lagrangians for quantum field theories.

Besides invariance under Lorentz transformations, the invariance under space-time translations is also required. Translations plus Lorentz group form a group, called the inhomogeneous Lorentz group or commonly called the *Poincaré group*. Independently of their Lorentz properties (scalars, spinors, ...), all the fields behave as scalars under space-time translations. The action of the generators of translations on the fields is

then identified by the components of the energy-momentum four-vector  $P^\mu$ . Hence, the Poincaré algebra is generated by 10 generators: 6 Lorentz generators and 4 translation generators, it reads

$$\begin{aligned} [P^\mu, P^\nu] &= 0, \\ [P^\rho, M^{\mu\nu}] &= i(\eta^{\rho\mu}P^\nu - \eta^{\rho\nu}P^\mu), \\ [M^{\mu\nu}, M^{\rho\sigma}] &= -i(\eta^{\mu\rho}M^{\nu\sigma} - \eta^{\mu\sigma}M^{\nu\rho} - \eta^{\nu\rho}M^{\mu\sigma} + \eta^{\nu\sigma}M^{\mu\rho}). \end{aligned} \quad (1.1)$$

These relations mean that the translations  $P_\mu$  commute between them, however, translations do not commute with Lorentz rotations. Furthermore, the second commutation relation indicates that, under Lorentz group, translations transform as vectors. The Poincaré algebra is then not a direct sum of the Lorentz algebra and the translations group algebra, and it is said to be a semi-direct sum.

In quantum field theory of particle physics, the physical states of elementary particles are classified in terms of irreps of the Poincaré algebra given in eq. (1.1) where irreps are labeled by the eigenvalues of the Casimir-operators of the Poincaré algebra, that is, those operators that commute with the whole algebra. The first Casimir of Poincaré algebra is the square of the energy-momentum four-vector  $P^2 = P^\mu P_\mu$ . On single particle state it has as eigenvalue the mass square  $m^2$ . The second Casimir operator is given by  $W^\mu W_\mu$ , where

$$W^\mu = -\frac{1}{2}\epsilon^{\mu\nu\rho\sigma}M_{\nu\rho}P_\sigma \quad (1.2)$$

is called the Pauli-Lubanski pseudovector.  $\epsilon_{\mu\nu\rho\sigma}$  is the invariant tensor of  $SO(3,1)$  completely anti-symmetric with  $\epsilon^{0123} = +1$ . Furthermore, the  $W^\mu$  pseudovector obeys the following relation

$$[W_\mu, W_\nu] = i\epsilon_{\mu\nu\rho\sigma}P^\rho W^\sigma. \quad (1.3)$$

Then the Poincaré algebra has two Casimir operators

$$\{P^2, W^2\}. \quad (1.4)$$

To classify the representation, one must study the distinct interpretations of the Casimir  $W^2$  separately for the massive and the massless representations.

**Massive representations:** If the rest frame of the massive particle  $P^\mu = (m, 0, 0, 0)$  is considered,  $P^\mu$  can be left invariant by a group of transformations forming the *little group* which is in this case the group  $SU(2)$ . The Pauli-Lubanski pseudovector reads

$$\begin{aligned} W^0 &= 0, \\ W^i &= mJ^i, \end{aligned} \quad (1.5)$$

where  $J^i$  are the generators of the angular momentum algebra  $\mathfrak{su}(2)$ . The Pauli-Lubanski pseudoscalar extends to notion of spin where the relation in eq. (1.3) may be considered

as relativistic description of the angular momentum algebra. Therefore, on a single-particle state with mass  $m$  and spin  $j$  the square of the Pauli-Lubanski pseudovector is proportional to the Casimir of  $\mathfrak{su}(2)$  which yields the spin of the particle:

$$W^2 = -m^2 j(j+1) \quad , m \neq 0 . \quad (1.6)$$

The massive representations are therefore labeled by the mass  $m$  and by the spin  $j = 0, \frac{1}{2}, 1, \dots$ , which have  $2j + 1$  degrees of freedom.

**Massless representations:** In the massless case  $P^2 = 0$  and  $W^2 = 0$  there is no rest frame, but  $P^\mu$  can be reduced to the form  $P^\mu = (E, 0, 0, E)$  which describes a massless particle moving along the  $z$  axis. The rotations in the  $(x, y)$  plane leave  $P^\mu$  invariant and the little group can be restricted to be  $SO(2)$ . The "spin" for massless particle has another interpretation as for massive ones. The little group is generated by the angular momentum  $J^3$  and all its irreducible representations are one-dimensional. Therefore, a representation of the Poincaré algebra (a massless particle state) is labeled by one number; the eigenvalue  $h$  of  $J^3$  where  $h = 0, \pm 1/2, \pm 1, \dots$ . It is called *helicity*. Considering the constraint

$$W^\mu W_\mu |p\rangle = W \cdot P |p\rangle = P^\mu P_\mu |p\rangle = 0 , \quad (1.7)$$

on a physical massless state  $|p\rangle$  suggest that  $W^\mu$  is proportional to  $P^\mu$

$$W^\mu = h P^\mu . \quad (1.8)$$

The helicity represents the projection of the angular momentum along the direction of motion. Thus, the helicity can be written as

$$h = \frac{\mathbf{P} \cdot \mathbf{J}}{|\mathbf{P}|} . \quad (1.9)$$

However, the parity can also label the representation. Thus, under parity the helicity  $h$  transforms into  $-h$ , and the two helicity state must enter the theory preserving parity in a symmetric way. For example in electromagnetic the photon is defined as a representation of Poincaré group and also of parity, consequently the photon has two physical states with helicity  $h = \pm 1$  but not  $h = 0$ , which would appear if the photons were massive.

This is quite beautiful that we can label all the known fields in the universe according to the eigenvalues of the Casimirs of the Poincaré algebra. It is then obvious that except the two classes studied above, other classes can be also defined as irreducible representations of the Poincaré algebra. For example massless particles with continuous  $j$  and imaginary mass particles known as *tachyon* where  $P^2 < 0$ . Such classes are, however, probably unphysical while they have been never observed in the nature.

## 1.2 All possible (super-)symmetries of the S-matrix

The representations of Poincaré algebra correspond to physical particles in the real worlds like photons, electrons, ... etc. These particles can initially enter into interactions in particular process called the *scattering process* resulting in a final state of particles. The relations between the initial and final states in an interaction process are encoded in the scattering matrix: the  $S$ -matrix.

The **Coleman, Mandula theorem** (CM) [25] is generally accepted as the most precise and powerful in a series of no-go theorems about all possible symmetries of the scattering matrix. It is a rigorous result on the impossibility of combining the Poincaré algebra and other continuous symmetries in any but a trivial way. The proof of the CM theorem is based on some reasonable assumptions. These are: The  $S$ -matrix is nontrivial and analytic, the vacuum is non degenerate and each mass multiplet contains only finite number of different types of particles. A pedagogical review of the theorem may be found in [26]. The theorem makes the following statement on the full Lie algebra  $\mathcal{L}$  pertaining to all continuous symmetries of the  $S$ -matrix of a quantum field theory. *This Lie algebra contains as Lie subalgebras both the Poincaré algebra  $\mathcal{P}$  and any other Lie algebra  $\mathcal{T}$ . Then, the Lie algebra  $\mathcal{L}$  must be a direct sum of the two*

$$\mathcal{L} = \mathcal{P} \oplus \mathcal{T} . \quad (1.10)$$

In other word, the generators of the full algebra, apart from Poincaré generators, must be Lorentz scalars. Moreover, if the Lie algebra  $\mathcal{T}$  is defined by its generators as

$$[T^a, T^b] = iC_c^{ab}T^c , \quad (1.11)$$

then it must fulfill

$$\begin{aligned} [T^a, P_\mu] &= 0 , \\ [T^a, M_{\mu\nu}] &= 0 . \end{aligned} \quad (1.12)$$

The Poincaré algebra can only be conjoined with any other continuous symmetry of the  $S$ -matrix in a trivial way, as the case for internal symmetries.

However, there is a structure of Lie algebra which can be defined to evade the strait-jacket of the CM theorem. It does this by going beyond the notion of Lie algebras and embracing *graded* Lie algebras which involve, beside commutation relations, also anti-commutation relations of the form

$$h_a h_b - (-1)^{\eta_a \eta_b} h_b h_a = iC_{ab}^c h_c . \quad (1.13)$$

Here  $h_a$  are the generator of the graded algebra and  $\eta_a$  for each  $a$  are either 1 or 0 and is known as the grading of the generator  $h_a$ . In particular, this is the case of a  $Z_2$ -graded



Lie algebra<sup>1</sup>, where generators  $h_a$  for which  $\eta_a = 1$  are called fermionic; the other, for which  $\eta_0 = 0$  are called bosonic. The graded algebra is the mathematical concept behind the *supersymmetry*. The  $Z_2$ -graded structure can be then represented as

$$\begin{aligned} [bosonic, bosonic] &= bosonic, \\ [bosonic, fermionic] &= fermionic, \\ \{fermionic, fermionic\} &= bosonic. \end{aligned} \tag{1.14}$$

Here  $\{, \}$  stands for anti-commutator between fermionic generators. The subalgebra eq. (1.11) and eq. (1.12) must still obey the CM theorem and is identified to the bosonic sector of the graded algebra. The anti-commuting generators are fermionic degrees of freedom and hence have a spinor character by transforming as spinors under Lorentz group; these form the fermionic sector of the graded algebra and are called the *supercharges*  $Q_\alpha^I$  ( $\alpha = 1, 2; I = 1, \dots, \mathcal{N}$ ) or commonly SUSY generators, the subscript  $\alpha$  being the spinor index and  $I$  is a positive integer, and are included as extra spinorial fermionic generators of supersymmetry transformations. We restrict ourselves to one supercharge  $\mathcal{N} = 1$  (*simple supersymmetry*) as it is the case relevant in this work. In the presence of the fermionic generators  $Q_\alpha^I$ , the CM theorem is no longer valid and non-trivially combination of space-time symmetry (Poincaré) and other continuous symmetries can be constructed within the purview of graded algebra. Wess and Zumino [27] were the first to construct field theoretical models with a type of symmetry (originally called "supergauge symmetry") which connects bosonic and fermionic fields. The idea of supersymmetry was not envisaged by Coleman and Mandula and this concept had been covered by the **Haag, Lopuszanski, Sohnius theorem** [28] (HLS). Most of the assumptions of the CM theorem were used by HLS to determine all graded algebra structures consistent with relativistic quantum field theory.

The theorem states the following: *the most general continuous symmetry of the S-matrix, consistent with the assumptions of the CM theorem, is that pertaining to a  $Z_2$ -graded Lie algebra where the fermionic generators belong to the left/right representations  $(\frac{1}{2}, 0)$  and  $(0, \frac{1}{2})$  of the homogenous Lorentz group and the bosonic generators are a direct sum of the Poincaré and other (internal) symmetry generators (i.e the latter two subalgebras combined trivially).*

The HLS theorem states in part that fermion symmetry generators can only belong to the  $(\frac{1}{2}, 0)$  and  $(0, \frac{1}{2})$  representations. Thus, using the spinor notation, the complete set of fermionic symmetry generators can be divided into Weyl spinor  $(\frac{1}{2}, 0)$   $Q_\alpha^I$  generators and their  $(0, \frac{1}{2})$  hermitian adjoints  $\bar{Q}_{\dot{\alpha}}^I = (Q_\alpha^I)^\dagger$ , indicating the different transformation character by dotted or undotted indices. Furthermore, the HLS theorem allows non-trivial commutation relations between  $Q_\alpha$ ,  $\bar{Q}_{\dot{\alpha}}$  and  $P_\mu$ ,  $M_{\mu\nu}$  and that the fermionic

---

<sup>1</sup>The structure of Lie algebra can be, however, generalized to  $Z_n$ -graded algebra where  $n$  is positive integer.



generators may be defined so as to satisfy the anti-commutation relations

$$\begin{aligned}\{Q_\alpha, \bar{Q}_{\dot{\beta}}\} &= 2\sigma_{\alpha\dot{\beta}}^\mu P_\mu, \\ \{Q_\alpha, Q_\beta\} &= 0, \\ \{\bar{Q}_{\dot{\alpha}}, \bar{Q}_{\dot{\beta}}\} &= 0.\end{aligned}\tag{1.15}$$

Here, the first anti-commutator has very important properties which becomes more relevant when trying to construct SUSY on the lattice. It is probably the most amazing property of SUSY transformations: two successive SUSY-transformations are equivalent to a space-time translation. Finally, since  $Q, \bar{Q}$  are Weyl spinors their transformation properties with respect to the Poincaré group are already determined by the following commutation relations

$$\begin{aligned}[P_\mu, Q_\alpha] &= [P_\mu, \bar{Q}_{\dot{\alpha}}] = 0, \\ [M_{\mu\nu}, Q_\alpha] &= -(\sigma_{\mu\nu})_\alpha^\beta Q_\beta, \\ [M_{\mu\nu}, \bar{Q}^{\dot{\alpha}}] &= -(\bar{\sigma}_{\mu\nu})^{\dot{\alpha}}_{\dot{\beta}} \bar{Q}^{\dot{\beta}}.\end{aligned}\tag{1.16}$$

The simplest SUSY algebra  $\mathcal{N} = 1$  has one pair of supercharges  $Q$  and its hermitian adjoint  $\bar{Q}$ . These supercharges are two-component Weyl spinors and may be combined in terms of four-component Majorana spinor  $Q_a$  ( $a = 1, \dots, 4$ ) defined by

$$Q_a \begin{pmatrix} Q_\alpha \\ \bar{Q}_{\dot{\alpha}} \end{pmatrix}, \quad \bar{Q}_a (Q^\alpha \bar{Q}_{\dot{\alpha}}).\tag{1.17}$$

In two-component notation, the super-Poincaré algebra with simple supersymmetry now follows from equations (1.1), (1.15) and (1.16):

$$\begin{aligned}[P^\mu, P^\nu] &= 0, \\ [P^\rho, M^{\mu\nu}] &= i(\eta^{\rho\mu} P^\nu - \eta^{\rho\nu} P^\mu), \\ [M^{\mu\nu}, M^{\rho\sigma}] &= -i(\eta^{\mu\rho} M^{\nu\sigma} - \eta^{\mu\sigma} M^{\nu\rho} - \eta^{\nu\rho} M^{\mu\sigma} + \eta^{\nu\sigma} M^{\mu\rho}), \\ \{Q_\alpha, \bar{Q}_{\dot{\beta}}\} &= 2\sigma_{\alpha\dot{\beta}}^\mu P_\mu, \\ \{Q_\alpha, Q_\beta\} &= 0 = \{\bar{Q}_{\dot{\alpha}}, \bar{Q}_{\dot{\beta}}\}, \\ [P_\mu, Q_\alpha] &= 0 = [P_\mu, \bar{Q}_{\dot{\alpha}}], \\ [M_{\mu\nu}, Q_\alpha] &= -(\sigma_{\mu\nu})_\alpha^\beta Q_\beta, \\ [M_{\mu\nu}, \bar{Q}^{\dot{\alpha}}] &= -(\bar{\sigma}_{\mu\nu})^{\dot{\alpha}}_{\dot{\beta}} \bar{Q}^{\dot{\beta}}.\end{aligned}\tag{1.18}$$

A structure like above has evidently the structure of  $Z_2$ -graded Lie algebra defined in eq. (1.14), since it contains anti-commutators as well as commutators. The super-Poincaré algebra has 14 generators:  $P_\mu, M_{\mu\nu}$  and  $Q_\alpha, \bar{Q}_{\dot{\alpha}}$ .

We note that if the number of spinors pairs  $Q_\alpha, \bar{Q}_{\dot{\alpha}}$  is greater than one,  $\mathcal{N} > 1$ , one talks about extended supersymmetry in which additional index appears on the

generators  $Q_\alpha$ , so they become  $Q_\alpha^I, I = 1, \dots, \mathcal{N}$ . From the algebraic point of view there is no limit on  $\mathcal{N}$ , but with increasing  $\mathcal{N}$  the theories also must contain higher spin particles and there seem to be no consistent quantum field theories with spins larger than two (i.e supergravity) which make the restriction  $\mathcal{N} \leq 4$  or  $\mathcal{N} \leq 8$ . Extended supersymmetry is outside the scope of the present work which deals with theories with simple supersymmetry.

The supersymmetric particle spectrum of the super-Poincaré algebra can be derived in the same way as in the case of the Poincaré algebra, where the determination of the Casimir operators is relevant, and hence by constructing its irreducible representations (which are called supermultiplets) in both massless and massive case. For each irreducible representation the supersymmetry requires that the known particles (quark, leptons, ...) have to be accompanied by *superpartners* which have spins differing by units of one half to the particles spins. The number of the particles is then doubled.

### 1.3 Supersymmetry multiplets

The SUSY algebra contains the Poincaré algebra as a subalgebra, this means any representation of the SUSY algebra is also a representation of the Poincaré algebra, although in general not irreducible. Since each irreducible representation of the Poincaré algebra corresponds to a particle, a supermultiplet corresponds to several particles (particles and their superpartners). Furthermore, supersymmetry gives rise to some basic properties:

- In a (massive) supermultiplet all the particles have equal mass. This is obvious since the mass-squared operator  $P^2$  is still a Casimir operator of the supersymmetry algebra, since we have

$$[P^2, Q_\alpha] = 0 = [P^2, \bar{Q}_{\dot{\alpha}}] . \quad (1.19)$$

- The energy  $P^0$  of any non-vacuum state is positive definite. Let  $|\psi\rangle$  be any state, then from SUSY algebra we have

$$\begin{aligned} 4\langle\psi|P^0|\psi\rangle &= \langle\psi|\text{Tr}(\bar{\sigma}^0)\{Q, \bar{Q}\}|\psi\rangle \\ &= \langle\psi|Q_1\bar{Q}_1 + Q_2\bar{Q}_2 + \bar{Q}_1Q_1 + \bar{Q}_2Q_2|\psi\rangle \\ &= \langle\psi|Q_\alpha(Q_\alpha)^\dagger + (Q_\alpha)^\dagger Q_\alpha|\psi\rangle \\ &= ||Q_\alpha|\psi\rangle||^2 + ||(Q_\alpha)^\dagger|\psi\rangle||^2 \geq 0 , \end{aligned} \quad (1.20)$$

by positivity of the Hilbert space. Unlike the case of Poincaré symmetry, tachyons have not to be considered - they are forbidden by the fact that  $\{Q, \bar{Q}\}$  is positive definite.

- A supermultiplet contains an equal number of bosonic and fermionic states. We know that  $Q$  and  $\bar{Q}$  change a bosonic state  $|B\rangle$  into a fermionic one  $|F\rangle$ , and a fermionic state into a bosonic state. If  $N_F$  is defined as the fermionic number which takes 0 on bosonic state and 1 on fermionic state, then  $Q$  and  $\bar{Q}$  each changes the fermionic number by one unit, one may write

$$\begin{aligned}
Q(-)^{N_F}|B\rangle &= Q|B\rangle \\
&= |F\rangle \\
&= -(-)^{N_F}|F\rangle \\
&= -(-)^{N_F}Q|B\rangle \\
\Leftrightarrow Q(-)^{N_F} &= -(-)^{N_F}Q .
\end{aligned} \tag{1.21}$$

For any finite dimensional supermultiplet, one can compute the following trace on the representation space using the cyclic property and eq. (1.21)

$$\begin{aligned}
\text{Tr}[(-)^{N_F}\{Q_\alpha, \bar{Q}_{\dot{\beta}}\}] &= \text{Tr}[(-)^{N_F}(Q_\alpha \bar{Q}_{\dot{\beta}} + \bar{Q}_{\dot{\beta}} Q_\alpha)] \\
&= \text{Tr}[(-)^{N_F}Q_\alpha \bar{Q}_{\dot{\beta}} + Q_\alpha (-)^{N_F} \bar{Q}_{\dot{\beta}}] \\
&= \text{Tr}[(-)^{N_F}Q_\alpha \bar{Q}_{\dot{\beta}} - (-)^{N_F}Q_\alpha \bar{Q}_{\dot{\beta}}] \\
&= 0 .
\end{aligned} \tag{1.22}$$

It follows from the SUSY algebra eq. (1.18) that

$$2\sigma_{\alpha\dot{\beta}}^\mu \text{Tr}[(-)^{N_F}P_\mu] = 0 , \tag{1.23}$$

and hence for non-zero  $P_\mu$ , this reduces to

$$\text{Tr}[(-)^{N_F}] = 0 . \tag{1.24}$$

This means that the number of bosonic states is equal to the number of fermionic states in the supermultiplet, since  $(-)^{N_F}$  has value +1 on bosonic state and -1 on fermionic state. Furthermore, the state with zero-energy, the vacuum  $|0\rangle$ , the Poincaré invariant vacuum state  $P_\mu|0\rangle = 0$  is unique and SUSY invariant

$$\langle 0|P^0|0\rangle = 0 \Leftrightarrow Q_\alpha|0\rangle = 0 \text{ and } \bar{Q}_{\dot{\beta}}|0\rangle = 0 \text{ for all } Q . \tag{1.25}$$

Since we wish to characterize the irreducible representations of supersymmetry on asymptotic single particle states, exhibition of Casimir operators is needed. This can be done for  $\mathcal{N} = 1$ , the extension to  $\mathcal{N} > 1$  is straightforward. In order to classify the irreducible representations of the SUSY-algebra, it is worth finding the corresponding Casimir operators. The first immediate Casimir as discussed above is the mass squared

operator  $P^2$ . Due the supersymmetry algebra eq. (1.18), the energy-momentum generator  $P_\mu$  commutes with the supersymmetry generators  $Q$  and  $\bar{Q}$ , hence  $P^2$  also commutes. However, the square of Pauli-Lubanski spin pseudovector operator  $W^2$  is still not a Casimir of SUSY-algebra

$$[W^2, Q_\alpha] \neq 0. \quad (1.26)$$

This fact means that irreducible representations of SUSY-algebra contain different particles with different spins. One may construct the second Casimir from a generalization of the spin operator  $W^\mu$ . This generalized Pauli-Lubanski pseudovector does not depend only on  $P_\mu$  and  $M^{\mu\nu}$  but also on the SUSY generators  $Q$  and  $\bar{Q}$ . A simple choice is the four-component vector operator

$$Y^\mu = W^\mu - \frac{1}{4}Q\sigma^\mu\bar{Q}, \quad (1.27)$$

where the spinor indices in the last term are omitted. After some algebra, the commutator of  $Y_\mu$  reads

$$[Y_\mu, Y_\nu] = i\epsilon_{\mu\nu\rho\sigma}P^\rho Y^\sigma, \quad (1.28)$$

which has the same structure as the relation that the Pauli-Lubanski pseudovector obeys (1.3). It is called the *superspin* possessing in the rest frame  $P^\mu = (m, 0, 0, 0)$  the eigenvalues

$$\mathbf{Y}^2 = (Y^1)^2 + (Y^2)^2 + (Y^3)^2 = m^2 y(y+1) \text{ with } y = 0, \frac{1}{2}, 1, \dots \quad (1.29)$$

One can derive that the operator

$$C^{\mu\nu} = Y^\mu P^\nu - Y^\nu P^\mu \quad (1.30)$$

commutes with the momentum generator and the supersymmetry generators, and hence its square also does. Furthermore, the square of  $C_{\mu\nu}$  is Lorentz scalar

$$C^2 = C^{\mu\nu}C_{\mu\nu}, \quad (1.31)$$

which obviously commutes with the Lorentz generators  $M^{\mu\nu}$ . In the rest frame the eigenvalues of  $C^2$  are given by

$$C^2 = -2m^4 y(y+1), \quad (1.32)$$

Here,  $y$  are the super spin defined in eq. (1.29) which takes integer or half-integer values. Finally, the SUSY-algebra has two Casimir operators

$$\{P^2, C^2\}. \quad (1.33)$$

In the massive case, each supersymmetric irreducible representation is characterized by the pair  $(m, y)$ . Moreover, the states inside the representation are classified by the

eigenvalue  $my^3$  of  $Y^3$  and also by the eigenvalue  $mj^3$  of  $W^3$  because the latter commutes with  $Y^3$  exactly as they are classified by the Poincaré algebra  $|m, j, j^3\rangle$ .

Let us consider massless and massive particles separately:

**Massive case:** In this case we place in the rest frame  $P_\mu = (m, 0, 0, 0)$ . The anti-commutator of  $Q$  and  $\bar{Q}$  reads

$$\{Q_\alpha, \bar{Q}_{\dot{\beta}}\} = \begin{pmatrix} 2m & 0 \\ 0 & 2m \end{pmatrix}_{\alpha\dot{\beta}}, \quad (1.34)$$

and using the redefinition

$$a_\alpha = \frac{1}{\sqrt{2m}} Q_\alpha, \quad a_\alpha^\dagger = \frac{1}{\sqrt{2m}} \bar{Q}_{\dot{\alpha}}, \quad (1.35)$$

then the algebra (1.34) becomes the usual Clifford algebra

$$\{a_\alpha, a_\beta\} = \{a_\alpha^\dagger, a_\beta^\dagger\} = 0 \text{ and } \{a_\alpha, a_\beta^\dagger\} = \delta_{\alpha\beta}. \quad (1.36)$$

Let us now consider states  $|m, y^3, j^3\rangle$  from the representation  $(m, y)$  where  $y^3$  is fixed. These states are eigenstates of  $\mathbf{Y}^2, Y^3, \mathbf{W}^2$  and  $W^3$ . From among these states, one may always find one state which is annihilated by  $a_\alpha$ . This state is called the Clifford vacuum defined by

$$a_\alpha |\Omega_{Cliff}\rangle = a_\alpha |\Omega\rangle = 0. \quad (1.37)$$

Usually the vacuum corresponds to the absence of particles, however, the Clifford vacuum which satisfies the vacuum property being annihilated by  $a_\alpha$  corresponds to one particle states with superspin  $y^3 = s^3$ . Moreover by application of the creation operators  $a_\alpha^\dagger$  one constructs the following four states

$$|\Omega\rangle, a_\alpha^\dagger |\Omega\rangle, a_\alpha^\dagger a_\beta^\dagger |\Omega\rangle. \quad (1.38)$$

Sine one has the commutation  $[Y^3, Q] = [Y^3, \bar{Q}] = 0$ , the eigenvalue  $y^3$ , which is the same for the states in (1.38), is unchanged by application of  $Q$  or  $\bar{Q}$  operators. Therefore, each SUSY representation  $(m, y)$  has the dimension  $4(2y + 1)$  where each  $y^3$  has a corresponding Clifford vacuum. For  $y = 0$  and  $y = 1/2$  one obtains the chiral and vector supermultiplets respectively.

**Massless case:** Since  $P^2 = 0$ , one may choose the frame in which the four momentum is  $P_\mu = E(1, 0, 0, 1)$ , where  $J^3$  measures the helicity  $h = \pm j^3$  and  $W^\mu = hP^\mu$ . In this case

$$\begin{aligned} C^2 &= -2E^2(Y_0 - Y_3)^2 \\ &= -2E^2(W_0 - \frac{1}{4}Q\sigma_0\bar{Q} - W_3 + \frac{1}{4}Q\sigma_3\bar{Q})^2 \\ &= -2E^2(W_0 - W_3 + \frac{1}{4}Q(\sigma_3 - \mathbb{1})\bar{Q})^2, \\ &= E^2(Q^2\bar{Q}^2)^2, \\ &= E^2(Q_1\bar{Q}_1)^2. \end{aligned} \quad (1.39)$$

The anti-commutator of  $Q$  and  $\bar{Q}$  can be written

$$\{Q_\alpha, \bar{Q}_{\dot{\beta}}\} = \begin{pmatrix} 0 & 0 \\ 0 & 4E \end{pmatrix}_{\alpha\dot{\beta}}. \quad (1.40)$$

In particular, the anti-commutator  $\{Q_1, \bar{Q}_1\}$  vanishes. Thus, on the positive definite Hilbert space  $Q_1 = \bar{Q}_1 = 0$  and hence eq. (1.39) yields  $C^2 = 0$ . Only the  $Q_2$  and  $\bar{Q}_2$  are left, which means half of the fermionic generators. Moreover, they may be redefined as

$$a = \frac{1}{2\sqrt{E}}Q_2, \quad a^\dagger = \frac{1}{2\sqrt{E}}\bar{Q}_2 \quad (1.41)$$

so that the supersymmetry algebra is now

$$\begin{aligned} \{a, a^\dagger\} &= 1, \\ \{a, a\} &= \{a^\dagger, a^\dagger\} = 0. \end{aligned} \quad (1.42)$$

In analogy to massless representation of the Poincaré group, for massless representation of the super-Poincaré algebra one can define a *superhelicity*  $\tilde{h}$ ;  $\tilde{h} = 0, \pm\frac{1}{2}, \pm 1, \dots$  where for a given superhelicity  $\tilde{h}$ , the corresponding representation (supermultiplet) describes two massless particles of helicities  $\tilde{h}$  and  $\tilde{h} + \frac{1}{2}$ .

The representations of the super-Poincaré representations can be realized in terms of fields on a superspace in analogy to Poincaré representations on Minkowski space. Therefore, supersymmetric quantum field theories can be constructed through a super-fields formalism. This introduces a superspace  $(x^\mu, \theta, \bar{\theta})$  which is a space enlarged by two anti-commuting Grassmannian coordinates  $\theta$  and  $\bar{\theta}$ . The superfields are then fields defined on superspace  $\Phi \equiv \Phi(x^\mu, \theta, \bar{\theta})$ . In the following we will show the case of supersymmetric quantum field theory, which are of our interest in this work, with gauge invariance and one supercharge  $\mathcal{N} = 1$ . Their related features are discussed in the next Section.

## 1.4 $\mathcal{N} = 1$ Super Yang-Mills theory

A construction of models of gluodynamics with SUSY and gauge invariance is based on the vector superfield  $V(x, \bar{\theta}, \theta)$  satisfying  $V^\dagger = V$  which transforms under transformations of the non-abelian gauge group as

$$e^V \rightarrow e^{-i\Lambda^\dagger} e^V e^{i\Lambda}, \quad (1.43)$$

with  $\Lambda$  a chiral superfield. A gauge and SUSY invariant action is obtained by introducing the spinor SUSY field strength  $W_\alpha$  as

$$W_\alpha = -\frac{1}{8}\bar{D}\bar{D}(e^{-2V}D_\alpha e^{2V}), \quad (1.44)$$

with the superspace derivative

$$D_\alpha = \partial_\alpha + i\sigma_{\alpha\dot{\beta}}^\mu \bar{\theta}^{\dot{\beta}} \partial_\mu, \quad \bar{D}_{\dot{\alpha}} = -\bar{\partial}_{\dot{\alpha}} - i\theta^\beta \sigma_{\beta\dot{\alpha}}^\mu \partial_\mu. \quad (1.45)$$

The  $\mathcal{N} = 1$  SYM action of  $SU(N_c)$  gauge group can be written

$$S_{SYM} = \text{Re} \left\{ \int d^4x d\theta d\bar{\theta} \text{Tr}_c [W^\alpha W_\alpha] \right\}. \quad (1.46)$$

The trace is over color space. In the Wess-Zumino (WZ) gauge the particle content of the vector  $V$  can be reduced to include a bosonic vector field  $A_\mu(x) = -igA_\mu^a(x)T^a$  ( $g$  denotes the gauge coupling), its supersymmetric partner, a complex Weyl spinor field  $\lambda_\alpha(x) = \lambda_\alpha^a(x)T^a$ , and an auxiliary non-dynamical field  $D$ . The fields are Lie-algebra-valued where  $T^a$   $a = 1, \dots, N_c^2 - 1$  are the generators of the gauge group  $SU(N_c)$ . In terms of these fields and after performing the Grassmannian integration on  $\theta$  the action (1.46) can be rewritten as

$$S_{SYM} = \int d^4x \mathcal{L}_{SYM} = \int d^4x \left\{ -\frac{1}{2} F_{\mu\nu}^a F^{a\mu\nu} + \frac{i}{2} \lambda^a \sigma_\mu (\mathcal{D}_\mu \bar{\lambda})^a - \frac{i}{2} (\mathcal{D}_\mu \bar{\lambda})^a \bar{\sigma}_\mu \lambda^a + \frac{1}{2} D^a D^a \right\}, \quad (1.47)$$

where  $F_{\mu\nu}^a$  is the field strength and the covariant derivative in the adjoint representation reads

$$(\mathcal{D}_\mu \bar{\lambda})^a = \partial_\mu \bar{\lambda}^a + g f_{abc} A_\mu^b \bar{\lambda}^c. \quad (1.48)$$

The SUSY transformations relate bosons and fermions and leave the action invariant. These transformations also commute with gauge transformations so that the resulting Noether current  $S_\mu(x)$  is gauge invariant. For  $\mathcal{N} = 1$  SYM the supercurrent is given by

$$S_\mu(x) = -\frac{1}{2} \sigma^{\nu\rho} F_{\nu\rho}^a \gamma_\mu \Psi^a. \quad (1.49)$$

where the Weyl spinor  $\lambda, \bar{\lambda}$  can be expressed in terms of Majorana bi-spinor  $\Psi$  in the adjoint representation of the gauge group as

$$\Psi = \begin{pmatrix} \lambda_\alpha \\ \bar{\lambda}^{\dot{\alpha}} \end{pmatrix}, \quad (1.50)$$

and consider the case where the Majorana field  $\Psi$  has a mass  $m_{\tilde{g}} \neq 0$ , the Lagrangian can be written

$$\mathcal{L}_{SYM} = -\frac{1}{4} F_{\mu\nu}^a(x) F^{a\mu\nu}(x) + \frac{i}{2} \bar{\Psi}^a \gamma^\mu (\mathcal{D}_\mu \Psi)^a - \frac{m_{\tilde{g}}}{2} \bar{\Psi}^a \Psi^a. \quad (1.51)$$

The auxiliary scalar field  $D^a$  are integrated out by usual Gauss integration since it has no kinetic term. The Lagrangian in (1.51) is now no longer invariant under supersymmetry transformations since the mass term breaks softly SUSY. However, in

the massless case besides SUSY invariance, the Lagrangian is invariant under a  $U(1)_A$  transformation of the gluino field  $\Psi$  which coincides with the so-called  $R$ -symmetry in supersymmetry. The  $U(1)_A$  transformation reads

$$\Psi \rightarrow e^{i\phi\gamma_5} \Psi . \quad (1.52)$$

This global *chiral* symmetry is anomalous with associated axial current  $J_\mu^5 = \bar{\Psi}^a \gamma_\mu \gamma_5 \Psi^a$  satisfying

$$\partial^\mu J_\mu^5 = \frac{N_c g^2}{32\pi^2} \epsilon_{\mu\nu\rho\sigma} F^{a\mu\nu} F^{a\rho\sigma} . \quad (1.53)$$

The anomaly leaves, however, a  $Z_{2N_c}$  subgroup of  $U(1)_A$  unbroken where the elements corresponds to

$$\phi = \phi_k \equiv \frac{k\pi}{N_c} , (k = 0, 1, \dots, 2N_c - 1) . \quad (1.54)$$

The discrete global chiral symmetry  $Z_{2N_c}$  is expected to be spontaneously broken to  $Z_2$  by a value of  $\langle \bar{\Psi}\Psi \rangle \neq 0$ . The consequence of this spontaneous chiral symmetry breaking is the existence of a first order transition at  $m_{\tilde{g}} = 0$ . There are  $N_c$  degenerate vacua related by transformations in the quotient group  $Z_{2N_c}/Z_2$ . A non-vanishing gluino mass  $m_{\tilde{g}} \neq 0$  breaks the degeneracy of the  $N_c$  ground states, such that in case of  $N_c = 2$   $\langle \bar{\Psi}\Psi \rangle > 0$  for  $m_{\tilde{g}} > 0$  and  $\langle \bar{\Psi}\Psi \rangle < 0$  for  $m_{\tilde{g}} < 0$ .

## 1.5 Low energy effective actions

In analogy with QCD, color confinement is expected to occur in SYM and the spectrum of the SYM is expected to consist of colorless bound states formed out from fundamental fields, namely gluons and gluinos. The exploration of the bound states can be carried out by means of low-energy effective actions. For  $\mathcal{N} = 1$  SYM theory a low-energy effective action has been constructed by Veneziano and Yankielowicz (VY) [15]. The low energy theory is found to be governed by three massive bound states occurring in a Wess-Zumino chiral supermultiplet:

- $\Psi^a \gamma_5 \Psi^a$ : a pseudo-scalar  $J^{PC} = 0^{-+}$  which is analogous to  $\eta'$  in QCD, hence the name  $a\text{-}\eta'$  is adopted.
- $\Psi^a \Psi^a$ : a scalar  $0^{++}$  which is named  $a\text{-}f_0$ .
- $\chi = F^{a\mu\nu} \sigma_{\mu\nu} \Psi^a$ : a spin- $\frac{1}{2}$  Majorana fermion. It has no analogy in QCD and it is consisting of a gluon and a gluino. This bound state is called gluino-gluonball.

One observes the absence of the glueballs in the VY formulation. Indeed, Farrar *et al.* [17] introduced an extra term in the YV action which solves the question of including pure gluonic dynamical degree of freedom in the low energy spectrum of  $\mathcal{N} = 1$  SYM.



Besides the heavier supermultiplet of VY, the theory has a lower massive supermultiplet which contains:

- $F^{\mu\nu}F_{\mu\nu}$ : a scalar glueball  $0^{++}$ .
- $\epsilon_{\mu\nu\rho\sigma}F^{\mu\nu}F^{\rho\sigma}$ : a pseudo-scalar  $0^{-+}$ .
- A lower gluino-glueball  $\chi$  bound state.

Moreover, in this formulation, a non-zero mixing of bound state in the  $0^{++}$  channel is expected. In the SUSY point  $m_{\tilde{g}} = 0$  the masses in each supermultiplet are degenerate. However, the introduction of a massive gluino breaks SUSY softly and the degeneracy within each supermultiplet is lifted. The picture of the qualitative behavior of SUSY soft breaking is presented in Fig. 0.2.

One of the major goal of lattice computations is the determination of the masses of the bound states presented above in order to study the behavior of soft breaking in supersymmetry. The methods needed to investigate the model using the lattice techniques will be discussed in the next chapter.

## 2 Simulation of $\mathcal{N} = 1$ SYM on the lattice and measurement methods

Multi-Boson algorithms with stochastic correction are applied in numerical simulation of SYM theory on the lattice with dynamical gluinos. In this chapter the lattice formulation of SYM in the Wilson fashion for gluinos and the algorithmic implementation of two-step multi-boson and two-step polynomial hybrid Monte Carlo are presented. The methods of measurements of relevant lattice quantities such the spectrum analysis techniques are also reported.

### 2.1 Lattice action

Several works in the past focused on answering the possibility of the successful formulation of the supersymmetry on the lattice [5, 9]. Some successful construction had been achieved for  $2d$  Wess-Zumino model [8]. Other constructions have been recently proposed for lattice supersymmetric theories with extended supersymmetry  $\mathcal{N} > 1$  [10]. But for higher dimensions and  $\mathcal{N} = 1$  supercharges a fairly big amount of work has been invested for showing the restoration of SUSY in the continuum limit. It can be seen from the anti-commutator

$$\{Q_\alpha, \bar{Q}_\beta\} \sim P_\mu, \quad (2.1)$$

that a lattice regularized version of a gauge theory is not SUSY since the Poincaré algebra (a sector of the superalgebra) is lost. A pioneering solution began in the work of Curci-Veneziano [12]. The simple idea behind this proposal is that, rather than trying to have some version of SUSY on the lattice, one should *let the lattice spoil SUSY if it so wishes*. The requirement is that SUSY, like chiral symmetry, should only be recovered in the continuum limit; that is, the limit of vanishing renormalized gluino mass. This formulation introduces the Wilson term in the action to solve the doubling problem [3] since a naive lattice formulation results in more fermions which could corrupt the exact balance of the bosonic (gluons) and fermionic (gluinos) modes required by supersymmetry.

Based on the above arguments the effective gauge lattice action of Curci-Veneziano

for  $\mathcal{N} = 1$  SYM theory with  $SU(N_c)$  gauge group reads

$$S_{CV} = \beta \sum_x \sum_{\mu\nu} \left[ 1 - \frac{1}{N_c} \text{ReTr} U_{\mu\nu} \right] - \frac{1}{2} \ln \det Q(U) . \quad (2.2)$$

where  $Q$  is the non-hermitian Dirac-Wilson fermion matrix for gluino with site, color and Dirac indices  $(xa\alpha)$  defined by

$$Q_{xy}^{ab}[U] = \delta_{xy} \delta^{ab} - \kappa \sum_{\mu=1}^4 (\delta_{x,y+\hat{\mu}} (1 + \gamma_\mu) V_\mu^{ab}(y) + \delta_{x+\hat{\mu},y} (1 - \gamma_\mu) V_\mu^{T*ab}(x)); \quad (2.3)$$

$V_\mu(x)$  is the gauge link in the adjoint representation, a real orthogonal matrix:

$$V_\mu^{ab}[U](x) = 2\text{Tr}\{U_\mu^\dagger(x) T^a U_\mu(x) T^b\} = V_\mu^{*ab}(x) = [V_\mu^{-1ab}(x)]^T. \quad (2.4)$$

( $T^a$  are the generators of the  $SU(N_c)$  group. In case of  $SU(2)$  one has  $T^a = \frac{1}{2}\sigma^a$  with the Pauli matrices  $\sigma^a$ .) Observe that  $\det Q \geq 0$  for Majorana fermions.

However,  $U_\mu(x)$  is the gauge link in the fundamental representation of the gauge group  $SU(N_c)$  which is related to the continuum parallel transporter  $A_\mu(x)$  by

$$U_\mu(x) = e^{-aA_\mu(x)} . \quad (2.5)$$

Such action is a particular case of an ordinary gauge theory with a Majorana fermion in the adjoint representation. Therefore, the only two parameters that define the continuum theory are the bare gauge coupling  $\beta = 2N_c/g_0^2$  and the bare gluino mass  $m_{\tilde{g},0} \propto \kappa^{-1}$  or equivalent  $\kappa^{-1} = (2m_{\tilde{g},0} + 8)$ . The continuum is realized by tuning the bare parameter to their critical values which coincides with  $\kappa \rightarrow \kappa_{cr}$  and  $g_0 \rightarrow 0$  (see Appendix D).

The factor in front of  $\ln \det(Q)$  in the Curci-Veneziano action eq. (2.2) reproduces the *absolute* value of the *Pfaffian* for Majorana fermions (see below). Effectively, it corresponds to a flavour number  $N_f = \frac{1}{2}$ . The sign of the Pfaffian can be included in a reweighting procedure (see below).

In terms of 4-component Majorana fermions  $\lambda_x$  the action for the gluino can be written

$$S_f = \frac{1}{2} \sum_{xy} \lambda_{yb\beta} C Q_{yb\beta, xa\alpha} \lambda_{xa\alpha} , \quad (2.6)$$

and the fermionic path integral reads

$$\int [d\lambda] e^{-\frac{1}{2} \lambda C Q \lambda} = \text{Pf}(CQ) = \text{Pf}(M) . \quad (2.7)$$

Here the *Pfaffian* of the anti-symmetric (in Dirac space) matrix  $M \equiv CQ$  of order  $N$  is introduced ( $C$  is the charge conjugation matrix). The explicit formula of the Pfaffian of a general anti-symmetric  $(2m \times 2m)$  matrix  $\mathcal{M}$  reads

$$\text{Pf}(\mathcal{M}) = \frac{1}{m! 2^m} \epsilon_{\alpha_1 \alpha_2 \dots \alpha_{2m-1} \alpha_{2m}} \mathcal{M}_{\alpha_1 \alpha_2} \dots \mathcal{M}_{\alpha_{2m-1} \alpha_{2m}} . \quad (2.8)$$

One can construct Dirac fields from Majorana fields and show that the path integral over Dirac fermions is the square of the path integral over Majorana fermion and therefore

$$\det(Q) = [\text{Pf}(M)]^2 . \quad (2.9)$$

The fermion matrix  $Q$  is not hermitian but can be related to the hermitian fermion matrix by

$$\tilde{Q} \equiv \gamma_5 Q = \tilde{Q}^\dagger , \quad (2.10)$$

hence the determinant  $\det(Q)$  is real.

Moreover, the spectrum of  $\tilde{Q}$  is doubly degenerate and, consequently, the fermion determinant is always non-negative. Therefore, the Pfaffian  $\text{Pf}(M)$  is real, but it can have any sign

$$\text{Pf}(M) = \sqrt{\det(Q)} \text{sgn}(\text{Pf}(M)) . \quad (2.11)$$

In the effective CV action eq. (2.2) the absolute value of the Pfaffian is considered. The omitted sign can be included in the reweighting procedure (see Section 2.5). The sign of Pfaffian can become an issue at lighter gluino masses where several configurations with negative sign of the Pfaffians are produced. However, it turns out that their effect on the averages is still smaller than the statistical fluctuations. We calculated explicitly the sign of the Pfaffian applying ARPACK Arnoldi, we followed in this case Ref. [24, 29]. The sign of the Pfaffian can be computed concentrating on the lowest real eigenvalue of the non-Hermitian fermion matrix  $Q$  where we have

$$\text{Pf}(M) = \prod_{i=1}^{N/2} \tilde{\lambda}_i = \prod_i |\lambda_i|^2 \prod_{j \neq i} \bar{\lambda}_j , \quad (2.12)$$

where  $\tilde{\lambda}$  are the doubly degenerate real eigenvalues of  $\tilde{Q}$ ,  $\lambda$  are complex eigenvalues of  $Q$  appearing in doubly degenerate complex pair  $(\lambda, \lambda^*)$  and  $\bar{\lambda}$  are doubly degenerate real eigenvalues of  $Q$ . Therefore, eq. (2.12) shows that the sign depends only on the real eigenvalues  $\tilde{\lambda}_i$  where all negative eigenvalues have to be determined explicitly in order to find the sign of the Pfaffian.

We turn now to calculate the expectation values of Majorana field by defining the path integral with an external source  $J_x$  [30] for the theory entirely in terms of gauge fields  $U$ ,

$$\mathcal{Z}[J] = \int \mathcal{D}[U] e^{-S_{CV}[U] - \frac{1}{2} \sum_{x,y} J(x) Q^{-1}(x,y) C^{-1} J(y)} , \quad (2.13)$$

$$= \int \mathcal{D}[U] \text{Pf}[CQ[U]] e^{-S_g - \frac{1}{2} \sum_{x,y} J(x) Q^{-1}(x,y) C^{-1} J(y)} . \quad (2.14)$$

$$(2.15)$$

The simplest case which is the two-point correlation function can be expressed by

$$\begin{aligned} \langle \mathcal{T} \{ \lambda_\alpha^a(x_1) \lambda_\beta^b(x_2) \} \rangle_S &= 2^2 \cdot \left\langle \frac{\delta}{\delta J(x_1)} \frac{\delta}{\delta J(x_2)} e^{-\frac{1}{2} \sum_{x,y} J(x) Q^{-1}(x,y) C^{-1} J(y)} \right\rangle_U \\ &= \langle \Delta_{\alpha\rho}^{ab}(x,y) C_{\rho\beta}^{-1} \rangle_U . \end{aligned} \quad (2.16)$$

where  $\Delta \equiv Q^{-1}$  is the gluino propagator matrix. The propagators  $\Delta$  are the relevant quantities needed to evaluate any correlation function involving several pairs of Majorana fields.

## 2.2 Improved actions and stout smearing

The lattice action defined in eq. (2.2) is a function of the lattice spacing  $a$  and bare parameters  $\beta$  and  $\kappa$ . This bare action is in the universality class of the SYM theory where  $a$  can be taken to zero. This choice is however not unique. There is in fact a wide class of actions belonging to the same universality class of the desired theory in the continuum limit. Some of these actions can be obtained by improvement which gives smaller discretization errors. In the gauge action part of the CV action besides the simple Wilson action (gauge part of eq. (2.2)), we have applied the tree-level Symanzik (tlSym) improved action. Therefore, besides plaquette  $U_{pl}$ , rectangular Wilson loops of perimeter six  $U_{rec}$  are included in the gauge action which now reads

$$S_g = \beta(c_0 \sum_{pl} \{1 - \frac{1}{N_c} \text{ReTr} U_{pl}\} + c_1 \sum_{rec} \{1 - \frac{1}{N_c} \text{ReTr} U_{rec}\}) , \quad (2.17)$$

with  $c_0 = 1 - 8c_1$  and  $c_1 = -1/12$  in the case of tlSym action.

Another improvement of our simulations is carried out by applying *stout* smearing [31] for the links  $U_\mu(x)$  in the Wilson-Dirac operator (2.3), which are defined as

$$U_{x,\mu}^{(1)} \equiv U_{x,\mu} \exp \left\{ \frac{1}{2} (\Omega_{x,\mu} - \Omega_{x,\mu}^\dagger) - \frac{1}{4} \text{Tr} (\Omega_{x,\mu} - \Omega_{x,\mu}^\dagger) \right\} , \quad \Omega_{x,\mu} \equiv U_{x,\mu}^\dagger C_{x,\mu} \quad (2.18)$$

where  $C_{x,\mu}$  is a sum over staples

$$C_{x,\mu} \equiv \sum_{\nu \neq \mu} \rho_{\mu\nu} \left( U_{x+\hat{\mu},\nu}^\dagger U_{x+\hat{\nu},\mu} U_{x,\nu} + U_{x-\hat{\nu}+\hat{\mu},\nu} U_{x-\hat{\nu},\mu} U_{x-\hat{\nu},\nu}^\dagger \right) . \quad (2.19)$$

We apply one step of smearing with smearing parameters  $\rho_{\mu\nu} = 0.15$  in all lattice directions.

## 2.3 Algorithms for numerical simulations

In this section we will give brief recapitulations of the updating algorithms used to produced the SYM configurations analyzed in this study. We used two variants of multi-boson algorithms to prepare our samples: i) at gauge coupling  $\beta = 2.3$  three ensembles

at hopping parameter values  $\kappa = 0.1955$ ,  $\kappa = 0.196$  and  $\kappa = 0.1965$  were prepared by the Two-Step Multi-Boson (TSMB) algorithm [22] on  $16^3 \cdot 32$  lattices. ii) at gauge coupling  $\beta = 2.1$  several  $16^3 \cdot 32$  and  $24^3 \cdot 48$  lattices were generated by the Two-Step Polynomial Hybrid Monte Carlo (TS-PHMC) algorithm [23].

In the multi-boson picture [32] for a theory with  $N_f$  mass-degenerate flavors the fermion determinant is approximated by a polynomial  $P_{n_1}^{(1)}$  of degree  $n_1$

$$|\det(Q)|^{2\alpha} = \{\det(Q^\dagger Q)\}^\alpha \simeq \frac{1}{\det P_{n_1}^{(1)}(Q^\dagger Q)}, \quad (2.20)$$

where  $N_f = 2\alpha$ . For SYM  $\alpha = 1/4$  and the polynomial satisfies

$$\lim_{n_1 \rightarrow \infty} P_{n_1}^{(1)}(x) \simeq x^{-\frac{1}{4}}, \quad x \in [\epsilon, \lambda], \quad (2.21)$$

where the interval covers the spectrum of  $Q^\dagger Q$ .

In the multi-bosonic representation of the determinant, the polynomial  $P_{n_1}^{(1)}$  can be written using its roots  $\rho$  occurring in complex conjugate pairs. Introducing local, complex boson (pseudo-fermion) fields  $\Phi^i(x)$ ,  $i = 1, \dots, n_1$  one can write the bosonic representation as

$$|\det(Q)|^{2\alpha} \simeq \prod_{i=1}^{n_1} \det \left[ (\tilde{Q} - \rho^*)(\tilde{Q} - \rho) \right]^{-1}, \quad (2.22)$$

$$= \int \mathcal{D}[\Phi^\dagger, \Phi] \exp \left\{ - \sum_{i=1}^{n_1} \sum_{xy} \Phi^{(i)\dagger}(y) \left[ (\tilde{Q} - \rho^*)(\tilde{Q} - \rho) \right]_{yx} \Phi^{(i)}(x) \right\} \quad (2.23)$$

The multi-boson action in eq. (2.23) is *local*, similarly to the gauge action, and now algorithms like Metropolis, heatbath or overrelaxation used in usual updating algorithms can be applied. This is used in the two-step multi-boson algorithm. An alternative is the use of an appropriate global algorithm like Hybrid Monte Carlo for the updating of the fields. In the following we discuss both implementations for the fermion determinant.

### 2.3.1 Two-Step Multi-Boson algorithm (TSMB)

The exact updating algorithm corresponds to extrapolate  $n_1 \rightarrow \infty$ . However, at light fermion bare mass, the fermion matrix  $Q^2$  assumes large condition number  $\frac{\lambda_{max}}{\lambda_{min}}$  which would require very high degree polynomials with  $n_1$  of the order  $10^3$ - $10^4$ . In turn, this produces large autocorrelations and a slow down of the algorithm. In the two-step approximation scheme a second polynomial  $P_{n_2}^{(2)}$  is introduced to correct for small deviations

$$\lim_{n_2 \rightarrow \infty} P_{n_1}^{(1)}(x) P_{n_2}^{(2)}(x) \simeq x^{-\frac{1}{4}}. \quad (2.24)$$

The multi-bosonic local updates are only realized in the first step with  $P_{n_1}^{(1)}$  which gives a crude approximation and hence  $n_1$  can be kept down to moderate values.  $P_{n_2}^{(2)}$

is taken into account by a *noisy correction step* (NC). In this step, a random vector  $\eta$  is generated according to the normalized distribution

$$\frac{e^{-\eta^\dagger P_{n_2}^{(2)}(\tilde{Q}[U]^2)\eta}}{\int [\mathcal{D}\eta] e^{-\eta^\dagger P_{n_2}^{(2)}(\tilde{Q}[U]^2)\eta}}, \quad (2.25)$$

and accept the change  $[U] \rightarrow [U']$  with probability

$$\min\{1, A(\eta; [U] \rightarrow [U'])\}, \quad (2.26)$$

where

$$A(\eta; [U] \rightarrow [U']) = \exp\left\{-\eta^\dagger P_{n_2}^{(2)}(\tilde{Q}[U']^2)\eta + \eta^\dagger P_{n_2}^{(2)}(\tilde{Q}[U]^2)\eta\right\}. \quad (2.27)$$

The noise vector  $\eta$  can be obtained from Gaussian-distributed vector  $\eta'$  by introducing a third polynomial  $P_{n_3}^{(3)}$  which approximates the the inverse square root of the polynomial  $P_{n_2}^{(2)}$  such we have

$$\eta = P_{n_3}^{(3)}(\tilde{Q}[U]^2)\eta' \simeq P_{n_2}^{(2)}(\tilde{Q}[U]^2)^{-\frac{1}{2}}\eta'. \quad (2.28)$$

The polynomial approximation in eq. (2.24) becomes only exact for infinite  $n_2$ . However, in most case finite values of  $n_2$  already give errors which are negligible compared the statistical fluctuations. A *correction step* is necessary when the smallest eigenvalue of  $\tilde{Q}^2$  drops below the low bound  $\epsilon$  of the approximation (see Section 2.5).

### 2.3.2 Two-Step Polynomial Hybrid Monte Carlo algorithm (TS-PHMC)

The Hybrid Monte Carlo (HMC) algorithms represent the most popular methods for the simulation of dynamical fermions. In our work we have produced a set of gauge samples using a more general version of HMC which can be applied for theories with odd number of flavors as in our case, the so-called Polynomial Hybrid Monte Carlo [33, 34, 35] combining HMC and multi-bosonic techniques. The correction of the algorithm within a two-step scheme as in TSMB was developed in Ref. [23] and the algorithm we used is called two-step polynomial hybrid Monte Carlo (TS-PHMC).

The only difference between TS-PHMC and TSMB is in the first updating step which produces new configuration. In TS-PHMC this can be replaced by PHMC trajectories. The rest within a two-step correction scheme is the same as in TSMB.

HMC algorithm are based on Molecular Dynamics by integrating discretized evolution equations a long a trajectory of length  $\tau$  divided in  $n$  some finite step-size  $\Delta\tau = \frac{\tau}{n}$ . Recall the polynomial approximation in eq. (2.21), PHMC algorithm is based on the Hamiltonian

$$H[P, \pi, U, \phi] = \frac{1}{2} \sum_{x\mu a} P_{x\mu j}^2 + \frac{1}{2} \sum_{xi} \pi^{(i)\dagger}_x \pi^{(i)}_x + S_g[U] + \underbrace{\sum_{yxi} \Phi^{(i)\dagger}(y) P_{n_1}^{(1)}(\tilde{Q}[U]^2) \Phi^{(i)}(x)}_{S_\Phi[U]} \quad (2.29)$$

where  $P_{x\mu i}$  and  $\pi_x^{(i)}$  are conjugate momenta for the gauge links  $U_\mu(x)$  and the pseudo-fermions  $\Phi^{(i)}(x)$ . In our simulations we omitted the term of the conjugate momenta  $\pi$  and we consider only the gauge conjugate momenta  $P_{x\mu a}$  in the adjoint representation ( $a = 1, 2, 3$ ) of the gauge group  $SU(2)$ . The partition function can be written in phase space as follows

$$\mathcal{Z} = \int \mathcal{D} [P, U, \Phi, \Phi^\dagger] e^{-H} . \quad (2.30)$$

Using HMC the starting configuration  $H[P, U, \Phi]$  can be changed along the discretized trajectory in phase space by solving the equations of motion up to end point  $H[P', U', \Phi']$ .

The computation of the trajectory needs classical equations of motion for the Hamiltonian and for the variables  $P$  and  $U$  to be solved using an integrator approximation. A popular integration is the Leapfrog integrator. We opted for an improved Leapfrog integrator introduced by Sexton-Weingarten [36] which is area conserving and reversible. In this integration scheme *multiple-time scales* division of the trajectory is used. To use the multiple-time scale we rewrite the Hamiltonian in eq. (2.29) as

$$H[P, U] = \frac{1}{2} \sum_{x\mu a} P_{x\mu j}^2 + S_0[U] + S_1[U] \quad \text{with} \quad S_0 = S_g, \quad S_1 = S_\Phi . \quad (2.31)$$

$n_0$  and  $n_1$  are the numbers of steps for  $S_0[U]$  and  $S_1[U]$ . For a trajectory with a length  $\tau$  the decreasing step-sizes for integration are defined by multiple-time scales as

$$\epsilon_1 = \frac{\tau}{n_1}, \quad \epsilon_0 = \frac{\tau}{n_1 n_0}, \quad (2.32)$$

where the explicit formulas for  $U$  and  $P$  steps as function of a given step-size  $\epsilon$  can be written

$$T_U(\epsilon) : U'_\mu(x) = U_\mu(x) \exp \left\{ i\epsilon \sum_{j=1}^3 \sigma_j P_{x\mu j} \right\}, \quad (2.33)$$

$$T_{S_i}(\epsilon) : P'_{x\mu j} = P_{x\mu j} - \epsilon D_{x\mu j} S_i[U], \quad i = 0, 1. \quad (2.34)$$

Here  $\sigma_j$  are the Pauli matrices, and the derivative  $D_{x\mu j}$  is defined by

$$D_{x\mu j} f(U_\mu(x)) = \left. \frac{\partial}{\partial \alpha} \right|_{\alpha=0} f(e^{i\alpha \sigma_j} U_\mu(x)). \quad (2.35)$$

The Sexton-Weingarten is a higher-order integrator which in the case of the Hamiltonian (2.31) consists of performing  $n_1$  of the following step

$$T_{S_1}(\epsilon_1/2) [T_0(\epsilon_0)]^{n_0} T_{S_1}(\epsilon_1/2), \quad (2.36)$$

where

$$T_0(\epsilon) = T_{S_0}(\epsilon/2) T_U(\epsilon) T_{S_0}(\epsilon/2). \quad (2.37)$$

We now state the rules for updating the configuration  $\{P, U, \Phi\}$ , hence the implementation of TS-PHMC trajectory goes as follows:



- i) Generate the gauge links  $U_\mu(x)$  randomly.
- ii) Generate conjugate momenta  $P$  according to the Gaussian distribution  $dP e^{-\frac{1}{2} \Sigma P^2}$ .
- iii) Generate the pseudo-fermion fields  $\Phi$  according to the Gaussian distribution of vector  $\eta$  where:  $\Phi = \bar{P}_{\bar{n}(1)}^1(\tilde{Q}^2)\eta \simeq P_{n_1}^{(1)}(\tilde{Q}^2)^{-\frac{1}{2}}\eta$ .
- iv) At a constant background field  $\Phi$ , integrate the equations of motion (MD) with respect to  $P$  and  $U$  using an approximate integrator eq. (2.36).
- v) Calculate the energy difference:  $\Delta H = H[P', U'] - H[P, U]$  and accept/reject the configuration with the probability  $\min\{1, e^{-\Delta H}\}$ .
- vi) Return to ii) if subsequence of PHMC trajectories are required before correction step.
- vii) Perform the noisy correction (NC) step as in TSMB by a polynomial  $P_{n_2}^{(2)}$ .
- viii) Store the new configuration generated, or the old configuration, as dictated by Metropolis (NC) test.
- ix) Return to ii).

Recall that the area conservation and reversibility implies the condition

$$\langle e^{-\Delta H} \rangle_U = 1, \quad (2.38)$$

which should be satisfied. This relation provides an easy check of the consistency of the algorithm.

The polynomial approximations  $P_{n_1}^{(1)}, \dots$  needed in the updating algorithms TSMB and TS-PHMC can be obtained in a recursive scheme providing least square optimization (for details see [37, 38]). The *deviation norm*  $\delta$  which is minimised for a given polynomial of order  $n$  in the *least-square approximation* scheme is defined as

$$\delta \equiv \left\{ \frac{\int_\epsilon^\lambda dx w(x) [f(x) - P_n(x)]^2}{\int_\epsilon^\lambda dx w(x) f(x)^2} \right\}^{\frac{1}{2}}. \quad (2.39)$$

Here  $f(x)$  is the function to be approximated and  $w(x)$  is a positive weight function actually chosen in our case to be  $w_1(x) = w_2(x) = x^{1/(2n_B)}$  and  $\bar{w}_1(x) = \bar{w}_2(x) = 1$ , respectively.

Further optimization can be applied to the algorithms. The condition number of the fermion matrix can be lowered by almost a factor of two using the Even/odd preconditioning of the fermion matrix ( see Ref. [39] and Appendix. B. In addition we have used *determinant breakup* [40, 41] to speed up the algorithms. In this case the fermion measure in eq. (2.20) is decomposed in the product of  $n_B$  terms

$$|\det(Q)|^{2\alpha} = [|\det(Q)|^{2\alpha/n_B}]^{n_B} \quad (2.40)$$

## 2.4 Monte Carlo measurements and Autocorrelation times

In a dynamical Monte Carlo sample, the Markov process produces during the updating configurations which have lots of similarities, they are by no mean independent. Meaningful results from lattice simulations need a good estimation of both statistical and systematical (bias) errors. The systematic errors are usually related to finite size effects,  $\mathcal{O}(a)$  discretization errors, not sufficiently good determinant approximation, quenching and many other sources. The general law is that the contribution of the systematic errors to the total error should be less than the contribution of the statistical one.

The measurements of a set of physical *primary* quantities are characterized by their *integrated autocorrelation time*  $\tau_{int}$ . One has not to perform measurements on the whole produced configurations but only on a subset of selected (independent) configurations with respect to the quantity of interest. The determination of the autocorrelation times is the key to find this subset of configurations.

If we consider their exact expectation values  $A_\alpha$ ,  $\alpha = 1, 2, \dots, N$  in the measurement sequence of  $N$  configurations the observed estimates for  $A_\alpha$  are given by

$$\bar{a}_\alpha = \frac{1}{N} \sum_{i=1}^N a_\alpha^i. \quad (2.41)$$

The deviations of  $a_\alpha$  from their true values are introduced by

$$\bar{\delta}_\alpha = \bar{a}_\alpha - A_\alpha, \quad (2.42)$$

where we state that these estimators are unbiased,

$$\langle \bar{\delta}_\alpha \rangle = 0. \quad (2.43)$$

The averages  $\langle . \rangle$  here denote the expectation value in an infinite sequence of identical measurements having the same statistics  $N$  as the actual measurement. The variance of  $A_\alpha$  is

$$\begin{aligned} Var(A_\alpha) &= \sigma_\alpha^2 \\ &= \langle \bar{\delta}_\alpha^2 \rangle \\ &= \langle \bar{a}_\alpha^2 - \langle A_\alpha \rangle^2 \rangle. \end{aligned} \quad (2.44)$$

The unnormalized autocorrelation function of the primary quatity  $A$  is given by [42, 43]

$$C(t) \equiv C_{AA}(t) = \langle a^i a^{i+t} \rangle - \langle a^i \rangle \langle a^{i+t} \rangle, \quad (2.45)$$

and the normalized autocorrelation function is given by

$$\rho(t) = \frac{C(t)}{C(0)}, \quad (2.46)$$

where  $i$  denotes the  $i$ -th configuration in the Markov chain and  $t$  its distance in the update iteration. The average  $\langle . \rangle$  here denotes the average on the sample of finite but large  $N$  configurations. For  $t \gg 1$  this function typically behaves exponentially like

$$C(t) \propto e^{-|t|/\tau} \quad (2.47)$$

which leads to the definition of the exponential correlation length  $\tau_{exp}$ :

$$\tau_{exp} = \lim_{t \rightarrow \infty} \sup \frac{t}{-\log|C(t)|}. \quad (2.48)$$

Thus,  $\tau_{exp}$  is the relaxation time of the lowest mode that couple to  $A$ , and it is finite on a finite set of generated configurations. In practice, the rate of convergence from an initial nonequilibrium distribution to the equilibrium is controlled by  $\tau_{exp}$ .

On the other hand, a more important quantity is the integrated autocorrelation time defined by

$$\tau_{int,A} = \frac{1}{2} \sum_{t=-\infty}^{\infty} \rho(t) = \frac{1}{2} + \sum_{t=1}^{\infty} \rho(t). \quad (2.49)$$

(the factor  $\frac{1}{2}$  is matter of convention.) The integrated autocorrelation time is more suitable to control the statistical errors in Monte Carlo measurement of  $\langle A \rangle$  where the true variance of  $A$  is given by

$$Var(\bar{a}) = \sigma^2(\bar{a}) \stackrel{N \rightarrow \infty}{\approx} \frac{2\tau_{int,A}}{N} (\bar{a}^2 - (\bar{a})^2). \quad (2.50)$$

Thus, the variance of  $\bar{a}$  is a factor  $2\tau_{int,A}$  larger than it would be if the configuration in the sample are independent. This means that the sample of  $N$  configurations contains  $N/(2\tau_{int,A})$  *effectively* independent configurations. It is then better in the measurement of  $A$  to skip about  $2\tau_{int,A}$  configurations between the measurements.

The autocorrelation times  $\tau_{exp}$  and  $\tau_{int,A}$  play different roles in Monte Carlo simulation.  $\tau_{exp}$  is characterizing the asymptotic decrease of the autocorrelation  $\rho(t)$ . At the equilibrium  $\tau_{int,A}$  tells us how often the measurements of the quantity  $A$  has to be performed for an effective use of computer time.

In practice, the calculation of  $\tau_{int,A}$  can be realized by introducing an optimized truncation (which introduces a bias [42])  $W$  in the sum in (2.49) with  $W \gg \tau$  and hence one needs a large sufficient number of available configurations about several hundred  $\tau$  ( $N \gtrsim 1000\tau$ ) [42]. In last years, new methods has been developed to find straightfully optimized values of  $W$  which is discussed in Ref. [44]. It is sometimes not possible to give reliable estimation of  $\tau_{int}$  due to low statistics at hands. For quantities (*secondary*) derived from primary quantities, other methods of estimationg errors can be used such Jackknifing with blocking (Section 2.13).

For a good estimation of  $\tau_{int}$  the summation cutoff  $W$

$$\tau_{int}(W) = \frac{1}{2} + \sum_{t=1}^W \rho(t), \quad (2.51)$$

has to be chosen with care. On one hand it has to be larger than the decay time  $\tau$  ( $W \gg \tau$ ) to get small bias, on the other hand with too large  $W$  the sample autocorrelations contain terms having excessive "noise" but negligible "signal". In previous works of the DESY-Münster Collaboration [45] for example, the exponential decay of the autocorrelation  $\rho(t)$  has been studied and at the first value of  $t$  where  $\rho(t)$  is negative (sign change) the value of the cutoff  $W$  is picked up, the autocorrelation starts to be dominated by its noise at this point.

In our work, besides this criterium of choosing  $W$ , we also use the "automatic windowing" introduced by Madras-Sokal in [42]:  $W$  is chosen to be smallest integer such that  $W \geq w\tau_{int}$  for some constant  $w$ . The experience shows that the constant  $w$  can be taken in the range  $6, \dots, 10$  then  $\rho(t)$  exhibits a slower decay than the expected exponential decay.

The variance of  $\tau_{int}$  is estimated using the Madras-Sokal formula [42] given by

$$Var(\tau_{int}) \approx \frac{2(2W+1)}{N} \tau_{int}^2. \quad (2.52)$$

Another estimation method of  $\tau_{int}$  has been proposed by Wolff in [44]. One starts from the hypothesis that  $\tau \sim c\tau_{int}$  where  $c$  is some scale factor  $c = 1, \dots, 2$  and the automatic windowing procedure is realized by studying the behaviour of the function  $g(W)$  for  $W = 1, 2, \dots$  defined by

$$g(W) = \exp[-W/\tau(W)] - \tau(W)/\sqrt{WN}. \quad (2.53)$$

where  $\tau(W)$  is defined as in eq. (2.51). One has to compute the function  $g(W)$  for  $W = 1, 2, \dots$  and pick up the value of  $W$  at which  $g(W)$  changes the sign (becomes negative.) The summation  $\tau_{int}$  is taken to the value of the found cutoff  $W$ . There is also a formula for estimating the error of  $\tau_{int}$  found within this method, it is given by

$$Var(\tau_{int}) \approx \frac{4}{N} (W + \frac{1}{2} - \tau_{int}) \tau_{int}^2. \quad (2.54)$$

For many primary quantities in work like plaquettes and smallest eigenvalue of  $\tilde{Q}^2$  we have seen that the windowing method of Madras-Sokal delivered  $W$  which is at most larger than the one obtained by the criterium of Wolff. However, the sum in eq. (2.51) from both methods is consistent which results in comparable values of error estimation.

The error computation for secondary quantities and related methods are postponed to Section 2.13 and Section 2.14.

## 2.5 Reweighting method

The multi-bosonic algorithms discussed in Section 2.3 are based on polynomial approximations and become exact only in the limit of infinitely high polynomial order:  $n_1 \rightarrow \infty$ . In the two-step scheme it becomes exact only for  $n_2 \rightarrow \infty$ . One would investigate the dependence of the quantities to fix the size of the systematic error of taking  $n_1, n_2$  finite. It is then enough that the error introduced by the polynomial approximations are smaller than the statistical error. However, this depends on the behavior of the smallest eigen-mode  $\lambda_{min}$  of  $Q^\dagger Q$ . For small fermion mass simulation and due to the limitation of the approximation some *exceptional configurations* with  $\lambda_{min} < \epsilon$  could be frequently generated. Instead of increasing the polynomial order it is better to perform another correction in a *measurement correction* step of expectation values. The measurement correction for SYM has been introduced in [46] by defining a fourth polynomial  $P_{n_4}^{(4)}(x)$ ,  $n_4 > n_3$ :

$$\lim_{n_4 \rightarrow \infty} P_{n_1}^{(1)}(x) P_{n_2}^{(2)}(x) P_{n_4}^{(4)}(x) = x^{-\frac{N_f}{2}} \quad , \quad x \in [\epsilon', \lambda] \quad . \quad (2.55)$$

We compute the correction factor by combining two methods: a fixed number  $m = 4-8$  of smallest eigenvalues  $\lambda_{min}^{(k)}$  are calculated exactly, then a stochastic estimation from noisy vectors  $\{\eta_i\}$  is performed on the subspace  $Q^\dagger Q$  orthogonal to the subspace of the computed smallest eigenvalues. The correction factor on a configuration  $U$  takes the form

$$C[U] \simeq \prod_{k \leq m} P_{n_1}^{(1)}(\lambda_{min}^{(k)}) P_{n_2}^{(2)}(\lambda_{min}^{(k)}) R[U] \quad , \quad (2.56)$$

where  $R[U]$  is given by

$$R[U] = \langle \exp\{\eta^\dagger [1 - P_{n_4}^{(4)}(\tilde{Q}^2)]\} \rangle_\eta \quad , \quad (2.57)$$

where the eigenspace of the set of computed eigenvalues has to be projected out from the noisy vectors  $\{\eta_i\}$ . Finally, the reweighted expectation value  $\langle \mathcal{O} \rangle$  including the Pfaffian sign is obtained by

$$\langle \mathcal{O} \rangle = \frac{\langle \mathcal{O} \text{sgn Pf}[U] R[U] \rangle}{\langle \text{sgn Pf}[U] R[U] \rangle} \quad . \quad (2.58)$$

The correction factor is a comfortable method to test the quality of the approximation. If the approximation by the first two steps  $n_1, n_2$  is already good enough, the expectation values are not affected by the correction factors ( $R[U] \simeq 1$ ).

The application of measurement correction is most important for quantities which are sensitive for small eigenvalues of the fermion matrix  $\tilde{Q}^2$  such as the gluino propagator  $Q^{-1}$ . An example is given in Fig. 2.1 where the effect of the correction factors on the effective mass of the adjoint pion  $a$ - $\pi$  is shown (left panel). The distribution of the correction factor on the ensemble simulated at lightest gluino mass  $\kappa = 0.202$  is presented in the right panel.

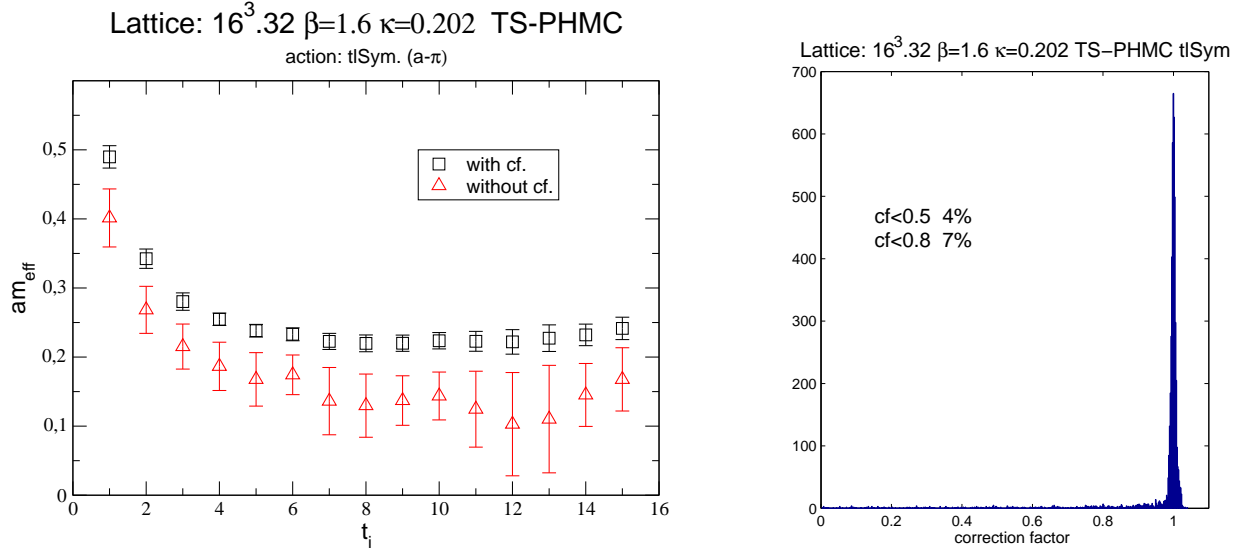


Figure 2.1: *Effect of the correction factor on the  $a - \pi$  effective mass (left panel). Distribution of reweighting factors. (Lattice:  $16^3 \cdot 32$   $\kappa = 0.202$ ).*

## 2.6 Matrix inversion

The correlation functions of operators having fermion degrees of freedom like adjoint mesons and the gluino-gluon correlators depends on the gluino propagators which are elements of inverse fermion matrix  $\Delta_{x\alpha\beta}^{yb\beta}$ . We use the standard inversion algorithm: Conjugate Gradient (CG) to invert the fermion matrix  $Q$ . Thus, instead of inverting the full matrix  $Q$ , an inversion is done by solving the equation

$$Qz = s, \quad (2.59)$$

to find a given column vector in the  $Q^{-1}$  matrix by fixing the source vector  $s$ . However, the conjugate gradient is used to invert positive hermitian matrix, where in the case of  $Q$  the matrix is neither hermitian nor positive definite. To reformulate the problem we multiply by  $Q^\dagger$  and the equation reads

$$Q^\dagger Qz = Q^\dagger s, \quad (2.60)$$

$$\tilde{Q}^2 z = b. \quad (2.61)$$

In praxis CG can be accelerated by using preconditioning and the simple  $L$ - $U$  decomposition. In our case we use the *even-odd preconditioning* (see Appendix B) where the preconditioned fermion matrix reads

$$\bar{Q} = L^{-1}QU^{-1}. \quad (2.62)$$

Using this relation in eq. (2.61) we find that the solution  $z$  can be written as

$$z = U^{-1} \gamma_5 (\tilde{Q}^2)^{-1} \tilde{Q} L^{-1} s. \quad (2.63)$$

Therefore, the source has to be multiplied by  $L^{-1}$  and  $\tilde{Q}$ , and then apply the conjugate gradient for the preconditioned matrix  $\tilde{Q}^2$ . The resulting vector has to be multiplied by  $U^{-1} \gamma_5$  to obtain the final solution  $z$ .

The number of iterations in the CG which encodes the number of Matrix-Vector-Multiplications (MVM) in the inversion depends on the source vector and the convergence condition. In our simulation we have fixed the residuum for CG stopping criterion in the inversion to  $10^{-12}$  for all runs. On  $16^3 \cdot 32$  lattices simulated in this work with TS-PHMC algorithm we observed that the number of CG iterations needed for the connected correlator  $a$ - $\pi$  varied from 470 to 20500 from  $\kappa = 0.18$  to  $\kappa = 0.202$  respectively.

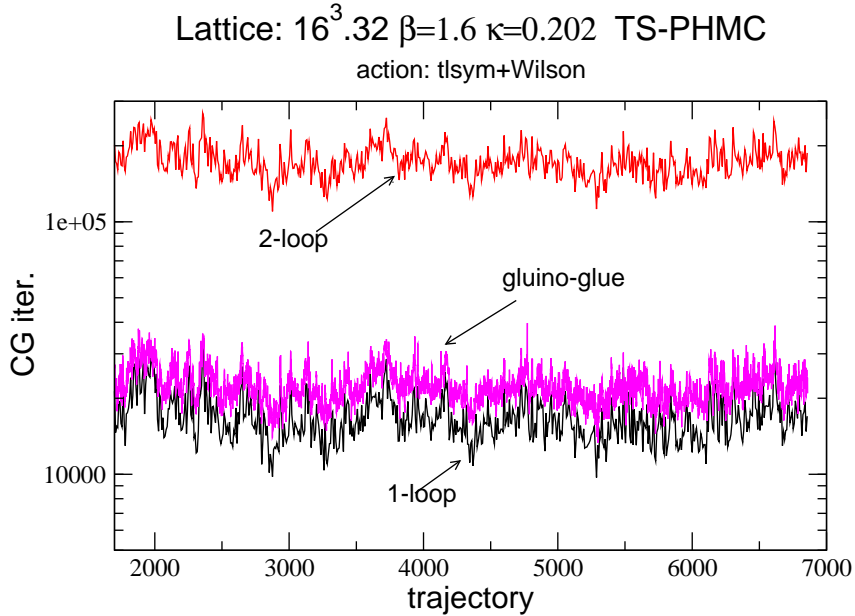


Figure 2.2: *History of CG iterations for the connected (1-loop), disconnected (2-loop) and gluino-gluon correlators.*

As can be seen in Fig. 2.2 the disconnected correlator is the most consuming of the computing time. Thus, the disconnected correlators need the computation of all-to-all propagators where the CG solver is called several times (up to  $\sim 44$ ). However, the connected and the gluino-gluon correlators need only  $2 \times 3$  inversions. Depending on the source vector as argued above the CG iterations in the inversion for the gluino-gluon correlator is greater than that for the connected correlator. In the latter the

source vector has one non-vanishing entry while the in the former the source vector has  $L^3$  non vanishing entires which rends the inversion less fast.

## 2.7 Correlators and mass determination

Spectroscopy is of great interest in lattice QCD calculations. Masses in QCD are determined from the asymptotic behavior of Euclidean-time correlation functions of interpolating operators. These operators are gauge invariant and are used to create the state of interest from the vacuum on the lattice. Of great interest in SYM theory with softly broken SUSY is the determination of the masses of particles (bound states) expected to be members of supermultiplets predicted by the low-energy effective actions [15, 17]. The structure of light color-singlet bound states is very similar to that of  $N_f = 1$  QCD which is actually investigated in our collaboration [24].

For the design of interpolating operators we use well-known operators in QCD for the adjoint mesons and the glueballs. The gluino-glueball states can be composed of any number of gluons and any number of gluinos, at least one of both.

In general there is a large number of choices of interpolating operators which have the same quantum number  $J^{PC}$  as the bound state. Some interpolating operators can have important projection on the bound state than the other. The experience, however, showed that the use of simplest color-singlets gives a good qualitative description. In the next subsections details will be given for interpolating operators used to simulate the low-lying bound states of SYM theory.

The correlation functions are used to measure many physical observables on the lattice. The main applications in our case besides the mass determination are the investigation of lattice SUSY Ward-Identities. A typical correlation function of an interpolating operator  $\mathcal{O}$  can be written as

$$C(x, y) = \langle \mathcal{O}^\dagger(x) \mathcal{O}(y) \rangle . \quad (2.64)$$

In physical process this is equivalent to a particle which is created at space-time point  $(y)$  *source*, from there it propagates in space-time to the point  $(x)$  *sink*. The Monte Carlo method allows us to represent the correlation function as the average of the operator  $\mathcal{A} = \mathcal{O}^\dagger(x) \mathcal{O}(y)$  evaluated on each of the  $N$  independent configurations  $U^{(i)}$  produced by the updating algorithm

$$\langle \mathcal{O}^\dagger(x) \mathcal{O}(y) \rangle_U \approx \frac{1}{N} \sum_{i=1}^N \mathcal{A}[U^{(i)}] . \quad (2.65)$$

For the extraction of masses the time-slice correlator is needed which is obtained by performing Fourier transform of the three spatial dimensions which fixes the momentum.



Fixing  $y$  in eq. (2.64) at the origin we write

$$C(x^0 = t, \mathbf{p}) = \frac{1}{L^3} \sum_{\mathbf{x}} C(x, 0) e^{i \mathbf{p} \cdot \mathbf{x}} . \quad (2.66)$$

It is common in spectroscopy to work in the rest frame by using the zero-momentum ( $\mathbf{p} = 0$ ) time-slice operators  $S_t$  by summing over the space site at a given time

$$S_t = \frac{1}{L^{3/2}} \sum_{\mathbf{x}} \mathcal{O}(\mathbf{x}, t) , \quad (2.67)$$

where now the correlation function at time-separation  $\Delta t = x^0 - y^0$  can be rewritten

$$C(\Delta t) = \langle S_{t+\Delta t}^\dagger S_t \rangle . \quad (2.68)$$

Inserting a complete set of energy eigen-states with zero-momentum that have the norm

$$\sum_n |n\rangle \langle n| = 1 , \quad (2.69)$$

into eq. (2.68) yields the spectral decomposition of the correlator

$$C(\Delta t) = \sum_{n=0} |\langle n | S_t | 0 \rangle|^2 e^{-E_n t} \pm |\langle 0 | S_t^\dagger | n \rangle|^2 e^{-E_n (T - \Delta t)} , \quad (2.70)$$

$$= a_0^2 + \sum_{n=1} a_n^2 e^{-E_n t} \pm a_n^2 e^{-E_n (T - \Delta t)} . \quad (2.71)$$

$T$  is the lattice extent in time direction. The signs ( $\pm$ ) refer to the chosen boundary conditions. In order to not break supersymmetry, periodic (+) boundary conditions in the spatial extent are applied for gluons and gluinos. In the temporal extent periodic (+) and anti-periodic (-) boundary conditions were adopted for gluons and gluinos respectively. Since we are in Euclidean space the correlator in eq. (2.71) is exponentially damped in time so as  $t \rightarrow \infty$  the lightest bound state corresponding to  $n = 1$  with energy  $E_1$  dominates the correlator. This lowest energy is the mass  $E_1 = m_1$  of the lowest bound state. The interpolating operator  $\mathcal{O}(x)$  has the same quantum  $J^{PC}$  as the lowest bound state of interest. Simple operators are created on one lattice site  $x$  known as *local* operators. It has been shown that for some bound states an interpolation operator that also includes some form of wave function between different lattice sites (extended operator) gives a better signal or overlap ( $a_1$ ). This technique is known as smearing as we will see below.

The constant  $a_0$  is non-vanishing for operators that can overlap with the vacuum such as scalars. It is common to omit this constant for scalars by redefining the time-slice operator  $S_t$  as

$$S_t \rightarrow \tilde{S}_t = S_t - \langle S_t \rangle_U , \quad (2.72)$$

where the vacuum expectation value of the time-slice operator is subtracted. The resulting subtracted time-slice operator  $\tilde{S}_t$  is inserted into eq. (2.68). At large time-separation  $\Delta t$  the mass of the lowest bound state can be extracted by fitting the numerically determined two-point correlation function eq. (2.68) to the following form

$$C(\Delta t) = a_1^2(e^{-m_1\Delta t} \pm e^{-m_1(T-\Delta t)}) , \quad (2.73)$$

in an interval  $\Delta t \in [t_{min}, t_{max}]$  with  $t_{min}$  high enough to ensure the dominance of the lowest mass  $m_1$  in the correlation function. This process should be done with care, because if  $t_{min}$  is set too high, there will be risks that useful information are thrown away, resulting on large error in the estimated value of the mass. One way to chose  $t_{min}$  can be done by varying  $t = t_{min}$  until chi square is good. By increasing  $t_{min}$  the excited states become less important and one would expect that the fitting function would be a good representation of the data. One common way to set the fitting interval is the calculation of the *effective mass* which is conceptually simpler to consider. It is defined at a given lattice time extension  $T$  and fixed time-slice pair  $t_1, t_2$  and denoted by  $m_{eff}(t_1, t_2; T)$  where throughout this work we used  $t_2 = t_1 + 1$ . The effective mass can be numerically determined through the formula [43]

$$m_{eff}(t) = \ln \frac{C(t)}{C(t+1)} . \quad (2.74)$$

If the fates are kind, plotting the effective mass  $m_{eff}(t)$  against time  $t$  will show a plateau where the lowest mass term dominates and the fitting range  $[t_{min}, t_{max}]$  can be set, allowing us to gain a lattice estimate of the mass. It is important to note that in practice the effective mass is much used as a rough guide since as noted above the effective mass depends only on pairs of time-slices and it does not incorporate as much information as the fitting procedure. We used both methods to extract the masses of the bound states. As described above we start by the effective mass calculation before performing one exponential fit to the function in eq. (2.73) in the  $t$ -range  $[t_1, t_2]$  where the effective mass stabilizes.

In the following we will give the form of the interpolating operators of our interest and their corresponding correlators which have to be numerically estimated by Monte Carlo methods.

### 2.7.1 Adjoint mesons

Colorless bound states of two gluino fields with spin-parity  $0^-$  and  $0^+$  are expected to be contained in a super-multiplet predicted by low-energy effective actions for  $\mathcal{N} = 1$  SYM theory. In analogy to single-flavor QCD we use the gauge invariant meson-type interpolating operators

$$\mathcal{O}_{a-f_0} = \bar{\lambda}\lambda \quad \text{and} \quad \mathcal{O}_{a-\eta'} = \bar{\lambda}\gamma_5\lambda , \quad (2.75)$$

for the adjoint mesons  $a$ - $f_0$  and  $a$ - $\eta'$  respectively, where  $a$  refers to adjoint representation.

Inserting the interpolating operator in the correlation function at source  $y$  and sink  $x$  and perform a straightforward calculation, we have

$$C(x, y) = \langle \bar{\lambda}(x) \Gamma \lambda(x) \bar{\lambda}(y) \Gamma \lambda(y) \rangle, \quad (2.76)$$

$$C(x, y) = \langle \text{Tr}_{sc}[\Gamma \Delta_{x,x}] \text{Tr}_{sc}[\Gamma \Delta_{y,y}] - 2 \text{Tr}_{sc}[\Gamma \Delta_{x,y} \Gamma \Delta_{y,x}] \rangle, \quad (2.77)$$

$$C(x^0 - y^0) = \frac{1}{L^3} \sum_x \sum_y \langle \text{Tr}_{sc}[\Gamma \Delta_{x,x}] \text{Tr}_{sc}[\Gamma \Delta_{y,y}] - 2 \text{Tr}_{sc}[\Gamma \Delta_{x,y} \Gamma \Delta_{y,x}] \rangle, \quad (2.78)$$

$$C(\Delta t) = \frac{1}{L^3} \sum_{x,y} \langle \text{Tr}_{sc}[\Gamma \Delta_{x,x}] \text{Tr}_{sc}[\Gamma \Delta_{y,y}] \rangle - 2 \sum_x \langle \text{Tr}_{sc}[\Gamma \Delta_{x,y_s} \Gamma \Delta_{x,y_s}^*] \rangle. \quad (2.79)$$

Here, we omitted the Dirac and color indices. The trace runs over Dirac and color spaces.  $\Gamma = \{\mathbb{1}, \gamma_5\}$  for scalar and pseudo-scalar respectively. The gluino propagator which is needed to calculate the correlation function is  $\Delta = Q^{-1}$ . In the last expression we use for the second term, which is known as *connected* term, translation invariance which allows instead of summing over  $x, y$  to fix the source  $y = y_s$  randomly on the lattice and calculate the all-to-point propagator  $\Delta_{x,y_s}$  within one inversion of the fermion matrix  $Q$ . The first term in eq. (2.79) is known as the disconnected term, appearing in singlet-flavor theories, needs the all-to-all propagators calculated from all sources to all sinks. This is, however, not computed exactly in Monte Carlo computation. Therefore, as the computation is considerably more difficult, methods based on stochastic processes are needed to estimate to a given degree the all-to-all propagators (see below).

Note that the factor 2 in front of the second term in eq. (2.79) is originating from Majorana character of the gluinos. The connected correlator is computed with standard methods. In the case of  $\Gamma = \gamma_5$  the connected term of the  $a$ - $\eta'$  correlator can usually be related to the unphysical pseudo-scalar particle  $a$ - $\pi$  which is used in SYM to signal the chiral limit  $m_{\tilde{g}} \rightarrow 0$ . The mass of  $a$ - $\pi$  should be vanishing in the chiral limit. Therefore, when approaching the supersymmetric limit the  $a$ - $\eta'$  is expected to remain massive and its correlator is dominated by its disconnected term.

### 2.7.2 Gluino-glueballs

A fermionic spin- $\frac{1}{2}$  bound state  $\chi_\alpha = \sigma_{\mu\nu} F_{\mu\nu}^a \lambda_\alpha^a$  of gluon and gluino is also predicted from low-energy effective actions to occur in a chiral supermultiplet. This color-singlet bound state has no analogy in QCD. A form of composite interpolating operator which can overlap with the gluino-glueball bound state has been proposed in [30]. We consider the local operator

$$\mathcal{O}^\alpha(x) = \sum_{i < j} \sigma_{ij}^{\alpha\beta} \text{Tr}_c[P_{ij}(x) \lambda^\beta(x)]; \quad (2.80)$$

where only spatial indices  $i, j$  are taken into account as to avoid contact terms from adjacent time-slices.  $P_{\mu\nu}$  is the clover-plaquette operator, the lattice transcription of the

field strength  $F_{\mu\nu}$ .

$$P_{\mu\nu}(x) = \frac{1}{8ig_0} \sum_{i=1}^4 (U_{\mu\nu}^{(i)}(x) - U_{\mu\nu}^{(i)\dagger}(x)) . \quad (2.81)$$

This choice gives the correct behavior under parity and time reversal transformations. The gluino-gluon time-slice correlator is built up from two plaquettes at source and sink connected by a gluino propagator line as illustrated in Fig. 2.3 and it reads

$$C^{\alpha\beta}(\Delta t) = -\frac{1}{4} \sum_{\vec{x}} \sum_{ij,kl} \left\langle \sigma_{ij}^{\alpha\alpha'} \text{Tr}[U_{ij}(x)\sigma^a] Q_{xa\alpha',ysb\beta'}^{-1} \text{Tr}[U_{kl}(y_s)\sigma^b] \sigma_{kl}^{\beta'\beta} \right\rangle . \quad (2.82)$$

where  $U_{ij}(x)$  is the simple plaquette.

To evaluate the correlator above we choose randomly a source  $y_s$  at time-slice  $y_s^0$ . Then, vector source  $w_{ij}^a(y_s) = \text{Tr}[U_{ij}(y_s)\sigma^a]$  is constructed on this time-slice covering it completely. Inversion is performed on  $w_{ij}^a(y_s)$  to obtain  $Q^{-1}w$  which is inserted in eq. (2.82) and the correlator is obtained by contracting and multiplying the remaining terms in eq. (2.82) accordingly.

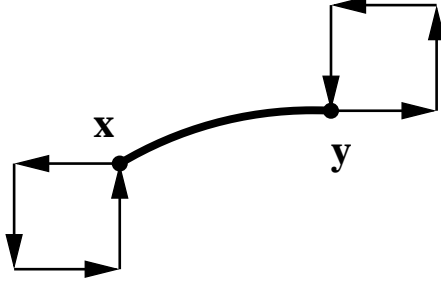


Figure 2.3: A graphical representation of the gluino-gluon correlator.

Because of the spinorial character of the gluino-gluon, its correlator  $C^{\alpha\beta}$  has a specific structure in Dirac space. By using various properties of parity  $\mathcal{P}$  and time reversal  $\mathcal{T}$  symmetries it can be shown [30] that the gluino-gluon correlation function has two non-vanishing components in the Dirac space differing by their time reversal symmetries

$$C^{\alpha\beta}(\Delta t) = C_{\mathbb{I}}(\Delta t)\delta^{\alpha\beta} + C_{\gamma_0}(\Delta t)\gamma_0^{\alpha\beta} , \quad (2.83)$$

where the real components  $C_{\mathbb{I}}$  and  $C_{\gamma_0}$  have the following properties under time reversal symmetries

$$C_{\mathbb{I}}(t) = -C_{\mathbb{I}}(T-t) , \quad (2.84)$$

$$C_{\gamma_0}(t) = C_{\gamma_0}(T-t) . \quad (2.85)$$

We used both components to have independent estimations of the gluino-gluon mass. These are also used in the evaluation of lattice SUSY WIs. However, the experience

showed that local interpolating operator  $\chi^\alpha$  does not lead to satisfactory signal, and smearing techniques have to be used for reliable extraction of low-lying mass.

### 2.7.3 Glueballs

The glueballs  $0^{++}$  and  $0^{-+}$  states are expected to occur in the lower supermultiplet of the low-energy spectrum of the  $SU(2)$  SYM. The glueball are well-established objects in Lattice Gauge Theory (for a review see [47]). The glueball presents difficulties, which closely resemble those encountered in glueball spectroscopy in QCD and, fortunately, can be overcome with the same type of techniques. In QCD, glueballs belong to the most notorious states to measure. The methods to extract their masses on the lattice are well known and largely used by the lattice community. As matter of information, the best results of the glueball masses in QCD available as today were obtained using the trick of anisotropic lattices by Morningstar and Peardon [48].

The glueball calculations face two major challenges, namely, constructing good lattice interpolating operators (Wilson loops of higher length, smearing techniques, etc..) and overcoming the noisy signal coming from their purely gluonic nature. The widely common simple interpolating operator which can be used to simulate the scalar glueball  $0^{++}$  on the lattice is the single space-like plaquette operators. The plaquettes are combined to give an operator which transforms irreducibly in the  $A_1$  representation of the cubic group on the lattice (see Appendix C.1). In the continuum this describes the ground state of particle with quantum number  $J^{PC} = 0^{++}$ .

As in the previous choice of the DESY-Münster collaboration, we used the single plaquette operator for the scalar glueball. The suitable interpolating operator on a lattice point  $x$  is a combination of spatial plaquettes given by

$$\mathcal{O}_{0^{++}}(U; x) = \text{Tr}[U_{12} + U_{23} + U_{31}] . \quad (2.86)$$

We also need an interpolating operator for the pseudo-scalar glueball with a content  $A_1^{-+}$  which is expected in  $SU(2)$  SYM. In order to create such operator from the vacuum with an operator built from closed loops, one needs a form of loops which cannot be rotated into their mirror image. When the gauge group  $SU(2)$  is considered, the traces of loop variable are real and the orientations become irrelevant. Operators with  $A_1^{-+}$  content obtained from Wilson loops of a length at least 8 were proposed for  $SU(3)$  in [49]. We use the loop  $\mathcal{C}$  shown in Fig. 2.4 in order to built  $SU(2)$  pseudo-scalar glueball.

The interpolating operator for the pseudo-scalar glueball is given by

$$\mathcal{O}_{0^{-+}} = \sum_{R \in \mathbf{O}_h} [\text{Tr } U(\mathcal{C}) - \text{Tr } U(\mathcal{PC})] . \quad (2.87)$$

The trace is over fundamental  $SU(2)$  indices. The sum is over all rotations  $R$  of the cubic group  $\mathbf{O}_h$  and  $\mathcal{PC}$  is Wilson parity-mirrored loop of the loop  $\mathcal{C}$ .

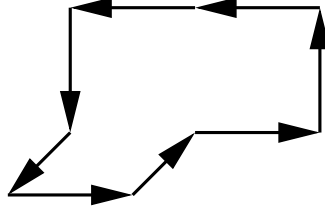


Figure 2.4: *Wilson loop  $\mathcal{C}$  of length eight used to build pseudo-scalar glueball*

We applied APE smearing and variational method [50, 48] to optimize the overlap of the glueball operators with the low-lying scalar glueball  $0^{++}$ . For the pseudo-scalar only APE smearing was applied. It turns out that the latter does not give a reasonable signal for mass extraction. This is postponed for future optimization of this channel. However, some interesting results were found for the scalar glueball in runs with stout smearing of the links in the Dirac-Wilson matrix (see Chapter 4).

## 2.8 Methods to compute all-to-all propagators

In this section the methods of computing all elements of the quark propagators are reviewed. The Hadron spectroscopy has traditionally been performed in lattice QCD by computing quark propagator from one point to all other points on the lattice the so-called point-to-all propagators which is done by inverting the fermion matrix with a point source on the lattice, and combining the resulting propagators with appropriate operators to determine for example the desired mesonic time-slice correlators  $C^{meson}(\Delta t)$ . This demands few computational efforts. In some theories with singlet flavour quantities, condensate and other quantities where the quark loops are occurring, building the correlators requires propagators with sources on all in lattice points. For this purpose, many methods have been used such noisy methods, variance reduction methods and some other methods [51, 52, 53, 54, 55, 56, 57, 58]. In this work the all-to-all propagators are required to build the adjoint mesons and the condensate. These methods can work fine for some theories and can be unsuitable for others, we have tested different methods in our case and compared them to find the optimal ones.

Because of the singlet-flavor nature of SYM, we have seen that the disconnected gluino loops appear in the adjoint meson correlation functions. These gluino closed loops are computed from the all-to-all propagators  $\Delta_{x,x}$  which cannot be calculated using standard matrix inversion technique. Furthermore, the signal for the correlation function is intrinsically noisy. There were many successful attempts to optimize computational techniques for an accurate determination of bound state masses in SYM. A novel method of computing disconnected diagrams in SYM was proposed in Ref. [51] which is based on

ideas of the volume source technique (VST) used in QCD [52]. The new version, which is applicable for SYM and in general for gauge theory with fermion in real representations of the gauge group, is called improved volume source technique (IVST) [51].

In the present work we applied IVST and Stochastic Estimator Technique in the spin explicit method variant (SET/SEM) introduced in Ref. [53] for the computation of the disconnected diagrams. We also performed some tests to implement other methods like spectral decomposition [54, 55] and dilution methods of Ref. [56] in addition to methods introduced in [57, 58] which should be used in the future investigations of the SYM project in order to obtain more accurate results.

In the following we will review the IVST and SET/SEM which are used throughout this work.

### 2.8.1 Improved Volume Source Technique (IVST)

As can be seen in the form of the adjoint meson correlation function eq. (2.79), the disconnected term of the correlator in the background of a gauge configuration  $\{U\}$  can be written

$$C_{disc}[U](\Delta t) = \frac{1}{L^3} \text{Tr}_s[\Gamma S(x_0)] \text{Tr}_s[\Gamma S(y_0)] \quad (2.88)$$

where  $S(x_0)$  is the time-slice operator which encodes the all-to-all propagators and is the trace over color and spatial indices of the fermion propagator which has to be evaluated on the background of the configuration  $\{U\}$

$$S_{\alpha\beta}(x_0) = \sum_{\mathbf{x}} \text{Tr}_c[\Delta_{x\alpha, x\beta}] . \quad (2.89)$$

The idea of volume source technique is based on inversion problem with a volume source  $\omega_V^{[a,\alpha]}$  which reads

$$Qz = \omega_V^{[a,\alpha]} = \sum_x \omega^{[x,a,\alpha]} , \quad (2.90)$$

The solution of the above equation is

$$z_{x\alpha}^{[b,\beta]} = \Delta_{x\alpha, x\beta} + \sum_{z \neq x} \Delta_{x\alpha, z\beta} . \quad (2.91)$$

The first term in the r.h.s of the last expression is the all-to-all propagator, but the method introduced the second term in r.h.s in the equation above. Based on gauge invariance arguments, the IVST version proposes to average  $z_{x\alpha}$  over a set of  $N_g$  random gauge transformations  $g$  performed on a single configuration  $[U]$  in order to remove the second term

$$\Delta_{x\alpha, x\beta}[U] \stackrel{N_g \rightarrow \infty}{=} \langle z_{x\alpha}^{[b,\beta]}[U] \rangle_g . \quad (2.92)$$

On each configuration  $N_g \times 2 \times 3$  inversions are performed. The number of  $N_g$  gauge transformations has to be chosen large enough in order the variance is dominated by the gauge noise.

### 2.8.2 Stochastic Estimators Technique (SET)

The stochastic estimators technique is widely applied in lattice QCD. We also use this method for the estimation of disconnected diagrams. In this method the all-to-all propagator are estimated by sampling the vector space stochastically. An ensemble of random, independent noise vectors  $\{\eta_{[1]}, \dots, \eta_{[N_r]}\}$  is generated. These noise vectors satisfy the property

$$\langle \eta_{[r]}^\dagger(x) \eta_{[r]}(y) \rangle_\eta = \delta_{x,y} \quad , \quad r = 1, \dots, N_r \quad , \quad (2.93)$$

where  $\langle \dots \rangle_\eta$  is the expectation value over the distribution of noise vectors  $\eta$ . The norm of each component of  $\eta_{[r]}(x)$  is 1. Therefore, we used the  $Z_2$  variant where the entries for the  $\eta_{[r]}(x)$  components are chosen randomly among the complex numbers  $\frac{1}{\sqrt{2}}(\pm 1 \pm i)$ .

The solution vectors  $z_{[r]xa\alpha}$  are obtained as usually by

$$z_{[r]xa\alpha} = \sum_{yb\beta} Q_{xa\alpha, yb\beta}^{-1} \eta_{[r]yb\beta} \quad . \quad (2.94)$$

The gluino propagator  $\Delta = Q^{-1}$  from any point  $x$  to any other point  $y$  is given by

$$\Delta_{xa\alpha, yb\beta} = \lim_{N_r \rightarrow \infty} \frac{1}{N_r} \sum_r \eta_{[r]yb\beta}^\dagger z_{[r]xa\alpha} \quad . \quad (2.95)$$

This method, however, results in large variance. Therefore, the method called *dilution* is used to substantially reduce the variance. We use the spin explicit method (spin dilution) where the noise vector is diluted in the Dirac space and the estimate is delivered at the price of a single inversion for each value of the Dirac index  $\alpha \in \{1, 2\}$

$$\eta_{[r]} = \sum_\alpha \eta_{[r]}^{[\alpha]} \quad , \quad (2.96)$$

where  $\alpha$  is a spin index and the source noise vectors for inversions are now

$$\eta_{[r]xb\beta}^{[\alpha]} = \delta_{\alpha\beta} \eta_{[r]xb}^{[\alpha]} \quad . \quad (2.97)$$

The solution of the propagator now reads

$$\Delta_{xa\alpha, yb\beta} \stackrel{N_r \rightarrow \infty}{=} \langle \eta_{[r]yb}^{[\alpha]} z_{[r]xa\beta}^{[\alpha]} \rangle \quad . \quad (2.98)$$

The stochastic estimators methods in its naive version eq. (2.95) or combined with dilution eq. (2.98) provides us with an estimate of all element of the propagator matrix  $\Delta$ . However, in IVST solution in eq. (2.92) gives only the estimate for the diagonal elements  $\Delta_{x,x}$  of the propagator matrix. In fact, in IVST the stochastic input is given by the random gauge transformations. For accelerating the inversion one can apply *deflating methods* [59, 60] as to solve problems with multiple right-hand sides  $Qz^{(i)} = w^{(i)}$  where in our case the noise vectors can be inserted in r.h.s of this equation. Deflating



cannot be applied for IVST since the matrix  $Q$  which has to be inverted changes during the stochastic process. As a part of the SYM project the deflating methods are tested and implemented for future use in the determination of the adjoint meson masses.

In all TS-PHMC runs generated for the present study we opted for the use of SET/SEM for the evaluation of disconnected diagrams. Of interest is the optimal choice of the number of stochastic sources  $N_r$  in order to minimize the computational load. To this end we select a subsample of independent configurations and carry out a study on the behavior of the disconnected term error  $\sigma(C_{disc})$  as function of the number  $N_r$  as shown in Fig. 2.5, then we pick up  $N_r$  from which the value of the disconnected error stabilizes.

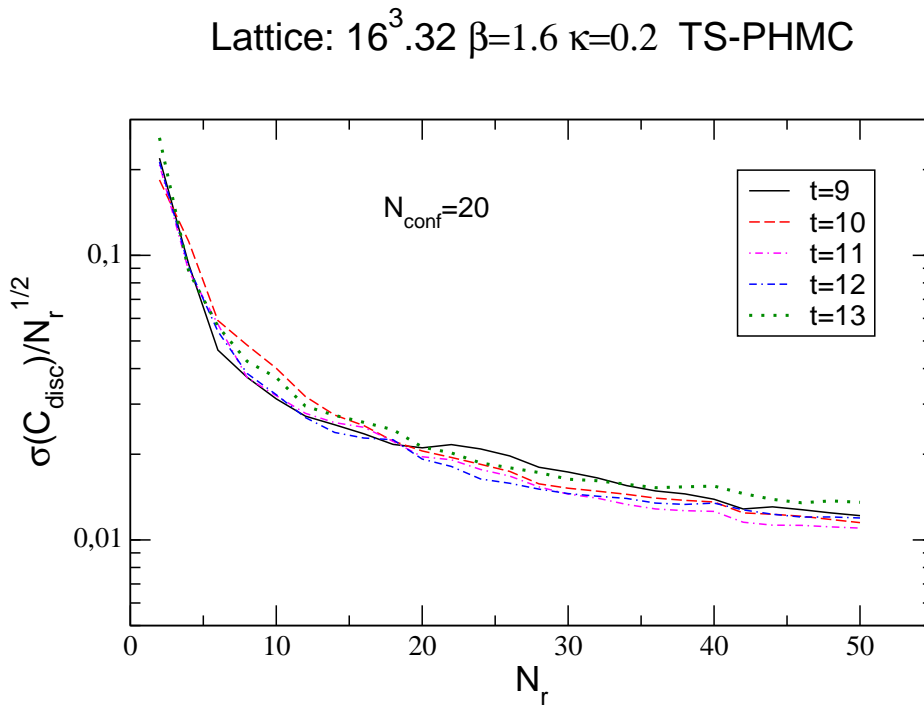


Figure 2.5: *Evolution of the disconnected correlator error as function of the number of stochastic estimator for 20 independent configurations.*

## 2.9 Lattice SUSY Ward Identities (WIs)

The formulation of  $\mathcal{N} = 1$  SYM on the lattice with Wilson fermions breaks SUSY by the Wilson term and by a gluino Majorana mass term. The lattice Ward Identities (WIs) provide in general a general theoretical framework to study the restoration of

SUSY in the continuum limit. The lattice SUSY WIs have been intensively investigated numerically by DESY-Münster-Roma collaboration [21].

A wide choice of lattice SUSY transformations can be defined even SUSY is not realized on the lattice. The SUSY WIs should reduce to their continuum form in the limit  $a \rightarrow 0$  which is the unique requirement for such lattice SUSY transformations. Among many possible SUSY transformations one can construct those minimizing the SUSY breaking at  $\mathcal{O}(a)$  by choosing an appropriate irrelevant operators.

Exploiting the lattice SUSY transformations and defining a gauge invariant operator  $Q(y)$ , the bare SUSY WIs can be written [21]

$$\sum_{\mu} \langle (\nabla_{\mu} S_{\mu}) Q(y) \rangle = \underbrace{m_0 \langle \chi(x) Q(y) \rangle}_{\text{mass breaking}} + \underbrace{\langle X_S(x) Q(y) \rangle}_{\text{Wilson+ } a \text{ breaking}} - \underbrace{\left\langle \frac{\delta Q(y)}{\delta \bar{\epsilon}(x)} \right\rangle}_{\text{contact term} \sim \delta(x-y)}, \quad (2.99)$$

where the lattice derivative is the symmetric one  $\nabla_{\mu} f(x) = (f(x + \hat{\mu}) - f(x - \hat{\mu}))/2a$ ,  $\bar{\epsilon}$  is some SUSY transformation parameter.  $S_{\mu}$  is some *local* lattice version of the super-current.  $\chi$  is taken to be same as the interpolating operator for the gluino-gluon in (2.80).

Besides the bare mass term  $m_0$ , the remaining breaking results in the presence of the  $X_S$  term. In order to renormalize the SUSY WIs, the mixing pattern of the operator  $X_S$  has to be investigated. Taking this into account, the resulting renormalized lattice SUSY WIs can be written [21]

$$Z_S \langle (\nabla_{\mu} S_{\mu}(x)) Q(y) \rangle + Z_T \langle (\nabla_{\mu} T_{\mu}(x)) Q(y) \rangle = m_S \langle \chi(x) Q(y) \rangle + \mathcal{O}(a), \quad (2.100)$$

or in compact form

$$Z_S C^{(S,Q)} + Z_T C^{(T,Q)} = m_S C^{(\chi,Q)} + \mathcal{O}(a), \quad (2.101)$$

where the subtracted mass  $m_S$  is given by

$$m_S = m_0 - a^{-1} Z_{\chi}. \quad (2.102)$$

$Z_S$ ,  $Z_T$  and  $Z_{\chi}$  are multiplicative renormalization factors.  $T_{\mu}$  is a mixing lattice current. In numerical simulations for a gauge invariant insertion operator the correlators pertaining the WI (2.100) can be computed. These correlators are  $4 \times 4$  matrices in Dirac space. Thus, by choosing two elements, a system of two equations can be solved for  $Z_T Z_S^{-1}$  and  $m_S Z^{-1}$ . For an insertion operator  $Q(y)$  in (2.100) we have considered the interpolating operator  $\chi$  as in (2.80).

Using the discrete parity  $\mathcal{P}$ , time-reversal  $\mathcal{T}$  and  $\mathcal{C}$  lattice symmetries and exploiting the spin structure, one can show that each zero-momentum correlator in (2.100) can

be decomposed into two non-vanishing independent coefficients of  $\mathbb{1}$  and  $\gamma_0$  matrices in Dirac space [21] yielding

$$C_{\mathbb{1}}^{(S,Q)}(t) + Z_T Z_S^{-1} C_{\mathbb{1}}^{(T,Q)}(t) = m_S Z_S^{-1} C_{\mathbb{1}}^{(\chi,Q)}(t) , \quad (2.103)$$

$$C_{\gamma_0}^{(S,Q)}(t) + Z_T Z_S^{-1} C_{\gamma_0}^{(T,Q)}(t) = m_S Z_S^{-1} C_{\gamma_0}^{(\chi,Q)}(t) . \quad (2.104)$$

The system of two equations above can be solved in two approaches: i) solving the system at each time-separation  $t$ , or ii) perform a linear fit by including all the time-separations in one fit procedure. The latter should work better since it includes more information comparing to the former which is local by using only one time-separation.

The experience showed a lower signal-to-noise ratios when local interpolating fields are used in the correlators. This is mainly due the gluonic content of both sink and source operators. Furthermore, the sink operators involve time-derivative which are subject to large fluctuations. We performed APE and Jacobi smearing for the insertion operator  $\chi$  in order to obtain better signals.

## 2.10 Smearing methods

As discussed in previous sections, the masses in Lattice Gauge Theory are calculated from the asymptotic behaviour of Euclidean time correlation functions. The contribution from the lowest mass state is expected to dominate for large time-separation. Thus, to get a clean signal one has to make the length in the time direction as large as possible. But this is computationally expensive. Furthermore, as the time-separation increases, the signal to noise ratio gets smaller which results in larger statistical errors. To reduce the statistical error, the number of measurements (configurations) has to be increased. This is also computationally expensive. Hence there is a practical need for techniques that allow one to reliably extract masses while still working on moderately sized time direction and not too large number of configurations. For some bound states the local operators are not suitable to extract masses on the lattice. It is then useful to use extended operators that have larger overlap with the physical states of interest. This will naturally decrease contamination from higher states and allow extraction of mass at early time-separations. *Smearing* of local operators is one way to achieve this goal.

In the following we will present the smearing techniques that we have applied in our spectrum analysis.

### 2.10.1 APE smearing

In order to improve the overlap of an lattice operator and to have better signal-to-noise ratio the smearing techniques have to be applied. There are several smearing procedures which can be used for the gauge links where in this study we used the APE smearing

[61]. The APE smearing is applied to the link  $U_\mu(x)$  by substituting this links by itself and the sum of space-like "staples" surrounding it, and perpendicular to its direction  $\mu$ , where the sum is multiplied by some factor  $\epsilon_{ape}$ . The new smeared link  $U_\mu^s(x)$  is obtained by projecting back the substitution into the gauge group  $SU(2)$ , one can write

$$U_\mu(x) \rightarrow U'_\mu(x) = U_\mu(x) + \epsilon_{ape} \sum_{\nu=\pm 1, \nu \neq \mu}^{\pm 3} U_\nu^\dagger(x + \hat{\mu}) U_\mu(x + \hat{\nu}) U_\nu(x) , \quad (2.105)$$

and the new smeared  $SU(2)$  gauge link is

$$U_\mu^s(x) = \mathcal{P}_{SU(2)} [U'_\mu(x)] . \quad (2.106)$$

The projection of a matrix  $U$  into the gauge group  $SU(2)$  is achieved by

$$\mathcal{P}_{SU(2)} [U] = \frac{U}{\sqrt{\frac{1}{2} \text{Tr} U^\dagger U}} . \quad (2.107)$$

This step is applied  $N_{ape}$  times to the complete lattice. Nevertheless, not too many steps can be applied as not to wash out the signal. For small values of  $\epsilon_{ape}$  this algorithm corresponds to solving the diffusion equation where the smearing radius is given by

$$R_s = N_{ape} \epsilon_{ape} . \quad (2.108)$$

### 2.10.2 Jacobi smearing

For operator  $\mathcal{O}$  involving fermionic degree of freedom  $\lambda$  the Jacobi smearing algorithm [50] can be applied in order to improve the signal.

To construct the extended operator  $\mathcal{O}^s$  the fermion field is smeared out by a suitable matrix  $F(x, x')$  acting on a fixed time-slice

$$\lambda^s(\vec{x}, t) = \sum_{\vec{y}} F(\vec{x}, \vec{y}) \lambda(\vec{y}, t) \quad (2.109)$$

For suitably small  $\kappa_J$  and large  $N_J$ ,  $F(\vec{x}, \vec{y})$  is defined as the solution kernel of the three dimensional Klein-Gordon equation. The kernel  $F$  has the form

$$F_{\beta b, \alpha a}(\vec{x}, \vec{y}) = \delta_{\vec{x}, \vec{y}} \delta_{ba} \delta_{\beta\alpha} + \delta_{\beta\alpha} \sum_{i=1}^{N_J} \left( \kappa_J \sum_{\mu=1}^3 [\delta_{\vec{y}, \vec{x} + \hat{\mu}} V_{\mu, ba}(x) + \delta_{\vec{y} + \hat{\mu}, \vec{x}} (V^\dagger)_{\mu, ba}(x)] \right)^i . \quad (2.110)$$

On the lattice the two number of iterations  $N_J$  and the Jacobi parameter  $\kappa_J$  has to be tuned in order to get optimal estimation for the operators of interest. Moreover, a smearing radius  $R_J$  defined by

$$R_J = \frac{\sum_{\vec{x}} |\vec{x}|^2 |F(\vec{x}, 0)|^2}{\sum_{\vec{x}} |F(\vec{x}, 0)|^2} \quad (2.111)$$

is used to establish whether or not the ground state wave function fits into the lattice. As can be seen in Fig. 2.6 the smearing radius increases rapidly in an interval of  $\kappa_J$  [0.15, 0.25]. Thus, to control the computational load which increases with  $N_J$  we have chosen the combination  $(N_J, \kappa_J)$  such that  $N_J$  is the lowest value giving a radius about half the spatial extent of the lattice.

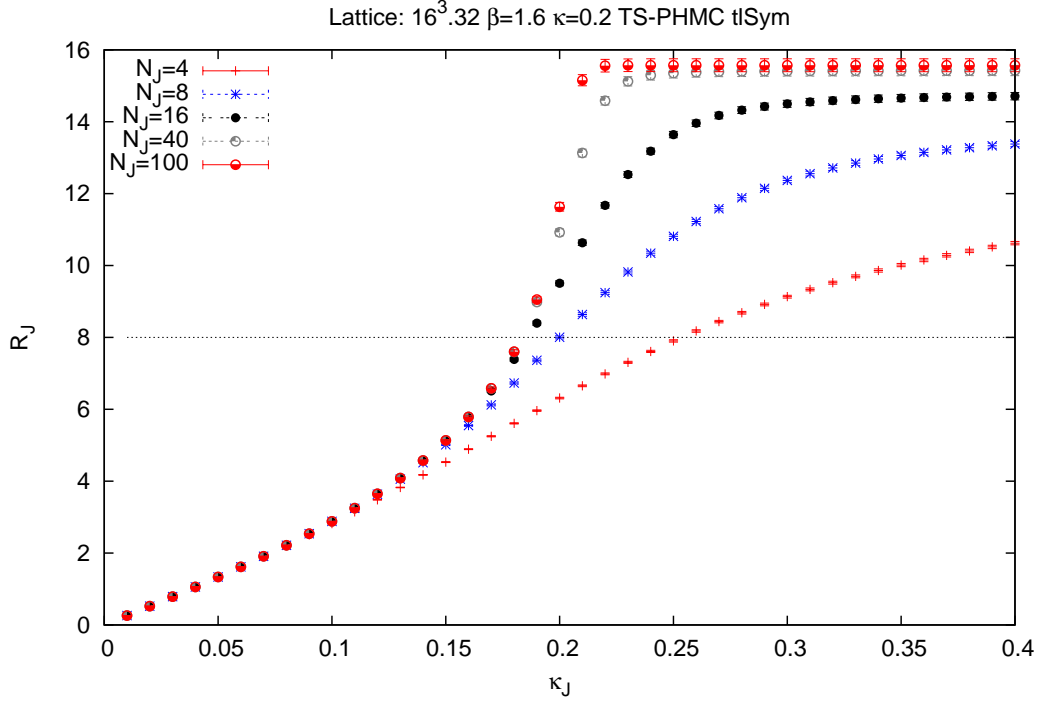


Figure 2.6: Value of Jacobi radius of smearing over a subsample of 100 configuration as function of  $\kappa_J$ .

The effect of Jacobi smearing on the  $a$ - $\pi$  effective mass is compared to that using local operator in Fig. 2.7. The effective mass is calculated from different combinations: no smearing neither of the source nor of the sink (L-L), local source and smeared sink (L-S), smeared source and smeared sink (S-S). In this example we observe a stabilization of the effective mass from the first time-separation at moderate smearing radius  $R_J$  obtained from the correlator of (L-S) operator with  $N_J = 6$  at  $\kappa_J = 0.2$ . From  $t = 4$  and onwards the effect of the smearing becomes irrelevant. In practice, this is useful for operators which have low signal for large time-separations but the signal is reasonable at short time-separations after smearing.

We note at the end of this section that no smearing was applied for adjoint meson

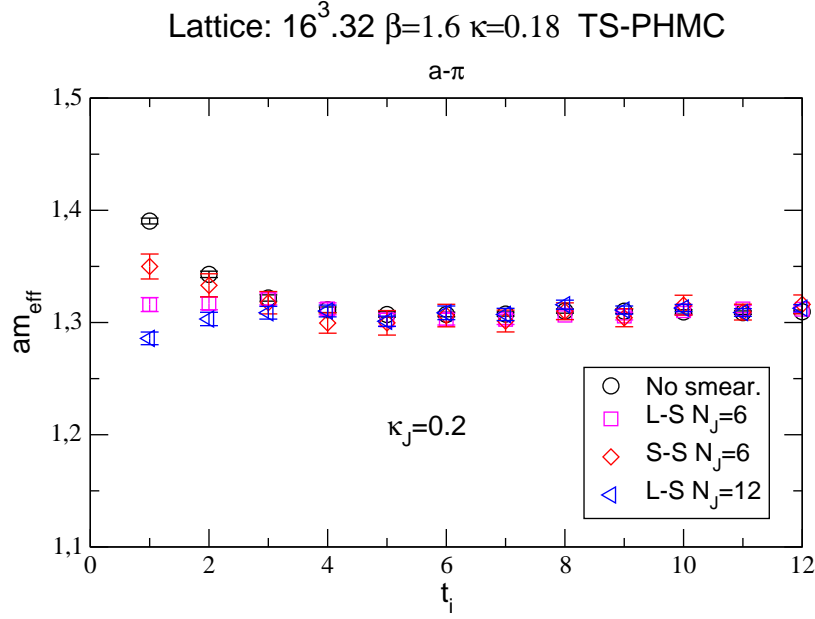


Figure 2.7: *Effects of different combination of smearing on the  $a$ - $\pi$  effective mass.*

operators in this work. For glueball and Wilson loops we applied APE smearing and for gluino-glueball and SUSY WIs we applied both APE and Jacobi smearing.

## 2.11 Variational method

The determination of the mass of a particle on the lattice can be also realized using the variational method [62] which is essential to separate excited states. The central idea is to use several different interpolating operators  $\{O_i, i = 1, \dots, N\}$  with the desired spin and parity quantum numbers content of the state  $J^{PC}$  and to compute all possible cross correlation functions

$$C_{ij}(t) = \langle O_i(t) O_j(0) \rangle. \quad (2.112)$$

Such operators can be constructed by exploiting link or fermion smearing techniques which will be combined with variational methods. In Hilbert space these correlators have the spectral decomposition

$$C_{ij}(t) = \sum_n \langle 0 | O_i | n \rangle \langle n | O_j^\dagger | 0 \rangle e^{-tm_n}. \quad (2.113)$$

The selected creation operators  $\{O_i(t)\}$  transform in the irreducible representation  $\mathcal{R}^P$  of the cubic group  $O_h$ . To determine the masses  $m_n$ , the variational method allows

first to select optimal combination of operators  $O = \sum_j c_j O_j$ ; this involves choosing the coefficients  $c_j$ 's such that  $C(t)/C(0)$  be a maximum where

$$C(t) = \sum_{ij} c_i c_j C_{ij}(t) , \quad (2.114)$$

is the correlator associated with the operator  $O$ .

Using the factorization of the amplitudes one can show [62] that the eigenvalues  $\lambda^k(t), k = 1, \dots, N$  of the generalized eigenvalue problem

$$C_{ij}(t) \mathbf{v}_j^{(k)} = \lambda^{(k)}(t) C_{ij}(0) \mathbf{v}_j^{(k)} , \quad (2.115)$$

behave as

$$\lambda^{(k)}(t) \propto e^{-tm_k} [1 + \mathcal{O}(e^{-t\Delta m_k})] , \quad (2.116)$$

where  $m_k$  is the mass of the  $k$ -th state.

The largest eigenvalue  $\lambda^{(0)}$  decays with the mass of the ground state, the second largest eigenvalue with the mass of the first excited state, etc. The eigenvector corresponding to the largest eigenvalue then yields the coefficients  $c_j^{(0)}$  for the operator  $O$  which best overlaps the lowest-lying state in the channel of interest.

In fact we have used two methods: i) a fixed-vector method which involves solving the eigenvalue problem eq. (2.115) on single time-slice  $t = t_b$  where the subscript  $b$  refers to "basis". ii)  $t$ -eigenvector method where diagonalizations were performed on each time step  $t$ . In the fixed-vector method we used the resulting eigenvectors  $\mathbf{v}^{(k)}$  for rotating the cross correlators for each time-slice and we read off the effective mass on adjacent time-slices

$$am_k(t) = \ln \left[ \frac{\sum_{ij} \mathbf{v}_i^{(k)} \mathbf{v}_j^{(k)} C_{ij}(t)}{\sum_{ij} \mathbf{v}_i^{(k)} \mathbf{v}_j^{(k)} C_{ij}(t+1)} \right] . \quad (2.117)$$

We are interested in this study to the lowest state with mass  $m_0$ , we proceed then as in standard methods by looking for a plateau region in the effective mass and then fix the  $t$ -range to perform single exponential fit as discussed in Section 2.7. We note that the quality of plateau can depend on the basis chosen  $t_b$ . In our application of variational method to the glueballs we have chosen  $t_b = 1$ .

The generalization to the  $t$ -eigenvector method is straightforward. Here, the basis is not relevant since one has to perform diagonalization (eq. (2.115)) at each  $t$  and pick up the eigenvalues, and hence the effective mass reads

$$am_k(t) = \ln \left[ \frac{\lambda^{(k)}(t)}{\lambda^{(k)}(t+1)} \right] . \quad (2.118)$$

Errors for such quantities are determined via jackknife procedure and linearization method. The latter is more complicated in this case and will be discussed in Section 2.14.2.

## 2.12 Confinement potential and Sommer scale $r_0/a$

Analogy with QCD suggests that SYM theory presents confinement realized by color singlet particle states. Confinement can be studied by computing the static quark potential  $V(r)$  as a function of the spatial separation  $r$  between sources in the fundamental representation of the gauge group.  $V(r)$  describes the gauge field energy between two static color sources corresponding to quark-antiquark pair separated by a distance  $r$ . The static potential  $V(r)$  can be extracted using the method described in [63].

The quantities measured in the lattice are obtained in lattice units. Therefore, we need to set the scale in order to convert the quantities into physical units. The Sommer parameter scale  $r_0$  is proposed to set the scale in dynamical simulations [64]. This method is used in the present work to set the scale in SYM simulations. In previous investigations, alternatively, the string tension  $\sigma$  was used to set the scale.

The Sommer scale is defined via the force  $F(r)$  between two static quarks at distance  $r$  by

$$r^2 F(r) \big|_{r=R(c)} = c, \quad (2.119)$$

with the requirement

$$R(1.65) \equiv r_0 \simeq 0.5 \text{fm}. \quad (2.120)$$

On the lattice  $r_0/a$  can be measured by several methods. We used two independent methods to measure  $r_0/a$ : i) force methods based on Creutz ratios [64, 65, 66] and ii) two-fits procedure potential method [63].

In both methods the rectangular Wilson loops averages  $\langle W(R, T) \rangle$  of sides  $R$  and  $T$  are computed. The signal, however, has to be improved using smearing methods such as APE-smearing for gauge link paths in order to reduce the contamination with excited states.

In the following details of methods to extract the static potential  $V(r)$  and the computation of  $r_0/a$  are presented.

### 2.12.1 Two-fit procedure potential method

We have used this method in order to study the confinement potential and also extract an estimation of the Sommer parameter scale  $r_0/a$ . There are equivalent ways to determine the potential  $V(R, T)$  through the Wilson loops  $W$ . For example a definition is given by

$$V(R, T) = \ln \left( \frac{\langle W(R, T) \rangle}{\langle W(R, T+1) \rangle} \right). \quad (2.121)$$

Also, one can use other definition like

$$V(R, T) = -\frac{1}{T} \ln W(R, T). \quad (2.122)$$



Both definitions can be used to extract the potential  $V(R)$  in a *first fit* procedure. In the case of definition in eq. (2.121) one performs fitting of the exponential decay in time of  $V(R, T)$  at each fixed  $R$  to the function

$$V(R, T) = V(R) + c_1(R)e^{-c_2(R)T}, \quad (2.123)$$

In the case of the definition in eq. (2.122), the data  $V(R, T)$  is fitted to the function

$$V(R, T) = V(R) + \frac{c_1(R)}{T}. \quad (2.124)$$

Since we are using a  $\chi^2$  minimization solver to find the best fit parameters some technical problems can happen, and it is necessary to find a strategy for the starting parameters. The minimization solvers search in a given direction only for a local minimum, and the choice of the starting guess are crucial to find reliable values. For a given  $R$ , we have data points  $y \equiv V(R, T)$  and in the range  $[t_{min}, t_{max}]$  are  $y_{t_{min}} \dots y_{t_{max}}$ . We fixed the starting parameters in the case of the fit function in eq. (2.123) as

$$c_2^{(0)} = \ln \left( \frac{y_{t_{min}}}{y_{t_{min+1}}} \right), \quad (2.125)$$

$$c_1^{(0)} = y_{t_{min}} e^{c_2^{(0)} t_{min}}, \quad (2.126)$$

$$v^{(0)} = y_{t_{min+2}} - c_1^{(0)} e^{-c_2^{(0)}(t_{min+2})}. \quad (2.127)$$

Having obtained data for the potential  $V(R)$ , we proceed now to a *second fit* procedure. The data are fitted to the standard potential form

$$V(r) = v_0 + \sigma r - e \left[ \frac{1}{r} \right] - f \left( \left[ \frac{1}{r} \right] - \frac{1}{r} \right) \quad (2.128)$$

in a range  $[r_{min}, r_{max}]$ , where  $\sigma$  is the string tension,  $e$  is the Coulomb term coefficient  $\pi/12$  and  $f$  is the correction lattice term.  $\left[ \frac{1}{r} \right]$  is given in eq. (2.140).

Depending on the quality of our data, we choose to perform three parameters fit instead of four where the coefficient  $e$  is kept constant. Observing that we have  $V(r) \xrightarrow{r \rightarrow \infty} v_0 + \sigma r$ , we use this property to fix the starting parameter values for the fit. As argued above in the first fit procedure, the strategy to begin the minimization procedure in an interval  $[r_{min}, r_{max}]$  depends strongly on the starting parameters. In the second fit we have chosen the starting paramaters as follows

$$\sigma^{(0)} = y_{r_{max}} - y_{r_{max}-1}, \quad (2.129)$$

$$v_0^{(0)} = y_{r_{max}-1} - \sigma^{(0)}(r_{max} - 1), \quad (2.130)$$

$$f^{(0)} = (y_{r_{min}} + e \left[ \frac{1}{r_{min}} \right]) \left( \left[ \frac{1}{r_{min}} \right] - \frac{1}{r_{min}} \right)^{-1} \quad (2.131)$$

$$e^{(0)} = (v_0^{(0)} + \sigma^{(0)} r_{min} - y_{r_{min}}) \left( \left[ \frac{1}{r_{min}} \right] \right)^{-1}. \quad (2.132)$$

Finally, we obtain the Sommer parameter  $r_0/a$  from this fit, using the formula

$$r_0 = \sqrt{\frac{1.65 - e}{\sigma}}. \quad (2.133)$$

Here the correction lattice term  $f$  is not taken into account. The two-fit procedure, as the name indicates, calls two  $\chi^2$  minimizations. This method used in our study seems to work good at most times. However, it can happen that the first fit ( $V(R, T)$ ) is not good enough, which results in worse in the second fit ( $V(R)$ ). There exists a comfortable alternative way to perform the first step ( $V(R, T)$ ) analytically. Therefore, the minimization is only carried for  $V(R)$  data through numerical solver.

In the following short indications of analytical determination of  $V(R)$  from the  $V(R, T)$  data are given.

### One-fit procedure

It is obvious to observe that the behavior of  $V(R, T)$  in eq. (2.123) should display a plateau at large  $T$  and fixed  $R$  corresponding to the value of  $V(R)$ . This motivates to fit  $V(R, T)$  to a constant in order to extract  $V(R)$ , which can be done analytically without calling a solver by

$$V(R) = \frac{1}{\sum_{T=t_i}^{t_f} \frac{1}{\sigma_{R,T}^2}} \sum_{T=t_i}^{t_f} \frac{V(R, T)}{\sigma_{R,T}^2}. \quad (2.134)$$

For  $t_i$  large enough a plateau is expected in the range  $[t_i, t_f]$ . After that, one can apply the second fit procedure as discussed above to extract  $r_0/a$ .

### $R_T$ -fit

In this procedure the first fit procedure is also eliminated. This method leads to an effective string tension *i.e.*  $\sigma(T)$  [67, 63]. In the  $R_T$ -fit procedure one has to keep  $T$  constant and fit the  $V(R, T)$  data computed from eq. (2.122) in an interval of  $R$  to the form in eq. (2.128). Therefore, one obtains for each time  $T$  the estimated parameters  $\sigma(T), v_0(T), \dots$  where we are interested only on  $\sigma(T)$ . The value of the string tension is read off from the first time  $T$  where  $\sigma(T)$  displays a plateau.

## 2.12.2 Force method and Creutz ratios

The Creutz-ratios  $\chi(r, t)$  are defined from Wilson loops  $W(r, t)$  by

$$\chi(r, t) = -\log \left( \frac{W(r, t)W(r-1, t-1)}{W(r, t-1)W(r-1, t)} \right). \quad (2.135)$$

For large  $r$  and  $t$ , the Wilson loops  $W(r, t)$  follow the perimeter law decay given by

$$W(r, t) \stackrel{r, t \rightarrow \infty}{\sim} C e^{-\sigma r t}, \quad (2.136)$$

where  $\sigma$  is the string tension, and consequently one has

$$\chi(r, t) \stackrel{r, t \rightarrow \infty}{\sim} \sigma. \quad (2.137)$$

This presents a direct measurement of the sting tension  $a^2\sigma$  in lattice units. However, to measure  $r_0/a$  we need the force between two quarks at intermediate distance  $r_I$  which is obtained by

$$F(r_I) = \lim_{t \rightarrow \infty} \chi(r, t). \quad (2.138)$$

The intermediate distance  $r_I$  between  $r$  and  $r - 1$  is related to  $r$  by the formula given by

$$\frac{1}{r_I^2} = \left[ \frac{1}{r} \right] - \left[ \frac{1}{r - \frac{1}{r}} \right], \quad (2.139)$$

with  $\left[ \frac{1}{r} \right]$  being the tree-level Coulomb term given by

$$\left[ \frac{1}{r} \right] = 4\pi \int_{-\pi}^{\pi} \frac{d^3 \vec{k}}{(2\pi)^3} \frac{\prod_{i=1}^3 \cos(r_i \cdot k_i)}{4 \left( \sum_{j=1}^3 \sin^2(k_j/2) - 4c_1 \sum_{j=1}^3 \sin^4(k_j/2) \right)}, \quad (2.140)$$

with  $c_1 = 0$  for Wilson gauge action and  $c_1 = -1/12$  for tISym action.

Now the force is interpolated from eq. (2.119) by

$$F(r_I) = f_1 + f_2 \frac{1}{r_I^2}. \quad (2.141)$$

We need a pair of Creutz ratios  $\chi(r, t)$  and  $\chi(r', t)$  at fixed large time  $t$  to determine  $r_0/a$ . We chose  $r' = r + 1$  and applying eq. (2.141) for  $r$  and  $r'$  we obtain

$$\frac{r_I^2 F(r_I) - r_I'^2 F(r_I')}{r_I^2 - r_I'^2} = f_1. \quad (2.142)$$

In particular, in the case where  $r_I = r_0$  we have to solve the equation

$$\frac{1.65 - r_I'^2 F(r_I')}{r_0^2 - r_I'^2} = \frac{r_I^2 F(r_I) - r_I'^2 F(r_I')}{r_I^2 - r_I'^2} \quad (2.143)$$

for the variable  $r_0$  (here the lattice spacing  $a$  is omitted).

We note that besides the choice of  $t$  sufficiently large, one can arbitrary choose  $r$  which would give consistent results for the estimation of  $r_0/a$ . The size of  $r$  is such the obtained  $r_0/a$  lies inside the interval  $[r, r + 1]$ .

## 2.13 Jackknifing and Blocking

As discussed in Section 2.4 the standard deviation defined in eq. (2.45) estimates the error in the  $N$  measurements of the observable  $A$ . However, the Monte Carlo measurements are correlated and the standard deviation is not the true error, hence the integrated autocorrelation-time  $\tau_{int}$  is to be considered in order to estimate the true error of the primary observable  $A$  given in eq. (2.50). However, when we are dealing with a secondary observable  $y(A)$  the estimation of the error needs more robust methods. The average of  $y(A)$  is simply defined as

$$\bar{y} = y(\bar{A}), \text{ and not } \overline{y(A)}. \quad (2.144)$$

The single-elimination jackknife procedure is one of the widely used methods in lattice gauge theory to estimate the errors of secondary observables. Having  $N$  measurements of the observable  $A$ , one has to remove one measurement from the sequence and build up the jackknife sample  $A^J$  defined by

$$A^{[j]:J} = \frac{1}{N-1} \sum_{i \neq j}^N A^{[i]} \quad j = 1..N. \quad (2.145)$$

Now, the jackknife sample of the secondary observable  $y(A)$  is simply defined by

$$y^{[j]:J} = y(A^{[j]:J}), \quad (2.146)$$

and its jackknife average is

$$\bar{y}^J = \frac{1}{N} \sum_{j=1}^N y^{[j]:J}. \quad (2.147)$$

Finally, the jackknife error (which is now to be considered as estimate of the error of  $y$ ) is given by

$$\sigma_y^2 = \frac{N-1}{N} \sum_{j=1}^N \{ \bar{y}^J - y^{[j]:J} \}^2. \quad (2.148)$$

However, for correlated data this version of jackknife method could not give a reliable estimate of the error. It is most common to average each  $B < N$  or subsequent measurements  $a^{(i)}, i = 1, \dots, B$  into blocks in order to eliminate the autocorrelation between data. The blocked  $N_B$  data are used now to calculate the average and the statistical errors. The size of the block is increased in repeating steps until the statistical error approaches a plateau from below. This results in a final error for uncorrelated data. Since the latter is the true error of the measurement, it is appropriate to use this definition to estimate  $\tau_{int}$  (see Ref. [68]).

## 2.14 Linearization method

The estimation of the statistical errors of secondary quantities is largely calculated applying the previous method: Jackknife and blocking analysis. There exists recently more accurate method which we have used to estimate the error in the measurements. This method has been first proposed in [44], also known as the *linearization method* or the  $\Gamma$ -method. The algorithm elaborated in [44] gives us good estimate of the error of the masses. The method is based on linearization of the deviation of the secondary quantity from its true value.

Let us consider the statistical error of a set of primary quantities with (exact) expectation values  $A_\alpha, \alpha = 1, \dots, M$ . The measurement of this quantity in the sequence of  $N$  Monte Carlo generated configurations is estimated by

$$\bar{a}_\alpha = \frac{1}{N} \sum_{i=1}^N a_\alpha^{(i)}, \quad (2.149)$$

where ( $|\bar{a}_\alpha - A_\alpha| \ll 1$ ). If the configurations used for the measurement are independent, the error can be estimated with the naive error estimate which is not the case in Monte Carlo processes.

For a secondary quantity such as the masses or generally any function  $f(A_\alpha)$  of the primary expectation values  $A_\alpha$ , one cannot compute the integrated autocorrelation in the straightforward way. Following the linearization method the deviation of the secondary quantity  $f(A_\alpha)$  at  $\bar{a}_\alpha$  from the true value is

$$f(\bar{a}) - f(A) \simeq \sum_{\alpha} (\bar{a}_\alpha - A_\alpha) \frac{\partial f(A)}{\partial A_\alpha}. \quad (2.150)$$

Since we can have the estimates

$$\frac{\partial f(A)}{\partial A_\alpha} \simeq \left. \frac{\partial f(A)}{\partial A_\alpha} \right|_{A=\bar{a}} \equiv \bar{f}_\alpha \quad (2.151)$$

we can express the deviation as

$$f(\bar{a}) - f(A) \simeq \sum_{\alpha} (\bar{a}_\alpha - A_\alpha) \bar{f}_\alpha = \bar{a}_f - A_f, \quad (2.152)$$

where

$$A_f \equiv \sum_{\alpha} A_\alpha \bar{f}_\alpha \quad (2.153)$$

is a linear combination of primary quantities  $A_\alpha$ , which is also a primary quantity. Its estimate is

$$\bar{a}_f \equiv \sum_{\alpha} \bar{a}_\alpha \bar{f}_\alpha = \frac{1}{N} \sum_{i=1}^N a_\alpha^{(i)} \bar{f}_\alpha. \quad (2.154)$$

If we consider an infinite set of identical measurements with the same statistics and denote the expectation value in this set by  $\langle \dots \rangle$ , then we have

$$\langle \bar{a}_\alpha - A_\alpha \rangle = 0 , \quad (2.155)$$

and the variance of  $A_\alpha$  is

$$\sigma_\alpha^2 = \langle (\bar{a}_\alpha - A_\alpha)^2 \rangle = \langle \bar{a}_\alpha^2 - \langle A_\alpha \rangle^2 \rangle . \quad (2.156)$$

The variance of any function  $f(A)$  is from above

$$\sigma_f^2 = \langle (\bar{a}_f - A_f)^2 \rangle , \quad (2.157)$$

which shows that the error of  $f(A)$  can be estimated from the integrated autocorrelation of the primary quantity  $A_f$ . Usually this is applicable to slightly complicated functions  $f$  as given in the next example for effective mass in standard method and in the variational method. For "any" complicated functions there still exist a quite convenient way to apply linearization method numerically. One obtains the derivations in eq. (2.151) by varying slightly the primary quantities.

### 2.14.1 Linearization error for effective mass

The mass of a given state can be extracted from the exponential decay of the time-slice correlation function. Let us consider periodic time boundaries and define the ratio [43]

$$r_{12} = \frac{C(t_1)}{C(t_2)} = \frac{e^{-m_{eff}t_1} + e^{-m_{eff}(T-t_1)}}{e^{-m_{eff}t_2} + e^{-m_{eff}(T-t_2)}} , \quad (2.158)$$

here

$$m \equiv m_{eff}(t_1, t_2; T) , \quad (2.159)$$

where for sake of brevity we use the short notation  $m$ .

The ratio defined above can be simplified by defining

$$\tau_\alpha = \left(\frac{T}{2} - t_\alpha\right); \quad \alpha = 1, 2 \quad \text{and} \quad x = e^{-m} . \quad (2.160)$$

Then, eq. (2.158) becomes

$$r_{12} = \frac{x^{-\tau_1} + x^{\tau_1}}{x^{-\tau_2} + x^{\tau_2}} . \quad (2.161)$$

The linear deviation sequence  $a_f^{(i)}$   $i = 1 \dots N$  is

$$a_f^{(i)} = C^{(i)}(t_1) \frac{\partial f}{\partial C(t_1)} \Big|_{C(t_1)=\bar{C}(t_1)} + C^{(i)}(t_2) \frac{\partial f}{\partial C(t_2)} \Big|_{C(t_2)=\bar{C}(t_2)} , \quad (2.162)$$

where

$$m \equiv f \left( r_{12} = \frac{C(t_1)}{C(t_2)} \right) . \quad (2.163)$$

Now replacing the derivations

$$\left. \frac{\partial f}{\partial C(t_\alpha)} \right|_{C(t_\alpha)=\bar{C}(t_\alpha)} = \left. \frac{\partial f}{\partial r_{12}} \right|_{r_{12}=\frac{\bar{C}(t_1)}{\bar{C}(t_2)}} \left. \frac{\partial r_{12}}{\partial C(t_\alpha)} \right|_{C(t_\alpha)=\bar{C}(t_\alpha)} , \quad (2.164)$$

in eq. (2.162) yields

$$a_f^{(i)} = \left. \frac{\partial f}{\partial r_{12}} \right|_{r_{12}=\frac{\bar{C}(t_1)}{\bar{C}(t_2)}} \frac{C^{(i)}(t_1)\bar{C}(t_2) - C^{(i)}(t_2)\bar{C}(t_1)}{\bar{C}(t_2)^2} , \quad (2.165)$$

which implies

$$\bar{a}_f = \frac{1}{N} \sum_{i=1}^N a_f^{(i)} = 0 . \quad (2.166)$$

It remains now to compute  $\frac{\partial f}{\partial r_{12}}$  from varying eq. (2.158)

$$1 = \frac{\partial r_{12}}{\partial r_{12}} \quad (2.167)$$

$$= \frac{\partial r_{12}}{\partial m} \frac{\partial m}{\partial r_{12}} \quad (2.168)$$

$$= \frac{\partial m}{\partial r_{12}} \left\{ \frac{-(x^{-\tau_2} + x^{\tau_2})(\tau_1 x^{-\tau_1} - \tau_1 x^{\tau_1}) + (\tau_2 x^{-\tau_2} - \tau_2 x^{\tau_2})(x^{-\tau_1} + x^{\tau_1})}{(x^{-\tau_2} + x^{\tau_2})^2} \right\} \quad (2.169)$$

$$(2.170)$$

and finally

$$\frac{\partial m}{\partial r_{12}} = \frac{x^{-\tau_2} + x^{\tau_2}}{\tau_2 r_{12}(x^{-\tau_2} - x^{\tau_2}) - \tau_1(x^{-\tau_1} - x^{\tau_1})} . \quad (2.171)$$

This expression has to be inserted in the eq. (2.162) leading to the quantities needed for the estimation of the effective mass error.

### 2.14.2 linearization error for effective mass with variational methods

In the case of glueball mass analysis the smearing is used on the interpolating fields resulting in cross correlation function as discussed in Section 2.11. The linear deviation needed for the error estimation of the effective mass has not the form of the one given Section 2.14.1. Combining different levels of smearing, one build up the cross correlation function, which is diagonalized on a given basis. Then, from the largest eigenvalues  $\lambda(t)$

one computes the effective mass of the lowest states. Consider the  $t$ -eigenvector version of variational method discussed in Section 2.11. The generalized eigenvalue problem to be solved is slightly different from the one in eq. (2.115). Here, diagonalization is performed on each time-slice  $t$ . One writes

$$\tilde{C}(t)\mathbf{v}^{(\alpha)}(t) = \lambda^{(\alpha)}(t)\tilde{C}(0)\mathbf{v}^{(\alpha)}(t) , \quad (2.172)$$

where  $\tilde{C}(t) \equiv \tilde{C}(t)_{ij}$   $i, j = 1, \dots, M$  is the cross correlator. The eigenvectors  $\mathbf{v}^{(\alpha)}$   $\alpha = 1, \dots, M$  are orthonormalized on the non trivial metric  $\tilde{C}_{ij}(0)$  *i.e.*

$$\mathbf{v}^{(\alpha)}(t)^T \tilde{C}(0)\mathbf{v}^{(\alpha)}(t) = \delta_{M \times M} \quad (2.173)$$

We denote the largest eigenvalues by  $\lambda^{(0)}(t)$  which decays as

$$\lambda^{(0)}(t) \sim e^{-m_{eff}t} \quad (2.174)$$

where the largest eigenvalue  $\lambda^{(0)}(t)$  is computed from

$$\lambda^{(0)}(t) = \mathbf{v}^{(0)}(t)^T \tilde{C}(t)\mathbf{v}^{(0)}(t) , \quad (2.175)$$

Let us define the ratio  $r_{12}$  analogous to eq. (2.158) as

$$r_{12} = \frac{\lambda^{(0)}(t_1)}{\lambda^{(0)}(t_2)} . \quad (2.176)$$

Now the effective mass is function of the eigenvalues which are functions of the primary quantities  $\tilde{C}_{ij}(t_1)$  and  $\tilde{C}_{ij}(t_2)$

$$m \equiv f(r_{12}) . \quad (2.177)$$

The linear deviation sequence needed to estimate the error is

$$a_f^{(k)} = \frac{\partial m}{\partial r_{12}} \sum_{\alpha=1,2} \frac{\partial r_{12}}{\partial \lambda^{(0)}(t_\alpha)} \sum_{ij} \tilde{C}_{ij}^{(k)}(t_\alpha) \frac{\partial \lambda^{(0)}(t_\alpha)}{\partial \tilde{C}_{ij}(t_\alpha)} , \quad (2.178)$$

noting that the derivations are evaluated at the averages  $\bar{\tilde{C}}_{ij}(t_\alpha)$ . Using eq. (2.176) and eq. (2.175) one finds

$$a_f^{(k)} = \frac{\partial m}{\partial r_{12}} \sum_{\alpha=1,2} \frac{\partial r_{12}}{\partial \lambda^{(0)}(t_\alpha)} \sum_{ij} \tilde{C}_{ij}^{(k)}(t_\alpha) v_i^{(0)}(t_\alpha) v_j^{(0)}(t_\alpha) \quad (2.179)$$

where  $v_i$  are the components of the eigenvector  $\mathbf{v}$ , and we have

$$\frac{\partial r_{12}}{\partial \lambda^{(0)}(t_1)} = \frac{1}{\bar{\lambda}^{(0)}(t_2)} , \quad \frac{\partial r_{12}}{\partial \lambda^{(0)}(t_2)} = -\frac{\bar{\lambda}^{(0)}(t_1)}{(\bar{\lambda}^{(0)}(t_2))^2} , \quad (2.180)$$



and  $\frac{\partial m}{\partial r_{12}}$  is given in eq. (2.171).

Now in the case when  $\mathcal{O}_i$  has a non vanishing vacuum expectation value  $V_i = \langle \mathcal{O}_i \rangle$ , the linearized deviation sequence in eq. (2.179) is modified since the secondary quantity  $m_{eff}$  depends also on the primaries  $V_i$  's. We have

$$\tilde{C}_{ij}(t) \longrightarrow \tilde{C}_{ij}(t) - V_i V_j , \quad (2.181)$$

and

$$\lambda^{(0)}(t) \longrightarrow \mathbf{v}^{(0)}(t)^T (\tilde{C}(t) - \mathcal{V}) \mathbf{v}^{(0)}(t) , \quad (2.182)$$

where  $\mathcal{V}$  is a matrix with elements  $V_i V_j$ . The eq. (2.179) becomes

$$a_f^{(k)} = \frac{\partial m}{\partial r_{12}} \sum_{\alpha=1,2} \frac{\partial r_{12}}{\partial \lambda^{(0)}(t_\alpha)} \sum_{ij} (\tilde{C}_{ij}^{(k)}(t_\alpha) - 2V_i^{(k)} \bar{V}_j) v_i^{(0)}(t_\alpha) v_j^{(0)}(t_\alpha) . \quad (2.183)$$

This is still true if the eigenvectors are orthonormalized as in eq. (2.173), but instead of solving the generalized symmetric eigensystem in eq. (2.172), we transform the latter to standard non-symmetric problem, where the eigenvectors are orthonormalized with the trivial metric  $\delta$ , as follows

$$\tilde{C}^{-1}(0) \tilde{C}(t) \mathbf{v}^{(\alpha)}(t) = \lambda^{(\alpha)}(t) \mathbf{v}^{(\alpha)}(t) , \quad (2.184)$$

and the eigenvalues are given now by

$$\lambda(t) = \frac{\mathbf{v}(t)^T \tilde{C}(t) \mathbf{v}(t)}{\mathbf{v}(t)^T \tilde{C}(0) \mathbf{v}(t)} . \quad (2.185)$$

Finally, the linear deviation sequence needed for the estimation of effective mass error when variational method is used is given by

$$a_f^{(k)} = \frac{\partial m}{\partial r_{12}} \sum_{\alpha=1,2} \frac{\partial r_{12}}{\partial \lambda^{(0)}(t_\alpha)} \frac{1}{\mathbf{v}(t_\alpha)^T \tilde{C}(0) \mathbf{v}(t_\alpha)} \sum_{ij} \left[ \tilde{C}_{ij}^{(k)}(t_\alpha) - 2V_i^{(k)} \bar{V}_j (1 - \lambda^{(0)}(t_\alpha)) \right] v_i^{(0)}(t_\alpha) v_j^{(0)}(t_\alpha) . \quad (2.186)$$

In our analysis, we applied jackknife, the above formula and the numerical implementation of the linearization method. It turned out that results from different methods are compatible.

# 3 Numerical Analysis and Spectrum

## Results: TSMB

In the Wilson fermion approach we performed Monte Carlo investigations of the  $\mathcal{N} = 1$  SYM theory in four-dimensions on the lattice. The dynamical gluinos are in the adjoint representation of the  $SU(2)$  color gauge group. We perform fine tuning of the gluino bare mass to its critical value. Our aim is to determine the mass spectrum of the low-lying bound states which is expected to be organized in supermultiplets in the infinite volume continuum limit. Furthermore, we investigate the lattice WI's. For this purpose we perform simulations on large lattices to decrease the finite size effects using the TSMB updating algorithm. In this chapter we present the results of the analysis of the TSMB ensembles. These ensembles were previously produced with TSMB algorithm at three points of light gluino mass at bare gauge coupling  $\beta = 2.3$ . This value of  $\beta$  is believed to be within the region of reasonably good scaling.

This chapter is organized as follows: we begin by giving details of the simulation setup and the algorithmic tuning. Then, we discuss some physics of lattice SYM like confinement and static potential. Details of the spectrum analysis are presented. Before giving a summary of this chapter, the numerical analysis of lattice SUSY WI's and the localization of the chiral limit are explored.

### 3.1 Simulation details

The TSMB ensembles studied here have been produced on larger lattices compared to those previously studied within the DESY-Münster collaboration project. The goals were to approach the limit of vanishing gluino mass and to study the finite size effects by simulations of  $\mathcal{N} = 1$  SYM theory with gluino mass closed to their critical values. The bare gauge coupling is kept  $\beta = 2.3$ . This value is known to be in the lower end of the scaling region from studying pure  $SU(2)$  gauge theory on the lattice. The preparation of the ensembles with the TSMB algorithm was carried out at larger values of the hopping parameter (small gluino mass), at three points:  $\kappa = 0.1955$ ,  $\kappa = 0.196$  and  $\kappa = 0.1965$ . These values were chosen on the basis of the experience with the model so far realized by the DESY-Münster collaboration. At larger hopping parameter  $\kappa$ , the simulations suffer from critical slowing down due to the smallness of the minimal eigenvalues of  $\tilde{Q}^2$ .

Moreover, to ensure that the smallest eigenvalues of the squared fermion matrix  $\tilde{Q}^2$  lie in the interval of the polynomial approximation one must decrease the lower bound of the interval of the approximation  $\epsilon$ . This results in higher order polynomials, and gives rise to high number of Matrix-Vector-Multiplication (MVM) in the updating steps.

### 3.1.1 Simulation parameters

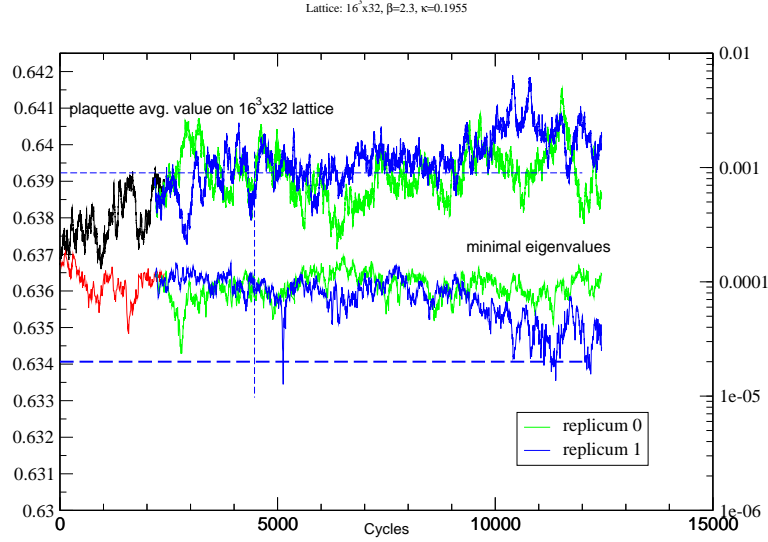


Figure 3.1: Average plaquette and smallest eigenvalue histories of the TSMB run (a) on the  $16 \cdot 32$  lattices.

The summary of the algorithmic parameters of the TSMB runs and the acceptance rate  $A_{NC}$  in the noisy correction step are displayed in Table 3.1.

Table 3.1: Gauge and fermionic bare couplings, Algorithmic parameters of the TSMB algorithm, the total statistics and the acceptance rate in the noisy correction step.  $n_5$  is a second higher input for  $n_3$  (see notations in the text).

run	Lat	$\beta$	$\kappa$	$\epsilon$	$\lambda$	$n_1$	$n_2$	$n_3$	$n_4$	$n_5$	Updates	offset	$A_{nc}$ %
(a)	$16^3 \cdot 32$	2.3	0.1955	$2.0 \cdot 10^{-5}$	4.0	40	800	300	700	760	$\sim 12500$	5	50-80
(b)	$16^3 \cdot 32$	2.3	0.1960	$4.0 \cdot 10^{-6}$	4.0	40	1800	2000	2030	2080	$\sim 23500$	5	50-80
(c)	$16^3 \cdot 32$	2.3	0.1965	$4.0 \cdot 10^{-6}$	4.0	40	1800	2000	2030	2080	$\sim 18000$	10	50-62

The Table 3.1 shows that the hopping parameter was gradually increased by a step of 0.0005. Also, the lower bound for the polynomial approximation for the runs (b) and

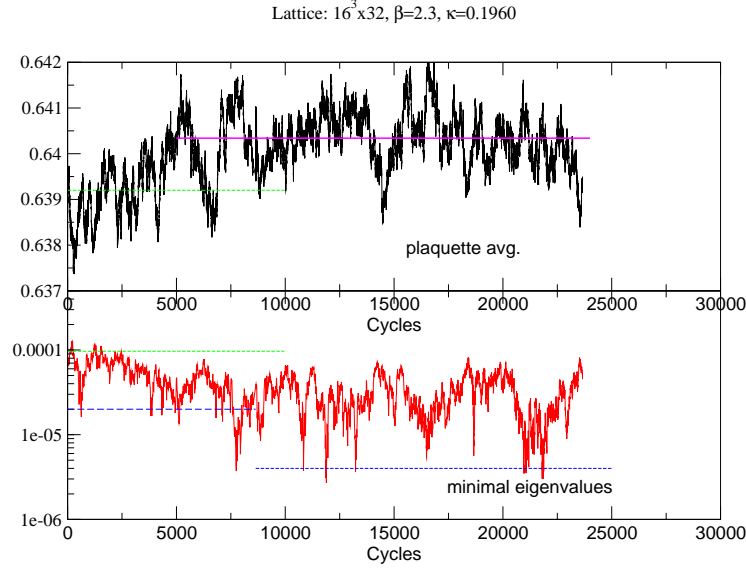


Figure 3.2: *Average plaquette and smallest eigenvalues histories of the TSMB run (b) on the  $16 \cdot 32$  lattices.*

(c) is of order  $\mathcal{O} = 10^{-1}$  smaller than the one of the run (a).  $\lambda$  is the upper bound of the polynomial approximation. The eigenvalues of  $\tilde{Q}^2$  are expected to be in the interval  $[\epsilon, \lambda]$  which is the domain of validity of the polynomial approximation. However, in Figs. 3.1, 3.2 and 3.3 one observes that some smallest eigenvalues lie below the lower bound  $\epsilon$ . The configurations with such small eigenvalues are called exceptional. In the run (c) an important number of exceptional configurations was observed. The first polynomial order  $n_1$  used in the multi-bosonic representation of the local update  $P_{n_1}^{(1)}$  was maintained to  $n_1 = 40$  instead of been increased in order to keep the simulations time reasonable. The order of the polynomial used in the noisy correction step  $P_{n_2}^{(2)}$  is relatively large to ensure higher acceptance rate  $A_{NC}$  in the noisy correction step.  $n_3$  is the order of the third polynomial  $P_{n_3}^{(3)}$  which approximates the inverse square root of the second polynomial  $P_{n_2}^{(2)}$ .  $n_4$  is the order of the polynomial used in the reweighting step and  $n_5$  is the order of a second polynomial  $P_{n_5}$  which can replace  $P_{n_3}^{(3)}$  (see Section 2.3 for details). The column 12 to 14 reports the number of update at equilibrium, the offset between saved configurations and finally  $A_{NC}$  is the global accept-reject acceptance rate which is  $> 50\%$  for all runs. The number of heat-bath, over-relaxation and Metropolis sweeps performed at each step of local updating was 2, 2 and 36 respectively. The number of Metropolis sweeps separating two noisy correction steps was 12 which means that 3 noisy correction steps were performed. Finally, after 10 updating steps global quasi-heath-bath for pseudofermions was performed to reduce the long tail in the autocorrelations.

The histories of the runs are collected in in Figs. 3.1, 3.2 and 3.3. The histories show the thermalization process during the run production for the time-like plaquette and the

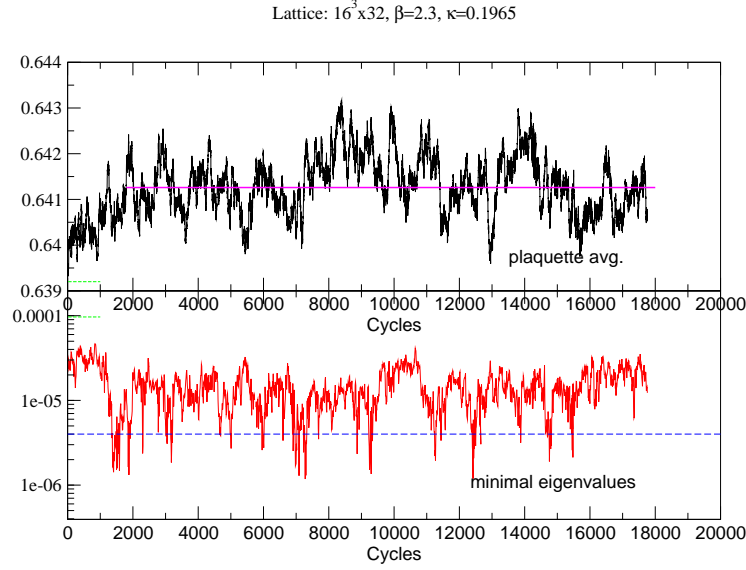


Figure 3.3: *Average plaquette and smallest eigenvalues histories of the TSMB run (c) on the  $16 \cdot 32$  lattices.*

smallest eigenvalues of the preconditioned hermitian square fermion matrix for the saved configurations. In the run at  $\kappa = 0.1955$  two independent lattices (two replicas) were simulated. However, only informations for one replica are displayed in the Table 3.1. The second replica was omitted in the analysis due to some discrepancies which have been found. The adjoint pion mass measured on the two replicas shows inconsistencies. We concluded that the process of thermalization might be not reached in the case of this replica.

In the Table 3.2 we summarize the average of the plaquette  $\langle \text{plaq} \rangle$  and the smallest eigenvalues  $\langle \lambda_{\min} \rangle$  which are also plotted in Fig. 3.4, we give also an estimate of their integrated autocorrelation-times  $\tau_{\text{observable}}$  and their window  $w$  computed by the windowing method introduced in Section 2.4. In the TSMB algorithm it is known that larger values of  $n_1$  have the effect of increasing the integrated autocorrelation-times. Here, even  $n_1$  was maintained constant for all runs, we observed that at lighter gluino mass the plaquette integrated autocorrelation-time grows and are relatively large. That means, at light gluino mass, long time of updating is necessary in order to obtain reliable statistics suitable for the spectrum measurements.

### 3.1.2 Smallest eigenvalues

During the updating process the smallest eigenvalue and the largest eigenvalue of  $\tilde{Q}^2$  are computed. The extremal eigenvalues lie in the interval  $[\epsilon, \lambda]$  for a good approximation of the first polynomial  $P_{n_1}^{(1)}$ . However, for some configurations a drop of the smallest

Table 3.2: *Plaquettes and minimal eigenvalues averages and autocorrelations and the windows ( $w$ ) of the integrated time-autocorrelation sum.*

run	$\langle \text{plaq} \rangle$	$\tau_{\text{plaq}}$	$w$	$\langle \lambda_{\min} \rangle$	$\tau_{\lambda_{\min}}$	$w$
(a)	0.639126(169)	167.6	535	$9.55(50) \cdot 10^{-5}$	38.2	101
(b)	0.64034(10)	181.1	550	$3.04(37) \cdot 10^{-5}$	37.0	124
(c)	0.64126(11)	254.2	742	$1.48(13) \cdot 10^{-5}$	10.9	66

eigenvalue below  $\epsilon$  can occur and the accuracy for the approximation on such configurations has to be corrected, either by computing the correction factor, or by selecting a subsample for measurements which does not include them. In fact, the correction factor should be in principle computed for each saved configuration, but within the experience of the DESY-Münster collaboration the correction factor distribution turned out to be gaussian distributed with average  $\sim 1$ . Furthermore, negative Pfaffian is more probable for exceptional configurations. The lower bound of the approximation interval is shown by the lower dashed lines in the history figures. Moreover, the computation of the correction factors and the sign of Pfaffian requires additional computing time. At the time where the ensembles were produced there was not enough allocated computing time for such purposes. We limited ourselves by selecting subsamples without exceptional configurations. For the TSMB ensembles correction factors including the Pfaffian sign were not computed. Note here that removing exceptional configurations<sup>1</sup> from the subsample introduces a bias. This bias is, however, small for few removed exceptional configurations.

In Fig. 3.4 the smallest eigenvalue average and the plaquette average are displayed as function of the inverse hopping parameter  $1/\kappa$ . One can observe, that the smallest eigenvalue average becomes rather small and can fluctuate practically down to zero. As best estimate of the critical hopping parameter for zero gluino mass we found  $\kappa_{cr} \simeq 0.1969$ , as will see in the chiral limit extrapolation, and hence  $1/\kappa_{cr} \simeq 5.078$ .

The smallest eigenvalues of the fermion matrix  $\tilde{Q}^2$  are fermionic (related to gluinos) quantities and may be eventually used to study the chiral phase structure which is expected from the spontaneous discrete chiral symmetry breaking in the model. One expects to see two gaussian behavior of the smallest eigenvalue distribution near the critical region. The distribution of the smallest eigenvalues for the TSMB ensembles are reported in Fig. 3.5. A good data of a promising observable to investigate the chiral phase would exhibit a two-gaussian distribution. More precisely, one would see two-peak structure of the data distribution in the chiral limit at  $\kappa_{cr}$ . But for fermionic observables

<sup>1</sup> Configuration with extremely small smallest eigenvalue

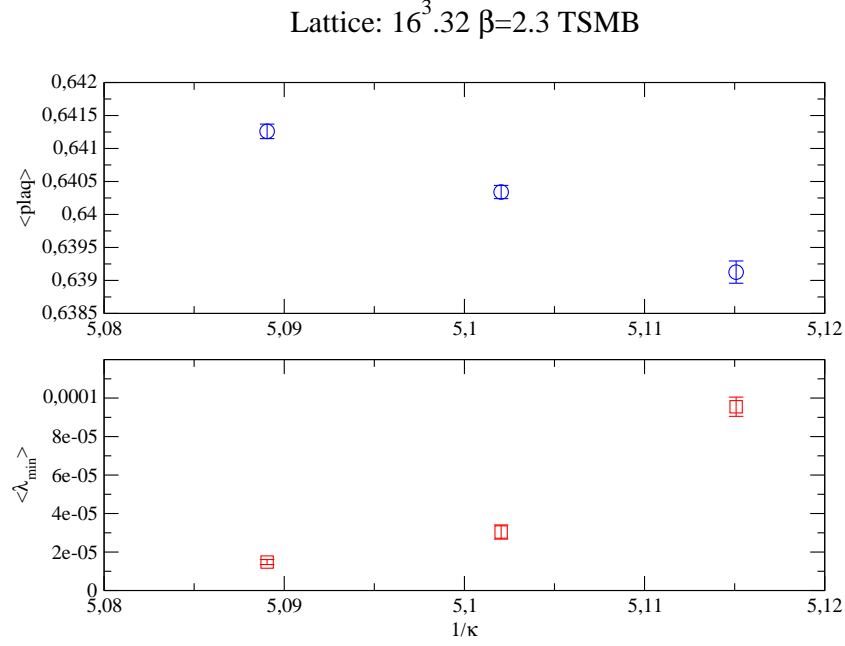


Figure 3.4: *Plaquette and smallest eigenvalues averages for all TSMB runs on the  $16^3 \cdot 32$  lattices.*

like the smallest eigenvalue or the gluino condensate in the Wilson formulation a shift of the two-peak distribution due to the additive renormalization observation is expected [69]. It turns out that the smallest eigenvalues on our samples are rather less sensitive to the chiral transition. However, in Fig. 3.5 at  $\kappa = 0.1955$  one could observe qualitatively that the two-gaussian behavior with equal weights is clearer than one gaussian, and this may encode the information on the signal of the chiral phase. At  $\kappa = 0.196$  a drop of the weight of the gaussian at larger minimal eigenvalues can be observed. At lighter gluino mass ( $\kappa = 0.1965$ ) the contribution of the gaussian at larger smallest eigenvalue becomes weaker, and one expects a single gaussian behavior beyond this value.

### 3.1.3 Autocorrelation-time

The autocorrelation-time of the plaquette is an essential observable to study the optimization of the TSMB updating algorithm. The experience has shown the strong dependence of the autocorrelation-time on the TSMB algorithmic parameters:  $\epsilon, \lambda, n_1, n_2, n_3, \dots$ . We considered here as optimization criterion the integrated autocorrelation-time  $\tau_{int}$ . The windowing method of Sokal *et al.* [42] or of Wolff [44] are very useful in finding an estimate of  $\tau_{int}$  through introducing the cut-off (called also window)  $w$  in the summation (2.51) which defines the  $\tau_{int}$  summation. It is expected that larger values of  $n_1$  have the effect of increasing the integrated autocorrelation-time. In our TSMB simu-

Lattice:  $16^3.32$ ,  $\beta=2.3$

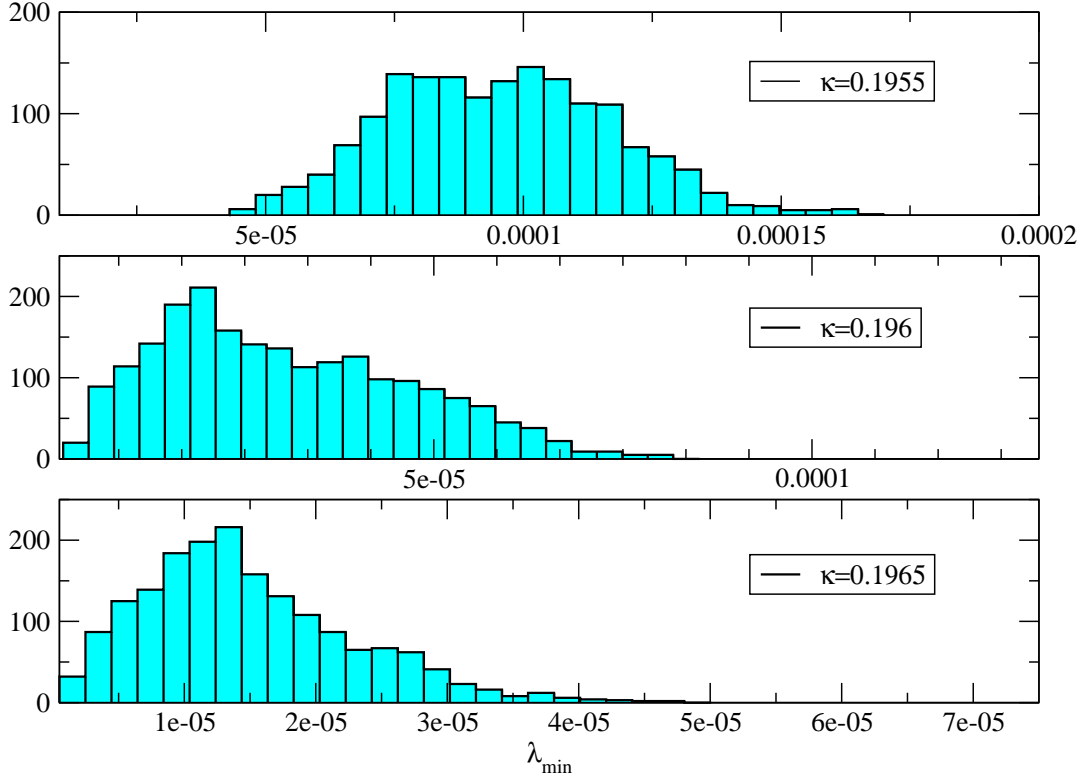


Figure 3.5: *Distribution of the smallest eigenvalues for all TSMB runs on the  $16 \cdot 32$  lattices.*

lations,  $n_1$  was kept constant for ensembles at different hopping parameter. It turns out that while keeping  $n_1$  constant the integrated autocorrelation-time of the plaquette increases slightly at an increasingly light gluino mass as we have shown in Table 3.2. The autocorrelation-time of the plaquette as function of the updating sweeps and its integrated autocorrelation-time as function of the window for all TSMB runs are displayed in Fig. 3.6. The window corresponds to the value of the autocorrelation time at which  $\tau_{int}$  becomes independent of the cutoff  $w$ . However, at large  $w$  values the autocorrelation-time is dominated by its noise hence a fluctuation of  $\tau_{int}$  is displayed.



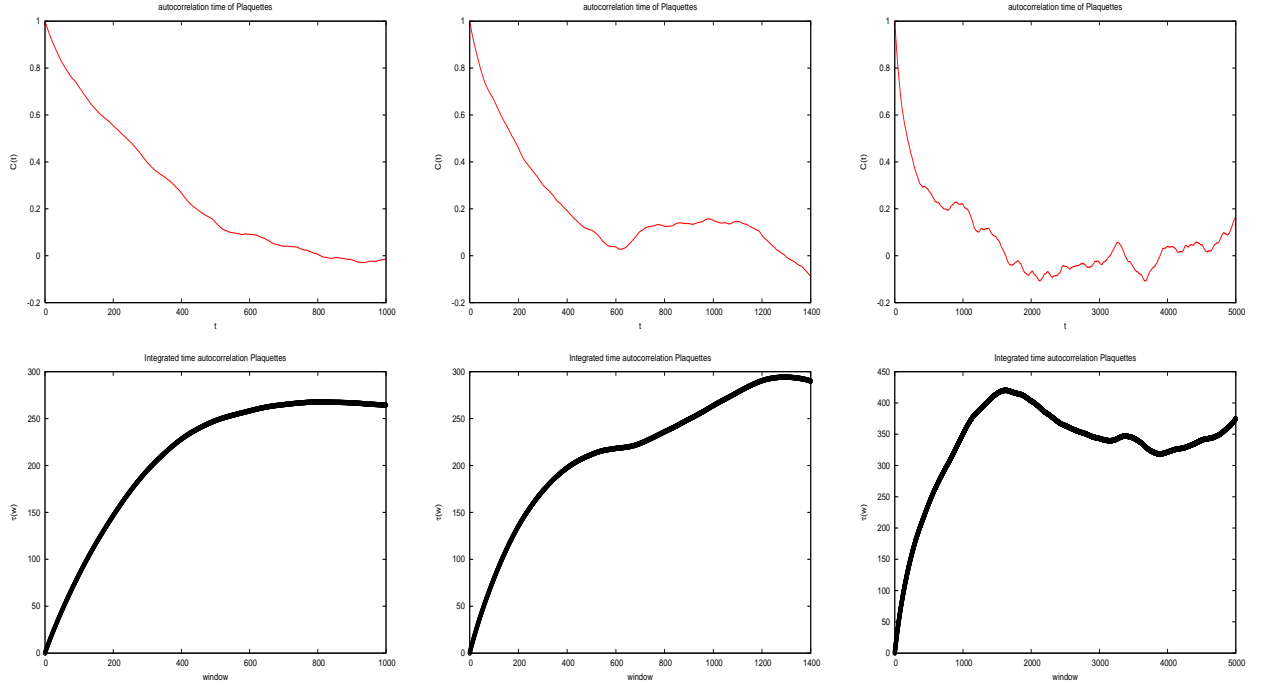


Figure 3.6: *Autocorrelation-times of plaquettes (upper panels) and integrated autocorrelation-time in function of the window  $w$  (lower panels) for runs (a), (b) and (c) from left to right.*

## 3.2 Confinement and physical scale

### 3.2.1 Static potential

In a standard non-abelian gauge theory quark confinement is expected. The consequence of confinement in SYM is color singlet bound states of gluons, gluinos or mixing of them (at least two of them.) In SYM these are the adjoint mesons, the glueballs and the gluino-glueballs (see Section 2.7). The confinement can be checked by studying the static potential  $V(r)$  as function of the spatial separation  $r$  between two color sources in the fundamental representation. The two quarks can be represented as two particles connected to each other with a tube of energy flux. The string tension  $\sigma$  is the relevant quantity which can be extracted from  $V(r)$  in this case. The non vanishing value of the string tension indicates that there is no screening effect of the adjoint dynamical gluinos on the fundamental sources.

To compute the static quark potential  $V(r/a)$  we determined first the smeared and unsmeared Wilson loops  $\mathcal{W}(r, t)$ . The resulting potential data are then used to be fitted to the potential model in order to extract the string tension  $a\sqrt{\sigma}$ . As mentioned in Section (2.12) there are different methods that can be used for this purpose; the

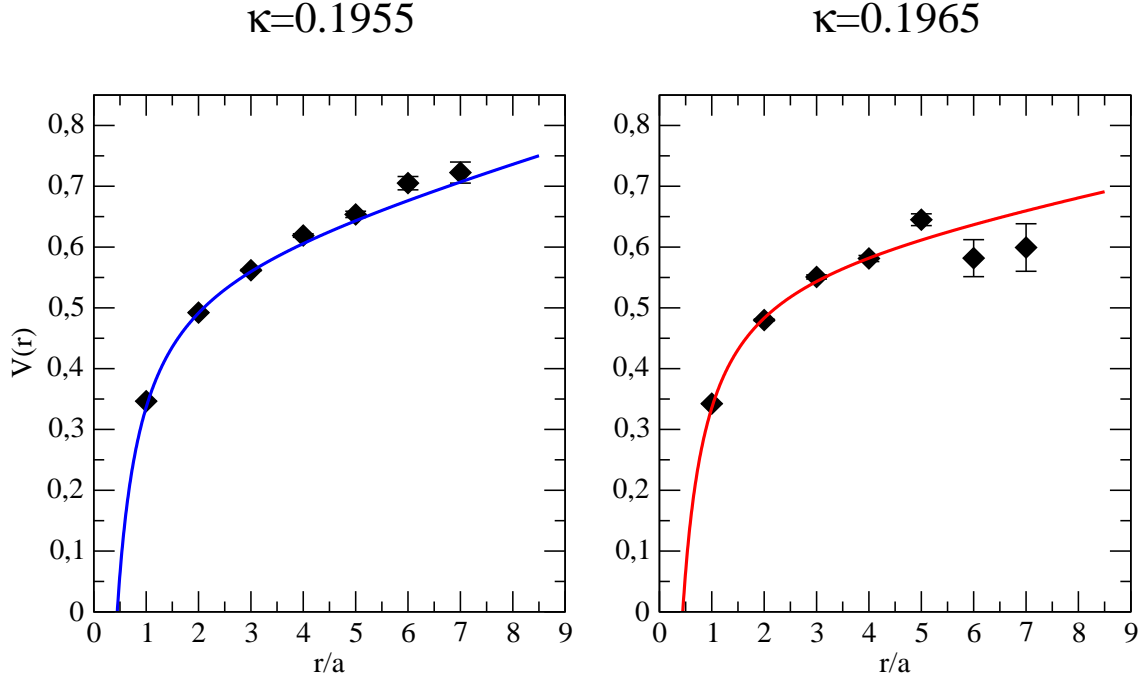


Figure 3.7: *Static quark potential:  $\beta = 2.3$  and lattices  $16^3 \cdot 32$ .*

potential method or the Creutz-ratio method. For the TSMB runs we determined the potential based on the two-fit procedure method.

The values of the static potential as function of the distance  $r$  are displayed in Fig. 3.7. At large separation distance  $r$  the string tension is non zero which signals no screening effects for SYM in four dimensions. This is in agreement with the previous investigations of the DESY-Münster collaboration. The potential which rises linearly with large separation of the gluinos is what is expected from a flux-tube picture of confinement. The screening effects occur only in the case of massless SYM in two dimensions as it was predicted theoretically and seems to be specific for low dimension SYM. Moreover, in two dimensions the screening disappears and confinement is restored as soon as a soft breaking is introduced [70].

### 3.2.2 Physical scale

We use the QCD scale to set the SYM simulations scale. The lattice spacing is set by the value of the Sommer scale  $r_0/a$  or the string tension  $a\sqrt{\sigma}$  as introduced in Section 2.12.

The potential  $V(r, t)$  data are fitted in the first step in the  $t$ -fit range  $[t_1, t_2]$  to the model in eq. (2.123) and the resulting quantities are the potential values  $V(r)$  for all  $r$ . In the second step the  $V(r)$  data are fitted to the model in eq. (2.128) in the  $r$ -fit range  $[r_1, r_2]$  to extract the value of the string tension and the Coulomb strength constant. The value of the Sommer scale is obtained from formula (2.133).

Table 3.3: Run (a); the values of  $r_0/a$  and the string tension fitted over different  $t$  and  $r/a$  ranges.

$t$ fit range	$r/a$ -fit range	$r_0/a$	$a\sqrt{\sigma}$	$\chi^2$
1-8	1-3	5.68(21)	0.207(7)	$\sim 0$
	1-4	5.72(14)	0.205(5)	0.026
	1-5	6.06(15)	0.194(4)	10.34
	1-6	6.10(15)	0.193(4)	10.69
	1-7	6.17(15)	0.190(4)	13.67
	1-8	6.11(14)	0.192(4)	18.32

Some selected fitted values of  $r_0/a$  and  $a\sqrt{\sigma}$  are displayed in Table 3.3 and Table 3.4 for the runs (a) and (c) respectively. The scale values of the TSMB simulations are shown in Table. 3.5. We observe that the values of  $r_0/a$  are slightly smaller than the values obtained previously by the DESY-Münster collaboration. In one side, the previous values were computed on smaller lattices in the range  $6^3 \cdot 12$  to  $12^3 \cdot 24$  lattices. The difference in the  $r_0/a$  values could be explained as finite size effects. Moreover, in ref. [71] and ref. [18] the  $r_0/a$  was measured at equal value of the gluino mass on  $12^3 \cdot 24$  and  $16^3 \cdot 32$  lattices where the value of  $r_0/a$  on  $16^3 \cdot 32$  lattice was slightly smaller than its value on  $12^3 \cdot 24$  lattice. The measured values are reported in Table 3.6. On the other side, the low statistics of the present run could be not suitable for good estimate of  $r_0/a$ .

A better estimate of  $r_0/a$  could be obtained by using previous accurate DESY-Münster data obtained on  $12^3 \cdot 24$  lattices. Assuming that the statistics of previous measurements are sufficiently high, we take some values of  $r_0/a$  for a range of  $\kappa$  and extrapolate to  $\kappa_{cr} = 0.1969$  as displayed in Fig. 3.8. This provides a way to estimate  $r_0/a$  in the chiral limit which will be used in the comparison with the TS-PHMC measurements (Chapter 4) realized at different scale. We obtain then the extrapolated value

$$r_0/a \simeq 8.57(35) . \quad (3.1)$$

Using the QCD value for comparison,  $r_0 = 0.5$  fm, the conversion to the physical units gives a lattice spacing  $a(\beta = 2.3) \approx 0.06$  fm and its inverse is  $a^{-1} \approx 3.28$  GeV. The

Table 3.4: *Run (c); the values of  $r_0/a$  and the string tension fitted over different  $t$  and  $r/a$  ranges.*

$t$ fit range	$r/a$ fit range	$r_0/a$	$a\sqrt{\sigma}$	$\chi^2$
1-8	1-3	4.94(32)	0.238(15)	$\sim 0$
	1-4	7.13(63)	0.165(14)	9.28
	1-5	6.83(52)	0.172(13)	10.05
	1-6	7.23(58)	0.162(13)	16.43
	1-7	7.55(69)	0.156(14)	21.28
	1-8	7.63(72)	0.154(14)	33.06
1-9	1-3	5.03(35)	0.233(16)	0
	1-4	7.14(65)	0.164(15)	7.52
	1-5	6.87(54)	0.171(13)	8.08
	1-6	7.30(62)	0.161(13)	14.67
	1-7	7.65(73)	0.153(14)	19.60
	1-8	7.90(83)	0.149(15)	48.22

simulated lattices are quite fine and the box volumes are roughly  $L^3 \sim (1\text{fm})^3$ , which would be rather small for a reliable determination of the spectrum. In QCD, the volume of  $L^3 = (2\text{fm})^3$  or larger is required for such a purpose. However, the DESY-Münster collaboration has concluded that at least this physical volume is appropriate for short range gluonic quantities such as  $r_0/a$  and for the study of lattice SUSY Ward Identities [21, 18], also valid in a finite volume. A first alternative to have larger physical volume is to simulate larger lattices. But this seems to be hard since the lattice simulation costs will increase while keeping the lattice spacing small. A second alternative to solve the common problem of the physical volume in the TSMB simulation is to perform simulations at a smaller value of the parameter  $\beta$  (*i.e.* at a larger lattice spacing.) But, this could introduce larger  $\mathcal{O}(a)$  lattice artifacts and larger scaling violations. However, an alternative lattice action discretization with smaller scaling violations can be considered. This techniques are called “improvement” which is used in our second part of this work where we applied improved gauge action in the gauge sector of the SYM lattice action at larger lattice spacing.

Table 3.5: *The values of the Sommer scale and the square root of the string tension in lattice units of the TSMB ensembles (a) and (c).*

Ensemble	$N_{\text{conf}}$	$r/a$ fit range	$r_0/a$	$a\sqrt{\sigma}$	$L/r_0$
(a)	371	1-7	6.17(15)	0.190(4)	$\sim 2.59$
(c)	100	1-8	7.90(83)	0.149(15)	$\sim 2.02$

Table 3.6: *Finite size effects of  $r_0/a$ . values of  $r_0/a$ . data recorded from Ref. ??*

$L^3$	$\kappa$	$r_0/a$
$12^3$	0.1940	7.37(30)
$16^3$	0.1940	7.16(25)
$12^3$	0.1955	7.98(48)
$16^3$	0.1955	7.30(50)

### 3.3 The low-lying spectrum

The general strategy in calculating the different masses will be to determine the time-slice correlation functions of the interpolating fields (see Section 2.7). The relevant time-slice correlators  $C(\Delta t)$ ,  $\Delta t \in [0, T]$  are (where  $T$  is the lattice time extension) calculated on the configurations that were produced by the TSMB algorithm. Considering only to contribution of the ground states to the correlation function one can rewrite (2.71) as

$$C(t) = a_0^2 + a_1^2(e^{-mt} \pm e^{-m(T-t)}) , \quad t \in [0, T] . \quad (3.2)$$

Recall that  $m$  is the mass of the lowest state having the quantum numbers as those of the interpolating field.

Depending on the properties of the correlators under time-reversal symmetry, it is useful to use of the symmetric/anti-symmetric version of the above expression given by

$$C_{\pm}(\Delta t) = \frac{1}{2} [C(\Delta t) \pm C(T - \Delta t)] , \quad \Delta t \in [0, \frac{T}{2}] , \quad (3.3)$$

where the time-separation  $\Delta t$  is to be taken up to half the lattice time extension  $T$ .

In the case of the mesons the correlation functions are time-reversal symmetric, the energies  $m_n$  of intermediate states  $|n\rangle$  are achieved by fitting the correlators  $C(\Delta t)$  to the (general) *symmetric* function

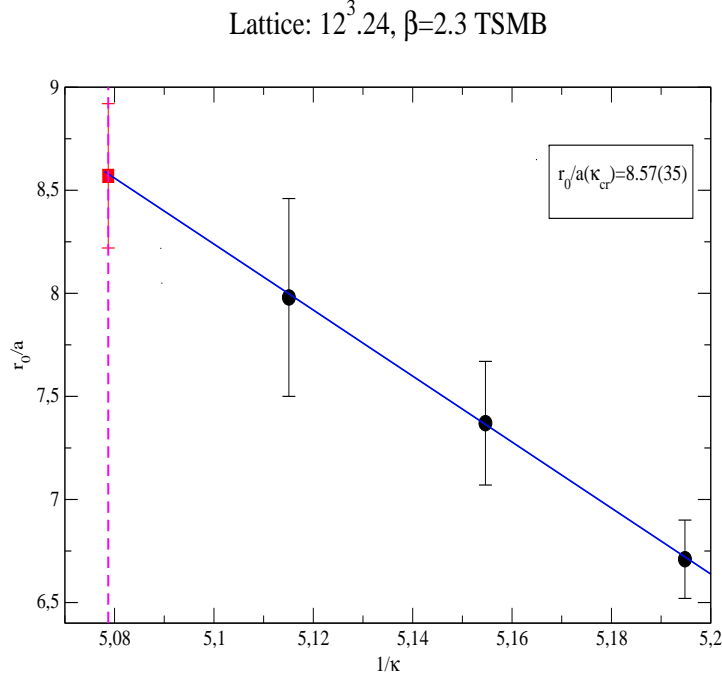


Figure 3.8: *Extrapolation of  $r_0/a$  to the massless gluino region (TSMB).*

$$C(\Delta t) = a_0^2 + \sum_n a_n^2 (e^{-m_n \Delta t} + e^{-m_n (T - \Delta t)})], \Delta t \in [0, \frac{T}{2}]. \quad (3.4)$$

Here  $m_1$  is again the lowest energy of the bound states, namely the mass of the particle to be determined by the fitting, the next higher energies  $m_n, n \geq 2$ , are those of the next excited state of the particle; for large values of time-slice separation  $\Delta t$  the contribution of these states to the correlator decreases exponentially and dies off, since  $m_n > \dots > m_1$ , and only lightest state survives

$$C(\Delta t) = a_0^2 + a_1^2 (e^{-m_1 \Delta t} + e^{-m_1 (T - \Delta t)}). \quad (3.5)$$

This function is the basic object to be used for the determination of the amplitude  $a_1$  and masses in (3.5) of the states created from the vacuum and then destroyed on the lattice. The constant  $c_0$  is only to be considered when the creation operator has positive parity, and so its vacuum expectation value is not vanishing like for  $a \cdot f_0$ .

The first step is to determine the effective mass  $m_{eff}$  to localize the plateau. The idea is to have a first orientation (by performing one mass fit) on the range where the mass of the lowest lying state can be isolated from the signal and try to estimate the mass. From some point  $t_b$  onwards to some end point  $t_e$ , the fit stabilizes and fit parameters show a plateau in an interval  $[t_b, t_e]$ . Then, the reliability of this result is

to be checked, by performing now a one mass fit to (3.5) in the interval  $[t'_b, t_e]$  where  $t_e$  is kept fixed and we increase the starting point  $t'_b$  from  $t_b$ ; we fit then in the intervals  $[t_b, t_e], [t_b + 1, t_e] \dots [t_e - 1, t_e]$ . The idea is that by increasing  $t_b$  we successively exclude more and more higher mass states from the measured correlator in this range. If we can observe again that the mass extracted from these fits is stable and fluctuates only within a reasonable error we conclude that the mass of the lowest lying state has been isolated.

In many situations, it is though that the influence of the next higher state is not small at the considered range, and the operator can display a significant overlap  $a_2$  with next higher state. A common way to deal with this situation is to take into account also the contribution of this state in the considered time-slice range by performing now a two mass fit to the function

$$C(\Delta t) = a_0^2 + a_1^2 (e^{-m_1 \Delta t} + e^{-m_1 (T - \Delta t)}) + a_2^2 (e^{-m_2 \Delta t} + e^{-m_2 (T - \Delta t)}). \quad (3.6)$$

However, one can carry out a two mass fit which leads to stable results only when the the projection onto the lowest state by the interpolating operator is very good. Hence it is not reasonable in much cases to perform a two mass fit to (3.6). In the case of this work we have carried out one mass fits as explained above.

The determination of the scalar mesons mass is one of the actual challenge in QCD (see for example [72]). In the case of  $SU(2)$  SYM the determination of  $a$ - $f_0$  mass is still difficult, in addition to disconnected part of the correlator, the  $a$ - $f_0$  interpolating lattice operator has non trivial vacuum expectation value (VEV). The operator has a positive parity, and hence can overlap with the vacuum. The experience of the DESY-Münster collaboration has shown that the quality of data for the adjoint scalar meson are not good to extract a reliable  $a$ - $f_0$  mass. To deal with this problem new methods of estimation of all-to-all propagators should be implemented. One of the new interesting methods which is expected to give more accuracy results was elaborated in Ref. [56]. We have also tried to analyze the scalar correlator on our new generated TS-PHMC ensembles in the next chapter. The full correlator has a large error coming from disconnected and the non trivial VEV contributions. Nevertheless, if we consider only the connected part which is analogous to the  $a$ - $a_0$  correlator in QCD a mass estimate of this unphysical particle (in our model) can be extracted.

In the following, we discuss the analysis of the adjoint mesons and their connected counterpart. Then, we discuss a construction of possible mesonic spin-1 state called  $a$ - $f_1$ . We will proceed to the analysis of the glueballs and the gluino-glueballs.

### 3.3.1 The adjoint pion $a$ - $\pi$

The correlation function of the adjoint pseudo-scalar meson  $a$ - $\eta'$  is obtained from the gluino propagators, and it has two parts, a connected and a disconnected one. The connected correlator gives rise to the adjoint pion  $a$ - $\pi$  particle. The latter particle is not

physical in the  $SU(2)$  SYM theory since the theory contains a single flavor Majorana. However, the mass of the  $a$ - $\pi$  is necessary to discuss the chiral limit as we will see in Section 3.5.1. The flavor-singlet nature of the theory gives rise to the disconnected contributions to the correlators. Their computation is known in lattice gauge theory to be a difficult task, requiring a long computing time as argued in Section 2.8.

### Ensemble (a)

Two independent sets of configurations are investigated at the hopping parameter  $\kappa = 0.1955$ . The number of the analyzed configurations is 368 for each lattice. For both lattices we determine independently the low-lying states; the estimations should be usually combined.

We focus here on the connected correlator of the pseudo-scalar field  $\bar{\lambda}\gamma_5\lambda$ . The connected time-slice correlators are fitted to the form in (3.5) where  $a_0 = 0$ . We determine the effective mass shown on Fig. 3.9 for the first replica run. We perform a fit in the intervals  $[t_i, t_i + 1]$  where  $t_i$  runs from 1 to 15. In this way we observe that from  $t = 5$  to  $t = 10$  the mass stabilizes and begins to fluctuate within the error. This behavior would then allow us to have a first estimate of the lowest mass. We then perform a one mass fit in intervals  $[10, 15], \dots, [14, 15]$  to extract the best estimate of the mass of the  $a$ - $\pi$ , the fit results are shown on Table. 3.7. For the second replica run the  $a$ - $\pi$  effective mass in Fig. 3.10 displays a plateau in the interval  $[11, 15]$ , then we present the estimated values of the mass in Table. 3.8.

Table 3.7: *Low-lying mass for the  $a$ - $\pi$  from one mass fit in the interval  $[t_i, 15]$  (replica 1).*

$[t_i, 15]$	$t_i = 10$	$t_i = 11$	$t_i = 12$	$t_i = 13$	$t_i = 14$
$am$	0.347(3)	0.346(3)	0.345(3)	0.345(3)	0.346(4)

Table 3.8: *Low-lying mass for the  $a$ - $\pi$  from one mass fit in the interval  $[t_i, 14]$  (replica 2).*

$[t_i, 14]$	$t_i = 12$	$t_i = 13$
$am$	0.247(9)	0.246(11)

One observes that the difference between the masses of  $a$ - $\pi$  obtained from the the two independent replica runs is very significant yielding discrepancies. This inconsistency can be attributed in the case of the second replica (replica 1 in Fig. 3.1) to the thermalization



$16^3.32 : \kappa=0.1955$  rep1 :  $\beta=2.3$  TSMB

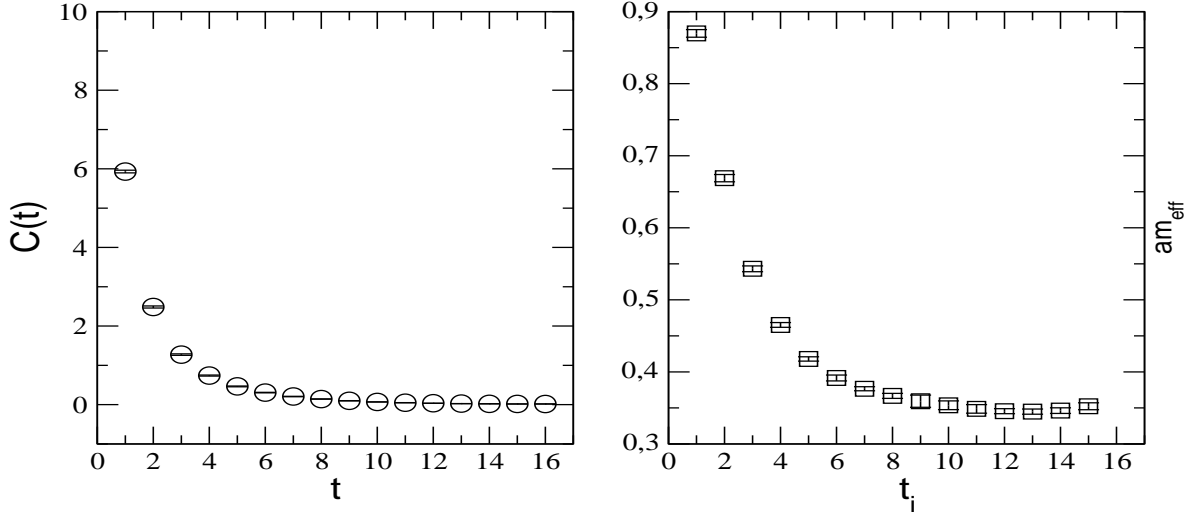


Figure 3.9: *Time-slice correlation function of the  $a$ - $\pi$  (left) and its effective mass as function of  $t_i$  (replica 1) (right), run (a).*

process. In Fig. 3.1 it seems that the this replica has not been thermalized, hence the estimated value of the  $a$ - $\pi$  mass is not the true one. Therefore, this replica is discarded from the analysis in the next and we consider only replica 1 for analysis of the spectrum at  $\kappa = 0.1955$ .

### Ensemble (b)

This is the second ensemble prepared with the TSMB algorithm and analyzed in the present work on  $16^3 \cdot 32$  lattice at  $\beta = 2.3$ . Our goal is to simulate a hopping parameters which is close to the critical value  $\kappa_{cr} \sim 0.1969$  obtained from the Ward-Identities in the work of Ref. [71]. A few number of "thermalized" configurations has been produced at this point. We used 765 configurations at  $\kappa = 0.196$  to determine the mass of the  $a$ - $\pi$  adjoint meson. The time-slice connected correlator and the effective mass are shown in Fig. 3.11.

The effective mass shows a presence of a plateau in the interval  $[t_b = 9, t_e = 14]$ . The fitted mass values in this interval are given in Table 3.9. Finally, we perform one mass fit in this interval and the estimated adjoint pion mass is

$$am = 0.264(5) . \quad (3.7)$$

$16^3.32 : \kappa=0.1955$  rep2 :  $\beta=2.3$  TSMB

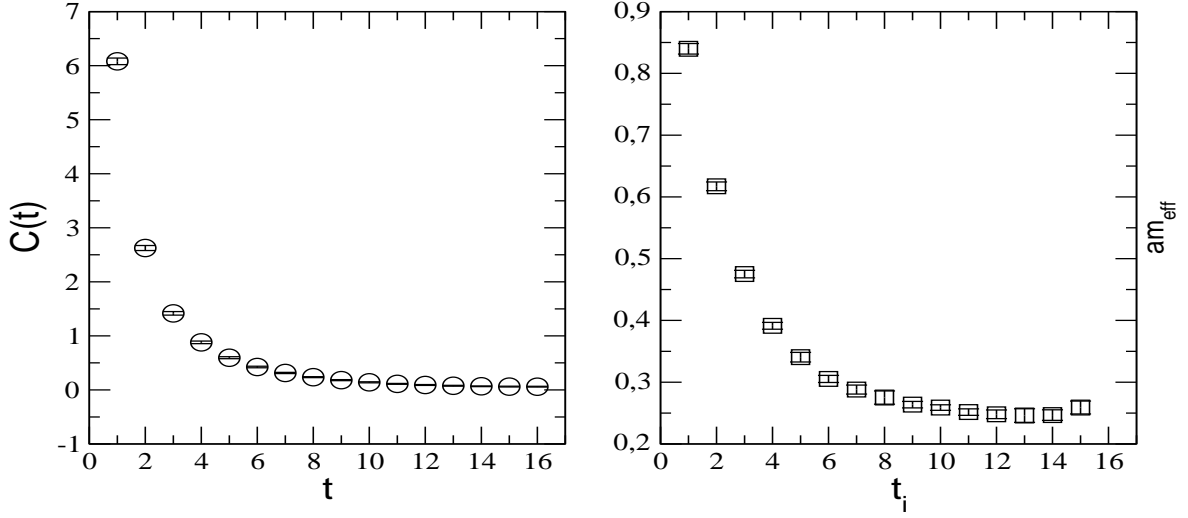


Figure 3.10: *Correlation time-slices of the  $a$ - $\pi$  (left) and its effective mass as function of  $t_i$  (replica 2) (right), run (a).*

$[t_i, 14]$	$t_i = 9$	$t_i = 10$	$t_i = 11$	$t_i = 12$	$t_i = 13$
$am$	0.264(5)	0.264(6)	0.266(5)	0.267(4)	0.266(4)

Table 3.9: The estimated mass of  $a$ - $\pi$  from two fit parameters in the interval  $[t_i, 14]$ .

The results of the pion mass obtained from this ensemble at  $\kappa = 0.1960$  can be compared with the previous ensemble (a) in order to elevate the discrepancy. The pion mass of the ensemble (b) is heavier than the one extracted from the ensemble at  $\kappa = 0.1955$ , replica 2. This is, however, not expected. Comparing to QCD the pion mass becomes smaller and smaller while going toward the critical region, and tends to vanishing mass in the chiral limit. The present analysis reveals that the correct estimated pion mass is the one extracted from the replica 1 *i.e.*  $am = 0.345(3)$ . Here, we should note that the estimated pion mass on replica 2 is in agreement with the estimation extracted from the ensemble  $\kappa = 0.1955$  on  $12^3 \cdot 24$  considered in the work of Ref. [18]. However, in the work of Ref. [18] the mass of  $a$ - $\eta'$  low-lying state was smaller than the estimated mass of the  $a$ - $\pi$ . In QCD, the mass of  $a$ - $\eta'$  is greater than the mass of  $a$ - $\pi$  at small sea quark mass.

$16^3.32 : \kappa=0.1960 : \beta=2.3$  TSMB

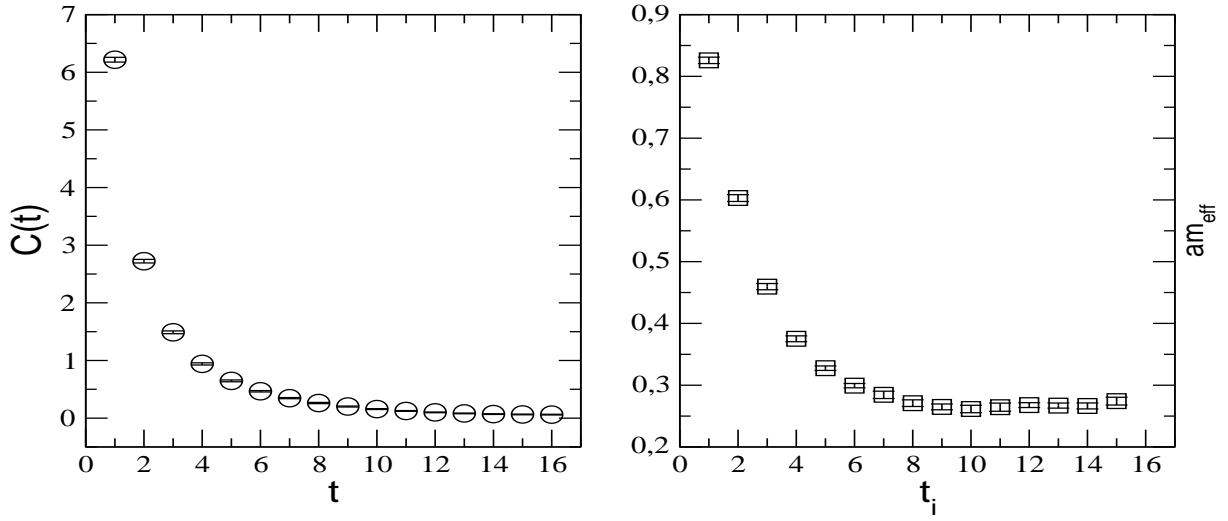


Figure 3.11: *Time-slice correlation function of the  $a$ - $\pi$  (left panel) and its effective mass as function of  $t_i$  (right panel), run (b).*

### Ensemble (c)

From the last ensemble prepared with TSMB at  $\kappa = 0.1965$  we selected only 100 configurations for analysis and the many exceptional configurations had to be discarded. This implies a low statistics for spectrum calculations. The mass of some bound states can be nevertheless estimated with acceptable accuracy. The time-slice correlator and the effective mass of the  $a$ - $\pi$  are presented in Fig. 3.12.

The effective mass displays a plateau in the range from  $t_b = 9$  to  $t_e = 15$  where a further global fit is performed to confirm the estimated pion mass (see Fig. 3.12). The fitted pion mass in the interval  $[9, 15]$  is presented in Table 3.10. This leads us to estimate the  $a$ - $\pi$  to be

$$am = 0.208(13) , \quad (3.8)$$

which is smaller than the previous mass on the ensemble (b). It is expected that the square pion mass behaves approximately linearly as function of the inverse hopping parameter. This fact, as we will see below, is used to estimate the critical hopping parameter where the  $a$ - $\pi$  vanishes in the OZI approach.

$16^3.32 : \kappa=0.1965 : \beta=2.3$  TSMB

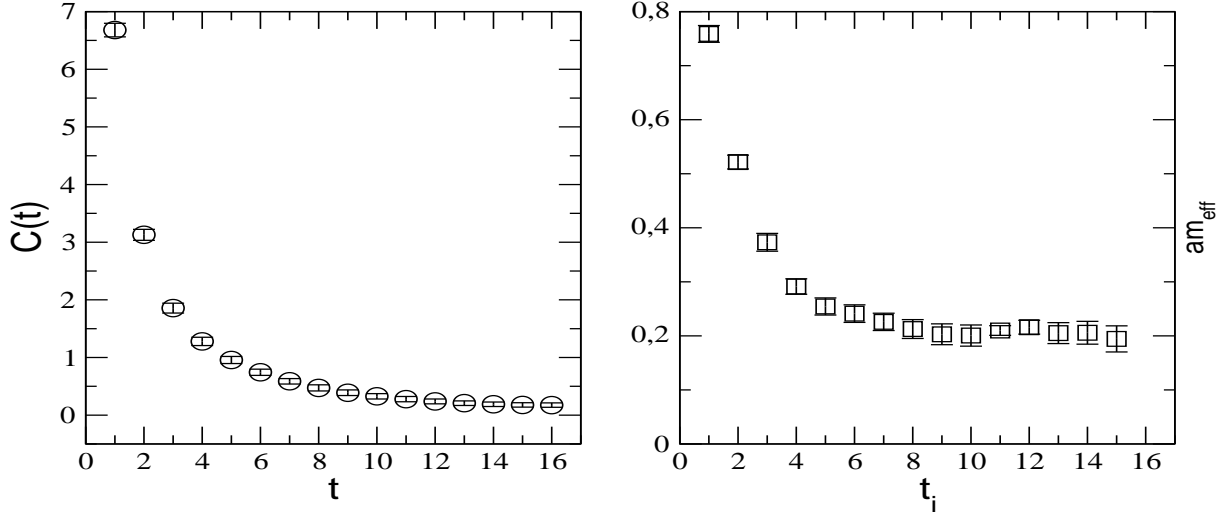


Figure 3.12: Correlation time-slices of the  $a$ - $\pi$  (left) and its effective mass as function of  $t_i$ (right), run (c).

$[t_i, 15]$	$t_i = 9$	$t_i = 10$	$t_i = 11$	$t_i = 12$	$t_i = 13$	$t_i = 14$
$am$	0.206(14)	0.208(13)	0.210(14)	0.209(16)	0.205(19)	0.205(21)

Table 3.10: The estimated mass of  $a$ - $\pi$  from two fit parameters in the interval  $[t_i, 15]$ .

### 3.3.2 The pseudo-scalar $0^{-+}$ adjoint meson $a$ - $\eta'$

The study of the adjoint mesons involves the most computational work. The correlation function of the pseudo-scalar  $a$ - $\eta'$  has two contributions; the first contribution comes from the connected correlator and the second one from disconnected correlator. The disconnected correlator appears since the theory contains a single flavor. The form of the pseudo-scalar correlator is given by

$$C(\Delta t) = -2 \left( C_{conn}(\Delta t) - \frac{1}{2} C_{disc}(\Delta t) \right). \quad (3.9)$$

The  $C_{conn}$  is the correlator of the  $a$ - $\pi$  particle discussed above. The disconnected correlators have been calculated using an improved version of the Volume Source Technique (VST) which was proposed in [51] for single flavor quantities. The new version is called Improved Volume Source Technique (IVST) and it is based on random gauge trans-

formations of the gauge configuration. In this variant of variance reduction methods, a systematic error is removed by performing  $N_g$  random gauge transformations of the inverted fermion matrix  $Q$ . We also applied the Stochastic Estimators Technique with spin-dilution (SET/SEM) which involves  $N_e$  noisy estimators for the all-to-all propagators (see Section 2.8 for details).

The selection of the samples of each ensemble for the analysis is based here on the behavior with respect to the smallest eigenvalues of the  $\tilde{Q}^2$  matrix. At given  $\kappa$  value, a subset of configurations was chosen on the basis of the integrated autocorrelation-time of the smallest eigenvalue reported in Table 3.2. One exception is the ensemble (c) where all the configurations were analyzed since we have in this case low statistics.

It is reported in [18] that on larger  $16^3.32$  lattice the computed pseudo-scalar correlator displays an offset, *i.e.* its long-time behaviour is not purely exponential. At large time separation a constant offset appears and hence the correlator would have an additional constant term. A given constant term is excluded by the nature of the pseudo-scalar interpolating operator which is not a parity invariant object. Moreover, this means that to study this state one has to perform fitting to the form (3.5) with  $a_0 \neq 0$ . The origin of the offset is probably from the averaged disconnected correlator which is computed in a stochastic estimators method. The number of random estimation  $N_e$  could be too low to decrease the statistical error and the systematic error associated to the stochastic estimation.

### Ensemble (a)

For large time separation the disconnected correlator converges to a plateau with negative values, which is probably the source of the offset term in the total pseudo-scalar correlator as can be observed on Fig. 3.13. The connected and the total correlators are also presented in order to compare the behavior of the two correlator parts at  $\kappa = 0.1955$ . At this point, we have used the IVST with a number  $N_g = 30$  of random gauge transformations to estimate the time-slices.

We proceed here in different way to determine the mass of the pseudo-scalar: in the first way we perform one mass fit of the correlator (3.5) with vanishing  $a_0$  and we extract the estimated mass. However, this analysis could lead to wrong results because it does not take into account the presence of the offset. In a second analysis, assumed to be the correct one, we perform one mass fit to (3.5) but now with non-vanishing  $a_0$  even the pseudo-scalar interpolating field has a null vacuum expectation value. The estimated mass is then extracted. In the third way, we first perform a linear fit of the total adjoint pseudo-scalar correlator  $C^{\eta'}(t)$  to a constant  $c$  at the large time-slice separation, in a given  $t$ -interval  $[t_1, t_2]$ . Then, the obtained constant  $c$  from linear fit is subtracted from the total correlator

$$C_{\text{sub}}^{\eta'}(t) = C^{\eta'}(t) - c \quad (3.10)$$

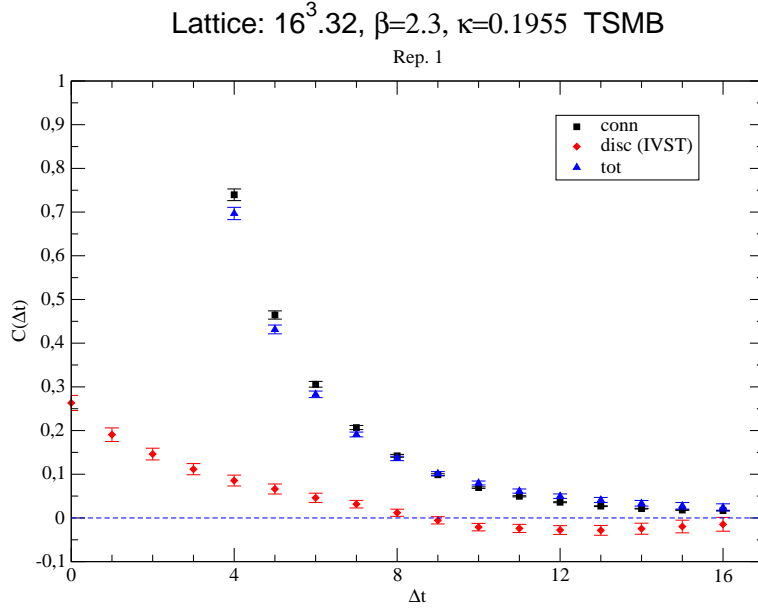


Figure 3.13: *The  $a$ - $\eta'$  disconnected, connected and the total correlators.*

for all  $t$ . The obtained subtracted correlator is fitted with one mass fit to the form (3.5) with  $a_0 = 0$ ; then we proceed as above to extract the mass of the lowest-lying state.

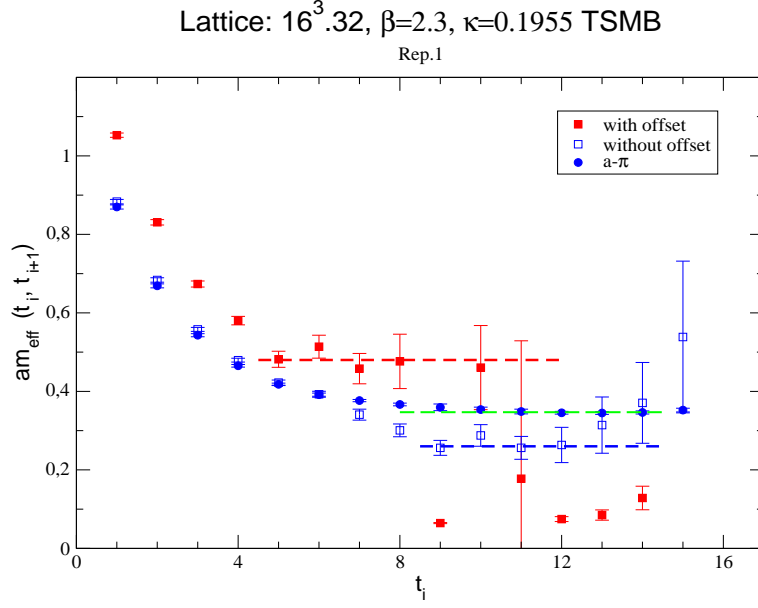
The numerical results of the three analysis approaches of the adjoint pseudo-scalar are discussed in the following. Here, we consider the ensemble (a) of Table 3.1.

#### • Two parameters fit of the $a$ - $\eta'$ correlator

The one mass fit is considered where the mass of the ground state is extract from a two parameters fit to (3.5) with  $a_0 = 0$ . The effective mass gives an orientation where the lowest lying state is located. In Fig. 3.14 the plot displays a plateau in the range from  $t_b = 9$  to  $t_e = 13$ . Since the effective mass is rather well determined in this range we perform the one mass fit to isolate the mass of the  $a$ - $\eta'$  particle were the mass stabilizes within the error (see Table 3.11 ). Our best estimate for the  $a$ - $\eta'$  mass is

$$am = 0.26(2) . \quad (3.11)$$

One observes that the estimated mass of the low-lying state  $a$ - $\eta'$  is smaller than the estimated mass of the  $a$ - $\pi$  particle. However, at smaller (larger hopping parameter) the adjoint pseudo-scalar correlator is expected to be dominated from its disconnected part. Hence, one expects a smaller adjoint pion mass compared to the mass of the adjoint pseudo-scalar  $a$ - $\eta'$ . A source of this discrepancy is the

Figure 3.14: *Effective mass of the  $a-\eta'$  as function of  $t_i$ .*Table 3.11: *Low-lying mass for the  $a-\eta'$  from one mass fit in the interval  $[t_i, 13]$ , run (a) Rep. 1.*

$[t_i, 13]$	$t_i = 9$	$t_i = 10$	$t_i = 11$	$t_i = 12$
$am$	0.26(2)	0.27(3)	0.25(3)	0.26(4)

presence of the offset in the correlator sample data which is ignored here. The fitting to the two parameters (one mass) function (3.5) leads in this case to wrong results since the observed offset in the correlator is not taken into account. The alternative fit model to the correlator data is then the three parameters function (3.5) with non-vanishing  $a_0$ . We consider this case in the next section.

#### • Three parameters fit of the $a-\eta'$ correlator

It is now expected that the estimated mass will increase when taking into account the appearing offset in the pseudo-scalar correlator. The offset has been ignored in the previous approach. The interpretation of the presence of the offset is that it mimics a particle with very small mass. The pseudo-scalar correlator in Fig. 3.13 is now fitted to the function (3.5) with  $a_0 \neq 0$  in the intervals  $[t-1, t+1]$  (at least three data points are needed.) In Fig. 3.14, besides the two parameters fit,

the results of the effective mass of  $a\text{-}\eta'$  resulting from three parameters fit to the function (3.5) are also presented.

As the effective mass stabilizes from the fifth time-slice to the tenth time-slice, we read off a first guess to the mass of the  $a\text{-}\eta'$ . After that, a further one mass fit is also performed in this range  $[t_b = 5, t_e = 10]$  with increasing  $t_b$  from 5 to 8. The results are reported in the Table 3.12, and the estimation of the  $a\text{-}\eta'$  mass is

$$am = 0.48(1) . \quad (3.12)$$

Table 3.12: *Low-lying mass for the  $a\text{-}\eta'$  from three parameters fit in the interval  $[t_i, 10]$ .*

$[t_i, 10]$	$t_i = 5$	$t_i = 6$	$t_i = 7$	$t_i = 8$
$am$	0.48(1)	0.48(2)	0.46(3)	0.47(7)

Of interest are the offset values, we have reported in Fig. 3.15 the effective value of the constant  $a_0$  from the three parameters fit. The plot shows a plateau from 5 to 10, where the first estimate of the offset can be extracted. In Table 3.13 we summarize the results of the fit for the offset  $a_0$  in the range  $[5, 10]$ .

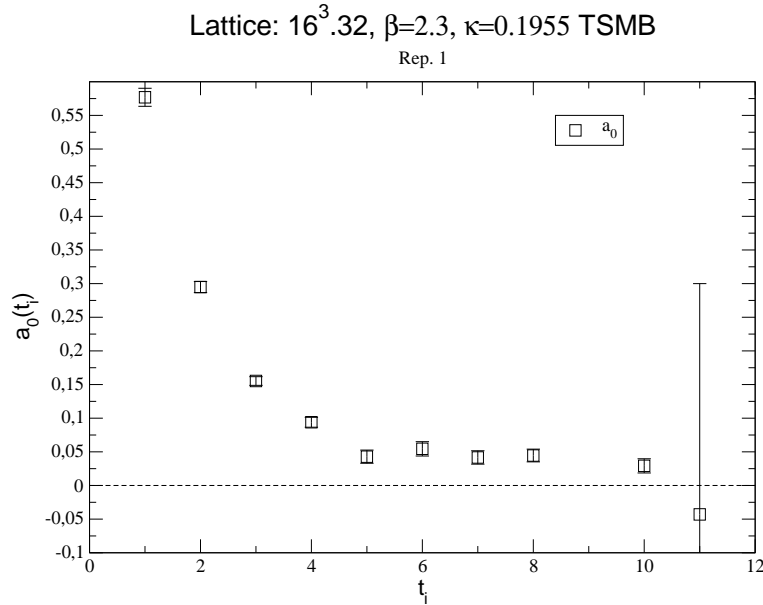


Figure 3.15: *The estimation of the constant  $a_0$  á la effective as function of  $t_i$ .*



Table 3.13: *Estimations of the constant  $a_0$  from three parameters fit in the interval  $[t_i, 10]$ , run (a) Rep. 1.*

$[t_i, 10]$	$t_i = 5$	$t_i = 6$	$t_i = 7$	$t_i = 8$
$a_0$	0.046(6)	0.046(6)	0.043(7)	0.044(9)

• **Two parameters fit of the  $a$ - $\eta'$  subtracted pseudo-scalar correlator**

In Ref. [51] the authors have tried to resolve the problem of the offset appearing in the adjoint pseudo-scalar correlator by hand by subtracting out a constant from the disconnected correlator. Then, the two parameters fit to the resulting (subtracted) total correlator is performed. However, we subtract out the constant term from the total correlator instead from the disconnected correlator. The latter is the assumed source of the rising offset. The question is still, what is the most elegant subtraction method one should choose. Here, we proceed by noting that the disconnected correlator begins to have negative values from the time-slice  $t_i = 9$  and displays a plateau which fluctuates within error in the range  $[10, 13]$  (see the disconnected correlator on Fig. 3.13). Then, we proceed by performing a linear fit to a constant of the total correlator in the intervals  $[t_i, 13]$  with  $t_i = 10, 11, 12, 13$  (see Table 3.14). The goal here is to extract an estimate of the offset  $c$  appearing in the correlator at large time separation. We scan the values of the constant systematically to search for value that gives a plateau for the effective mass. From Table 3.14 we quote as our best estimate

$$c = 0.045(4). \quad (3.13)$$

Table 3.14: *Estimation of the offset from linear fit in the interval  $[t_i, 13]$ , run (a) Rep 1.*

$[t_i, 13]$	$t_i = 10$	$t_i = 11$	$t_i = 12$	$t_i = 13$
$c$	0.060(2)	0.051(3)	0.045(4)	0.041(8)

The estimated constant above is now taken as a reference value to be subtracted from the total pseudo-scalar correlator defined in eq. (3.10). From the two parameters fit (one mass fit) the effective mass of the subtracted correlator in Fig. 3.16 provides us in the range from  $t_b = 5$  to  $t_e = 9$  with an estimate of the lowest mass. The results of the fit in the intervals  $[t_i = 5, 9]$  are presented on Table 3.15. The results are compatible to the values in Table 3.12. The estimation of the  $a$ - $\eta'$

mass is

$$am = 0.47(1) , \quad (3.14)$$

which is in agreement with the value discussed above obtained from three parameters fit of the adjoint pseudo-scalar correlator.

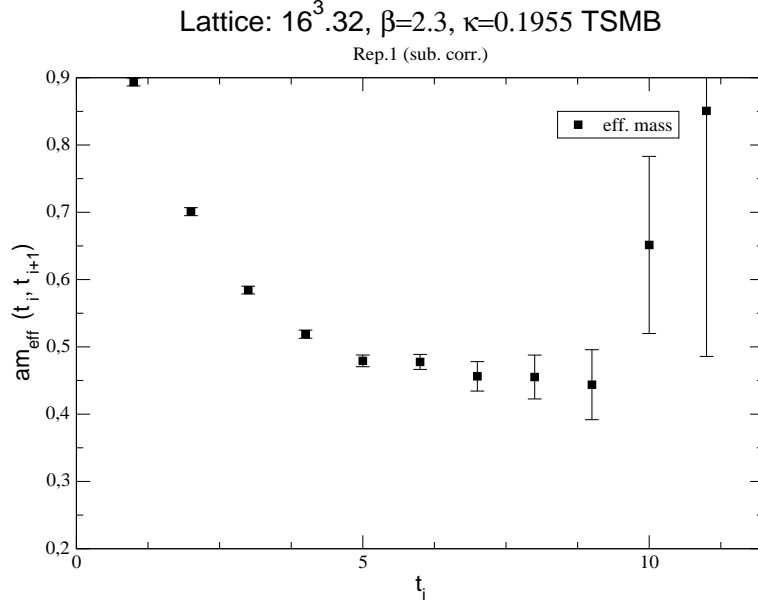


Figure 3.16: *Effective mass from the subtracted  $a\text{-}\eta'$  correlator as function of  $t_i$  with two parameters fit.*

Table 3.15: *Low-lying mass for the  $a\text{-}\eta'$  (subtracted) from two parameters fit in the interval  $[t_i, 9]$ .*

$[t_i, 9]$	$t_i = 5$	$t_i = 6$	$t_i = 7$	$t_i = 8$
$am$	0.47(1)	0.46(2)	0.45(2)	0.45(3)

### Ensemble (b)

In general the quality of the data degrades appreciably with decreasing light gluino mass. On this ensemble at  $\kappa = 0.1960$  we selected a subset of 192 configurations for the pseudo-scalar correlator analysis. Here we follow the methods of analysis on the ensemble (a) and we perform in this case the single-exponential fit to the  $a\text{-}\eta'$  with

three parameters since the offset also appears here in the disconnected correlator. The time-slice correlator of  $a\text{-}\eta'$  and the effective mass are illustrated in Fig. 3.17. We also plotted the mass extracted from mass fit in intervals  $[t_i, 16]$  with increasing initial time  $t_i$ . We applied here SET/SEM with 40 noisy estimators to compute the disconnected correlator. We observed that for a number of noisy estimators  $N_{est} > 40$  does not yield smaller statistical uncertainties, and only the gauge noise dominates the disconnected correlator. The effective mass stabilizes within error in the for  $6 \leq t \leq 10$  and it signals the localization of the low-lying state. The mass estimation of the adjoint pseudo-scalar meson in the time interval  $[6, 10]$ , where the effective masses agree within error, reads

$$am = 0.399(45) . \quad (3.15)$$

**$16^3.32 : \kappa=0.1960 : \beta=2.3$  TSMB**

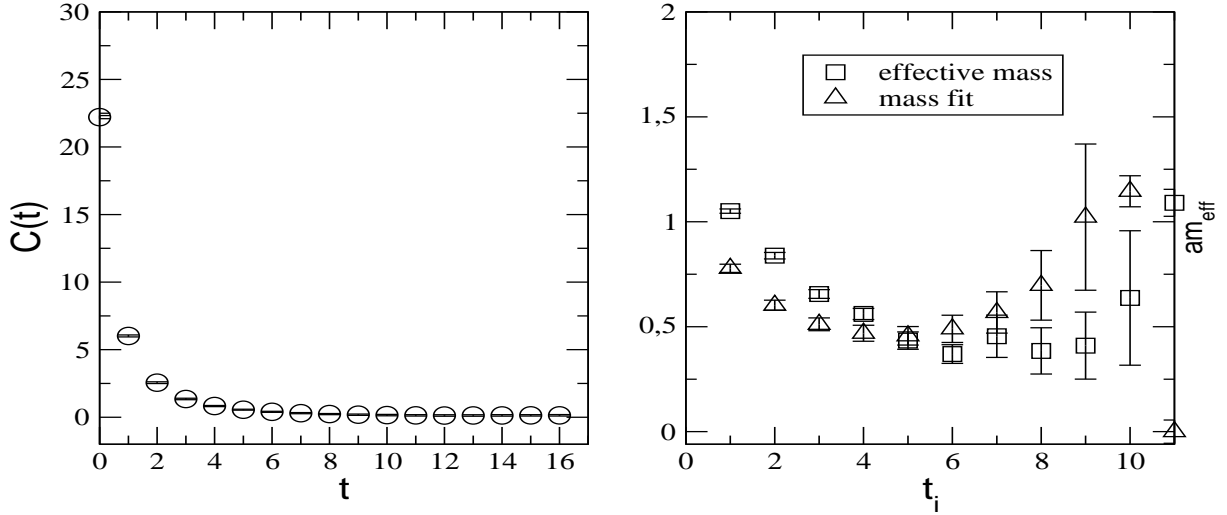


Figure 3.17: *Correlation timeslices of the  $a\text{-}\eta'$  (left). Effective mass as function of  $t_i$  and mass fit in interval  $[t_i, 16]$  (right), run (b).*

### Ensemble (c)

On this ensemble at larger hopping parameter  $\kappa = 0.1965$  we were confronted with several problems. Besides the low statistics of 100 available configurations, the statistical error of the disconnected correlator have large statistical error as illustrated in Fig. 3.19 compared to the one of the connected correlator in Fig. 3.12. Hence, this will

induce a low signal-to-noise ratio of the total correlator. Increasing the number of noisy estimations does not improve the signal-to-noise ratio of the  $a\text{-}\eta'$ .

### $16^3.32 : \kappa=0.1965 : \beta=2.3$ TSMB

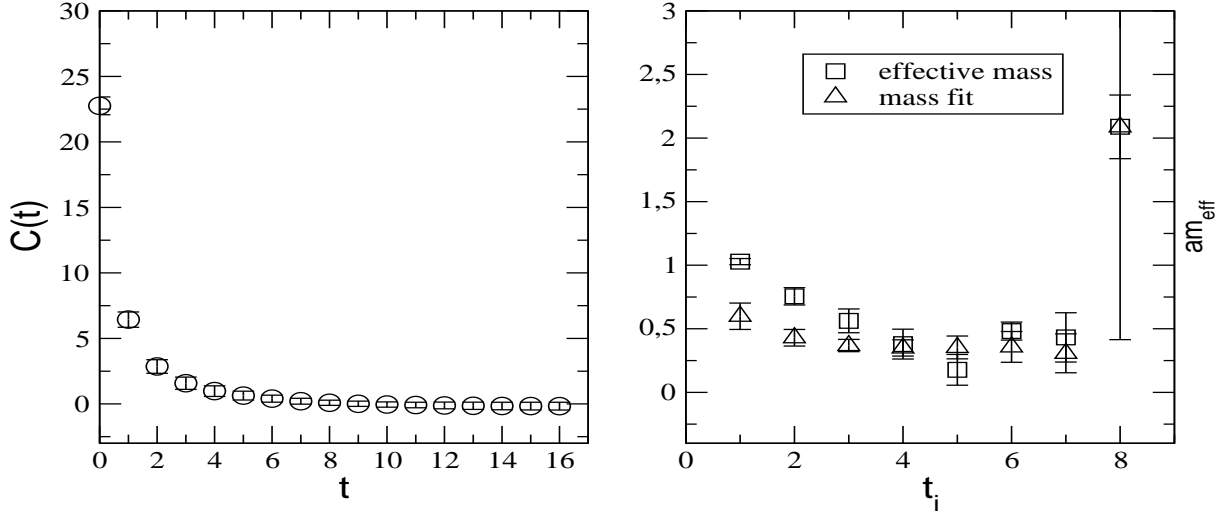


Figure 3.18: *Correlation timeslices of the  $a\text{-}\eta'$  (left) and its effective mass as function of  $t_i$  (right), run (c).*

At too light gluino mass, the estimation of the disconnected correlator is a real challenge. Indeed, the smallest eigenvalue of the square hermitian fermion matrix is too small, and hence the cost for inversions grows. We applied here also the conventional SEM/SET to compute the disconnected correlator with 40 noise samples on each configuration. A strategy to extract the mass of the ground state and reduce the contamination of higher states would be to extract exponentials of higher masses from the total correlators as in Ref. [71]. However, this method introduces a systematic error in the fit procedure as it was discussed in the study of Ref. [73]. Furthermore, a study of the European Twisted-Mass collaboration (ETMC) has revealed that the disconnected contribution is only big for the ground states, not the excited states as it was discussed in [74]. The subtraction of the excited states has to be performed only on the disconnected contribution. Comparing the effective mass in Fig. 3.12 and Fig. 3.19 one can observe that the *disconnected* effective mass stabilizes from small time separations, whereas for the  $a\text{-}\pi$  the effective mass stabilizes for larger time separation where the higher states die off. This picture confirms the strategy of removing the excited states only from the connected contribution to the  $a\text{-}\eta'$  and it has to be considered in future investigations.

$16^3.32 : \kappa=0.1965 : \beta=2.3$  TSMB

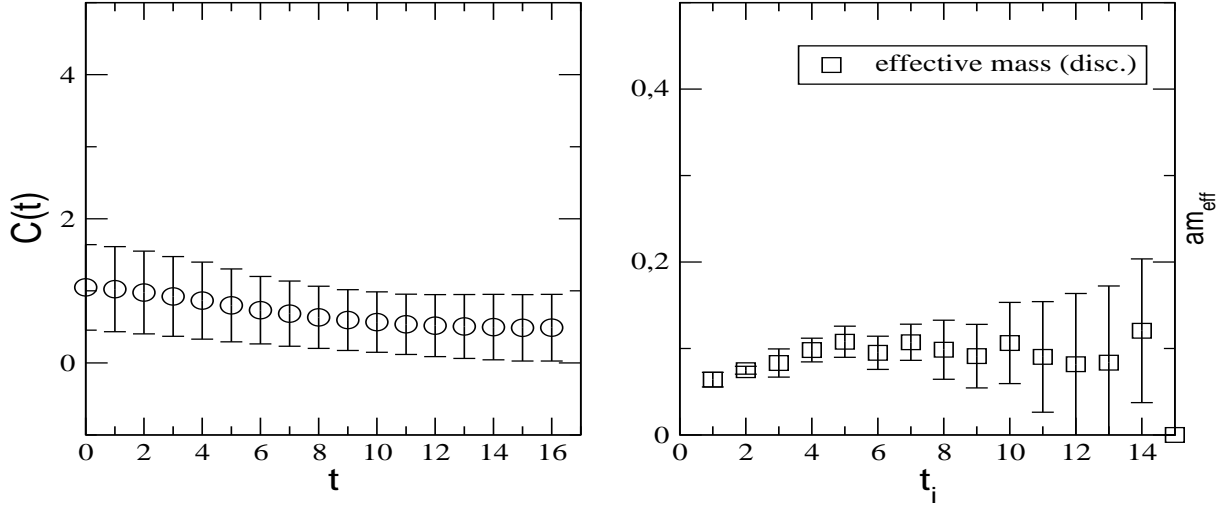


Figure 3.19: *Disconnected correlation time-slice of the  $a$ - $\eta'$  (left) and its corresponding effective mass as function of  $t_i$  (right), run (c).*

Finally, we perform single-exponential fit to the correlator data to extract the mass on this ensemble. We quote for our best estimate the mass extracted in the interval  $[4, 8]$  which reads

$$am = 0.319(77) . \quad (3.16)$$

At the end, following our observations during the analysis of the adjoint pseudo-scalar meson we attribute the offset, appearing in the time-slice correlator to statistical effects. Our expectation is that the offset disappears in higher statistics analysis.

### 3.3.3 The $a$ - $a_0$ adjoint meson

The time-slice correlation function of the  $a$ - $a_0$  and its effective mass is shown in Fig. 3.20 on the ensemble (a). This correlator is the connected contribution to the  $a$ - $f_0$  correlator. We note here that our convention for the correlation function is given in the eq. (3.9). The connected timeslice correlation functions are negative for all time separations except for the time separation  $\Delta t = 0$  where the correlator has a positive value. This behavior has been already observed in quenched or partially quenched QCD investigations of the structure content of the scalar meson for model with small quark mass (see for example [75, 76]).

The effective mass plot in Fig. 3.20 displays a plateau in the interval  $[10, 12]$ , where an estimate of the mass can be extracted. The results are summarized in Table 3.16. Here, the ensemble (a) is considered. One observes that the  $a$ - $a_0$  is not much heavier than  $a$ - $\pi$  at  $\kappa = 0.1955$ . In Ref. [77] it was found that the  $a$ - $a_0$  is of order  $\mathcal{O}(1)$  in lattice unit heavier than the  $a$ - $\pi$  is the SUSY limit. This does not agree with the finding here where the masses can become degenerate in the SUSY limit as the mass difference is getting smaller when approaching the SUSY limit. However, the results of Ref. [77] are explorative since small lattices were considered in the quenched approximation and hence the results are affected by could finite size effects and the absence of gluino loops.

For the remaining ensembles (b) and (c) we apply the same analysis. The estimated masses on all ensembles are collected in Table 3.17.

$16^3.32 : \kappa=0.1955 \text{ rep1} : \beta=2.3 \text{ TSMB}$

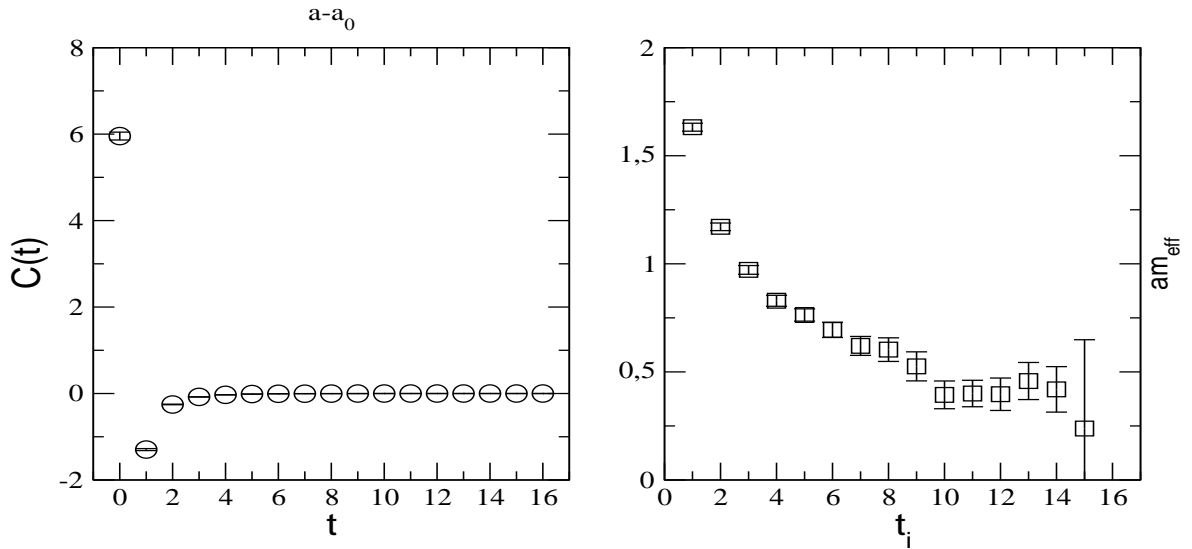


Figure 3.20: Correlators of the  $a$ - $a_0$  (left) and its effective mass as function of  $t_i$  (replica 1) (right), run (a).

Table 3.16: Low-lying mass for the  $a$ - $a_0$  in the interval  $[t_i, 12]$ , run (a).

$[t_i, 12]$	$t_i = 10$	$t_i = 11$
$am$	0.396(53)	0.399(61)

Table 3.17: *Low-lying mass for the  $a$ - $a_0$ .*

Ensemble	$t_1 - t_2$	$a$ - $a_0$ mass
(a)	10-12	0.396(53)
(b)	11-14	0.258(91)
(c)	12-13	0.332(79)

### 3.3.4 The scalar $0^{++}$ $a$ - $f_0$ adjoint meson

Unlike the adjoint pseudo-scalar  $a$ - $\eta'$  which is expected to be heavier than its  $a$ - $\pi$  the scalar  $a$ - $f_0$  is expected to be lighter than its connected part  $a$ - $a_0$  if one consider the analogy with QCD, where the disconnected part of the  $a$ - $f_0$  plays an important role in making its mass light. The signal we obtained for the  $a$ - $f_0$  exhibits an exponential behavior, but the fluctuation of the errors estimation is large and we cannot arrive to a reliable determination of the adjoint scalar mass in our study. Nevertheless, this is used as a guide for us for new implementation of methods in order to compute the hairpin (disconnected) diagrams which require the all-to-all propagators.

The ambiguities in estimating a reliable error is originates from the disconnected correlator and the non-trivial VEV, both estimated by IVST and SET/SEM. A further source of making the extraction of the mass difficult in this case is the presence of an offset coming also from the disconnected contribution. This has been also observed in the analysis of the adjoint pseudo-scalar  $a$ - $\eta'$ . As it has already been mentioned in the analysis of the  $0^{-+}$  channel, the problem of finding an optimal way of subtracting this offset from the correlator is still in the course of study.

The different parts of correlators of the adjoint scalar are shown in Fig. 3.21 for the ensemble (a). In the left panel, the plot scale has been blowed up to allow seeing with more details the behavior of the correlators. If we compare the correlators considering their absolute values we see that the *subtracted* disconnected part dominates the scalar correlator. Following the convention in eq. (3.9) and the negative behavior of the connected part, the scalar correlator becomes negative. The effective plot is also shown in Fig. 3.21, but it allows only to see the plateau for small time-slice separations, and the mass estimated here is presented in Table 3.18 (as a guide) without error estimation.

Table 3.18: *A guide to low-lying mass for the  $a$ - $f_0$  particle.*

$[t_i, 5]$	$t_i = 2$	$t_i = 3$	$t_i = 4$
$am$	0.673	0.642	0.682

Unlike QCD, a first orientation showed that the adjoint scalar is heavier than its connected part corresponding to the particle  $a$ - $a_0$ . It is difficult to have an estimate of this mass on the present ensemble. This is still a challenge in  $SU(2)$  SYM where new ideas and trial methods should be implemented to optimize the study of this quantity; in particular, promising methods for optimizing the two-loop correlator computation have to be used.

A rough estimates of the masses of all ensemble is collected in Table 3.19. We note here, that on the ensemble (a) we have checked possible offset appearing in the correlator. A linear fit was performed to the disconnected part of the correlator after subtracting the vacuum expectation value  $v^2 = \langle \text{Tr} Q^{-1} \rangle^2$ . The resulting offset was subtracted from the original disconnected correlator data. Finally, the single-exponential fit with two parameters is applied to the  $a$ - $f_0$  correlator. On the remaining ensembles (b) and (c), the three parameters single-exponential fit to the correlator data after subtracting  $v^2$  to the disconnected correlator was applied.

$16^3.32 : \kappa=0.1955 \text{ rep1} : \beta=2.3 \text{ TSMB}$

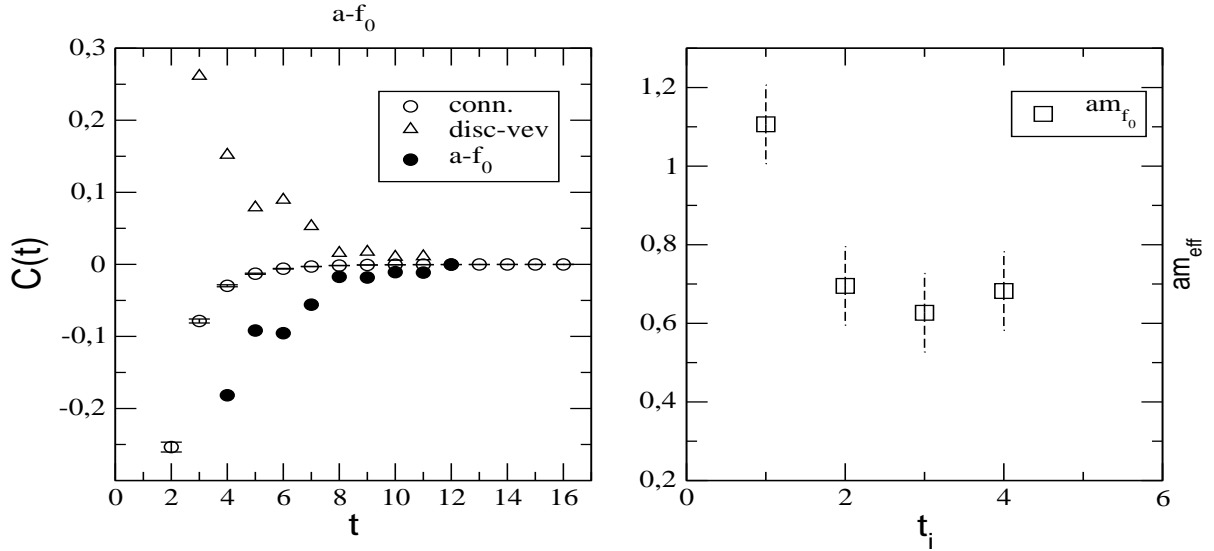


Figure 3.21: Correlators of the  $a$ - $f_0$  (left) and its effective mass as function of  $t_i$  (replica 1) (right), run (a).

### 3.3.5 The $1^{++}$ $a$ - $f_1$ adjoint meson

This particle can be simulated on the lattice using the interpolating local operator  $\bar{\lambda}\gamma_\mu\gamma_5\lambda$ . This state has the quantum number  $J^{PC} = 1^{++}$ , and its analogous in QCD is



Table 3.19: *Low-lying mass for the  $a$ - $f_0$ .*

Ensemble	$t_1 - t_2$	$a$ - $f_0$ mass
(a)	2-5	0.673(-)
(b)	1-4	1.135(95)
(c)	1-3	0.649(46)

the particle  $f_1$ , where for brevity we keep the same nomenclature. The  $a$ - $f_1$  particle does not appear in the Veneziano-Yankielowicz spectrum. However, this is a candidate for supermultiplet with spin-1 content. The first Monte Carlo investigation of this particle has been carried out in [78], where the exploratory study was realized on small lattice. Here, the extraction of the mass is done on large lattices and small gluino mass where the spectrum is expected to be close to the critical region. The computation of the  $a$ - $f_1$  correlator has two parts which are similar to the correlators of  $a$ - $\eta'$  except that  $\gamma_5$  is replaced by  $\gamma_\mu$ ,  $\mu = 1, 2, 3$ . The form of the correlation can be found in Section 3.8.6. The connected as well as disconnected correlators of the  $a$ - $f_1$  are computed with the same gluino propagators  $\Delta$  needed for the  $a$ - $\eta'$  correlator. The disconnected correlator of  $a$ - $f_1$  is computed from  $\text{Tr}_{sc}\{\gamma_\mu \Delta\}$ .

In Fig. 3.22 the  $a$ - $f_1$  full correlator on the ensemble (a) is presented and the its two parts: connected part which corresponds to the particle  $a$ - $a_1$  with QCD notation and the disconnected part. Here, we do not observe the appearance of an offset. Furthermore, the signal of the connected part is relatively better than the one of the disconnected part which was estimated using IVST method like for the spin-0 adjoint mesons on the ensemble (a). The estimated mass can be extracted at small time-slice in the interval  $\Delta t \in [2, 5]$  (see Fig. 3.22.) The single-exponential fit with two parameters yields the results summarized in Table. 3.20 for the interval  $[2, 5]$ .

The disconnected contribution has an important impact which increases the  $a$ - $f_1$  mass. This results in a heavy mass for the  $1^{++}$  state, which is difficult to extract from the correlation function. As in QCD, variational techniques are strongly recommended for the measurement heavy states as in this case. Here, we do not extend the study of the  $a$ - $f_1$  particle using variational method since this is out the scope of the actual work where we concentrate on the low-energy particle spectrum. Moreover, the variational techniques are used in the analysis of the glueballs states.

### 3.3.6 The Glueball $0^{++}$

The mass is extracted from the zero-momentum two-point time-slice correlator of the interpolating operator introduced in Section 2.7.3. The time-slice is given by the sum

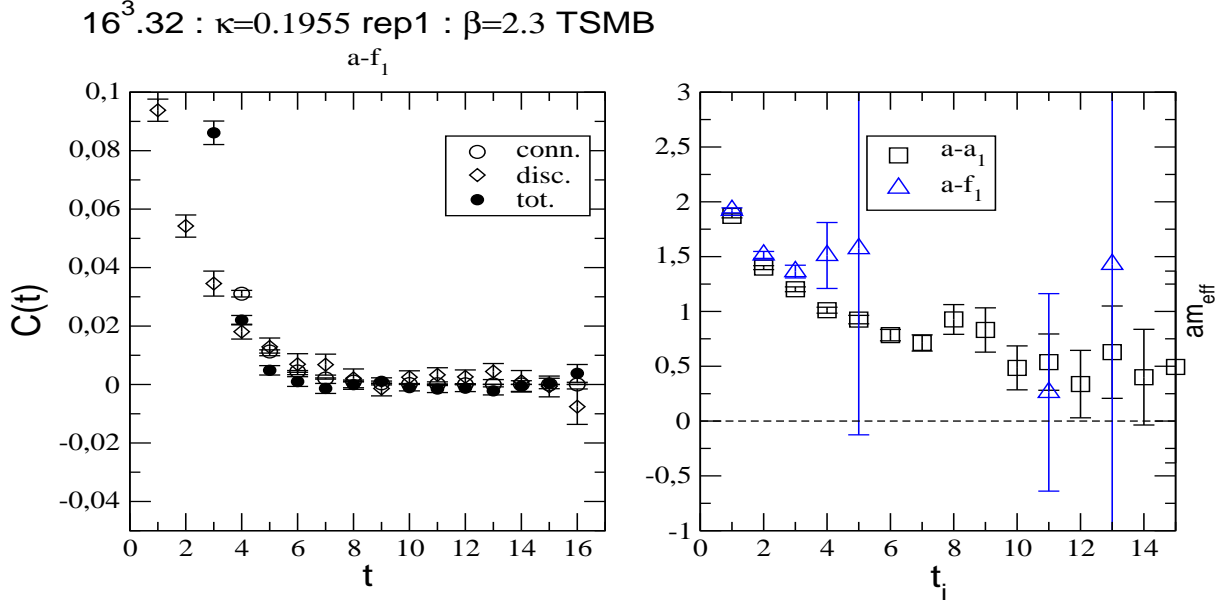


Figure 3.22: Correlators of the  $a-f_1$  (left) and their corresponding effective mass as function of  $t_i$  (replica 1) (right), run (a).

Table 3.20: Low-lying mass for the spin-1  $a-f_1$  particle.

$[t_i, 5]$	$t_i = 2$	$t_i = 3$	$t_i = 4$
$am$	1.465(32)	1.380(55)	1.51(30)

over all the lattice space points as

$$S_{0++}(t) = \frac{1}{\sqrt{V_s}} \sum_{\vec{x}} \mathcal{O}_{0++}(U; \vec{x}, t) . \quad (3.17)$$

To increase the overlap of the lattice operator with the glueball state we used the APE-smearing technique which has two tuning parameters ( $\epsilon, N_{APE}$ ). The analyzed statistics were not sufficiently high. This gives rise to large statistical errors. We used the effective mass as the first orientation to the fit interval and then we performed the one mass single-exponential fit. The single plaquette operator used for the glueballs has non-vanishing vacuum expectation value  $v = \langle \sum_t S_{0++}(t) \rangle$ . The vacuum expectation value is computed and then subtracted from the correlator. The two-parameters fit is

applied then to the resulting (subtracted-vacuum) time-slice correlation function

$$\tilde{S}_{0^{++}}(t) = S_{0^{++}}(t) - \langle S_{0^{++}} \rangle . \quad (3.18)$$

Note that the vacuum expectation value  $\langle S_{0^{++}} \rangle$  is independent of time  $t$ . The estimated masses extracted in the interval  $[1, 2]$  depending on the smearing level are summarized in the Table 3.21. The determination of the glueball masses for the ensembles treated here is a very hard task. The glueball correlator has very large fluctuations. Only an upper bound of the masses could be estimated on the  $16^3 \cdot 32$ . We were not able to extract masses beyond time separation  $\Delta t = 2$ . This outcome has been already observed in [71] where no argument has been found for the increase of the noise when large lattices are considered. It has been conjectured that the purely gluonic states are not affected dramatically by the finite volume of the lattice. This should be verified when more reliable data are available.

However, our general strategy here is to use the APE-smearing as an indicator of the location of the glueball mass. Several APE-smearing iterations are applied in order to remove the contribution of higher states at short time separations. This can be carried out by studying the value of the effective mass at short time separation, say  $[1, 2]$  or  $[2, 3]$ , as function of the smearing radius. The smearing parameters are then tuned and the smearing radius is increased to values to which the estimated mass becomes independent of the the smearing radius. The latter should be not too large in order to have values (in lattice units) which fit into the lattice. The resulting mass, extracted at short time separation, is determined at the beginning of the effective mass plateau. Hence, this value can be quoted as an estimate for the glueball mass.

In the case of pure gauge theory [47], it was observed that the finite size effects are present in the glueball masses. The increase of the masses as function of the volume is only slight in the case of the scalar  $0^{++}$ , leading to the conclusion that the glueball mass of  $0^{++}$  is independent of the volume size. On the other side, the scalar glueball  $2^{++}$  has been observed to have dependence on the volume size and its mass increases with the volume size. Unfortunately, in our case it is not possible to draw a conclusion about the finite size effects since we have only estimates of the mass upper bound for the larger lattices.

### Determination of glueball mass

As discussed in the beginning of this Section, the scalar glueball correlators are very noisy. On the ensemble (a) at  $\kappa = 0.1955$  we have tried to extract an estimate of the mass upper bound after using the effective mass  $m(t_1, t_2, T) = m(1, 2, T)$ . The optimal smearing parameters we found are  $(\epsilon_{APE}, N_{APE}) = (0.045, 22)$ . The plot in Fig. 3.23 shows the stabilization of the mass to a plateau at larger smearing radius  $R_{APE} = 0.99$  in lattice unit. We plotted the mass values as function of APE-smearing levels of step size

equal to 4. The data at higher time separation are considered as noise. The estimated mass on this ensemble is

$$am_{0++} < 0.40(21), \quad (3.19)$$

which is considered as upper bound of the mass and the true estimate is still below this value. We report here the estimated value of the scalar glueball mass found in [71] on  $12^3 \cdot 24$  lattice at the same simulation point ( $\beta = 2.3, \kappa = 0.1955$ ) which is

$$am_{0++} = 0.36(4). \quad (3.20)$$

On the ensemble at  $\kappa = 0.196$  the effective mass  $m(1, 2, T)$  is plotted as function of the APE-smearing levels in Fig. 3.24. A plateau of the mass within error emerges from the APE-smearing step ( $\epsilon_{APE} = 0.51, N_{APE} = 28$ ). After this number of steps the mass decreases slightly but the error estimate increases rapidly. However, we quote at this value of the smearing parameters our estimate of the upper bound of scalar glueball

$$am_{0++} < 0.7(1). \quad (3.21)$$

On the ensemble at  $\kappa = 0.1965$  the situation is also complicated, and we are not able to extract a stable mass estimate since the statistics is too low. Our best estimate of the upper bound has been obtained at the APE-smearing parameters ( $\epsilon_{APE} = 0.5, N_{APE} = 28$ ) and the value is

$$am_{0++} < 0.51(14). \quad (3.22)$$

Table 3.21: *Masses of glueballs on  $16^3 \cdot 32$  lattices (TSMB).*

$\kappa$	$N_{conf}$	$(\epsilon_{APE}, N_{APE})$	Mass $am_{eff}$
0.1955	186	(0.045, 22)	0.40(21)
0.196	192	(0.51, 22)	0.7(1)
0.1965	100	(0.5, 28)	0.51(14)

Unfortunately, our TSMB statistics were not enough high for reliable extractions of the glueball masses. More robust method and high statistics have to be considered in the future in the glueball analysis.

### 3.3.7 The Gluino-glueballs

In Section 2.7.2 we introduced the gluino-glueballs  $\chi(\equiv \tilde{g}g)$ . These are spin- $\frac{1}{2}$  colour singlet bound states of a gluon and a gluino. They are supposed to complete the Wess-Zumino supermultiplet of the adjoint mesons [15] and also the Wess-Zumino supermultiplet of the glueballs [16]. The full correlator is built up from plaquettes connected by

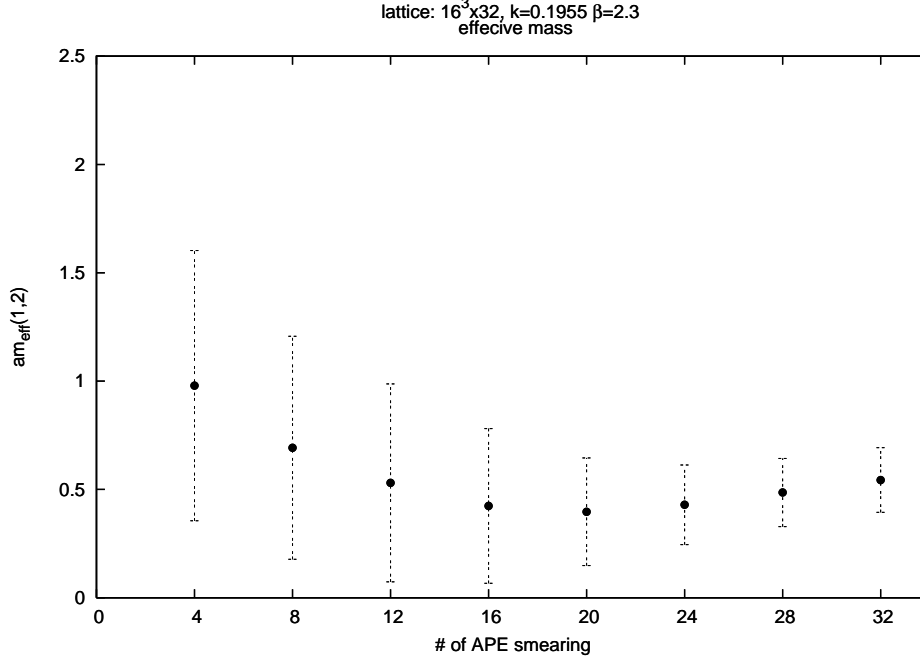


Figure 3.23: Effective masses of the scalar glueball in function of APE-smearing steps,  $\epsilon_{APE} = 0.045$ .

a gluino propagator line as shown in Fig. 2.3 . Recall that in Section 2.7.2 it has been shown that by using various symmetry properties, the  $\chi$  correlator can be split up into two independent real part components in Dirac space:

$$C_{\bar{g}-g}^{\alpha\beta}(\Delta t) = C_{\mathbb{I}}(\Delta t)\delta^{\alpha\beta} + C_{\gamma_4}(\Delta t)\gamma_4^{\alpha\beta} . \quad (3.23)$$

The full correlator is firstly calculated on the gauge configuration, and then the correlator is projected out onto the  $\mathbb{I}$  and  $\gamma_4$  matrices in order to isolate the two independent components. Both components are used for two independent determinations of the lowest mass of  $\chi$ . However, a naive use of these components does not yield an effective mass since the signal-to-noise ratio is poor. Moreover, besides the noise expected at large time separation, the signal is also noisier for short time separation. In order to improve the signal-to-noise ratio and to obtain an earlier plateau in the effective mass, we apply APE smearing for the links  $U_\mu(x)$  and Jacobi smearing for the fermion fields  $\lambda_x$ . We use, for all TSMB ensembles, values of the optimized smearing parameters fixed in the analysis of Ref. [71]. Both source and sink are smeared with the same smearing parameters. The results are obtained by the following smearing parameters

$$(\epsilon_{APE}, N_{APE}) = (0.5, 9) , \quad (3.24)$$

$$(\epsilon_{Jac}, N_{Jac}) = (0.2, 18) . \quad (3.25)$$

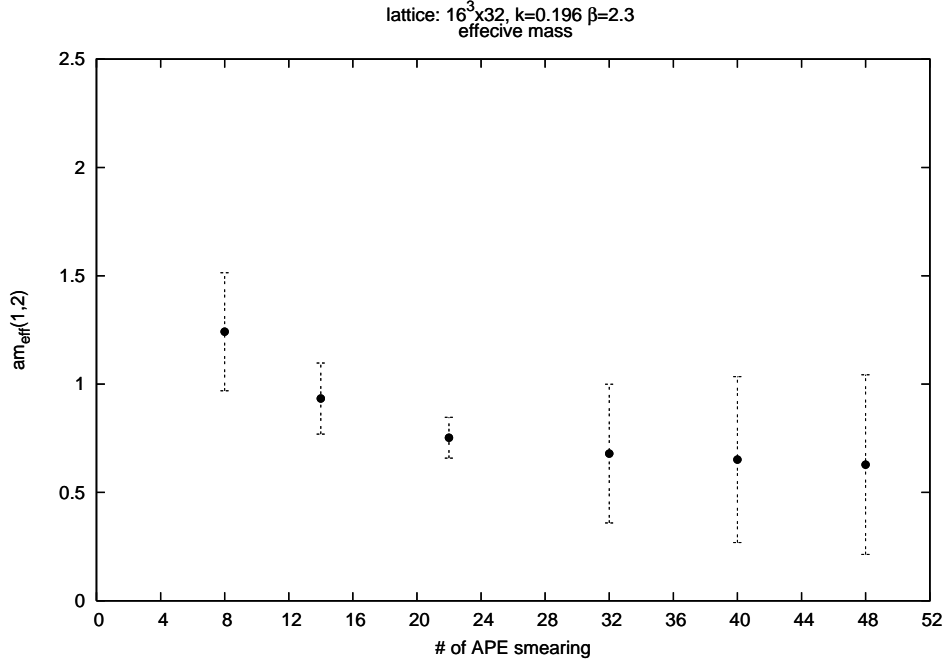


Figure 3.24: Effective masses of the scalar glueball in function of APE-smearing steps,  $\epsilon_{APE} = 0.51$ .

The effective mass extracted from the two components  $C_{\mathbb{1}}$  and  $C_{\gamma_4}$  for all TSMB ensembles are shown in Fig. 3.25 and 3.26 respectively. The results in most cases show a plateau at short time separations from  $\Delta t = 1$  for the  $C_{\mathbb{1}}$  component. The effective mass fluctuate within error up to time separation  $\Delta t = 5$ . From this time separation onwards, effective mass is unstable. For the  $C_{\gamma_4}$  component short plateaus can be seen starting at  $\Delta t = 4$  up to  $\Delta t = 8$  on the ensemble (b) for example. From  $\Delta t = 9$  there is no stabilization of the effective mass. We notice here, however, that we assumed the correlator to decay as single-exponential mode, which could be not true and more than one exponential modes would be considered. This can also be checked by observing the correlators using the logarithmic scale as illustrated in Fig. 3.27. The observed non-linear behavior starting at almost from  $\Delta t = 8$  of the correlators suggests the presence of heavier modes in the  $\chi$  correlator and the signal becomes noisier.

Of interest here is also the consequence of the application of the smearing on both components of the  $\chi$  correlator. The correlator in Fig. 3.27  $C_{\mathbb{1}}$  have somewhat better linear behavior at short time separations than the  $C_{\gamma_4}$  correlator. Since the signal obtained from the antisymmetric correlator  $C_{\mathbb{1}}$  is cleaner than of the symmetric correlator  $C_{\gamma_4}$ , we have used the former correlator in order to extract the best estimate for the mass of  $\chi$  bound state.

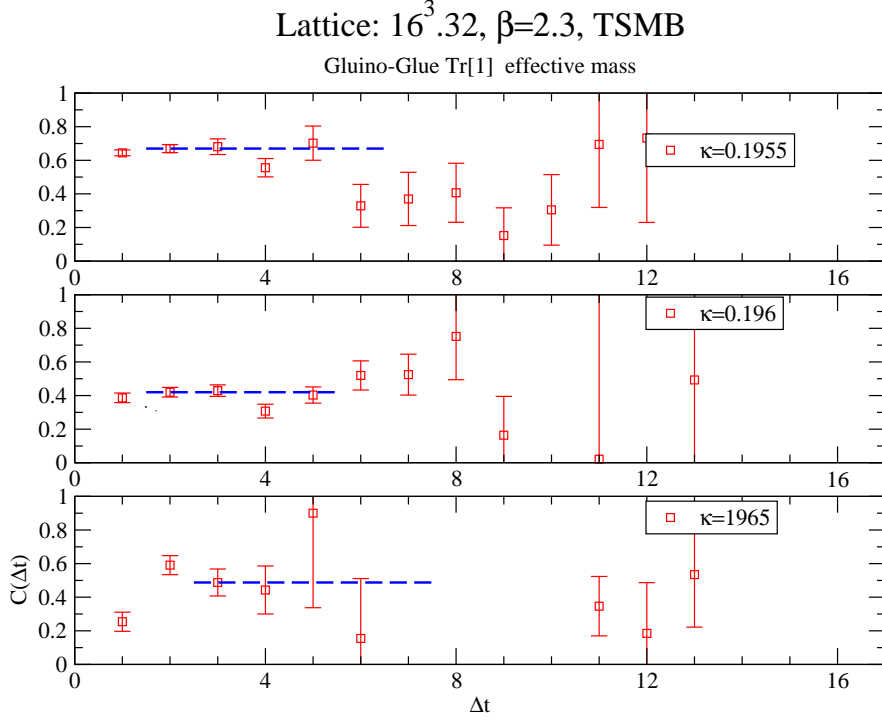


Figure 3.25: *Effective mass of the  $C_{\parallel}$  correlator for all TSMB ensembles. APE and Jacobi smearing are used.*

#### Ensemble (a)

For the ensemble (a) we analyzed 368 configurations with respect to  $\chi$ . For the  $C_{\parallel}$  component the effective mass displays a plateau starting from the first time separation up to  $\Delta t = 5$ . However, a drop of the mass occurs from  $\Delta t = 5$  to  $\Delta t = 12$ . This can indicate the presence of two states: lowest and next-to-lowest states. But assuming the smearing was enough to wash out the heavier states and that the wave function overlaps only with the lowest state, we can discard the signal of the lower plateau. Furthermore, the  $C_{\parallel}$  correlator begins to have large statistical fluctuations at larger time-separations which suggests that the latter plateau is a statistical effects and the effective mass in this region is not taken into account. To extract an estimate of the lowest  $\chi$  mass we perform a single-exponential fit in the interval  $2 \leq t \leq 4$  where the data leads to the convergence of the fit routine, and we obtain the value

$$am = 0.673(20) . \quad (3.26)$$

The effective mass from the  $C_{\gamma_4}$  component indicates presence of the higher states from the first time-slice  $\Delta t = 1$ . We notice here the effect of the smearing which does not necessary wash out the signal from higher states contribution as it was assumed in

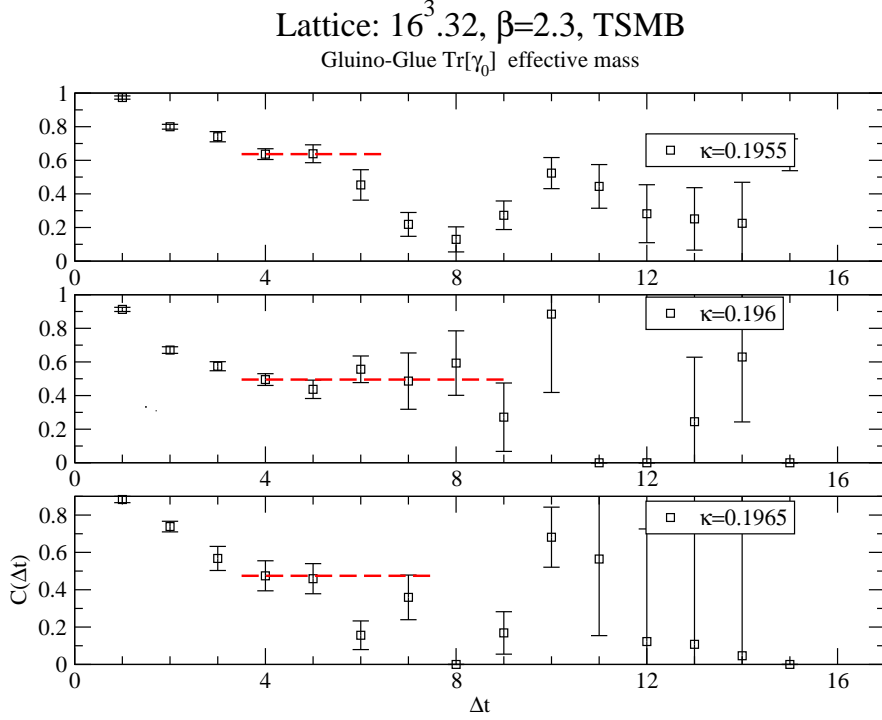


Figure 3.26: *Effective mass of the  $C_{\gamma_4}$  correlator for all TSMB ensembles. APE and Jacobi smearing are used.*

the  $C_{\parallel}$  channel. From time separation  $\Delta t = 4$  the effective mass begins to stabilize, but only up to the next time separation  $\Delta t = 5$ . Then, the value drops to lower effective mass starting at  $\Delta t = 6$  which is considered as statistical effects as in the above case. The fitted value of the mass in the interval  $[3, 5]$  yields

$$am = 0.700(21) , \quad (3.27)$$

which is consistent with the value obtained in the  $C_{\parallel}$  channel.

### Ensemble (b)

Now we consider the ensemble (b) which corresponds to lighter gluino. We computed the  $\chi$  correlator on a sample of 192 configurations on this ensemble. The effective mass of the  $C_{\parallel}$  component produces a plateau in the range  $[1, 5]$ , then the signal is corrupted by noise for the next three time-separations. After that, the signal becomes completely noisy. This might be due to the high noise in the  $C_{\parallel}$  correlator characterized by large statistical error. Nevertheless, as in the above, we assume that at short time-separations the mass of the lowest state can be extracted since the smearing was sufficient to increase



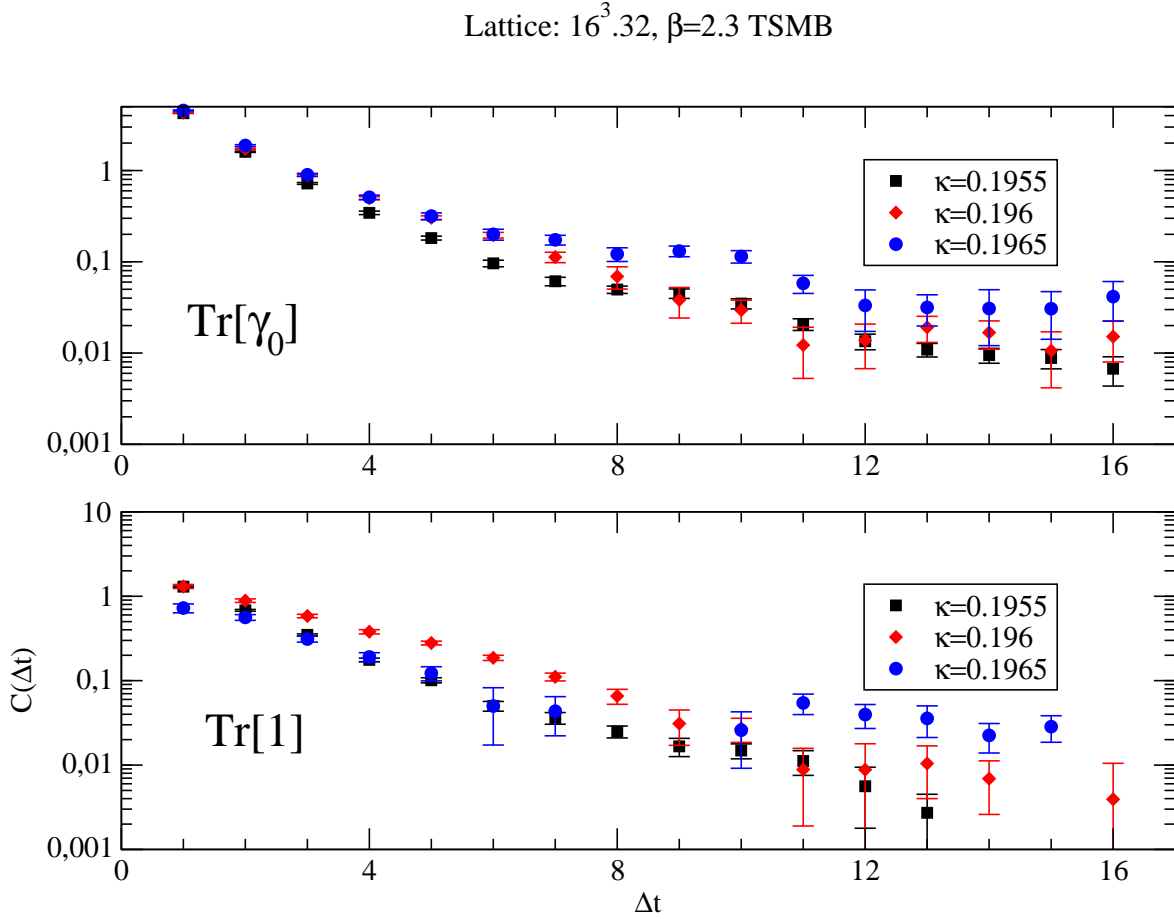


Figure 3.27: *Time-slice correlation function from  $C_{\mathbb{1}}$  and  $C_{\gamma_4}$  for all TSMB ensembles.*

the overlap with lowest state. The fit in the interval  $[2, 4]$  yields

$$am = 0.424(22) . \quad (3.28)$$

The correlator  $C_{\gamma_4}$  on the ensemble (b) displays of a plateau in the effective mass in the range  $[4, 10]$  with an exception of a drop at time-slice  $t_i = 9$ . This suggests the existence of a ground state mass. The plateau and the drop of the effective mass can be seen in the more or less linear behavior of the  $C_{\gamma_4}$  correlator in the above range. The estimation of the mass in the interval  $[4, 6]$  yields

$$am = 0.472(31) , \quad (3.29)$$

which seems to be in line with the previous determination from  $C_{\mathbb{1}}$ .

### Ensemble (c)

On the last ensemble at lighter gluino mass  $\kappa = 0.1960$ , the available configurations for analysis were 100 which might be too low statistics for a good signal for the  $\chi$  state. The effective mass from the  $C_{\mathbb{I}}$  shows the missing of several data points. We observe strong fluctuations in the effective mass which renders difficult the localization of the fit interval. The same conclusion can be drawn for the data of its corresponding correlator. Keeping in mind the low statistic on this ensemble we quote as a mass estimate the value

$$am = 0.469(85) . \quad (3.30)$$

Turning now to the  $C_{\gamma_4}$  channel, the effective mass shows a fall-off up to time-slice  $t_i = 4$  and then stabilizes up to time  $t_i = 7$  with the exception of a drop at time  $t_i = 6$ . The next points correspond to noise and the effective mass is no longer helpful. In the correlator we see also the fluctuation of the data points starting from time separation  $\Delta t = 9$ . This might be, besides the low statistic, the effect of the reweighting which has not been applied on this ensemble. We suspect that some configurations may be exceptional, and the correction factor would be necessary for the reweighting procedure. Nevertheless, the single-exponential fit in the range  $[3, 5]$  yields the value

$$am = 0.472(75) , \quad (3.31)$$

which is also in agreement with the value extracted in the  $C_{\mathbb{I}}$  channel.

### Conclusion

Table 3.22: *Masses of the gluino-gluonball  $\chi$  on the TSMB ensembles.*

Ensemble	$am_{\mathbb{I}} [t_1, t_2]$	$am_{\gamma_4} [t_1, t_2]$
(a)	0.673(20) [2,4]	0.700(21) [3,5]
(b)	0.424(22) [2,4]	0.472(31) [4,6]
(c)	0.469(85) [4,6]	0.472(75) [3,5]

In the conclusion of this Section of the  $\chi$  analysis we notice that the data from the two component  $C_{\mathbb{I}}$  and  $C_{\gamma_4}$  allow at most extracting compatible mass estimates. Our guide was only the effective mass which has a local character, and uses adjacent time-slices to extract a local mass estimate. This may ignore the lowest mass for some time-slices. The mass fit or commonly called the global fit is considered to be more efficient since it takes into account the lowest state by using large data on time-slices. In our case the global fit was performed on chosen intervals guided from the local effective mass stabilization

instead of larger intervals. In our analysis, the statistics was relatively low and the signal becomes noisier at large time-separations, so we do not anticipate to consider those data at larger time separations which could yield wrong results. However, we would use large fit interval for better data.

The component  $C_{\mathbb{I}}$  is advantageous in the sense that it is more reactive to the smearing procedure by displaying a plateau of in the effective mass at early time-slices. This was also our argument for considering the mass estimations in this channel in the final determinations. In the previous works of the DESY-Münster on small lattice the symmetric component  $C_{\gamma_4}$  was largely explored than the anti-symmetric correlator  $C_{\mathbb{I}}$  since the data of the former were better than those of the latter. A firm conclusion about the best choice could not however be drawn. This was a motivation for going to larger lattices at least for the gluino-gluon. The two components describe the same low-lying state and should yield compatible results as in the case of the present analysis. We notice here, that in a quenched investigation of the SYM theory of Ref. [30] the  $C_{\mathbb{I}}$  was used to extract the  $\chi$  mass. Finally, going to larger lattices as will be discussed in the next chapter could help to draw firmer conclusions on the  $\chi$  analysis. At the end of this section, we collect the analysis and summarize our results of the  $\chi$  mass on the TSMB ensembles in Table 3.22.

## 3.4 Lattice SUSY Ward-Identities

We turn now to the use of lattice SUSY Ward-Identities for the numerical determination of the ratio of renormalization constants  $Z_T Z_S^{-1}$  and the subtracted gluino mass  $am_s Z_S^{-1}$ . The methods of the determination of the ratio of renormalization constants  $Z_T Z_S^{-1}$  and the subtracted gluino mass  $am_s Z_S^{-1}$  are discussed in Section 2.9 .

On the TSMB ensembles, we take as starting point the results of the DESY-Münster collaboration summarized in [21]. We performed analysis of the WI's involving the local super-current  $S_\mu^{(loc)}$  and the insertion operator is the same one used for the gluino-gluon called now  $\chi^{(sp)}$ ,  $sp$  stands for spatial. The latter interpolating field at the source involved in the correlator pertaining the WI's is smeared. Since the gluino-gluon projecting operator is the insertion operator, both APE and Jacobi smearing are applied with the same set of smearing parameters used in Section 3.3.7. With the choice of the local super-current, The lattice SUSY WI's eq. (2.100) hold only up to  $\mathcal{O}(a)$  discretization effects. The operators in the sinks are not smeared. Moreover, the source site  $y_s$  of the insertion is chosen randomly on each configuration as in the case of the gluino-gluon correlator. This insures the de-correlation of the propagators necessary for the computation of the correlators. The statistical error, however, is determined using both Jackknife with binning and  $\Gamma$ -method. Our analysis indicates that the error estimations using the two methods are similar.

The results of the determinations of  $am_s Z_S^{-1}$  and  $Z_T Z_S^{-1}$  are reported in Fig. 3.28 and Fig. 3.29 respectively as function of the time-separation  $\Delta t$ . For each time separation the system of two equations is solved. We assumed that starting from  $t \geq 3$  the signal is not contaminated by contact terms. The values of the ratios illustrated in Fig. 3.28 confirm the influence of the contact terms at small time-separations. The measured quantities are expected to be independent of time-separation, and to stabilize in a plateau as in the effective mass. Moreover, the signal is rapidly washed out for large time separation as shown in Fig. 3.28. The starting time of the plateau is taken in most cases from  $t \geq 3$ . From this time to onwards a linear fit procedure is applied which involves several data points in the fit instead of resolving the system of equations for each time-separation. The linear fit has the advantageous effect of involving the maximal number of correlator for the overdetermination of the system of equations. We perform the linear fit in intervals  $[t_i, T/2 - 1]$  where  $t_i \geq 3$ . The results of the global linear fit of the ratio of renormalization constants and the subtracted gluino mass are listed in Table 3.23 and 3.24 respectively.

The plateau-like behavior is observed on all ensembles for the ratios. On the ensemble (a) this can be observed between  $t = 3$  and  $t = 5$  for  $am_s/Z_S$  and between  $t = 3$  and  $t = 6$  for  $Z_T/Z_S$ . For larger time-separations the signal starts to fluctuate and the statistical error grows. We expected that the signal will become noisy as the lighter gluino mass is simulated. A first source of the noise is the presence of small eigen-mode of the fermion matrix in the sample giving rise to wrong statistical measurements of observables on the sample which have to be corrected. The second source is the long autocorrelation-times which results in low statistics for the reliable determination of the ratios appearing in the WI's.

On the ensemble (b) the value of the subtracted gluino mass and the ratio of renormalization constants stabilizes within statistical error in the interval  $[3, 5]$ . The signal here was less good than the previous ensemble. It is washed out for the  $Z_T/Z_S$  from  $t = 6$ . The optimization of smearing parameters could yield a better signal. However, we still use the same parameters tuned in previous investigations of the DESY-Münster collaboration which were considered to be optimal for the ensembles produced with TSMB algorithm at  $\beta = 2.3$ . The most probable source of the statistical fluctuations is the low statistics and the possible presence of exceptional configurations in the sample.

On the last ensemble present in this study at lightest gluino mass, the run history in Section 3.1 reflects the difficulty expected in the analysis of this ensemble with respect to quantities sensitive to the reweighting of the statistical measurements. Due to limitation of computing time available at the beginning of this study, we do not explore the correction factors and the Pfaffian signs on this ensemble. We have tried to select a sample where the presence of the exceptional configuration is less probable. Our strategy in this selection was to discard configurations with smallest eigenvalue lying below the lower bound of the approximation interval. However, we were not sure about the

presence of configurations with negative sign of Pfaffian which can occur even for configurations respecting the polynomial approximation interval. Our best estimates of the constant ratios appearing in the WI's on this ensemble are listed together with the best estimates for the previous ensemble in Tables 3.23 and 3.24. We notice at the end of this section that we have used only one insertion operator  $\chi^{(sp)}$ , and we have not explored the different discretization effects resulting in using different kind of insertion operators.

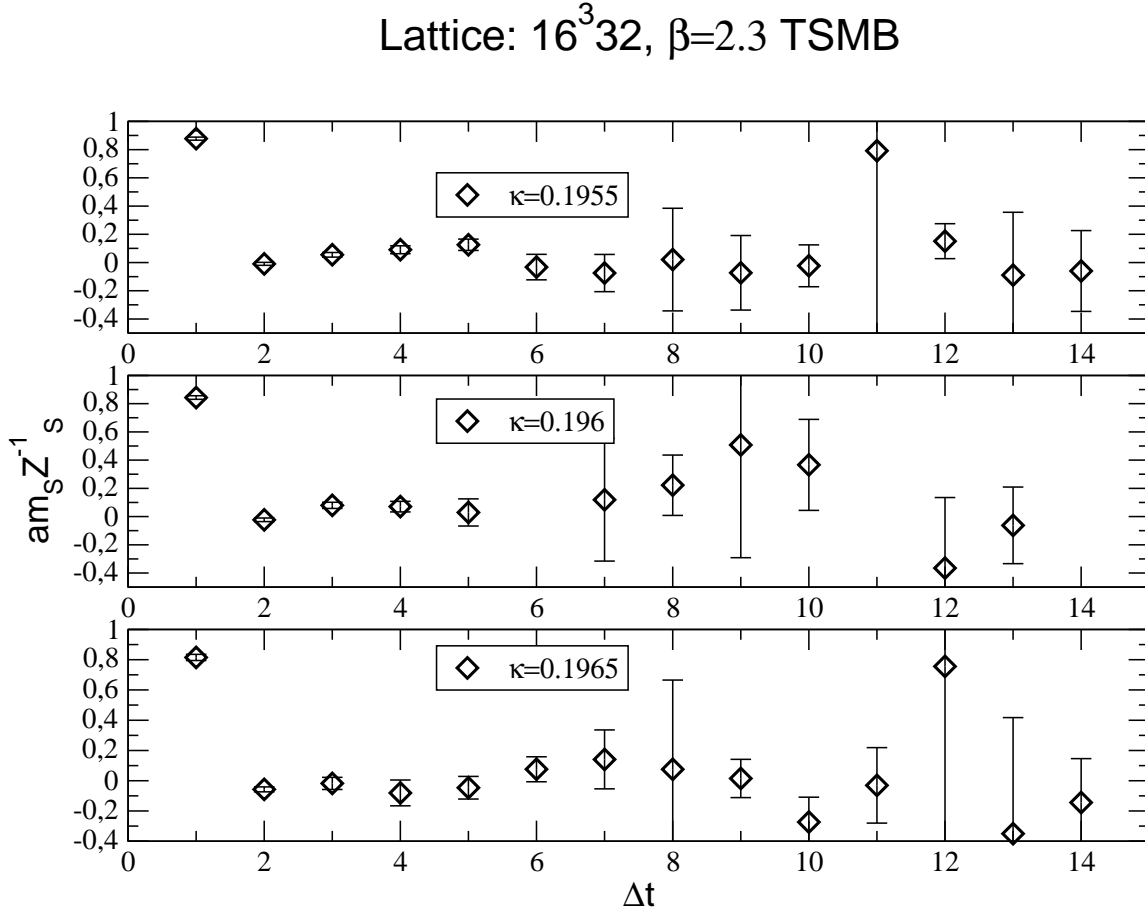


Figure 3.28:  $am_s Z_s^{-1}$  as function of  $\Delta t$  for local current  $S_\mu^{loc}$  and insertion operator  $\chi^{(sp)}$ , for all TSMB ensembles.

### 3.5 The massless gluino limit

The gluino mass introduced in the lattice formulation breaks supersymmetry softly. The bare gluino mass  $m_{\tilde{g}}$  (bare hopping parameter  $\kappa$ ) in the lattice action has to be fine-tuned appropriately to its critical value, where the gluino mass vanishes, in order to restore SUSY and chiral symmetry. As discussed in the previous chapter, there exists

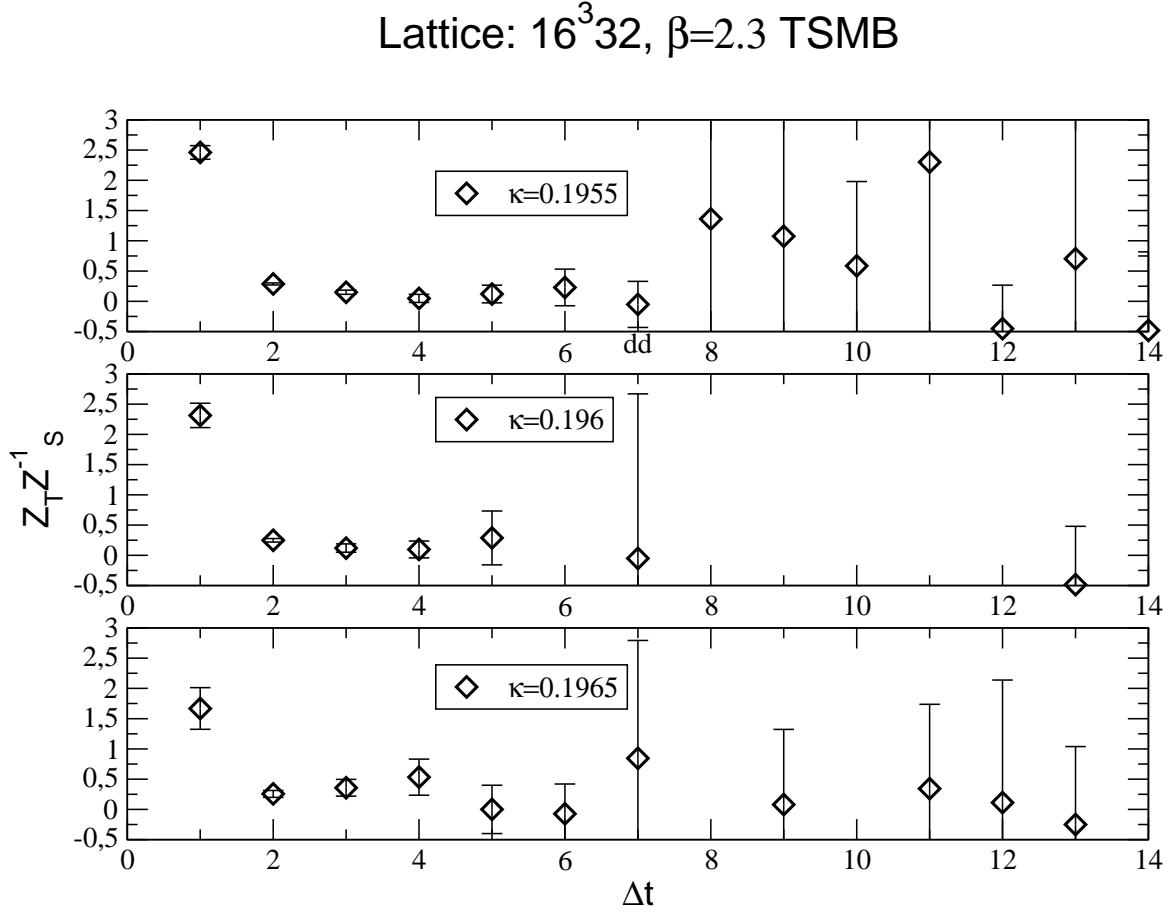


Figure 3.29:  $Z_T Z_S^{-1}$  as function of  $\Delta t$  for local current  $S_\mu^{loc}$  and insertion operator  $\chi^{(sp)}$ , for all TSMB ensembles.

two independent methods allowing an estimation of the critical hopping parameter  $\kappa_{cr}$ . One method is based on the OZI arguments in analogy to QCD, while the second allows estimating the region of vanishing gluino mass by checking the validity of lattice WI's.

In the following we point out our results of the critical hopping parameter by using the OZI arguments and by means of lattice SUSY WI's.

### 3.5.1 OZI arguments

The critical hopping parameter can be estimated using OZI arguments discussed in [30] where the adjoint pion mass is expected to vanish at vanishing renormalized gluino mass. Near the critical region, the square adjoint pion mass is assumed to behave linearly with the gluino mass  $m_\pi^2 \propto m_{\tilde{g}}$ . This arguments can be used to extrapolate the inverse hopping parameter  $1/\kappa$  to the massless gluino limit, where both SUSY and chiral symmetry are expected to emerge. The strategy is then to use the plot of the squared

Table 3.23:  $Z_T Z_S^{-1}$  as function of  $t_{min}$  from the linear fit. TSMB ensembles.

$\kappa$	$t_{min} = 2$	$t_{min} = 3$	$t_{min} = 4$
0.1955	0.268(14)	0.135(29)	0.051(57)
0.196	0.233(26)	0.112(60)	0.06(12)
0.1965	0.262(52)	0.33(11)	0.19(10)

Table 3.24:  $am_S Z_S^{-1}$  as function of  $t_{min}$  from the linear fit. TSMB ensembles.

$\kappa$	$t_{min} = 3$	$t_{min} = 4$	$t_{min} = 5$	$t_{min} = 6$
0.1955	0.061(12)	0.091(20)	0.092(30)	
0.196	0.079(15)	0.083(24)	0.123(30)	
0.1965			0.013(20)	0.035(27)

$a$ - $\pi$  mass as function of the inverse hopping parameter to find which data exhibit the most linear behavior taking the last point of the simulation as reference. The linear extrapolation of  $am_\pi^2 \rightarrow 0$  is then performed on the selected data point to find an estimate of the critical hopping parameter  $\kappa_{cr}$ .

In Fig. 3.30 (right panel) the squared  $a$ - $\pi$  mass is plotted as a function of the bare gluino mass for the three TSMB ensembles studied here on  $16^3 \cdot 32$  lattices at increasing hopping parameters. We also use one data of the analysis in Ref. [18] at  $\kappa = 0.194$ . For the ensemble (a) we considered the estimation of the replica 1. The data on Fig. 3.30, in the right panel, shows the expected linear behavior, and hence we consider all of them as input in the fit extrapolation. The line represents the linear extrapolation to the  $(m_{a-\pi})^2 = 0$  which yields as estimation of the critical hopping parameter with the value

$$\kappa_{cr} \simeq 0.19698(3) . \quad (3.32)$$

This value is in good agreement with the estimation of  $\kappa_{cr}$  extracted from WI's in the study of Ref. [18]. In that study qualitative agreement with a vanishing adjoint pion mass was observed. The analysis of the WI's on our ensembles will confirm this observation in the following.

### 3.5.2 Ward-Identities

One of the interesting outcome of studying the lattice WI's is the determination of the critical bare gluino mass. In Fig. 3.30, in the left panel, we report the dependence of the values of the subtracted gluino mass  $am_S/Z_S$  on the inverse hopping parameter  $\kappa$ .

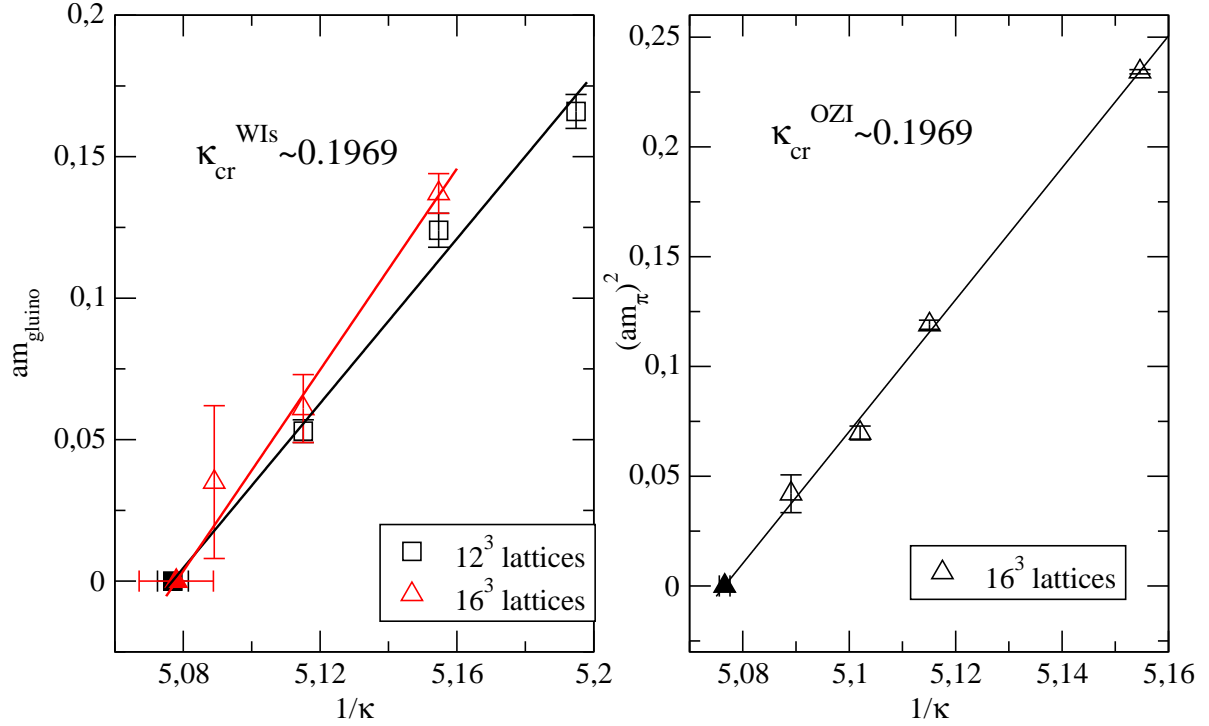


Figure 3.30: The gluino mass (left) and the pion mass square (right) as function of the inverse hopping parameter (TSMB runs). The data of  $12^3 \cdot 24$  are from Ref. [18]

In the region where  $\kappa$  approaches its critical value the one expects the linear behavior of the gluino mass as function of the inverse hopping parameters and  $am_S/Z_S$  vanishes linearly at  $\kappa_{\text{cr}}$ . This expectation is used to extrapolate to the critical hopping parameter  $\kappa_{\text{cr}}$  as shown by the solid line in Fig. 3.30 (left panel). We observe a clear decrease of the subtracted gluino mass as critical hopping parameter is approached. From the linear extrapolation we obtained

$$\kappa_{\text{cr}}^{\text{WI}} = 0.19697(17) . \quad (3.33)$$

Here, we supplement our data with the value of  $am_S/Z_S$  in Ref. [18] at  $\kappa = 0.194$  on  $16^3 \cdot 32$  lattice. We also excluded the data of the ensemble (b) where a reliable estimate of the subtracted gluino mass was difficult as discussed in Section 3.4. Comparing with the estimation from OZI arguments we observe the good agreement of both estimations. Furthermore, these estimation confirms the value of the hopping parameter found in the



work of Ref. [18] obtained from WI's. We also plotted in Fig. 3.30 the extrapolation to critical hopping parameter using the previous data of the DESY-Münster collaboration on  $12^3 \cdot 24$  lattices.

Since we observed the linear behavior of the subtracted gluino mass as function of  $1/\kappa$ , one can assume that the formula for the gluino mass

$$am_{\tilde{g}} \sim \frac{1}{2} \left( \frac{1}{\kappa} - \frac{1}{\kappa_{\text{cr}}} \right) \quad (3.34)$$

holds at leading order in  $1/\kappa$ . Hence, at lightest gluino  $\kappa = 0.1965$  simulated in this work the value of the gluino mass in lattice unit is  $am_{\tilde{g}} \sim 0.035$ . Turning this value to physical units where the inverse lattice spacing is  $a^{-1} \sim 3152$  MeV we find  $m_{\tilde{g}} \sim 115$  MeV. This small value of the gluino mass signals that the last simulation point is approaching the chiral limit. This is also suggested by the linear behavior as function of the inverse hopping parameter of the subtracted gluino mass and the square adjoint pion mass observed in Fig. 3.30.

## 3.6 Masses from ratios of correlators

Before concluding this chapter, we would return to the analysis of the TSMB ensembles with respect to the adjoint mesons. In Section 3.3.2 we performed a direct fit to the pseudo-scalar correlator  $C^{\eta'}(t)$  to extract an estimate of the mass of the ground state. It is also desirable to consider the ratio of correlators  $R(t) = C^{\eta'}(t)/C^{\pi}(t)$  of  $a\text{-}\eta'$  to the  $a\text{-}\pi$  correlator which helps to cancel the effect of excited state contributions [79, 80]. In the same way we apply also this method to the scalar adjoint meson  $a\text{-}f_0$ .

In this Section we then present the application of the method of the correlator ratio to study the adjoint mesons on the ensemble (a). This was an exploration study which can be extended in the future for better analysis of the particle spectrum. We consider here the existing data of the connected correlators and the disconnected correlators computed on the ensemble (a). The only difference is in the treatment of the data in the fitting procedures.

Previous pioneering work in QCD largely focussed on the two-step recipe to deal with the problem of determining the mass of the pseudo-scalar meson. Instead of fitting the total correlator directly as in the above Sections, the ratio of correlators (connected, disconnected and total) has to be used. The two-steps are: i) determine the  $a\text{-}\pi$  mass and ii) compute the mass gap  $\Delta m = m_{\eta'} - m_{\pi}$ , from the ratio of correlators,  $R(t)$  (see [79, 80]). The  $a\text{-}\eta'$  meson mass is then obtained by adding to  $\Delta m$  the adjoint pion mass  $m_{\pi}$ .

We will consider here two type of ratios of correlators defined as follows

$$R(t) = \frac{C_{tot}(t)}{C_{1-loop}(t)} , \quad (3.35)$$

$$R'(t) = \frac{C_{2-loop}(t)}{C_{1-loop}(t)} , \quad (3.36)$$

where  $1-loop$  and  $2-loop$  refer to the connected and disconnected parts of the total correlator respectively. Thus, the total correlator is given by

$$C_{tot}(t) = C_{1-loop}(t) - \frac{1}{2}C_{2-loop}(t) . \quad (3.37)$$

Alternatively, one may fit the ratio in  $R(t)$  eq. (3.35) to the exponential function

$$R(t) = Ae^{-\Delta mt} , \quad (3.38)$$

which is true for large times, and where  $\Delta m$  is the mass gap between  $a\text{-}\eta'$  and  $a\text{-}\pi$ .

This allows now to define the fit function of the second ratio  $R'(t)$  in eq. (3.36). One may write

$$\begin{aligned} C_{tot}(t) &= C_{1-loop}(t) - \frac{1}{2}C_{2-loop}(t) , \\ C_{2-loop}(t) &= 2(C_{1-loop}(t) - C_{tot}(t)) , \\ \frac{C_{2-loop}(t)}{C_{1-loop}(t)} &= 2\left(1 - \frac{C_{tot}(t)}{C_{1-loop}(t)}\right) , \\ R'(t) &= 2(1 - Ae^{-\Delta mt}) \text{ for } t \rightarrow \infty . \end{aligned} \quad (3.39)$$

$\Delta m$  is also the mass gap difference of the  $a\text{-}\eta'$  and the  $a\text{-}\pi$ , given by

$$\Delta m = m_{\eta'} - m_{\pi} . \quad (3.40)$$

Since the data for all correlators are available, one can in principle use different ratios of correlator given in eq. (3.35) and eq. (3.36) to extract the mass gap  $\Delta m$ . The estimations from both definitions are expected to be compatible.

### 3.6.1 The $a\text{-}\eta'$ adjoint meson from ratio of correlators

The masses of  $a\text{-}\eta'$  obtained in Section 3.3.2 have been determined using a direct fit to the total correlator. Now we apply the method of correlator ratio to extract an estimate of the mass. This method allows also the study of the structure of  $a\text{-}\eta'$  correlators which is expected to have similar behavior to  $\eta'$  in QCD. Moreover, the relative contributions of connected and disconnected parts of the total correlator can be compared. In Figs. 3.31, 3.32 and 3.33 comparison between different correlators are presented. In the two panels

Table 3.25: *Summary of  $a$ - $\eta'$  mass from global fit using different subtraction procedures on the ensemble (a).*

$am$	fit-interval	number of fit-parameters	subtracting method
0.26(2)	9 - 13	2	-
0.48(1)	5 - 10	3	-
0.47(1)	5 - 9	2	sub. total correlator (after linear-fit)
0.346(39)	10 - 11	2	sub. disconnected

of Fig. 3.31 the behavior of the disconnected versus disconnected correlators and the total correlator versus the connected correlator are shown. We have seen in Section 3.3.2 that this behavior yields a mass of the adjoint pion (connected contribution) greater than the mass of the adjoint pseudo-scalar  $a$ - $\eta'$ . We attributed this effect to the presence of an offset in the disconnected correlator which was interpreted as statistical effect.

In the panels of Fig. 3.32 the total correlator and the total correlator after subtracting its offset are compared (left panel). In the right panel we observe the behavior of the subtracted total correlator compared to its connected part (the pion correlator). Here, the subtracted total correlator is completely generated by a mass heavier than the mass generating the connected correlator. Finally, in the two panels of Fig. 3.33 the subtracted disconnected correlator is compared to the connected correlator in the left panel. In the right panel the total correlator resulting from its connected part and the subtracted disconnected part is compared to the non-subtracted total correlator. The subtraction procedure applied to the disconnected correlator shows no substantial decrease of the total correlator since we observe that the data point of the latter are almost equal those of the subtracted total correlator for large time-separations for  $t = 9$  onwards.

The subtraction procedure applied to the total correlator results in heavier mass (Fig. 3.31 right panel). The effect is different in the case where the offset is subtracted from the disconnected correlator only. This results in a mass equivalent to the adjoint pion mass (Fig. 3.33 right panel). We conclude that the correct way is to subtract the offset from the (physical) total correlator instead of the disconnected part only. The previously obtained results of pseudo-scalar mass are summarized in Table 3.25. Although subtracted disconnected correlator increases the mass of the adjoint pseudo-scalar, but it still in the same order of the pion mass.

Turning now to the ratios of correlators we expect the ratio involving the subtracted total correlator to give compatible results of the direct method. The results of the mass gap and the pseudo-scalar mass estimation using this method for different correlators are summarized in Table 3.26. We proceed in the following to discuss these estimations.

In Fig. 3.34 the ratio  $R(t)$  defined in eq. (3.35) is plotted as function of the time-

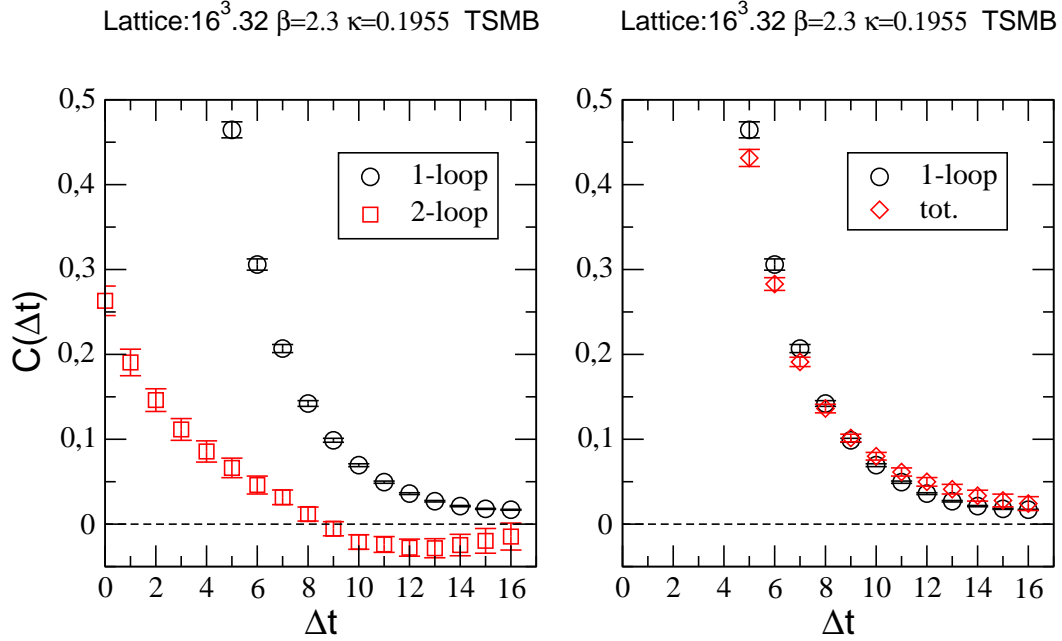


Figure 3.31: *1-loop and 2-loop contribution to  $a$ - $\eta'$  correlator (left panel). Total correlator compared to its connected part (right panel). Ensemble (a).*

separation (left panel). Although the statistical error grows with the time-separation, the contribution of excited states is substantially suppressed at short time-separation. The effective mass gap is shown in the right panel where it has a plateau-like behavior in the range  $[1, 4]$ . This enables us to perform the single-exponential fit defined in eq. (3.38) to extract an estimate of the mass gap of the value

$$\Delta m = 0.0148(34) . \quad (3.41)$$

This results in an adjoint pseudo-scalar mass of the pion mass order. However, if the subtracted total correlator is considered instead, one expects a heavier mass. In Fig. 3.35 the ratio  $R(t)$  and the corresponding effective mass gap is presented. Here, we observe quite different behavior of the ratio  $R(t)$  and the mass gap comparing to the previous case. The subtraction of the offset from the total correlator has the benefit of reducing the statistical error in the  $R(t)$  correlator, and an estimate of the mass gap could be extracted by fitting from  $t = 6$  onwards. In Fig. 3.36 the ratio  $R'(t)$  and the corresponding mass gap are presented in Table 3.26. Here, in the ratio  $R'$  the disconnected correlator is plugged in the definition in eq. (3.36) but after subtracting the constant

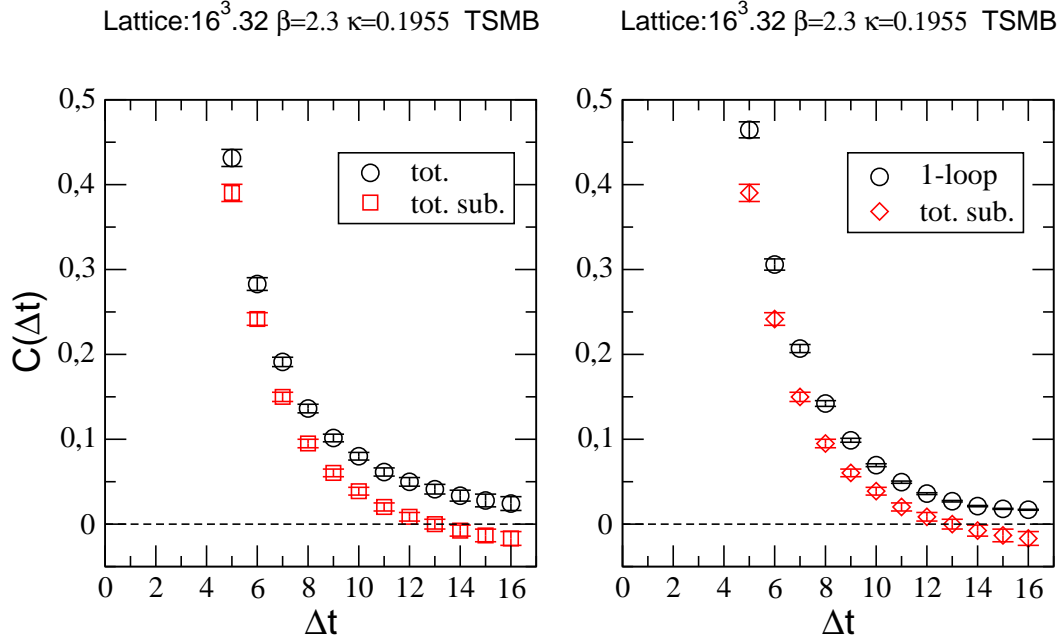


Figure 3.32: *Total correlator after subtraction of the offset compared to the original total correlator (left panel). Total correlator (after subtraction) compared to its connected part (right panel). Ensemble (a).*

term from the disconnected correlator. The effective mass gap in this case is unstable, and if one performs the global fit with respect to the fit function in eq. (3.40), say in the interval  $[5, 6]$ , we obtain a bigger mass gap and the resulting adjoint pseudo-scalar mass is slightly heavier than the previous estimation.

From the obtained values of the mass gap and hence the estimated mass of  $m_{\eta'}$  particle which are summarized in Table 3.26, we conclude that the second estimation gives compatible results. The slight decrease of the mass estimation obtained compared to the direct method is interpreted as the suppress of the excited state contributions.

### 3.6.2 The $a$ - $f_0$ adjoint meson from ratio of correlators

We followed in the same procedure as we have done for the pseudo-scalar case. We have tried to determine the mass gap  $\Delta m$  between the  $a$ - $f_0$  and its connected part the  $a$ - $a_0$ . One has to study here the behaviour of the ratio of the scalar correlator and the connected correlator. Unlike the pseudo-scalar, the scalar correlator contains the non-

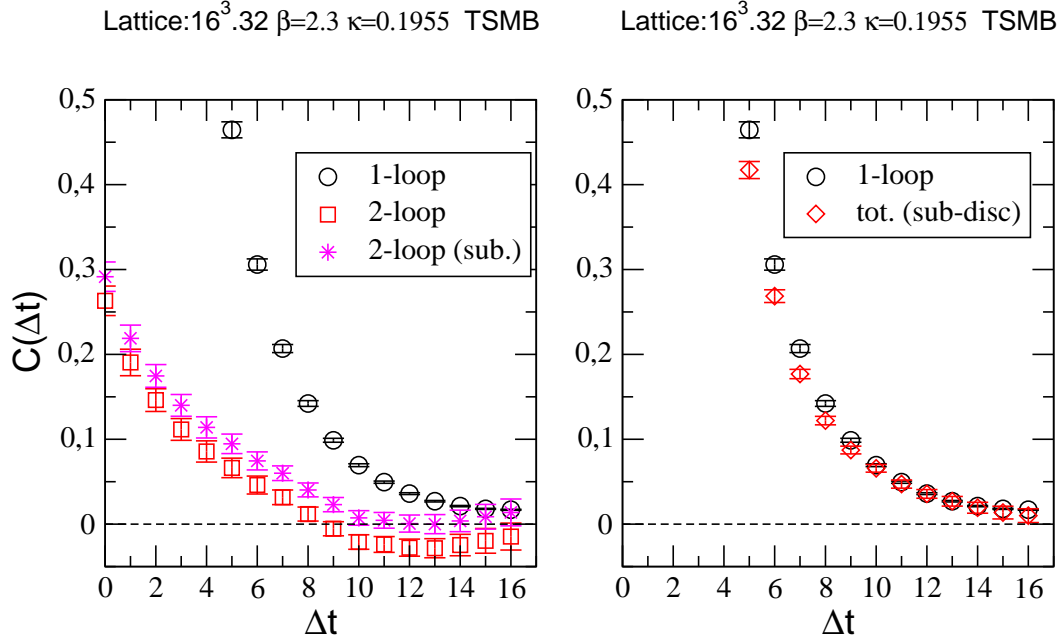


Figure 3.33: Comparison of 1-loop and 2-loop with 2-loop correlator after subtraction (left panel). Total correlator (after subtraction of the offset from its disconnected part) compared to its connected part (right panel). Ensemble (a).

zero vacuum expectation value VEV  $v$ . The values of  $v$  determined for each configuration are strongly correlated to the connected and disconnected correlators. This fact renders the task of mass estimation more difficult by poor signal-to-noise ratio. However, the ratio of correlators method can be used in this study to have an orientation of the scalar mass.

The ratio of correlators is presented in Fig. 3.37. The ratio  $R(t)$  grows with the time-separation, and the effective mass gap fit showed a negative mass gap values. This yields a mass estimation of the  $a$ - $f_0$  which is smaller than its connected counterpart ( $a$ - $a_0$ ). The fact that  $m_{a_0} > m_{f_0}$  indicates that the smallness of the  $a$ - $f_0$  is due to its disconnected contribution. This is quite similar to the scalar meson in QCD where the  $f_0(600)$  is lighter than  $a_0(980)$ .

This analysis does not agree with the direct fit procedure. We attribute this disagreement to the poor signal-to-noise ratio in the scalar meson and the probable presence of the offset as in the pseudo-scalar correlator. However, more efforts have to be done in order to obtain reliable mass estimation in the scalar channel.

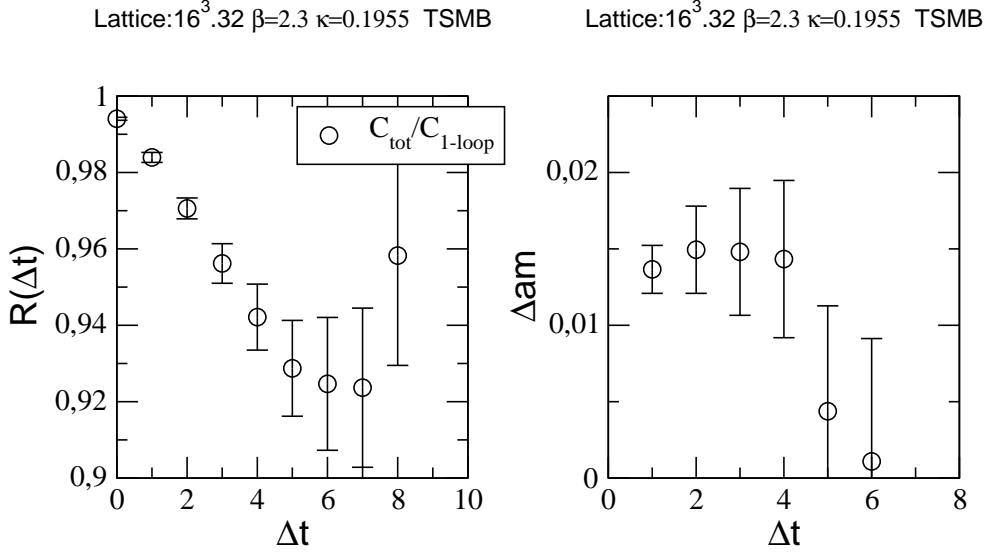


Figure 3.34: The ratio  $R(t)$  as function of time-separation (left panel). The effective mass gap  $\Delta m$  from  $R(t)/R(t+1)$ . Ensemble (a).

### 3.7 Summary of the spectrum analysis

We presented in this chapter the natural continuation of the investigations of the DESY-Münster collaboration of lattice SYM by means of Monte Carlo simulations. The results of our low-lying spectrum calculations are collected and summarized in Table 3.27. We were going towards small soft breaking by considering larger values of  $\kappa$  on  $16^3.32$  lattices at  $\beta = 2.3$ . The value of the gluino mass reached in this simulation is  $m_{\tilde{g}} \sim 115$  MeV where we used QCD units to set the lattice scale. This mass, at  $\kappa = 0.1965$  is of the order of the strange quark mass. We have used two independent methods to find an estimate of the chiral limit. The critical hopping parameter from OZI arguments and lattice SUSY WI's has been estimated to be  $\kappa_{\text{cr}} = 0.1969$ , and hence our present simulation is quite near the chiral limit. The ensembles were prepared by the TSMB algorithm by tuning its parameters in order to have relatively high acceptance rate in the noisy correction step. However, the run histories have shown a substantial increase of the autocorrelation-times and the frequently occurrence of low-lying eigen-modes which have the impact of slowing-down the production process. This requires long updating runs to reach enough statistics for the spectrum analysis. We argue that our statistics

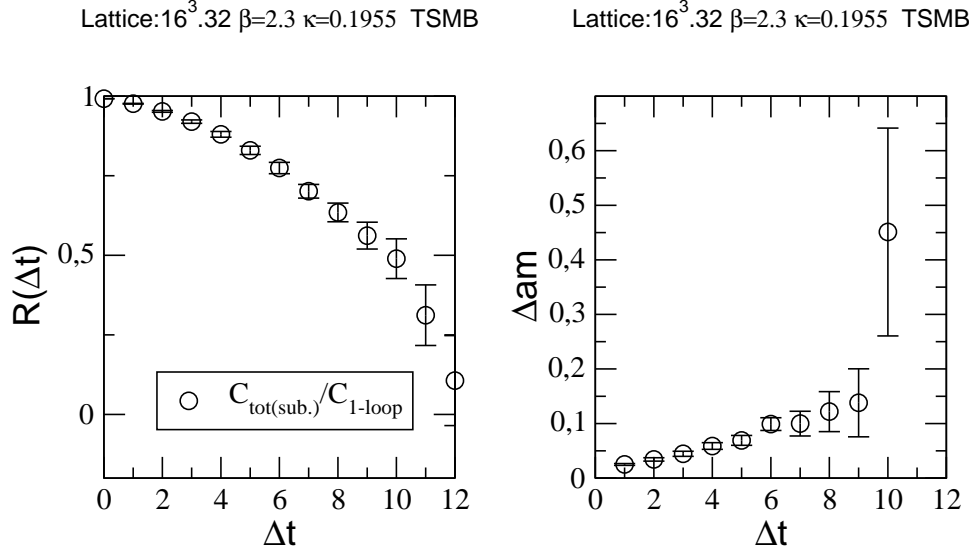


Figure 3.35: The ratio  $R(t)$  as function of time-separation using the total correlator after subtracting the constant term (left panel). The effective mass gap  $\Delta m$  from  $R(t)/R(t+1)$ . Ensemble (a).

were low for an accurate determination of the spectrum.

During the spectrum analysis we were confronted with several problems such as the appearance of an offset in the long time-separation of the adjoint mesons correlators, the low signal-to-noise ratio in the scalar channel and low statistics. Furthermore, our lattices are quite fine and the spatial volume extension of our  $16^3 \cdot 32$  lattice is roughly  $L^3 \sim (1\text{fm})^3$ . This could be not sufficiently large for spectrum computations and therefore finite size effects are expected to be important. But this setup was appropriate for the study of lattice SUSY WI's, also valid in small volume. Although the box size is small, the qualitative features of the mass spectrum could be also visible at this scale.

In the SUSY and therefore chiral point the low-energy effective actions describe the bound states spectrum by two massive chiral multiplets as discussed in the Introduction of this work. The picture of the mass spectrum near the region of massless gluino is illustrated in Fig. 3.38. The masses of bound states present in the spectrum are plotted as function of the inverse hopping parameter  $1/\kappa$ . The region where  $m_{\tilde{g}}$  vanishes is represented by the vertical wide line.

The spectrum results at lightest gluino mass indicate the degeneracy of the scalar



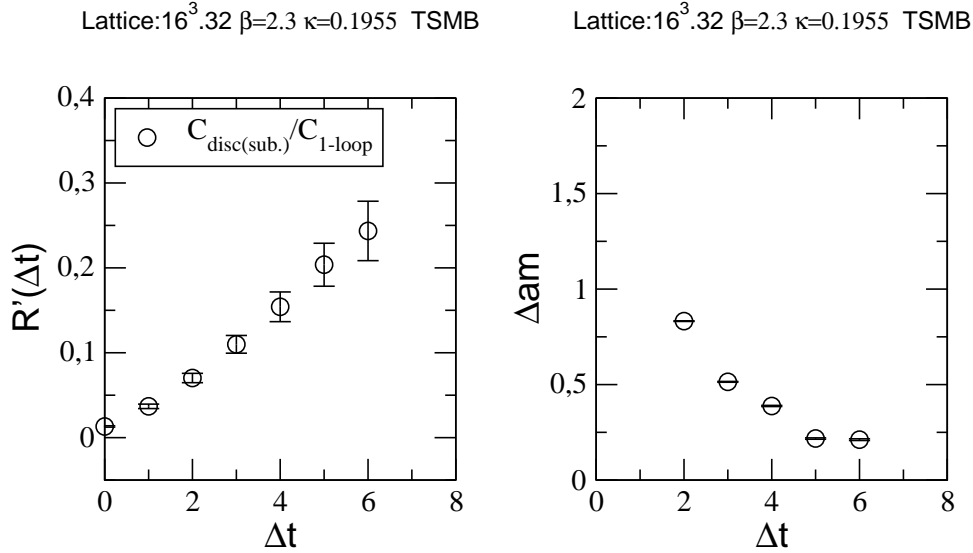


Figure 3.36: The ratio  $R'(t)$  as function of time-separation where the subtracted disconnected correlator is considered (left panel). The effective mass gap  $\Delta m$  from  $R'(t)/R'(t+1)$ . Ensemble (a).

glueball  $0^{++}$ ,  $\chi$  and  $a\text{-}\eta'$  within errors although the mass of the adjoint pseudo-scalar  $a\text{-}\eta'$  seems much smaller. Therefore, this suggests that at least two bound states, the scalar glueball and the gluino-glueball  $\chi$ , occur in a supermultiplet where the particles have comparable masses. The picture at the  $\kappa = 0.196$  is less clear since the  $a\text{-}\eta'$  seems to be rearranged in one supermultiplet together with the gluino-glueball. Moreover, the large error of the masses is an issue here which makes difficult drawing a conclusive picture of the supermultiplets, even if we are close to the massless gluino limit. Monte Carlo simulation of SYM requires more efforts to control several numerical issues and problems found here.

Next steps will be to consider larger physical volumes and to control  $\mathcal{O}(a)$  effects while remaining at lighter gluino mass. Furthermore, going towards a clear picture of the SYM spectrum needs the production of sufficiently high statistics. Thus, we can only reach this goal by finding a robust updating algorithm which remains efficient even at very small gluino mass. Candidates for this purpose algorithms based on Molecular Dynamics (MC) evolutions. In the next chapter, we will discuss the analysis of a second set of ensembles used in this study which were produced by the TS-PHMC algorithm.

Table 3.26: *Mass gap  $\Delta m$  and  $a\text{-}\eta'$  mass from ratio fit (ensemble (a)).*

$\Delta m$	fit-interval	$am_{\eta'}$	Ratio
0.0148(34)	1 - 4	0.360(7)	$C_{tot}/C_{1loop}$
0.090(17)	6 - 7	0.43(2)	$C_{tot}^{sub}/C_{1loop}$
0.217	5 - 6	0.562(7)	$C_{disc}^{sub}/C_{1loop}$

Table 3.27: *The spectrum of  $\mathcal{N} = 1$   $SU(2)$  SYM on  $16^3 \cdot 32$  at  $\beta = 2.3$  simulated with TSMB algorithm. At the point with the symbol  $^\dagger$  the results at  $\kappa = 0.194$  were recorded from Ref. [18] and Ref. [71].*

$\kappa$	$am_S Z_S^{-1}$	$Z_T Z_S^{-1}$	$am_{a-\pi}$	$0^+(\text{glub.})$	$a\text{-}f_0$	$a\text{-}\eta'$	$\tilde{g}g_{\gamma_0}$	$\tilde{g}g_1$
0.194 $^\dagger$	0.173(7)	0.22(2)	0.484(1)	0.52(1)	0.78	0.52(2)	0.43(1)	0.40(7)
0.1955	0.061(12)	0.135(29)	0.345(3)	0.4(2)	0.673	0.48(1)	0.700(21)	0.637(20)
0.196	0.079(15)	0.112(60)	0.264(5)	0.75(9)	1.135(95)	0.399(45)	0.472(31)	0.424(22)
0.1965	0.035(27)	0.33(11)	0.208(13)	0.51(14)	0.649(46)	0.319(77)	0.472(75)	0.469(85)

## 3.8 Further spin-1 states in the $\mathcal{N} = 1$ $SU(2)$ SYM theory

### 3.8.1 Introduction

Recall that a spin-1 candidate was analyzed on the TSMB ensembles in Section. 3.3.5. This was an exploratory study which can be extended in the future. A possible construction of interpolating fields for spin-0 and spin-1 mesons can also involve gauge links  $U_\mu(x)$ . One interesting construction is through gluino bilinear connected by gauge links first studied in Ref. [78, 81, 82]. These interpolating fields are called Majorana-link-Majorana operators. We have, at a stage of this thesis study, reconsidered this case and we have tried to reexamine it more deeply.

We want to re-discuss the construction of the representations of the  $O_h$  cubic group on the Majorana-Link-Majorana operator and consequently the possible spin  $J$  content of this operator first appearing in [82]. The Monte Carlo simulation of this operator on the lattice will allow us to estimate the mass of the particle represented by this lattice operator. The Majorana-Link-Majorana operator consists of two Majorana fermions on two lattice sites which are joined each to other by an adjoint link, this yields three independent operators in each direction. This operator has no analogous one in QCD and can exist in the  $N = 1$   $SU(2)$  SYM on the lattice due to Majorana nature of the

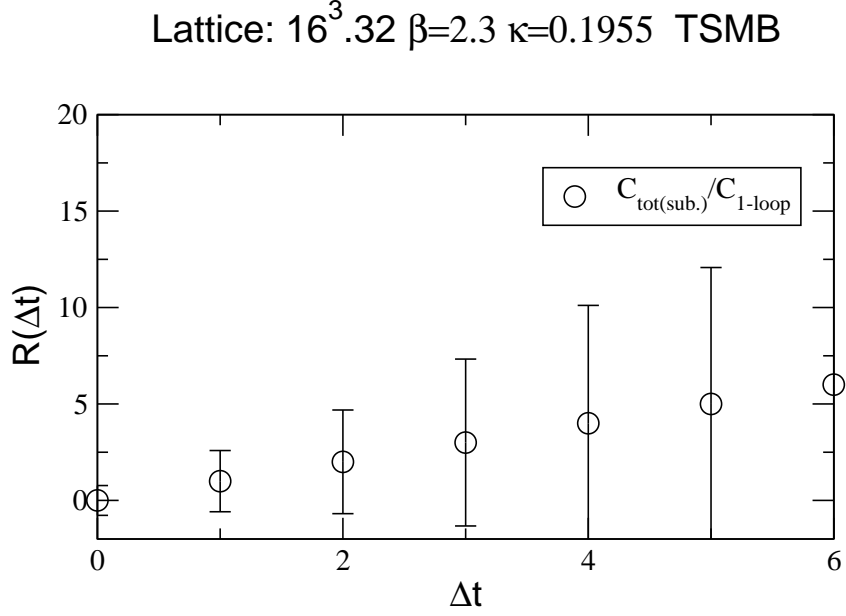


Figure 3.37: *The ratio  $R(t)$  as function of time-separation for the adjoint scalar meson. Ensemble (a).*

fermions of the theory which are in the adjoint representation of the gauge group.

### 3.8.2 Majorana-Link-Majorana Operator

The gauge invariant Majorana-Link-Majorana Operator is defined on the lattice as [82]

$$O_\mu(x) = \text{Tr}\{\bar{\lambda}(x)U_\mu^\dagger(x)\Gamma\lambda(x+a\hat{\mu})U_\mu(x)\} ; \quad \mu = 1, 2, 3 \quad (3.42)$$

where

$$\Gamma = \mathbb{1}, \gamma_5 .$$

This can be diagrammatically represented by

Lattice:  $16^3.32$ ,  $\beta=2.3$ , TSMB

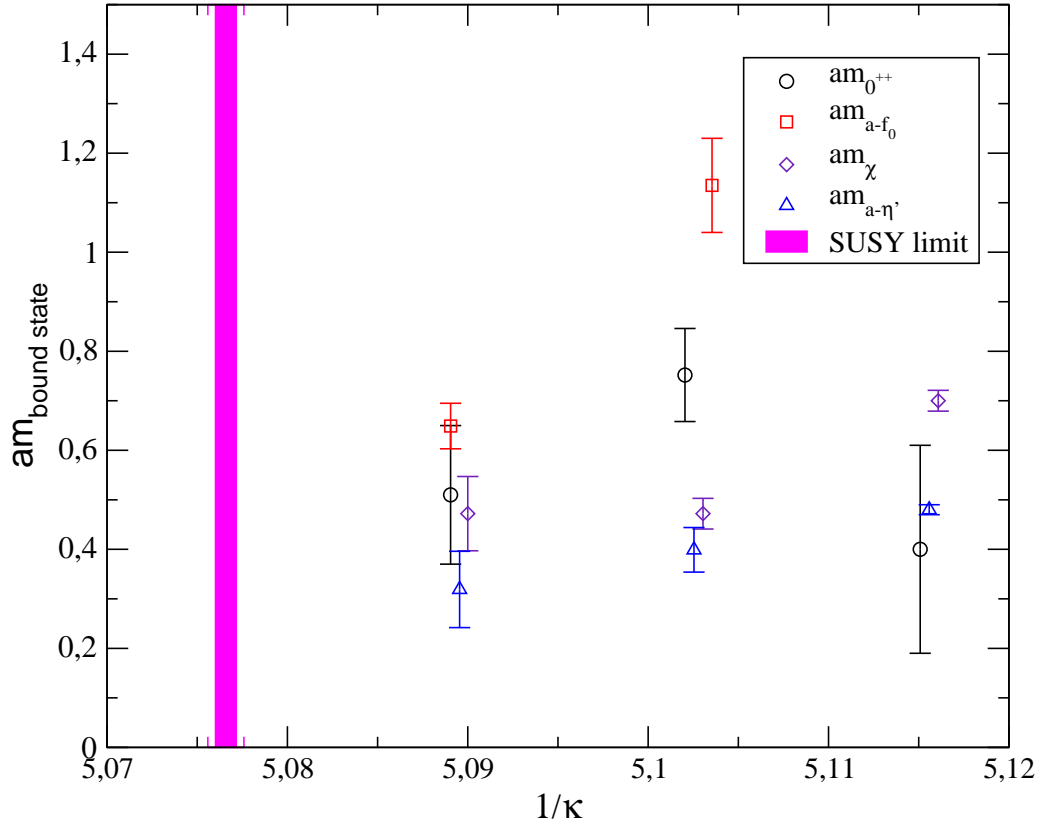


Figure 3.38: The mass spectrum of  $\mathcal{N} = 1$   $SU(2)$  SYM on  $16^3 \cdot 32$  at  $\beta = 2.3$  in lattice unit as function of the inverse hopping parameter  $1/\kappa$ . (TSMB)

We distinguish then three independent basic operators,

$$\begin{array}{c} \lambda \\ \nearrow \\ \bar{\lambda} \end{array} = O_1 \qquad \begin{array}{c} \lambda \\ \mid \\ \bar{\lambda} \end{array} = O_2 \qquad \bar{\lambda} \longleftarrow \lambda = O_3$$

The representation  $\mathcal{R}^{\mathcal{PC}}$  which has to be built is then of dimension three for each given channel of parity  $\mathcal{P}$  and charge conjugation  $\mathcal{T}$ . In the following analysis we will consider the case of  $\Gamma = \mathbb{1}$ , the case  $\Gamma = \gamma_5$  is straightforward.

### 3.8.3 Parity and Charge Conjugation transformations

- **Parity**

Choose the origin of the frame to be the point  $x$  and denote the operator  $O_\mu$  at this point, then perform a parity transformation through  $x$  using the parity properties in [30]

$$\begin{aligned}
\mathcal{P}_x\{O_\mu(x)\} &= \text{Tr}\{\bar{\lambda}^{\mathcal{P}}(x^{\mathcal{P}})U_\mu^{\dagger\mathcal{P}}(x^{\mathcal{P}})\lambda^{\mathcal{P}}((x+a\hat{\mu})^{\mathcal{P}})U_\mu^{\mathcal{P}}(x^{\mathcal{P}})\} \\
&= \text{Tr}\{\bar{\lambda}(x)\gamma_0 U_\mu(x-a\hat{\mu})\gamma_0 \lambda(x-a\hat{\mu})U_\mu^\dagger(x-a\hat{\mu})\} \\
&= \bar{\lambda}^a(x)\gamma_0^2 \lambda^b(x-a\hat{\mu})\text{Tr}\{T_a U_\mu(x-a\hat{\mu})T_b U_\mu^\dagger(x-a\hat{\mu})\} \\
&= \bar{\lambda}^b(x-a\hat{\mu})\lambda^a(x)\text{Tr}\{T_b U_\mu^\dagger(x-a\hat{\mu})T_a U_\mu(x-a\hat{\mu})\} \\
&= \text{Tr}\{\bar{\lambda}(x-a\hat{\mu})U_\mu^\dagger(x-a\hat{\mu})\lambda(x)U_\mu(x-a\hat{\mu})\} \\
&= O_\mu(x-a\hat{\mu}),
\end{aligned} \tag{3.43}$$

when performing the translation in the  $\hat{\mu}$ -direction, one obtains

$$\begin{aligned}
\mathcal{P}_x\{O_\mu(x+a\hat{\mu})\} &= \text{Tr}\{\bar{\lambda}(x)U_\mu^\dagger(x)\lambda(x+a\hat{\mu})U_\mu(x)\} \\
&= O_\mu(x).
\end{aligned} \tag{3.44}$$

This mean that  $O_\mu$  is parity invariant up to a translation. In the case of  $\Gamma = \gamma_5$  we have

$$\mathcal{P}_x\{O_\mu(x)\} = -O_\mu(x-a\hat{\mu}). \tag{3.45}$$

- **Charge Conjugation**

Under the charge conjugation transformation the Majorana is self anti-particle, the link is transformed into its complex conjugate. For the Wilson loop  $\mathcal{W}$  the charge conjugation reverses the orientation of the Wilson loop, this means  $\mathcal{W}$  to  $\mathcal{W}^\dagger$ , but in the case of  $SU(2)$  this becomes irrelevant because a product of links has real trace, and the Wilson loops are  $\mathcal{C}$  invariant. When treating the Majorana-Link-Majorana loop using the real adjoint links [71] we can write it

$$\begin{aligned}
O_\mu(x) &= \bar{\lambda}^a(x)\lambda^b(x+a\hat{\mu})\text{Tr}\{U_\mu^\dagger(x)T^b U_\mu(x)T^a\} \\
&= \frac{1}{2}\bar{\lambda}^a(x)V_\mu^{ba}(x)\lambda^b(x+a\hat{\mu}).
\end{aligned} \tag{3.46}$$

When applying the  $\mathcal{C}$  transformation, this yields

$$\begin{aligned}
\mathcal{C}\{O_\mu(x)\} &= \bar{\lambda}^C(x)^a[V_\mu^C(x)]^{ba}\lambda^C(x+a\hat{\mu})^b \\
&= \bar{\lambda}^a(x)[V_\mu^*(x)]^{ba}\lambda^b(x+a\hat{\mu}) \\
&= O_\mu(x).
\end{aligned} \tag{3.47}$$

### 3.8.4 Construction of the representation

It seems at a first look that the three Majorana-Link-Majorana operators behave like a three components vector living on the three dimensional space; this means that this operator transforms in the three dimensional irreducible representation  $T_1$  (see Appendix C.1) of the cubic group  $O_h$  as argued in [82], and hence describes a spin  $J = 1$  state on the lattice. The fast conclusion has led to some ambiguities because when simulating this operator on the lattice, the extracted mass was consistent with the one extracted from simulating the mesonic  $\bar{\lambda}\Gamma\lambda$  state which describes a spin  $J = 0$  state.

In fact, one can see intuitively that the Majorana-Link-Majorana operator has a spin 0 component when writing its continuum form. We are then in the situation to examine the representation of this operator. First, it is to be noted for example that this operator is invariant when rotated by  $\pi$ . In fact, the rotated operator is still invariant up to translation and this transformation leads to the same action as a parity transformation. This rotation of  $\pi$  has been considered in [82] as giving the operator with negative sign, which is not the case. Before giving an example we note that to avoid ambiguities, it is better to treat the whole operator instead of treating each sector (fermionic and bosonic) separately as done in [82]. Considering the basis  $\{O_\mu, \mu = 1, 2, 3\}$  and the case of the operator  $O_3(x)$  and rotate it through  $\pi$  over the  $x$  axis, one has

$$\bar{\lambda}(x) \begin{array}{c} \xrightarrow{U_3^\dagger(x)} \\ \text{---} \text{---} \text{---} \\ \xleftarrow{U_3(x)} \end{array} \lambda(x + a\hat{3}) \quad \xrightarrow{\mathcal{R}_x(\pi)} \quad \lambda(x - a\hat{3}) \begin{array}{c} \xrightarrow{U_{-3}(x)} \\ \text{---} \text{---} \text{---} \\ \xleftarrow{U_{-3}^\dagger(x)} \end{array} \bar{\lambda}(x) .$$

or formally,

$$\begin{aligned} \mathcal{R}_\pi\{O_3(x)\} &= \text{Tr}\{\bar{\lambda}'(x')U_3'^\dagger(x')\lambda'(x' + a\hat{3}')U_3'(x')\} \\ &= \text{Tr}\{\bar{\lambda}(x)S^{-1}U_{-3}^\dagger(x)S\lambda(x - a\hat{3})U_{-3}(x)\} \\ &= \text{Tr}\{\bar{\lambda}(x)U_3(x - a\hat{3})\lambda(x - a\hat{3})U_3^\dagger(x - a\hat{3})\} \\ &= \bar{\lambda}^a(x)\lambda^b(x - a\hat{3})\text{Tr}\{T_bU_3^\dagger(x - a\hat{3})T_aU_3(x - a\hat{3})\} \\ &= \bar{\lambda}^b(x - a\hat{3})\lambda^a(x)\text{Tr}\{T_bU_3^\dagger(x - a\hat{3})T_aU_3(x - a\hat{3})\} \\ &= \text{Tr}\{\bar{\lambda}(x - a\hat{3})U_3^\dagger(x - a\hat{3})\lambda(x)U_3(x - a\hat{3})\} \\ &= O_3(x - a\hat{3}) , \end{aligned} \tag{3.48}$$

where  $S$  is the Lorentz matrix in the Dirac space.

When translating in the  $\hat{3}$ -direction, one obtains

$$\begin{aligned} \mathcal{R}_\pi\{O_3(x)\} &= \text{Tr}\{\bar{\lambda}(x)U_3^\dagger(x)\lambda(x + a\hat{3})U_3(x)\} \\ &= O_3(x) . \end{aligned} \tag{3.49}$$

Contrary to vector components which transform to their negatives values when rotated by  $\pi$ , the operator  $O_\mu$  does not behave like a vector, and is still invariant under  $\pi$  rotation. Such a behaviour is already known in the case of the plaquette operator in the  $\mathcal{P} = 1$  and  $\mathcal{C} = 1$  channel, see for example [82, 49]. For a cross check, let us determine the transformation of the basic Majorana-Link-Majorana operator under a choosen element from each class of the cubic group<sup>2</sup>

- class  $E$

$Id$ :

$$\begin{aligned} O_{1\pm} &\longmapsto O_{1\pm} \\ O_{2\pm} &\longmapsto O_{2\pm} \\ O_{3\pm} &\longmapsto O_{3\pm} \end{aligned}$$

- class  $C_2$

$C_{2a}$ :

$$\begin{aligned} O_{1\pm} &\longmapsto CO_{1\pm} \\ O_{2\pm} &\longmapsto O_{3\pm} \\ O_{3\pm} &\longmapsto O_{2\pm} \end{aligned}$$

- class  $C_3$

$C_{3\alpha}$ :

$$\begin{aligned} O_{1\pm} &\longmapsto CO_{2\pm} \\ O_{2\pm} &\longmapsto O_{3\pm} \\ O_{3\pm} &\longmapsto CO_{1\pm} \end{aligned}$$

- class  $C_4$

$C_{4x}$ :

$$\begin{aligned} O_{1\pm} &\longmapsto O_{2\pm} \\ O_{2\pm} &\longmapsto CO_{1\pm} \\ O_{3\pm} &\longmapsto O_{3\pm} \end{aligned}$$

---

<sup>2</sup>See Ref. [82] and references therein for notations.

- class  $C_4^2$

$C_{2x}$ :

$$O_{1\pm} \longmapsto CO_{1\pm}$$

$$O_{2\pm} \longmapsto CO_{2\pm}$$

$$O_{3\pm} \longmapsto O_{3\pm}$$

where  $O_{\mu\pm}$  means positive or negative parity.

The operator  $O_\mu$  is transforming then in the same way as the parity invariant plaquette in the  $\mathcal{C} = 1$  channel, where the characters of the representation of the three dimensional representation  $\mathcal{R}$  of  $O_\mu$  are listed in the following table,

Conjugate classes $C_i$	$Id$	$C_2$	$C_3$	$C_4$	$C_4^2$
The characters $\chi^{\mathcal{R}}(C_i)$	3	1	0	1	1

The irreducible content is explored by means of the character relation. For fixed  $\mathcal{P}$  or  $\mathcal{C}$ -parity the multiplicity  $a_\mu$  of the occurrence of the irreducible representation  $\mathcal{R}^\mu$  in the decomposition of  $\mathcal{R}$  into irreducible representations is given by [82]

$$a_\nu = \frac{1}{n_G} \sum_i n_i \chi^{\nu\dagger}(C_i) \chi^{\mathcal{R}}(C_i) . \quad (3.50)$$

where  $n_G$  is the number of elements of  $O_h$  and  $n_i$  is the number of elements in the class  $C_i$ . An example of computing the characters  $\chi^\mu$  is given in the Appendix C.1).

When using the expression (3.50) in the case of Majorana-Link-Majorana operator, the only non vanishing multiplicities are

$$\begin{aligned} a_{A_1} &= 1, \\ a_E &= 1. \end{aligned} \quad (3.51)$$

The content of the representation  $\mathcal{R}$  is then

$$\mathcal{R}^{++} = A_1^{++} \oplus E^{++}. \quad (3.52)$$

This mean that as the case of the plaquettes, the representation space of  $\mathcal{R}$  has two invariant subspaces transforming in the one and two-dimensional  $A_1$  and  $E$  irreps of  $O_h$



respectively. The operator (3.42) is in the  $\mathcal{P} = -1$  channel when  $\Gamma = \gamma_5$ . The behaviour under the cubic group is analogous to the  $P = +1$  treated above, one would label the operator in (3.42) with a  $P$  index such as  $O_\mu^\pm$ . The content in the  $P = -1$  channel looks like in (3.52), only with negative parity. Finally, the members of the orthonormal basis (see appendix (C.2)) for each subspace can be read off directly from the case of the plaquettes. They are listed in the following Table 3.28

Table 3.28: *Representation from Majorana-Link-Majorana operator.*

Representation $\tilde{\mathcal{R}}$ of $O_h$	Majorana-Link-Majorana linear combinations
$A_1^{\pm+}$	$O_1^\pm + O_2^\pm + O_3^\pm$
$E^{\pm+}$	$-2O_1^\pm + O_2^\pm + O_3^\pm$ , $O_2^\pm - O_3^\pm$

The possible irreps of the cubic group which can be constructed from the Majorana-Link-Majorana operator are presented in the Table 3.28. The low spin state one can study is a zero spin state constructed from the linear combination as shown in Table 3.28, where the combination  $O_1^\pm + O_2^\pm + O_3^\pm$  transforms in the  $A_1^{\pm+}$  irrep of  $O_h$ . Nevertheless, the use of such operator to study  $J = 0^\pm$  is quite not necessary. The first reason is that we have already a simple Majorana-Majorana operator  $\bar{\lambda}\Gamma\lambda$  which can be simply used to simulate a spin null state on the lattice; the second reason is that the Majorana-Link-Majorana contains links and this can lead to noisier signal; finally the computer runtime increases to three times the time needed in case of Majorana-Majorana operator. To compute the correlation function one needs the three shifted propagators  $Q^{-1}(x, y + a\hat{\mu})$  instead of one propagator  $Q^{-1}(x, y)$  in the case of  $\bar{\lambda}\Gamma\lambda$  operator. However, it is of our interest to find an operator which can allow us to simulate a spin-1 particle with both parities. The trivial operator in analogy to QCD can be built in  $SU(2)SYM$  from the Dirac gamma matrix with a bilinear fermions as

$$A_\mu(x) = \bar{\lambda}(x)\gamma_5\gamma_\mu\lambda(x) ; \quad \mu = 1, 2, 3 \quad (3.53)$$

which transforms as a Lorentz vector in the continuum, and hence it transforms in the  $T_1^{++}$  irrep of the  $O_h$  group. The state which can overlap of the interpolating in eq. (3.53) has been analyzed in Section. 3.3.5

Using such operator one can simulate a  $J = 1^{++}$  state on the lattice in the  $SU(2) SYM$  theory, even this state does not belong to the predicted contents of the lighter supermultiplets which rise from the low energy effective action of Veneziano and Yankielowicz.

To extract the mass of the  $J = 1^{++}$  one needs the timeslice correlations, which can be constructed from the scalar like product of the axial vector in eq. (3.53) as follows

$$C(\Delta t) = \frac{1}{3} \sum_{i=1}^3 C_{ii}(\Delta t) = \frac{1}{3} \sum_{i=1}^3 \langle A_i(\Delta t + t) A_i(t) \rangle. \quad (3.54)$$

Nevertheless, it remains the case of spin  $J = 1^{-+}$ , which is of our interest, while  $\bar{\lambda}(x)\gamma_\mu\lambda(x) = 0$  due to the Majorana nature of the gluinos. In Section 3.9 operators with  $J = 1^{\pm+}$  content are proposed.

### 3.8.5 Correlation functions of Majorana-Link-Majorana (M-L-M) operator

As discussed above the M-L-M correlator would involve three propagators. It is convenient to simulate one component of the operator  $O_\mu^\pm$  on the lattice since one can determine the remaining correlators using rotation invariance. Simulating one component is then sufficient to extract the mass of the investigated candidate.

The zero-momentum two points correlation function on the lattice at the distance  $\Delta t$  is given by

$$C_{\mu\nu}(\Delta t) = \langle \tilde{S}_\mu^\dagger(t + \Delta t) \tilde{S}_\nu(t) \rangle \quad (3.55)$$

with,

$$\tilde{S}_\mu(t) = S_\mu(t) - \langle S_\mu(t) \rangle, \quad (3.56)$$

where  $S_\mu(t)$  is the timeslice of an operator  $\mathcal{O}_\mu[U]$ :

$$S_\mu(t) = \frac{1}{\sqrt{L^3}} \sum_{\mathbf{x}} \mathcal{O}_\mu[U](\mathbf{x}, t), \quad (3.57)$$

while  $L^3$  is the spatial volume of the lattice. The spectral decomposition of the correlator is written as

$$C(\Delta t) = \sum_{\mu}^3 C_{\mu\mu}(\Delta t) = c_0^2 + \sum_n c_n^2 (e^{-m_n \Delta t} \pm e^{-m_n(T-\Delta t)}). \quad (3.58)$$

The  $c_i$ 's are the amplitudes of overlaps of the lattice operator with the physical state.

Returning to the correlation function of the real operator<sup>3</sup>  $O_\mu$ , one can consider for simplicity the operators instead of its timeslice, and add the summation at the end.

---

<sup>3</sup>  $O_\mu$  is defined as the trace of bilinear Majorana and adjoint link on the fundamental indices of the gauge  $SU(2)$  group, and due the properties of bilinear fermions and reality of the adjoint links the operator  $O_\mu$  is Hermitian.

To determine the mass of the particle described by the split-point M-L-M operator the correlation function should be computed. This can be realized by creating a state on a lattice site  $x_1$  and destroy it on another lattice site  $x_2$  and then compute the decay which leads to

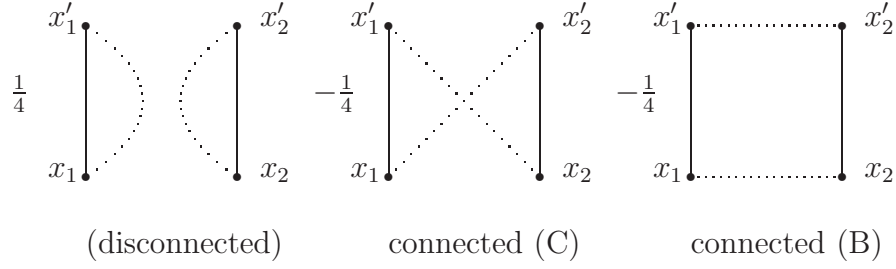
$$\begin{aligned}
\langle O_\mu(x_1) O_\nu(x_2) \rangle &= \langle \text{Tr} \{ \bar{\lambda}(x_1) U_\mu^\dagger(x_1) \gamma_\mu \lambda(x_1 + a\hat{\mu}) U_\mu(x_1) \} \\
&\quad \text{Tr} \{ \bar{\lambda}(x_2) U_\nu^\dagger(x_2) \gamma_\nu \lambda(x_2 + a\hat{\nu}) U_\nu(x_2) \} \rangle \\
&= \frac{1}{4} \langle \text{Tr}_{sc} \{ \Delta(x_1, x_1 + a\hat{\mu}) V_\mu(x_1) \} \text{Tr}_{sc} \{ \Delta(x_2, x_2 + a\hat{\nu}) V_\nu(x_2) \} \rangle_U \\
&\quad - \frac{1}{4} \langle \text{Tr}_{sc} \{ \Delta(x_2, x_1) V_\mu^T(x_1) \Delta(x_1 + a\hat{\mu}, x_2 + a\hat{\nu}) V_\nu(x_2) \} \rangle_U \\
&\quad - \frac{1}{4} \langle \text{Tr}_{sc} \{ \Delta(x_2 + a\hat{\nu}, x_1) V_\mu^T(x_1) \Delta(x_1 + a\hat{\mu}, x_2) V_\nu^T(x_2) \} \rangle_U
\end{aligned} \tag{3.59}$$

The details of obtaining the expression in (3.59) are left to Appendix E.  $\Delta_{xy}$  is the fermion propagator in the background of the gauge configuration  $U$ . it is needed to compute the correlation function and can be calculated from inverting the fermion matrix  $Q$ . This is computationally the most demanding part of the correlation. To obtain the timeslice correlation functions one has to sum  $O_\mu(x)$  over all space points in a given timeslice as in eq. (3.57); we write

$$\begin{aligned}
C(\Delta t) &= \frac{1}{4V_s} \sum_{\mathbf{x}_1, \mathbf{x}_2} \langle \text{Tr}_{sc} \{ \Delta(x_1, x_1 + a\hat{\mu}) V_\mu(x_1) \} \text{Tr}_{sc} \{ \Delta(x_2, x_2 + a\hat{\nu}) V_\nu(x_2) \} \rangle_U \\
&\quad - \frac{1}{4} \sum_{\mathbf{x}_1} \langle \text{Tr}_{sc} \{ \Delta(x_2^s, x_1) V_\mu^T(x_1) \Delta(x_1 + a\hat{\mu}, x_2^s + a\hat{\nu}) V_\nu(x_2^s) \} \rangle_U \\
&\quad - \frac{1}{4} \sum_{\mathbf{x}_1} \langle \text{Tr}_{sc} \{ \Delta(x_2^s + a\hat{\nu}, x_1) V_\mu^T(x_1) \Delta(x_1 + a\hat{\mu}, x_2^s) V_\nu^T(x_2^s) \} \rangle_U
\end{aligned} \tag{3.60}$$

where  $x_2^s$  is a randomly chosen fixed source. This induces only one summation over space points for the propagator instead of two summations due to the translation invariance of the correlation function. One can see that in the expression (3.59) three terms are found; the first term is the disconnected piece coming from the single flavor nature of the theory, the last two terms are the connected pieces which can be called the block connected (B) piece and the cross connected (C) piece respectively. The correlation function in (3.60) can be diagrammatically represented as

$$C(\Delta t) =$$



where the dashed lines are the fermion propagators  $Q^{-1}$ , the solid lines are the adjoint links  $V_\mu^{ab}$  and  $x'_{1,2}$  is the neighbour site of  $x_{1,2}$  in the  $\hat{\mu}$ -direction *i.e.*  $(x_{1,2} + a\hat{\mu})$ . In the diagram the color and spin indices are omitted.

However, the most demanding task in lattice theory is the computing the propagators. The connected pieces are obtained using standard methods for inverting the fermionic matrix on a randomly chosen point source being delta-like in spin, color and space. We choose to use here the Improved Volume Source Technique (IVST). Here we apply this method for the case of non local mesonic operators consisting of links (3.42) and hence an IVST has to be adapted to this case.

From the equation (3.60), we have the first disconnected term as the object of investigation, where the trace is over color and Dirac spaces of the inverse fermion matrix  $Q^{-1} = \Delta$ , *i.e.* the propagator in the background of gauge configuration. Let us focus now on the evaluation of the timeslice sum defined as

$$S_{\mu; \alpha, \beta}(x_0) = \sum_{\mathbf{x}} \text{Tr}_c \{ Q_{\alpha, \beta}^{-1}(x, x + a\hat{\mu}) V_\mu(x) \}, \quad (3.61)$$

where we write here explicitly the Dirac indices  $\alpha, \beta$ . The conjugate gradient is called to solve the equation for the vector  $Z$  given by

$$Q_{xa\alpha, yb\beta} Z_{yb\beta}^{[zc\gamma]} = \omega_{xa\alpha}^{[zc\gamma]}, \quad (3.62)$$

where  $\omega$  is the delta-like point source. Thus, single inversion is performed for each value of the color and Dirac index. The resulting vector  $Z$  projects exactly the  $zc\gamma$  column of the  $Q^{-1}$  matrix (*i.e.* the propagator from the source point  $(yb\beta)$  to any other site, color and spin component, the so-called *sink*.) However, the delta like source is not appropriate to estimate the all-to-all propagators appearing in eq. (3.61). The IVST is instead applied, where at first we define the *volume* source allowing the estimation of the timeslice sum in eq. (3.61). The volume source contains an adjoint link matrix  $V_\mu$  on each site as follows

$$\omega = \sum_z \omega_{\mu; xa\alpha}^{[zc\gamma]} = \sum_z \delta_{xz} \delta_{ad} \delta_{\alpha\gamma} V_\mu^{dc}(x - a\hat{\mu}); \quad (3.63)$$

we solve now the linear system of equations given by

$$Q_{xa\alpha, yb\beta} Z_{\mu; yb\beta}^{[c\gamma]} = \sum_z \omega_{\mu; xa\alpha}^{[zc\gamma]}, \quad (3.64)$$

with vector solution

$$Z_{\mu; yb\beta}^{[c\gamma]} = Q_{yb\beta, (y+a\hat{\mu})d\gamma}^{-1} V_{\mu}^{dc}(x) + \sum_{z \neq (y+a\hat{\mu})} Q_{yb\beta, zd\gamma}^{-1} V_{\mu}^{dc}(z - a\hat{\mu}), \quad (3.65)$$

where in the IVST variant the second error term in eq. (3.65) is averaged away over a sufficiently large number  $N_g$  of gauge configurations obtained from the original one by random gauge transformation (see Section 2.8.1). At this point the error in eq. (3.65) is removed, while, the second term is not gauge invariant and the timeslice sum in eq. (3.61) can be obtained in the limit  $N_g \rightarrow \infty$  as

$$\left\langle \sum_{\mathbf{x}; c} Z_{\mu; xc\alpha}^{[c\beta]} \right\rangle_g = S_{\mu; \alpha, \beta}(x_0) \quad (3.66)$$

In practice one cannot perform  $N_g = \infty$  random gauge transformations; however, the (small) residual error is still purely statistical for any finite number of  $N_g$ .

The non-local M-L-M operators have been also simulated on the lattice  $16^3 \cdot 32$  at the point  $\beta = 2.3$  and  $\kappa = 0.1955$  in both channels of parity. Like the case of the local operators, one can expect a signal in the negative parity channel whereas the signal in the positive parity channel is poor for the total correlator but its connected part displays a signal. The correlators and effective mass plots for the non-local operators are presented in Fig. 3.39 and Fig. 3.40

### 3.8.6 Axial vector-like correlator

Now, considering the timeslice sum of mesonic vector operator  $A_{\mu}$  as defined in eq. (3.53), which is built on a lattice site, and calculating out the correlation function to write explicitly the correlator  $C_{\mu\nu}$  in eq. (3.54) between two timeslices at  $x_0$  and  $y_0$ , one arrives at

$$\begin{aligned} C_{\mu\nu}(\Delta t) &= C_{\mu\nu}(x_0 - y_0) = \frac{1}{V_s} \sum_{\mathbf{x}, \mathbf{y}} \langle \text{Tr}_{sc} \{ \gamma_5 \gamma_{\mu} \Delta(x, x) \} \text{Tr}_{sc} \{ \gamma_5 \gamma_{\nu} \Delta(y, y) \} \rangle_U \\ &\quad - 2 \sum_{\mathbf{x}} \langle \text{Tr}_{sc} \{ \gamma_5 \gamma_{\mu} \Delta(x, y^s) \} \gamma_5 \gamma_{\nu} \Delta(y^s, x) \rangle_U \end{aligned} \quad (3.67)$$

where using the translation invariance on the lattice the  $y^s$  is the randomly fixed source on the the timeslice at  $y_0$ .

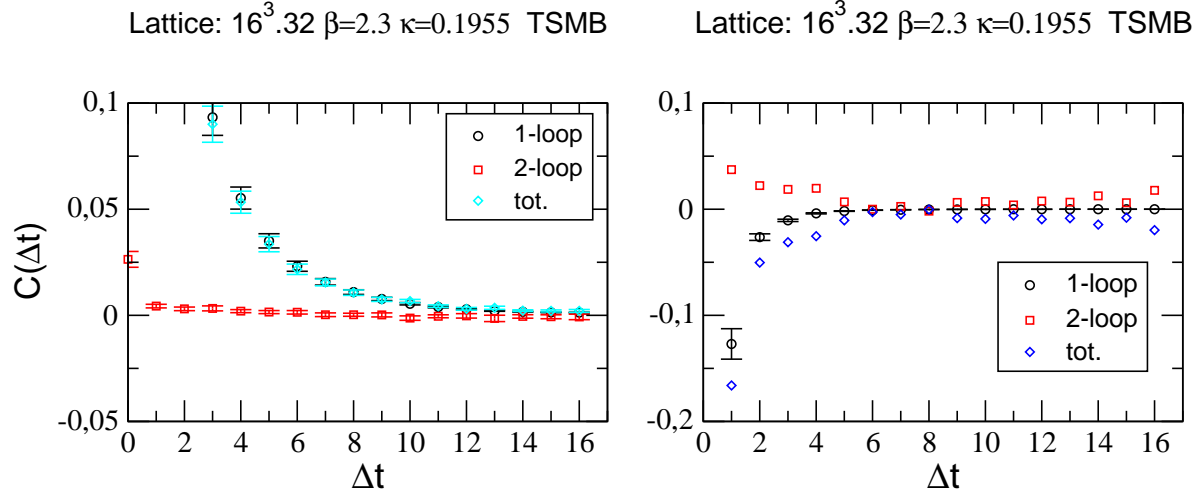


Figure 3.39: *Correlators of the non-local operators, left in negative parity channel and right in the positive parity channel*

Here, we observe also that the correlator consists of connected as well as disconnected pieces. But this seems exactly as the case of the mesonic scalar correlators, the all-to-all propagators needed here are exactly those used to calculate the mesonic disconnected correlator. One has only to add the gamma matrix elements when dealing with the mesonic axial vector correlator.

### 3.9 Spin-1 states from splitting point operator

It is now interesting to look for a splitting point M-L-M operator with a spin-1 content. To this end we insert vectorial Dirac Gamma matrices in (3.42)

$$O_\mu = \text{Tr}\{\bar{\lambda}(x)U_\mu^\dagger(x)\Gamma_\mu\lambda(x+a\hat{\mu})U_\mu(x)\} ; \quad \mu = 1, 2, 3 \quad (3.68)$$

where

$$\Gamma_\mu = \gamma_\mu, \quad \gamma_\mu\gamma_5.$$

We have now an operator which transforms as a three components pseudovector (vector) when  $\Gamma = \gamma_\mu, (\gamma_\mu\gamma_5)$ . Here the vector indices " $\mu$ " are the same for the Dirac

matrices as for the gauge links in the (3.68) operators. This means that one has three independent forms of  $O_\mu$  in each channel of parity, and the operator considered here transforms then in a three dimensional representation of the cubic group. One can see in appendix (C.1) that this is exactly the  $T_1$  irrep of  $O_h$ . The spin content of this operator with three polarisations is then a spin 1 in the continuum. The basis are shown in the following table,

Representation $\tilde{\mathcal{R}}$ of $O_h$	Spin-1 operator linear combinations
$T_1^{\pm+}$	$O_1^\pm$ , $O_2^\pm$ , $O_3^\pm$ .

The sign (+),(-) is for the pseudovector, vector respectively.

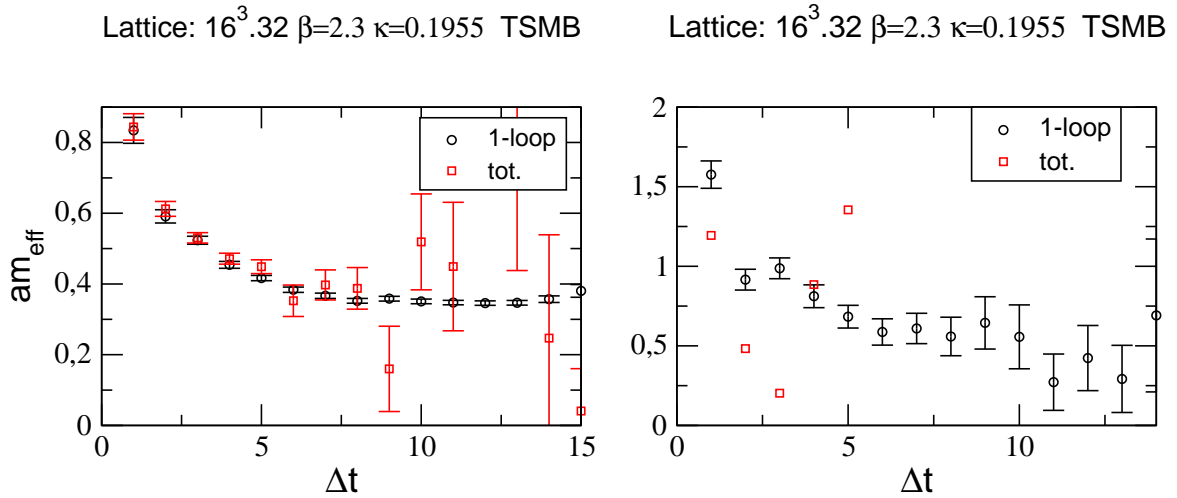


Figure 3.40: *Effective masses of the non-local operators, left in negative parity channel and right in the positive parity channel*

## 4 Numerical Analysis and Spectrum

### Results: TS-PHMC

This chapter is devoted to the second part of the analysis in this work. Thanks to the efforts undertaken by our collaborator I. Montvay from the DESY-Münster collaboration we are now able to accumulate relevant statistics for spectrum determination. This progress in algorithms and in available computer power on IBM Blue Gene L/P allows us to perform numerical simulations on lattices with large spatial extension, and hence the systematic errors are expected to be smaller.

We have observed from the integrated autocorrelation-times in the former chapter that for small gluino masses the TSMB algorithm produces few independent configurations in a long-time runs.

The new series of numerical simulations on larger lattices discussed in this chapter were carried out exploiting a new more efficient updating algorithm implementation by I. Montvay *et al.* introduced in Section 2.3.2 the Two-Step Polynomial Hybrid Monte Carlo (TS-PHMC) [23, 83]. This algorithm takes over some features of TSMB, is based on a two-step polynomial approximation [22] and it is very well suited for theories with odd number of flavors and small fermion mass. In preliminary tests, the algorithm has been extensively tested and optimized against other independent implementations which were at our disposal. Moreover, we perform comparison tests to check the functionality of the algorithm. The most important tests were to reproduce well determined quantities of previous TSMB simulations. We observed good agreement of the plaquette average values and the values of the Sommer scale parameter  $r_0/a$ .

Furthermore, the new algorithm supports an improved gauge action to reduce the lattice artifacts, and uses Stout-smearing in the Wilson fermion action. This will be advantageous for improving the signal-to-noise ratio of the glueball correlators and makes the analysis of the configurations in general 20% faster by reducing the fluctuation of the smallest eigenvalues.

In this chapter, we have performed analysis along the lines of the previous chapter. The global plan of this chapter is as follows: first we review the simulation setup and the ensembles produced in this study. Then, the results of the spectrum analysis are discussed. After that, we present results of the WI's analysis and the determination of the chiral limit. We conclude this chapter by giving a summary and discussion.



## 4.1 Simulation details

The main difference between TSMB and TS-PHMC is in the first updating step. In the former, sweeps of local updating are used to produce new gauge configurations, while in the latter, the first updating step is replaced by (Polynomial) Hybrid Monte Carlo trajectories; the rest of the scheme is the same as in TSMB. This new implementation of the TS-PHMC has motivated us to go towards larger lattices with the goal of simulating larger volumes. To control the  $\mathcal{O}(a)$  effects, renormalization gauge improved gauge action has been also implemented. We choose to apply the tree-level Symanzik (tlSym) improved gauge action defined in Section 2.2 for the gauge part for all TS-PHMC ensembles. Besides the usual plaquette term, the action includes the rectangular Wilson loop term. The weight for these two terms in the case of tlSym are

$$c_0 = 1 - 8c_1 \quad \text{and} \quad c_1 = -1/12. \quad (4.1)$$

At first, we choose the bare gauge coupling  $\beta = 1.6$  which results in coarse lattices comparing to the TSMB lattices. In the fermion part of the action we adopted, at first, the simple (unimproved) Wilson action with  $N_f = \frac{1}{2}$  flavor for a set of  $16^3 \cdot 32$  and  $24^3 \cdot 48$  lattices. Then, in order to improve the stability of the Monte Carlo evolution, especially at lighter gluino mass, we turn into simulations of  $24^3 \cdot 48$  lattices with Stout-smearing of links in the Dirac-Wilson fermion matrix. We apply the Stout-link procedure described in Ref. [31] for  $SU(3)$  and consider one step of isotropic smearing with stout parameter  $\rho = 0.15$  in all directions. The stout-link scheme is analytic, efficient, and produce smeared links that automatically are elements of the color gauge group without the need for projection back into  $SU(2)$ . Comparison of the plaquette average and the smallest eigenvalue average in the stout and their corresponding unstout runs is displayed in Fig. 4.7 The summary of the simulation points of all TS-PHMC ensembles is given in Table 4.1.

The stout smearing can also be applied during the measurements to interpolating operators involving gauge links. Here, the stout gauge links will only be used in the Dirac-Wilson operator. Therefore, the usage of smeared links is nothing else but a different discretization of the covariant derivative operator on the lattice.

**Tests.** Besides comparison tests to previous TSMB simulations, many other tests were performed to show the correctness of the new algorithm implementation before starting series of intensive productions. The simple test of the algorithm is to look at the value  $\Delta H$  and the expectation value  $\langle \exp(-\Delta H) \rangle$ , where  $\Delta H$  is the difference of the value of the Hamiltonian  $H$  at the beginning and at the end of a trajectory in the HMC evolution (see Section 2.3.2). This expectation value should always be 1, which indicates that each integration step is area preserving. This condition was satisfied for all our runs. Moreover, a good test for the exactness of the algorithm in generating the correct distribution is to check whether there is any dependence of any observable on

the integration step-size  $\delta\tau$ . A good observable to this purpose is the plaquette average because it can be measured with high accuracy. Tests on small lattices revealed that the plaquette average is consistently independent on  $\delta\tau$ .

As a further test, we measured the reversibility violations in the Sexton-Weingarten integrator. This is a necessary condition for the correctness of the algorithm. We measured the reversibility violations through  $\delta H = \Delta H_1 - \Delta H_2$ , where  $\delta H$  is defined as the difference between the Hamiltonian of the starting configuration and the one obtained from evolution of the system forward with  $\delta\tau$  for one full trajectory and then back (flipping the momenta  $\pi$ ) with  $(-\delta\tau)$  to the original position in phase space. We also use other quantities like gauge and gluino forces and compare the gauge links.

In an explicit check of reversibility, we compute the trajectory once, change the sign of all momentum variables, and then compute back a new trajectory with the same length and step-size. The resulting configuration should be identical with the starting configuration  $U$ , apart from unavoidable roundoff errors with a magnitude comparable to the machine precision. A measure for the error is the positive quantity

$$r = \frac{1}{4N_c^2 V} \sum_{\mu x ij} |[\tilde{U}_\mu(x)]_{ij} - [U_\mu(x)]_{ij}|, \quad (4.2)$$

where  $\tilde{U}$  is the endpoint configuration,  $N_c$  is the number of colors and  $(ij)$  are fundamental color indices and  $V$  is the space-time volume. Obviously, this observable is a more direct measure than typical observables only involving a subset of all degrees of freedom. With several initial configurations and parameters  $\tau$  and  $\delta\tau$  used in our study, we could see that this error measure is of the order  $10^{-16}$  on a PC-AMD with 64 bit arithmetics. Moreover, the absolute value of  $\delta H$  on this machine is of the order  $10^{-14}$ . We observe then no possibility of reversibility violations which can arise. This indicates indeed that the trajectory computation is indeed correct apart from roundoff errors.

To measure observables with fermionic content such as adjoint mesons and gluino-gluonballs we need to invert the fermion matrix. The Conjugate Gradient (CG) is used to invert the preconditioned hermitian fermion matrix  $\tilde{\tilde{Q}}$ . The residuum for CG stopping criterion was set to  $10^{-12}$  for all runs. The number of CG iterations varied from 470 to 20500 for  $\kappa = 0.18$  and  $\kappa = 0.202$  respectively. For the calculation of the extremal eigenvalues (minimal and maximal) and the correction factor we used the Kalkreuter-Simma algorithm [84].

### 4.1.1 Simulation parameters

In the TS-PHMC simulations on  $16^3 \cdot 32$  and  $24^3 \cdot 48$  lattices, the parameters were tuned to obtain better performance. The runs were performed at single lattice spacing corresponding to  $\beta = 1.6$ . This value of the gauge coupling is expected to be associated to a larger lattice spacing compared to the one previously considered at  $\beta = 2.3$  with the

Wilson gauge action. We notice that in TSMB runs, we simulated lattices at  $\beta = 2.3$ , which from quenched simulation is believed to be in the scaling region. In the simulation the periodic boundary conditions are chosen for gluons and gluinos in the spatial directions. On the time directions, periodic conditions are used for gluons and anti-periodic conditions for gluinos. Moreover, for all runs we used even-odd preconditioning of the fermion matrix and determinant break-up  $n_B = 2$ .

The simulation parameters of all TS-PHMC runs are reported in Table 4.1 and extended in Table 4.2. We explain the meaning of various notation used in Table 4.1; column 4 indicates the total number of the saved configurations. A configuration is saved after the noisy correction (NC) step.  $\tau$  (column 5) is total length of the sequence of PHMC trajectories between noisy correction step.  $A_{NC}$  (column 6) is the total acceptance rate in the noisy correction step.  $A_{PHMC}$  (column 7) is the total acceptance rate of the PHMC trajectories (first step).  $N_{traj}$  is the number of trajectories between two NC steps.  $N_\lambda$  and  $N_g$  (column 8 and 9) are the number of steps in the integration scheme along a PHMC trajectory for gluino and gluons respectively. As we use the Sexton-Weingarten integration scheme with multiple scale, the gluino step-size and the gluon step-size are

$$\delta_\lambda = \frac{\tau}{N_\lambda} \quad \text{and} \quad \delta_{\tau_g} = \frac{\tau}{N_\lambda N_g}, \quad (4.3)$$

respectively.

The values of the polynomial approximation interval  $[\epsilon, \lambda]$ , the polynomial orders and the values of the deviation norm  $\delta$ , which is minimized for a given polynomial order  $n$  using the least-square approximation scheme (see eq. (2.39)), are collected in Table 4.2.

A full trajectory of length  $\tau$  consists of a sequence of  $N_g$  individual trajectories, each prepared with  $P_{n_1}^{(1)}$ . A metropolis accept-reject test is performed after each individual trajectory integration. At the end of sequence of 2 – 4 individual trajectories, the second step is carried out by the stochastic correction with high precision polynomial  $P_{n_2}^{(2)}$ . Because the PHMC step-size  $\delta\tau$  is finite, discretization errors are introduced. Small step-size is used so that the errors are negligible when compared to statistical errors. In all case, a total trajectory length (0.9 – 1.5) and small enough step-sizes  $\delta\tau$  were required to obtain high total acceptance rate  $A_{PHMC}$  of the PHMC trajectories, which was between 85% – 99%. Moreover, the order of the first polynomial  $n_1$  is chosen as low as possible while maintaining its precision  $\delta$  of the order  $\mathcal{O}(10^{-4})$  for all runs. The second polynomial  $P_{n_2}^{(2)}$  used in the NC step is higher precision polynomial and its order is tuned such that its precision is about  $\delta \sim \mathcal{O}(10^{-7})$ . These tunings are necessary to ensure higher acceptance rate in the noisy correction step  $A_{NC}$  (82% – 97%). This resulted in high total acceptance of magnitude 67% – 96%. Furthermore, the optimization of the TS-PHMC parameters turned out to have a substantial impact on the integrated autocorrelation-times of the plaquette average (Table 4.3).

Table 4.1: *TS-PHMC runs algorithmic parameters with tlSym at  $\beta = 1.6$ . Runs labelled with subscript  $s$  have been performed with Stout-links. The notation is explained in the text. .*

Run	$L^3.T$	$\kappa$	$N_{conf}$	$\tau$	$A_{NC}$ %	$A_{PHMC}$ %	$N_{traj}$	$N_\lambda$	$N_g$
$A$	$16^3.32$	0.1800	2500	1.05	95.6	85.0	3	3	10
$B$	$16^3.32$	0.1900	2700	1.05	96.4	88.7	3	3-5	10
$Ca$	$16^3.32$	0.2000	1973	0.99	82.9	90.6	2-3	3-5	10
$Cb$	$16^3.32$	0.2000	8874	0.99	88.3	98.2	2-3	4-6	8-10
$D$	$16^3.32$	0.2020	6947	0.56	88.5	99.2	2-4	8	3-7
$\bar{A}$	$24^3.48$	0.1980	1480	0.9	89.6	87.7	2	6	8
$\bar{B}$	$24^3.48$	0.1990	1400	0.9	88.7	85.8	2	6	8
$\bar{C}$	$24^3.48$	0.2000	6465	1.0	88.6	89.1	2	6	8
$A_s$	$24^3.48$	0.1500	370	1.0	97.3	97.4	2	6	8
$B_s$	$24^3.48$	0.1550	1730	1.0	95.6	96.6	2	6	8
$C_s$	$24^3.48$	0.1570	2110	1.0	92.4	94.1	2	5	8
$D_s$	$24^3.48$	0.1575	2260	1.0	86.0	92.8	2	5	8

### 4.1.2 Smallest eigenvalues

Going to light gluino masses in SYM is a great challenge for computations because the actual algorithms have a substantial slowing down towards small gluino masses. The behavior of the smallest eigenvalue of  $\tilde{Q}^2$  matrix can help us to have an idea on the computational cost of the simulation. As we mentioned in the TSMB analysis, the smallest eigenvalue  $\lambda_{min}$  has to be studied numerically during the updating process. In the TS-PHMC this is also necessary for controlling the goodness of the polynomial approximation. At the beginning of the update, the numerical values of the smallest eigenvalue of a produced configuration help to fix the lower/upper bound  $[\epsilon, \lambda]$  of the polynomial approximation, and hence the polynomial orders which are related to the condition number  $c = \lambda_{max}/\lambda_{min}$ . For the thermalized configurations, the fluctuation of the largest eigenvalue  $\lambda_{max}$  is relatively weak so that fixing the upper bound  $\lambda$  does not present any problem for the polynomial approximation. The smallest eigenvalue fluctuates, however, very strongly as it is shown in Fig. 4.2 for the run ( $Cb$ ). Therefore, the condition number inherits the behavior of the smallest eigenvalue which dominates its behavior. In Fig. 4.2 the influence of the smallest eigenvalue fluctuation is clear on the fluctuation of the condition number, and the impact of the largest eigenvalue, which has very small fluctuation, is almost negligible.

The finite size effects on the smallest eigenvalue are shown in Fig. 4.3. At larger lat-

Table 4.2: *Algorithmic parameters for the simulations of TS-PHMC ensembles. The determinant-breakup is  $n_b = 2$ . The  $n_i$  are the polynomial orders,  $\epsilon$  and  $\lambda$  are the lower and upper bound, respectively, for the polynomial approximation,  $\delta_i$  are the deviation norms.*

Run	$\epsilon$	$\lambda$	$n_1$	$\bar{n}_1$	$n_2$	$\bar{n}_2$	$\delta_1$	$\bar{\delta}_1$	$\delta_2$	$\bar{\delta}_2$
$A$	$4.25 \cdot 10^{-3}$	3.4	50	80	100	140	1.2e-04	3.4e-08	7.2e-07	3.4e-09
$B$	$9.5 \cdot 10^{-4}$	3.8	80	130	300	360	1.9e-04	7.5e-08	2.1e-08	5.8e-10
$Ca$	$5.0 \cdot 10^{-5}$	4.0	180	270	700	820	2.8e-04	4.2e-07	6.3e-07	6.3e-08
$Cb$	$5.0 \cdot 10^{-5}$	4.0	200	300	700	820	2.2e-04	3.2e-07	6.1e-07	6.1e-08
$D$	$1.0 \cdot 10^{-6}$	4.0	800	1000	2700	3000	9.4e-05	8.8e-07	9.6e-07	2.5e-07
$\bar{A}$	$1.0 \cdot 10^{-4}$	4.0	200	270	600	700	1.3e-04	6.6e-07	2.6e-07	2.1e-08
$\bar{B}$	$4.0 \cdot 10^{-5}$	4.0	270	370	800	920	1.25e-04	5.4e-07	4.5e-07	5.1e-08
$\bar{C}$	$2.0 \cdot 10^{-5}$	4.0	350	500	1000	1150	1.1e-04	2.8e-07	5.95e-07	7.6e-08
$A_s$	$5.5 \cdot 10^{-5}$	2.2	200	270	600	700	1.3e-04	6.6e-07	2.6e-07	2.1e-08
$B_s$	$5.5 \cdot 10^{-5}$	2.2	200	270	600	700	1.3e-04	6.6e-07	2.6e-07	2.1e-08
$C_s$	$5.5 \cdot 10^{-6}$	2.2	400	550	1200	1350	1.3e-04	5.2e-07	9.2e-07	1.6e-07
$D_s$	$1.1 \cdot 10^{-6}$	2.2	600	800	2200	2500	1.2e-04	6.5e-07	8.6e-07	1.8e-07

tice volume one observe a small displacement of the center of the distribution to smaller value. The order of the first polynomial  $n_1$  increases then for larger lattice since the lower bound for the polynomial approximation becomes smaller than the one used for the  $16^3 \cdot 32$  lattice ( $Cb$ ) as reported in Table 4.2. However, from the computational costs point of view, the autocorrelation time has to be taken into account (here we use the plaquette observable). On the  $16^3 \cdot 32$  lattice ( $Cb$ ) is a factor two greater than on the  $24^3 \cdot 48$  lattice ( $\bar{C}$ ) (see Table 4.3). For a reliable estimation of the cost for producing one independent configuration, where independent means with respect to the quantity in question (plaquette, pion mass, ...), one has to take into account the measured autocorrelation times. In lattice QCD, some parametrized formulas for estimating the costs are proposed [68]. For the case of SYM with one flavor, one can perform independent study to find such formula. This study is beyond the scope of the present work.

Returning to the smallest eigenvalue distribution. The histograms at selected values of  $\kappa$  that describe the distributions are displayed in Fig. 4.3, Fig. 4.4 and Fig. 4.5. The spectrum of square hermitian fermion matrix has a clear gap, which becomes smaller as we simulate towards lighter gluino mass. The value of the average of the smallest eigenvalue does not reflect a smooth behavior of the simulations at the  $\kappa$  values considered here. In Fig. 4.6 (lower panel), the value of  $\langle \lambda_{min} \rangle$  decreases rapidly by about a factor  $10^{-1}$  towards smaller gluino (adjoint pion) mass (see also the values in Table 4.3). More-

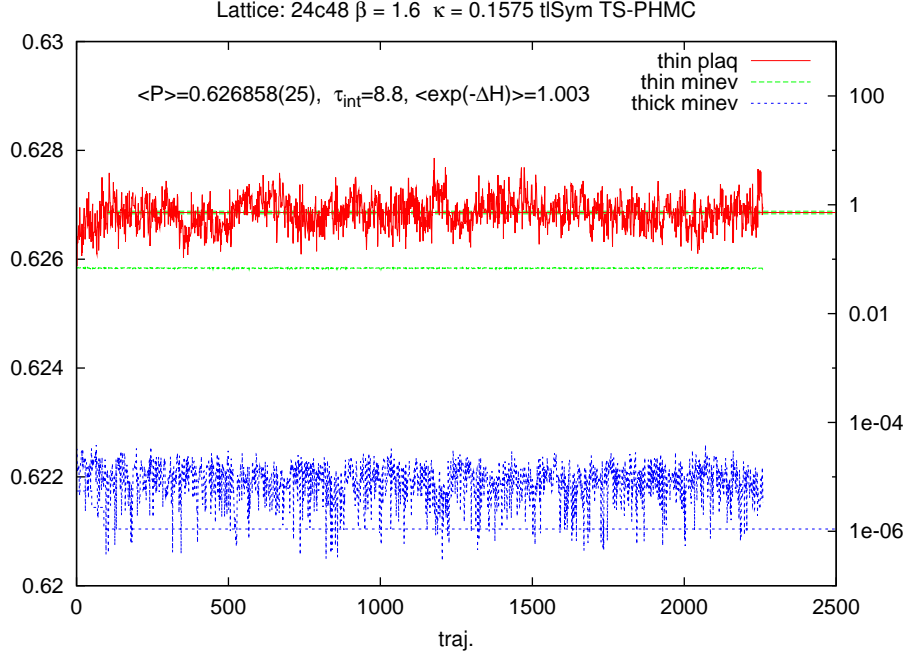


Figure 4.1: Run history of the ensemble  $D_s$  where stout (thick) and unstout (thin) smallest eigenvalue are shown.

over, at lighter gluino mass the smallest eigenvalue distribution becomes less compact than at heavier gluino mass. This is suggested by the behavior of the distribution width<sup>1</sup>. For example and for comparison, the width of the smallest eigenvalue distribution for the runs ( $Cb$ ) and ( $\bar{C}$ ) are 0.821 and 0.873 respectively. The distribution width in the run ( $\bar{C}$ ) is slightly larger because of the larger volume in this run than the one in the run ( $Cb$ ). The distribution width at lighter mass as in the run ( $D$ ) is wider and has the value 0.984. For the run ( $D_s$ ) a similar value  $w = 0.971$  is found. We note here that the runs ( $D$ ) and ( $D_s$ ) are expected to be simulated at closed values of gluino mass or  $r_0 m_\pi$  value. We also show the distribution of the *unstout* smallest eigenvalue of the run ( $D_s$ ) in Fig. 4.4 (left panel). The distribution has a width value  $w = 0.08$  and hence the distribution is compact, and one would see a narrow distribution peak when both stout/unstout distribution were plotted at the same scale.

### 4.1.3 Autocorrelation-time

The integrated autocorrelation time for time plaquette and smallest eigenvalue during the TS-PHMC runs is computed in units of Monte Carlo time following the windowing

<sup>1</sup>Instead of using the standard deviation  $\sigma$ , we defined the distribution width through  $w = \frac{u-v}{u}$ , where  $u$  is the maximum value in the data and  $v$  is the minimal value in the interval  $[\epsilon, \lambda]$ .

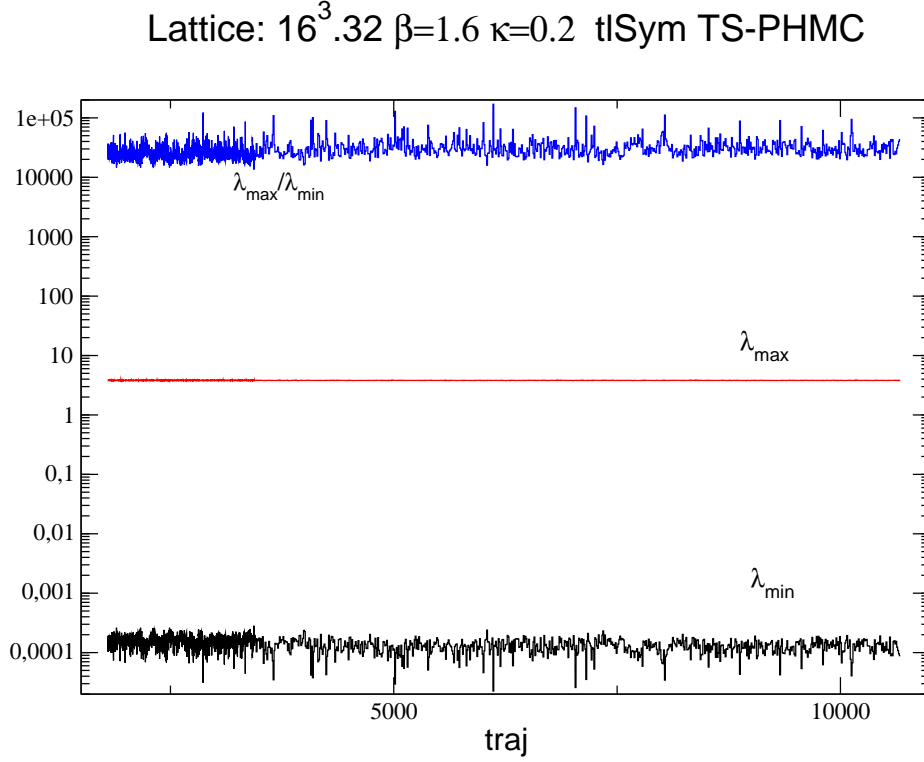


Figure 4.2: *History of the smallest/largest eigenvalue and the condition number for the run ( $C_b$ ) TS-PHMC.*

method of U. Wolff [44, 85]. The plaquette average and the smallest eigenvalue average and their integrated autocorrelation times are reported in Table 4.3 and Table 4.4 for unstout and stout runs respectively. The increase of the integrated autocorrelation time is clearly visible as we move to lighter gluino masses. However, the autocorrelation time is short compared to the total length of the simulation runs, which guarantees that we have sufficiently high statistics for the purpose of spectrum analysis. In most runs, the binned configurations result in independent ensembles, with respect to quantity in question, and therefore the statistical error can correctly be estimated from the variance of the ensembles. It is worthwhile to emphasize that the TS-PHMC simulations show that the autocorrelation time depends on the trajectory length and the TS-PHMC parameters. Our runs are all performed with trajectories of length  $\sim 1$  except the run ( $D$ ) where we used shorter trajectory length  $\tau = 0.56$ . We note here that one expects a greater autocorrelation as we approach the continuum limit since the lattice spacing becomes small. This issues need to be checked in the future simulation at greater value of the bare gauge coupling.

The imperfection of the polynomial approximation at very small gluino mass has to be corrected by the reweighting step. In most runs this correction is totally negligible



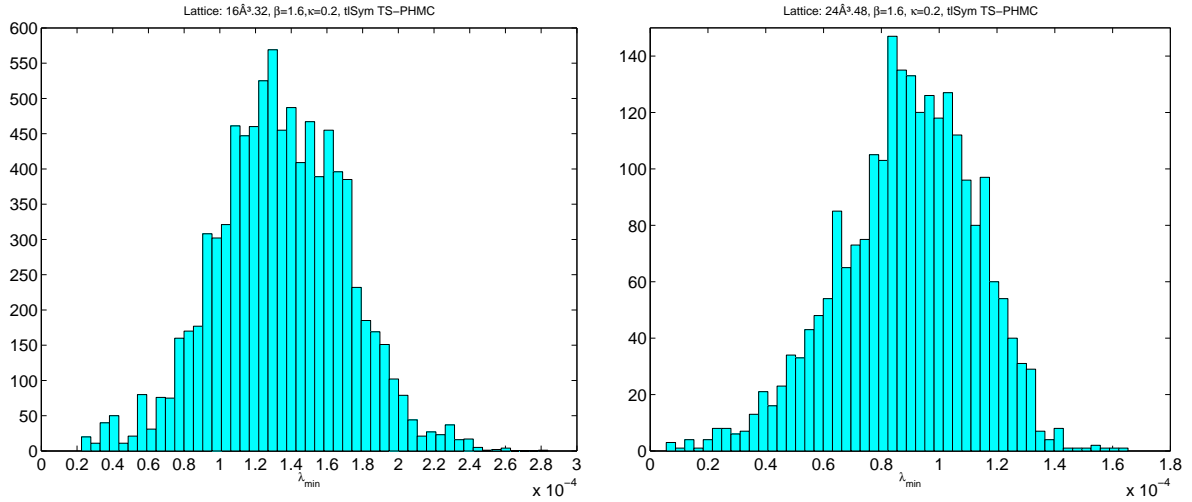


Figure 4.3: *Finite size effect on the smallest eigenvalue distribution at  $\kappa = 0.2$ .*

but even in these cases we have computed reweighting on small samples to check the correctness of the polynomial approximation. However, in runs ( $D$ ) and ( $D_s$ ) the effect of the reweighting factors was important in order to remove the *exceptional configurations* from statistical averages. The effect of exceptional configuration on the autocorrelations is negligible for gluonic quantities such as plaquette,  $r_0/a, \dots$ , however, the effect is important for the fermionic quantities like the adjoint meson mass, gluino-gluon mass (see below).

## 4.2 Confinement and physical scale

In analogy to lattice QCD, the study of the static potential  $V(r)$  helps to check a non-perturbative features of low energy SYM as confinement. In addition, the static potential can be used to extract quantities like the Sommer scale parameter and the string tension, which are relevant for setting the physical scale.

### 4.2.1 Static potential

As we have mentioned in the previous chapter for the TSMB analysis, the analogy with QCD suggests that the theory presents confinement with color singlet particle states. Confinement can be studied by computing the static quark potential  $V(r)$  as a function of the spatial separation  $r$  between sources in the fundamental representation of the gauge group.

The basic quantities which have to be computed to determine the static potential are the Wilson loops. The static potential  $V(r)$  in Fig. 4.8 was extracted from the single-



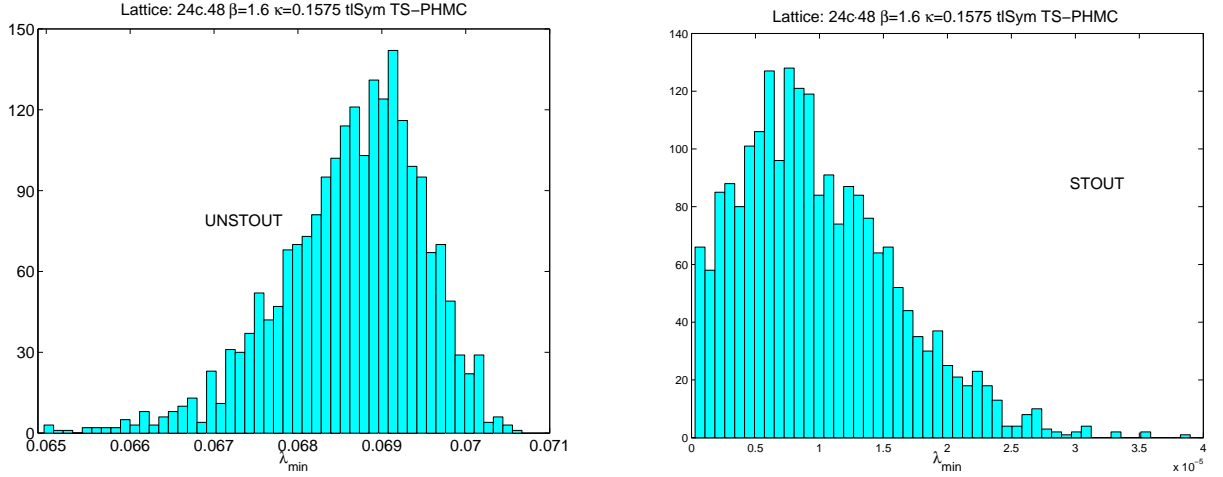


Figure 4.4: *Smallest eigenvalue distribution for the stout run  $D_s$  (right panel) compared to its unstout counterpart.*

exponential fit as described in [13] (details are presented in Section 2.12). We applied APE smearing ( $\epsilon_{APE} = 0.5, N_{APE} = 4$ ) for Wilson loops to improve the signal and to reduce the contamination from excited states.

Fig. 4.8 shows the behavior of the static potential as function of the spatial distance  $r$  as we go towards lighter gluino mass. The data of the static potential are well fitted by the usual formula of  $V(r)$  in eq. (2.128) (i.e. linear term + Coulombian term + correction). The lower curve in Fig. 4.8 corresponds to the lighter gluino mass at  $\kappa = 0.202$  simulated in our ensembles. This curve does not show a plateau at high separation  $r$  which could be interpreted as screening. Therefore, this support that our sample have been simulated in the confining phase of the theory. We note here that we measured also the Polyakov loops which vanish hence confirming that we are in the confining phase.

### 4.2.2 Physical scale

The physical scale is set by the value of the Sommer scale parameter  $r_0/a$ . The latter is determined by two independent methods: using the force method based on the Creutz-ratios and by fitting  $V(r)$  data directly (see Section 2.12). We have used both methods to check our estimations of  $r_0/a$  which is an important quantity to be determined. We find agreement in the estimations of  $r_0/a$  from force method and potential method; e.g. at  $\kappa = 0.2$  the direct fit of the  $V(r)$  data gives  $r_0/a = 4.206(35)$  and from the force method the obtained value is  $r_0/a = 4.242(87)$ . Once  $r_0/a$  is known one can transform any dimensionful quantity, for instance the bound state masses, from lattice to physical

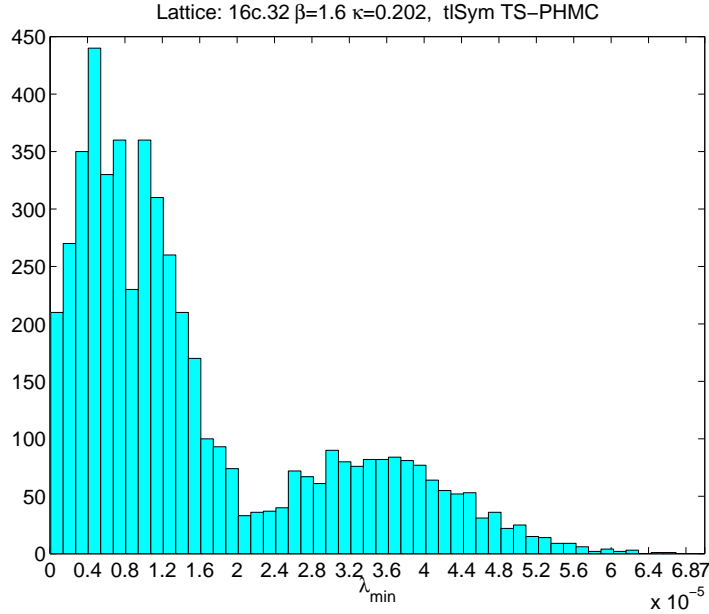


Figure 4.5: *Distribution of smallest eigenvalue for the run D (TS-PHMC).*

units. Therefore a careful determination of  $r_0/a$  is important. In addition one can use dimensionless mass definition  $r_0 m_{bound}$  to compare results obtained at different value of lattice spacing (TSMB/TS-PHMC) and different actions (stout/unsout). The results of measured  $r_0/a$  from the force method are summarized in Table 4.5 and Table 4.6 for unstout and stout runs respectively. As it is expected, the value of  $r_0/a$  increases for higher  $\kappa$ ; consistently with massless scheme the value of  $r_0/a$  should be extrapolated to the critical value  $\kappa = \kappa_{cr}$  where the gluino mass vanishes. Alternatively, the value of  $r_0/a$  at highest  $\kappa$  can be taken for fixing the physical scale. The dependence of  $r_0/a$  on the quark mass has been observed in lattice QCD simulations including dynamical quarks. However, how much of this dependence is a scaling violation has remained an intriguing question [86].

The effect of the correction factors is completely negligible for  $r_0/a$  in the runs  $D$  and  $D_s$  where several smallest eigenvalue were outside the approximation interval  $[\epsilon, \lambda]$ . This is not the case for the low lying bound state masses as we will see later on the spectrum determination. In all other runs the correction factor is equal 1 on every configuration.

Instead of taking the value of  $r_0/a$  at the highest  $\kappa$  we have extrapolated the value of  $r_0/a$  to the chiral limit as shown in Fig. 4.9 for all runs. The extrapolated values of  $r_0/a$  are 5.235, 4.923 and 5.6663 for  $16^3 \cdot 32$  lattices,  $24^3 \cdot 48$  lattices (unstout) and  $24^3 \cdot 48$  lattices (stout). In the unstout runs the extrapolation to the chiral limit is performed as function of the inverse hopping parameter  $1/\kappa$ , where the chiral limit is indicated by the value of  $1/\kappa_{cr}$ . The value of the critical hopping parameter was obtained by OZI

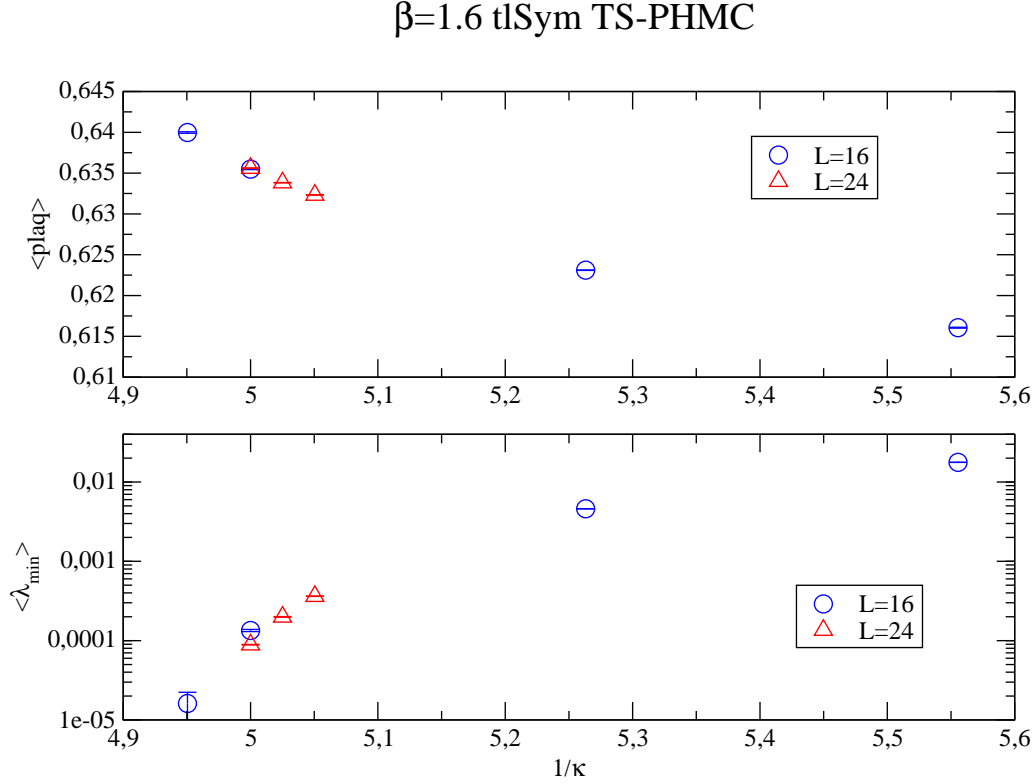


Figure 4.6: *Plaquette average and smallest eigenvalue average for all unstout runs.*

arguments (see Section 4.6). A small finite size effect can be observed on the value of  $r_0/a$  at  $\kappa = 0.2$  on  $16^3 \cdot 32$  and  $24^3 \cdot 48$  lattices. An approximately 6% difference can be observed for the extrapolated values of  $r_0/a$ . We hesitate to interpret this difference as a finite size effects, since for the small lattice only two points can be used for the extrapolation. The last point corresponding to the lightest gluino at which the  $r_0/a$  was determined was  $\kappa = 0.202$  on  $16^3 \cdot 32$  lattice. Moreover, we did not simulate this point on the  $24^3 \cdot 48$  lattice to draw a conclusive decision about which extrapolated value should be used to invert to physical units. As the value of the  $r_0/a$  at  $\kappa = 0.202$  is greater than the extrapolated value from the  $24^3 \cdot 48$  lattices (Fig. 4.9, upper panel) we assume that missing points at lighter gluino on  $24^3 \cdot 48$  lattice could deviate the extrapolation to a greater value of  $r_0/a$  expected to agree with the extrapolated value from  $16^3 \cdot 32$  lattices. In conclusion we adopt the value  $r_0/a = 5.235$ , which is obtained by extrapolation from 16 lattices, to be used in the conversion to dimensionless quantities.

In the stout runs three points are used to extrapolate  $r_0/a$ , the latter is which are plotted as function of the adjoint pion mass square in Fig. 4.9. The chiral limit corresponds to vanishing pion mass. The extrapolated value is  $r_0/a = 5.6663$  which is  $\sim 8\%$  greater than the value obtained in the unstout runs. In QCD, one observes similar values of

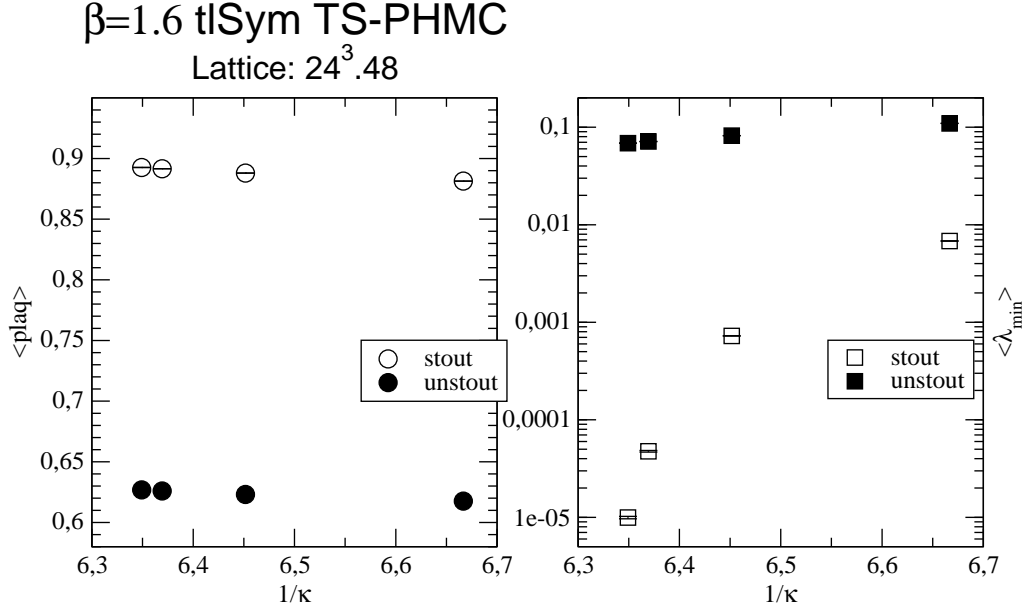


Figure 4.7: Comparison of plaquette average and smallest eigenvalue average of stout runs with their unstout counterpart (TS-PHMC).

$r_0/a$  from stout and unstout actions simulated at fixed  $\beta$  [24]. The analogy should not be pushed too far. SYM and QCD are, after all, two different theories. The effect on  $r_0/a$  from the stout links is a model related property. This issue has to be investigated in more detail in the future.

We use the QCD value of the Sommer scale parameter  $r_0 = 0.5 \text{ fm}$ . The lattice spacings are  $a \approx 0.096 \text{ fm}$  [ $a^{-1} \approx 2.1 \text{ GeV}$ ] and  $a \approx 0.088 \text{ fm}$  [ $a^{-1} \approx 2.27 \text{ GeV}$ ] for unstout and stout runs respectively. Therefore, for the unstout action the physical volume of the simulated boxes are  $L^3 \simeq (1.54 \text{ fm})^3$  on  $16^3 \cdot 32$  lattices and  $L^3 \simeq (2.3 \text{ fm})^3$  on  $24^3 \cdot 48$  lattices. The simulated box-size with stout fermion action is  $L^3 \simeq (2.11 \text{ fm})^3$ .

An indication of the lightness of the gluino is given by the adjoint pion mass,  $m_{a-\pi}$ , extracted from the connected part of correlator of the pseudoscalar gluino bilinear. The lightest simulated adjoint pion mass (run *D*) corresponds to  $m_{a-\pi} \sim 464(25) \text{ MeV}$  in QCD units using the extrapolated value of  $r_0/a$ .

These coarse lattices have sufficiently large volume so that the bound states of the theory can fit into, and hence are appropriate to study the mass spectrum of the theory. This is also large enough to keep finite volume effects under control. Remember in the TSMB samples discussed in the previous chapter that the lattices were quite fine,  $a \approx 0.08$ , but in a small volume,  $L^3 \simeq (1 \text{ fm})^3$ .

Table 4.3: *Plaquette average, smallest eigenvalue average and their integrated autocorrelation-times for TS-PHMC runs. For runs with subscript  $s$  the original (Unstout) values are given. (...)† During the updating process and after about 3000 PHMC trajectories the lower bound of the interval approximation was decreased which resulted in higher polynomial degree and a strong drop down of the smallest eigenvalue  $\lambda_{min}$ , hence this value could be underestimated due to this fact (see also Fig. 4.5)*

Run	$\langle P \rangle$	$\tau_P$	$\langle \lambda_{min} \rangle$	$\tau_{min}$
$A$	0.616060(54)	7.5	0.017699(17)	0.9
$B$	0.623105(32)	3.1	0.0045948(10)	1.5
$Cb$	0.635487(53)	31.9	1.342(41)e-04	58.4
$D$	0.639976(89)	48.2	1.61(62)e-05	361†
$\bar{A}$	0.632319(28)	6.1	3.631(20)e-04	0.8
$\bar{B}$	0.633827(23)	4.3	1.990(17)e-04	1.0
$\bar{C}$	0.635610(33)	15.0	8.883(71)e-05	1.1
$A_s$	0.617613(25)	0.9	0.109432(72)	0.6
$B_s$	0.623036(20)	4.6	0.081974(26)	0.6
$C_s$	0.625970(24)	7.2	0.071349(23)	0.8
$D_s$	0.626858(25)	8.8	0.068639(26)	1.0

### 4.3 Tuning the simulations towards massless gluino

In this section we present the strategy of our tuning of the simulation parameters to a region of sufficiently light (soft breaking) dynamical gluino. The strategy we adopt is to gradually increase the hopping parameter  $\kappa$  in the Wilson action while monitoring the adjoint pion mass. The bare gauge coupling  $\beta = 1.6$  is kept fixed, the physical volume corresponding to  $L \sim (1.5 - 2)$  fm, the simulation is pushed towards lighter and lighter gluinos.

The importance of the determination of the adjoint pion  $a\text{-}\pi$  has been pointed out in the previous chapter. The  $a\text{-}\pi$  is not a physical state in SYM since this theory has only one flavor type. Nevertheless, it is an alternative quantity used to localize the chiral limit, where in analogy to QCD  $a\text{-}\pi$  is expected to have vanishing mass. In lattice simulation, the  $a\text{-}\pi$  has very good signal-to-noise ratio, and hence its mass can be obtained with high accuracy. Furthermore, this state, built up from fermionic degrees of freedom, is associated to relatively low computing costs in the numerical simulations. All these properties make the  $a\text{-}\pi$  as one of the most promising quantities in SYM simulations. In the practice, the tuning of the hopping parameter is based on observing the adjoint

Table 4.4: *Plaquette average, smallest eigenvalue average and their integrated autocorrelation times for TS-PHMC runs with Stout-smearing.*

Run	$\langle P \rangle$	$\tau_P$	$\langle \lambda_{min} \rangle$	$\tau_{min}$
$A_s$	0.881373(44)	3.5	6.810(37)e-03	1.0
$B_s$	0.887983(27)	8.0	7.252(43)e-04	1.1
$C_s$	0.891546(31)	11.5	4.756(93)e-05	2.1
$D_s$	0.892600(31)	14.1	9.95(29)e-06	2.5

Table 4.5: *Measured Sommer scale parameter  $\frac{r_0}{a}$  for runs at lighter gluino mass. (Unstout)*

Run	$N_{conf}$	$r_0/a$
$Cb$	400-10669	4.242(87)
$D$	1700-6859	5.04(26)
$\bar{A}$	100-1479	3.885(63)
$\bar{B}$	200-1399	4.16(12)
$\bar{C}$	4100-6464	4.33(19)

pion mass.

Our starting point of these series of TS-PHMC simulations in this study was the run (A) on  $16^3 \cdot 32$  lattice at  $\kappa = 0.18$ . The estimated pion mass in lattice units was  $am_\pi = 1.3$  which turns to be  $\sim 2.7$  GeV in physical unit. At this point the simulated pion is too heavy and this value indicates us to simulate larger hopping parameter to go towards lighter gluino mass. Our next run was the run (B) at  $\kappa = 0.19$  corresponding to pion mass  $am_\pi = 1.0$ , in physical unit  $m_\pi \sim 2.1$  GeV. At this stage we started to find a rough estimate of the  $\kappa_{cr}$ , this is crucial to decide the next point to be simulated. From OZI extrapolation, we used the two pion masses at  $\kappa = 0.18$  and  $\kappa = 0.19$  to extrapolate to vanishing pion mass. The value of the critical hopping parameter found was  $\kappa_{cr} \sim 0.2063$ , hence the next simulated points were chosen to be  $\kappa = 0.2$  and  $\kappa = 0.202$  which are the relevant simulated points in this series on  $16^3 \cdot 32$  lattices. These point are thought to lye in the region of lighter gluino mass. Extensive runs were started at these points to collect high statistics for mass spectrum calculations; e.g. the longest run was the run (Cb) with 8870 configurations. The lightest pion mass corresponds to the run (D) where the estimated pion mass was  $am_\pi = 0.221(12)$  in lattice unit which is converted to  $m_\pi \sim 440$  MeV in physical unit using the value of  $r_0/a$

Table 4.6: Measured Sommer scale parameter  $\frac{r_0}{a}$  for runs at lighter gluino mass. (Stout)

run	$N_{conf}$	$r_0/a$
$B_s$	200-1729	4.324(39)
$C_s$	100-1919	5.165(88)
$D_s$	100-2259	5.561(99)

measured on the ensemble ( $D$ ). The true critical value of the hopping parameter could lie near the last simulated  $\kappa = 0.202$  since as we have changed the hopping parameter by about 1% the pion mass has decreased by about  $> 50\%$ , and hence a tuning of the fourth decimal digit of  $\kappa$  could give vanishing pion mass. Therefore, from the run ( $D$ ) the chiral limit is approached. To check this, we perform an OZI extrapolation to find the estimated critical hopping parameter value. Note that the OZI formula is valid for light gluino mass. Since the estimated critical value of  $\kappa$  from ( $A$ ) and ( $B$ ) is still greater than the true value, one should discard those points at heavy gluino masses from OZI extrapolation.

The values of extrapolated  $\kappa_{cr}$  are summarized in Table 4.7. The first column indicates the points taken into account for the linear fit. The value from the first two runs has been used as a guide which gives us an idea on the next points closer to the chiral limit to be simulated, here runs ( $C$ ) and ( $D$ ). The value of  $\kappa_{cr}$  obtained from using two points ( $C$ ) and ( $D$ ) (this is the minimal number of points required to perform the fit) is  $\kappa = 0.2025$ . However, the most probable value of  $\kappa_{cr}$  is the one obtained from fitting the data of ( $B$ ), ( $C$ ) and ( $D$ ) which include the run ( $B$ ) to balance the linear fit with three points.

In addition, one can use the pion masses determined on the  $24^3 \cdot 48$  runs to obtain a reliable estimate of  $\kappa_{cr}$ , being well aware of the limitations of the use of the OZI arguments. The three simulated points on  $24^3 \cdot 48$  lattices are close to each other and assumed to be in the region of light gluino. Nevertheless, the last estimate in Table 4.7 also includes the point ( $D$ ) to the previous three points which increases the number of data for the linear fit at lighter gluino mass. The value of the hopping parameter from these data is  $\kappa_{cr}(\beta = 1.6) = 0.2029$  which we will take as the most reliable estimate of  $\kappa_{cr}$  of our present simulations. What remains is to tune  $\beta$  to larger values and go sufficiently close to the continuum limit while still using improved actions to reduce the  $\mathcal{O}(a)$  effects in the gauge sector. Numerical Simulations at extremely light gluino masses in SYM is necessary since there is no chiral perturbation theory ( $\chi PT$ ) valid for SYM which might be used to extrapolate results to smaller gluino mass.

We want here also to recall that technically we perform the simulations in two main steps as it is the usual case in lattice gauge theory. The two steps are: the *updating* step

Lattice:  $16^3 \cdot 32$   $\beta=1.6$  PHMC-tlsym

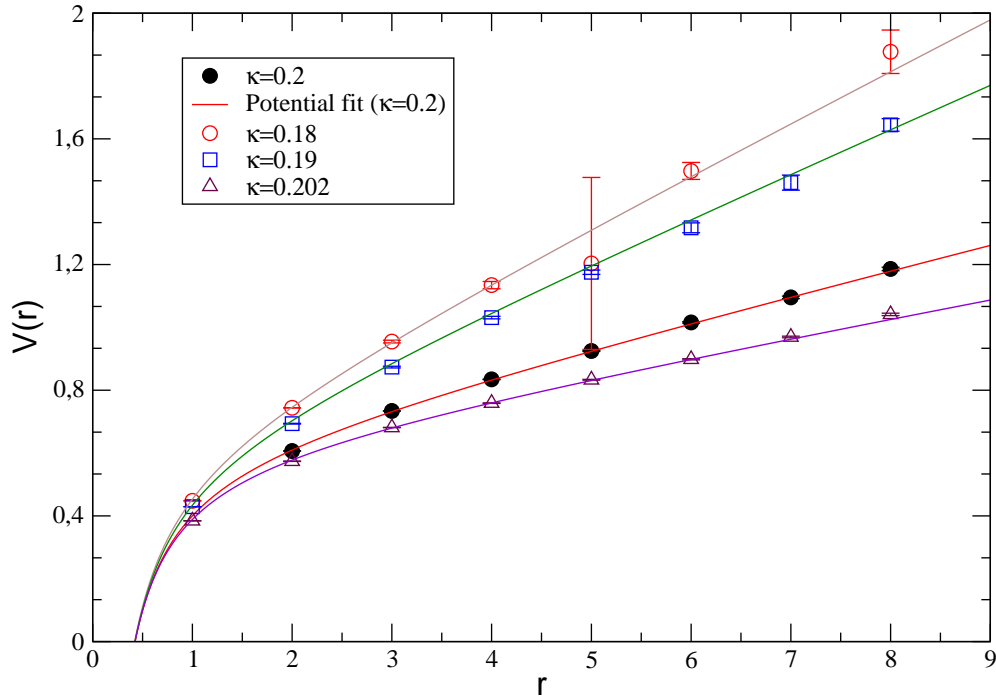
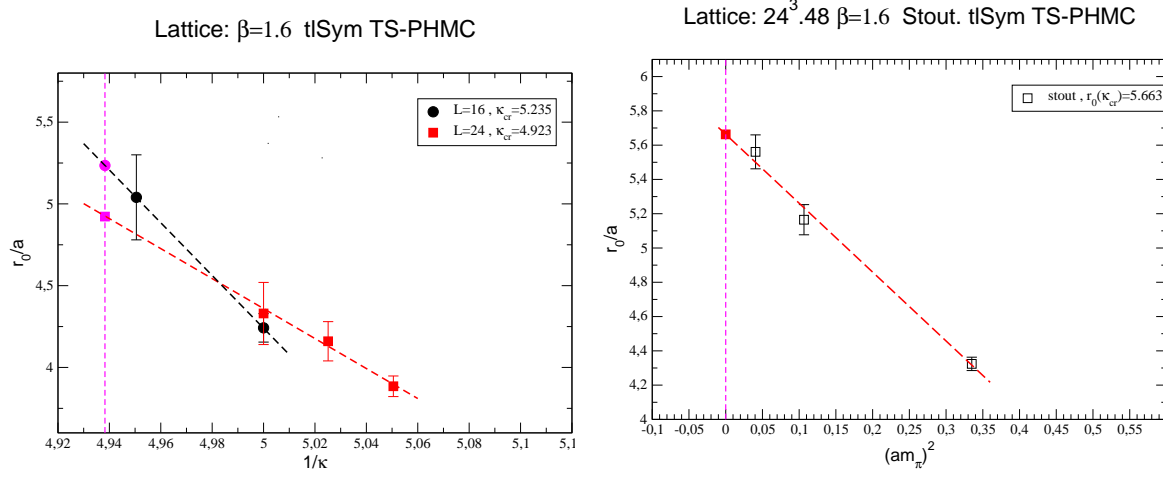


Figure 4.8: *Static gluino potential in  $\mathcal{N} = 1$   $SU(2)$  SYM (TS-PHMC).*

and the *measurement* step; in the former, the focus is on the production and storage of gauge configurations where few “cheap” observables are measured. In the latter, we essentially concentrate on the analysis of the spectrum of the theory in addition to some other observables like the Wilson loops which are necessary for the computation of the scale parameter  $r_0/a$ . As we started the TS-PHMC investigations, the configurations on the  $16^3 \cdot 32$  lattices were produced and then analyzed before starting the production on  $24^3 \cdot 48$  lattices. The results from  $16^3 \cdot 32$  lattice were taken as the basis for the further simulations on the larger lattices. From the results of the mass spectrum on  $16^3 \cdot 32$  we decided to produce samples at neighboring points where the gluino is sufficiently light while simulating one of the previous points to study the finite size effects. This leads us to simulate the points  $\kappa = 0.198$ ,  $\kappa = 0.199$  and  $\kappa = 0.2$ . In the case of the stout fermionic action, there were no reference so we started at  $\kappa_s = 0.15$  and then look at the adjoint pion mass.



Figure 4.9: *Extrapolation of  $r_0/a$  for all runs (TS-PHMC).*Table 4.7: *Critical hopping parameter from OZI arguments.*

data points	$\kappa_{cr}^{OZI}$
(A), (B)	0.20636(13)
(B), (C), (D)	0.20330(3)
(C), (D)	0.20250(7)
(A), (B), (C)	0.20300(5)
(A), (B), (C), (D)	0.20288(4)

## 4.4 Masses of the low-lying spectrum

We turn now to the most important characteristic of SYM theory, the mass spectrum of the lightest particles of the theory. In QCD the typical scale to study the hadronic spectrum is at the distance  $\sim 2$  fm where the interaction becomes strong and quarks and gluons do not appear as free particles, but rather they are confined into hadrons.

In SYM we have observed a non-vanishing string tension both in TSMB and TS-PHMC ensembles which is in accordance with the general expectation that the SYM theory is confining.

In SYM the low-energy effective actions describe the lower-end particle spectrum by two massive chiral supermultiplets [15, 17]. The predicted composite states are color singlet bound states: two scalars ( $a - f_0, 0^+$  glueball), two pseudoscalars ( $a - \eta', 0^-$  glueball) and two spin- $\frac{1}{2}$  states  $\chi$  (gluino-glueballs).

The physical states of the two supermultiplets result in general from mixing of these

states. The predicted ordering of these particles in supermultiplet from low energy effective actions can be checked or discarded by numerical simulations. We follow the standard method described in the previous chapter, treating the spectrum on the TSMB ensemble, to extract the masses from the time-slices correlation function of the interpolating fields  $\mathcal{O}$  on the lattice. In lattice simulations correlation functions of interpolating fields with the corresponding quantum numbers are computed for large time separations such that the lightest state with these quantum numbers (unmixed state) dominates. By this method, the masses of the bound states are extracted. The results for the mass spectrum are presented in details in the next sections on all ensembles produced with TS-PHMC algorithm and for each class of bound states: gluino-balls, gluino-glueballs and glueballs. The present TS-PHMC simulations are at smaller gluino masses and larger volumes than all previous simulations of the DESY-Münster collaboration.

We follow the same procedure of extracting the lowest mass used in the analysis of TSMB ensembles in the previous chapter. After computing the time-slice correlators  $C(t)$  the effective mass formula

$$am_{eff}(t, t+1) = \log[C(t)/C(t+1)] \quad (4.4)$$

is taken as the first orientation and then we try to estimate the lowest state by performing single exponential (one mass) fit with the asymptotic form of the correlator in an interval  $[t_1, t_2]$  in which the effective mass gave stable results. We note that the effective mass analysis works only with pairs of neighbor time-slices  $C(t)$  and  $C(t+1)$ , so it does not incorporate as much information as a full-fledged fit.

#### 4.4.1 The adjoint pion $a-\pi$

The adjoint pion  $a-\pi$  is, of course, not a physical particle in the SYM theory. Nevertheless, its mass is a well defined property, which can be computed on the lattice. We determine the adjoint pion mass on each ensemble to have idea on lightness of the gluino. The adjoint pion  $a-\pi$  is assumed to drive the low energy features of SYM, as the pion does in QCD. Hence, one can define the dimensionless quantity  $M_r \equiv (r_0 m_{a-\pi})^2$  to estimate the degree of soft breaking of SUSY. We have used this quantity as a reference for the gluino mass.

The adjoint pion correlator trivially coincides with the connected part of the  $a-\eta'$  correlator. The masses have been extracted on all ensembles without using smearing or extra computing of the correction factors, except for the runs ( $D$ ) and ( $D_s$ ) where the correction factors were needed for extracting the adjoint pion masses. The masses of the adjoint pion in lattice unit and in  $M_r$  are listed in Table 4.8 for all TS-PHMC runs.

In QCD, a major obstacle to direct lattice simulations is the difficulty in simulating with light dynamical quarks. Here, chiral perturbation theory allows extrapolation to physical masses up and down quarks. Validity of Next-to-Leading-Order (NLO) chiral

perturbation theory requires  $M_r \lesssim 0.8$ , which corresponds to  $m_{sea} \lesssim 0.25m_s$  ( $m_{sea}$  is the sea quark up and down mass,  $m_s$  is the physical mass of the strange quark) [87]. In SYM, we use the analogy to QCD to estimate the lightness of the dynamical gluino from the quantity  $M_r$ . In our present runs we have reached  $M_r \approx 1.3$  in runs ( $D$ ) and ( $D_s$ ), which would correspond in QCD to  $m_{sea} \approx 0.4m_s$ . This is a qualitative information about lattice SYM since QCD and SYM are, after all, two different theories.

Table 4.8: *The adjoint pion masses in lattice unit and the dimensionless quantity  $M_r$*

run	$am_{a-\pi}$	$M_r$
$A$	1.3087(12)	46.936(86)
$B$	1.0071(12)	27.795(66)
$Cb$	0.5008(13)	6.873(35)
$D$	0.221(12)	1.33(14)
$\bar{A}$	0.6415(13)	11.277(45)
$\bar{B}$	0.5759(17)	9.089(53)
$\bar{C}$	0.4947(13)	6.706(35)
$A_s$	0.9469(38)	28.78(23)
$B_s$	0.5788(16)	10.743(59)
$C_s$	0.3264(23)	3.420(48)
$D_s$	0.2015(93)	1.30(12)

#### 4.4.2 The adjoint pseudo-scalar meson $a-\eta'$ ( $J^{PC} = 0^{-+}$ )

The pseudo-scalar particle  $a-\eta'$  is usually the most promising particle to be determined in SYM. The lightest  $a-\eta'$  has delivered so far the most solid results found by DESY-Münster collaboration. These results were obtained with relatively high accuracy comparing to  $\eta'$  in QCD. But it is to be noted that the previous simulations did not reach a sufficiently small gluino mass as it is the case in the present work. In the TS-PHMC simulations very small gluino masses are simulated in a large volume: this is the real challenge for the masses estimations of the low-lying spectrum. With these more light gluino masses one expects to see SUSY effects in the bound states spectrum.

The adjoint meson-type correlators require the computation of two correlator type contributions, as we have discussed at length in the previous chapter. The connected correlators referring to the  $a-\pi$  are obtained as usual by inverting the fermion matrix on randomly chosen point source  $(y_0, \beta_0, b_0)$  for each configuration resulting in all-to-point propagator

$$Q_{x\alpha a, y_0 \beta_0 b_0}^{-1}[U], \quad (4.5)$$

for all sink locations  $x$ . We considered only local sources and sinks and no smearing procedure is used. The smearing is not needed for the disconnected correlator since both source and sink are constructed from local vectors. The disconnected contribution requires the estimation of the all-to-all propagator

$$\langle Q_{x\alpha a, x\beta b}^{-1} \rangle_U, \quad (4.6)$$

which means inverting the fermion matrix on each lattice point. There is a variety of strategies to compute the all-to-all propagators. Recall that the stochastic estimators technique (SET) and the improved volume source technique (IVST) were used in the previous chapter. However, the lattice community has made many new techniques available for a more accurate computation of the all-to-all propagator. In our case we still use SET/SEM with  $Z_2$  noise method to compute the disconnected correlators for all TS-PHMC simulated points since it gives satisfactory results. Nevertheless, some methods like the spectral decomposition [55] and the stochastic method with dilutions [56] were initially implemented and tested. However, these methods are out the scope of the present work and they have to be extended and optimized for future applications in the SYM spectrum investigations.

To select a subsamples for analysis of fermionic-type quantities, both  $a\text{-}\eta'$  and  $a\text{-}f_0$ , a popular choice is through the autocorrelation-times of the smallest eigenvalue of the fermion matrix, which is a primary quantity. The autocorrelation-times of  $\lambda_{min}$  reported in Table 4.3 and 4.4 give us a first information for the minimal offset required between measurements. The values of  $\tau^{\lambda_{min}}$  indicate a short autocorrelation among the saved configurations. Based on this information, in most cases it is better to skip at least about  $2\tau_{int}^{\lambda_{min}} = 2 - 4$  configurations between measurements to get effectively uncorrelated measurements. The computed values of integrated autocorrelation-time of the secondary quantity we want to estimate, the mass of the adjoint meson, confirm a posteriori this choice. In all ensembles we have

$$2\tau^{a-\eta'} < \text{offset}, \quad (4.7)$$

where "offset" is the number of configurations skipped in the adjoint meson measurements. Recall that the linearization method of Section 2.14 was applied for the estimation of  $\tau^{mass}$ .

In the following, we will proceed to discussing the results of our analysis of  $a\text{-}\eta'$  on the  $16^3 \cdot 32$  and  $24^3 \cdot 48$  lattices.

### **$16^3 \cdot 32$ ensembles**

The subsamples selected for analysis on the  $16^3 \cdot 32$  lattices are listed in Table 4.9 together with the offset in measurements and the integrated autocorrelation-times for adjoint mesons masses. Since we opted for the use of SET/SEM technique for estimation of the

disconnected correlator the number of noise vectors is also reported. The number of noise vectors  $N_{SET}$  was fixed by performing tests of variation of the disconnected correlator error at each time-slice as function of the number of noises. The number  $N_{SET}$  is fixed at the value for which any further noisy estimation would not bring further decreasing of the error (see Section 2.8.2). This results in about 16-22 stochastic estimates for this analysis.

Table 4.9: *Subsamples selected for adjoint mesons analysis. Lattice  $16^3 \cdot 32$  TS-PHMC.*

Run	$N_{conf}$	offset	$N_{SET}$	$\tau_{int}^{a-\eta'}$	$\tau_{int}^{a-f_0}$
<i>A</i>	550	4	20	0.5	0.5
<i>B</i>	600	4	16	0.5	0.5
<i>Ca</i>	394	4	16	0.7	0.8
<i>Cb</i>	1100	8	16	0.6	1.0
<i>D</i>	646	8	22	0.5	2.0

The starting point for the analysis of the  $a-\eta'$  bound state is the ensemble (*A*). The effective mass for  $a-\eta'$  and its connected part  $a-\pi$  is shown in Fig. 4.10 (upper panel). From  $t = 1$  to  $t = 3$  we observe identical values of effective mass of connected part and  $a-\eta'$  indicating complete dominance of the connected correlator in the physical correlator  $C^{a-\eta'}(t)$ . The decreasing of the effective mass in this interval signals the influence of higher states. The connected correlator decreases faster than the disconnected one as function of time-separation. The latter contribute to the  $a-\eta$  correlator and its errors are large. As a result only the interval  $t = 3$  to  $t = 5$  can be used for the mass extraction. An estimate from the mass fit in this interval leads

$$am_{a-\eta'} \sim 1.311(7) . \quad (4.8)$$

Starting from  $t = 5$  the disconnected contribution becomes negative which indicates that the signal of the physical correlator is lost. The reason is that noisy methods such SET/SEM used for computing the disconnected correlator are efficient only for sufficiently light quark (gluino) mass. Hence, at  $\kappa = 0.18$  the gluino is certainly heavy where the adjoint pion has a mass about  $am_{a-\pi} = 1.3$  and we have  $M_r \sim 47$ . The mass difference between  $a-\eta'$  and its connected contribution is practically negligible  $\Delta am \sim 0.003$ . When going towards small gluino mass a considerable mass gap is expected to show up. The ensemble (*A*) served as a first guide for the next simulated points.

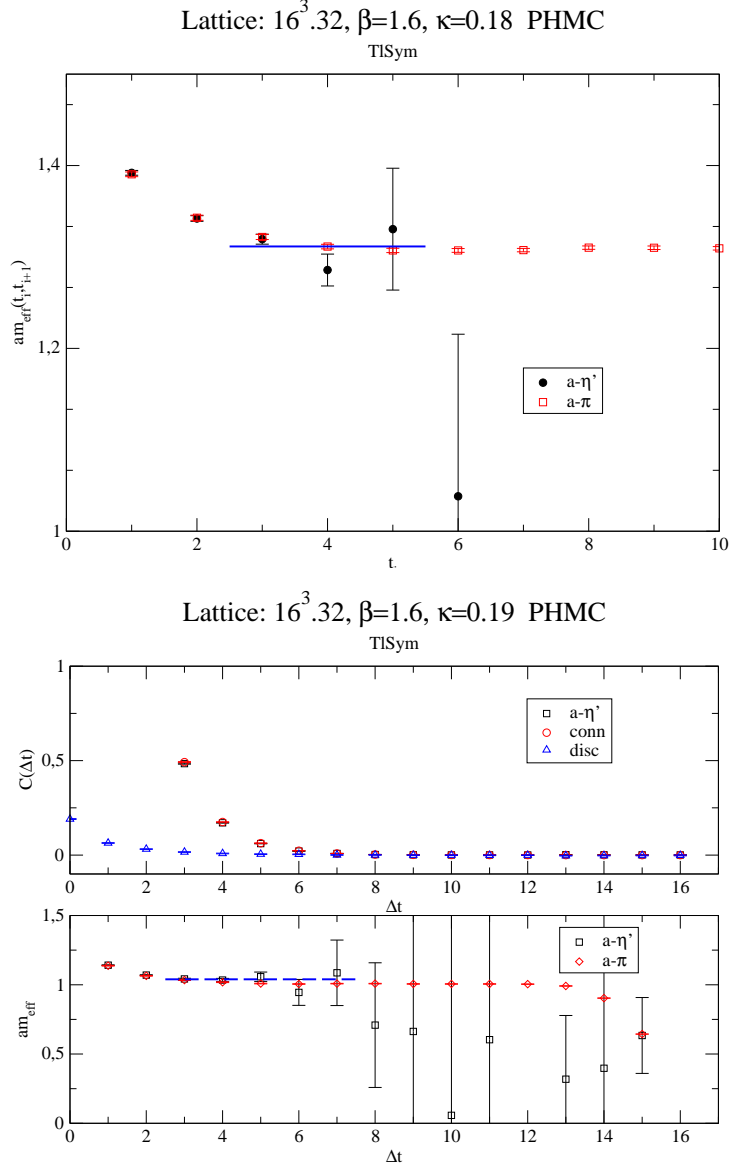


Figure 4.10: *Effective mass plots and correlators for ensembles A and B.*

As expected, on the ensemble (B) a first signs of a stabilization of the signal can be observed. As the quark mass is getting smaller the mass of the disconnected contribution also does since the disconnected correlator is now positive up to time-slice  $t = 9$ . The effective mass of  $a\text{-}\eta'$  and its connected counterpart in addition to their correlator are shown in Fig. 4.10 (lower panel). When we consider the time-slices range  $t = 3$  up to  $t = 8$  the  $a\text{-}\eta'$  effective mass displays a stability and fluctuates within error above the effective mass of  $a\text{-}\pi$ . From  $t = 9$  the signal is dominated by noise. As an estimation of

the  $a\text{-}\eta'$  mass fitted in the interval  $[3, 7]$  is

$$am_{a-\eta'} \sim 1.0396(72) . \quad (4.9)$$

Moreover, the mass gap is  $\Delta am \sim 0.03$  which is about a factor ten greater than the mass gap on the ensemble (A) above. The  $a\text{-}\eta'$  mass is still close to the  $a\text{-}\pi$  estimated mass.

The next ensembles are  $(C_a)$  and  $(C_b)$  produced independently at the bare gluino mass  $\kappa = 0.2$ . The ensemble  $(C_b)$  is the largest ensemble generated for this study. As reported in Table 4.9 we analyzed a subsample of 394 configurations from the ensemble  $(C_a)$  and 1100 configurations on the ensemble  $(C_b)$ . During the analysis of the subsample  $(C_b)$  we permanently checked the optimization of the disconnected correlator error as when increasing the number of the configurations included in the analysis until the statistics 1100 was reached. We observe that the error decreases considerably slower when increasing the statistics compared to the connected case. Note here that the measured integrated autocorrelation-time of the smallest eigenvalue  $\lambda_{min}$  estimated by taking into account all produced configurations was about  $\sim 60$  which is the largest observed value. However, the measured integrated autocorrelation-time of the mass observable reveals that the selected configurations for the analysis are almost de-correlated  $2\tau_m \sim 1.6$ . The  $a\text{-}\eta'$  effective mass on the ensembles  $(C_a)$ ,  $(C_b)$  and the two ensembles considered together are shown in Fig. 4.11. The  $a\text{-}\eta'$  correlator contributions for the  $(C_a)$  are also presented in Fig. 4.11 (upper panel) for giving an idea on the actual behavior of the correlator at  $\kappa = 0.2$ .

The  $a\text{-}\eta'$  correlators shown in Fig. 4.10 (upper panel) that the disconnected contribution begins to appear greater in magnitude than in previous ensembles, where heavy gluino masses were simulated. On this ensemble 394 configurations were analyzed. The  $a\text{-}\eta'$  effective mass on the subsample  $(C_a)$  indicates a suppression of high states contribution in the interval  $t = 4$  up to  $t = 8$  where stabilization of the effective mass is observed. After  $t = 9$  the signal is too noisy. The single exponential fit in the interval  $t \in [5, 7]$  gives the mass

$$am_{a-\eta'} \sim 0.542(23) . \quad (4.10)$$

In the analysis of 1100 configurations the subsample  $(C_b)$  the  $a\text{-}\eta'$  effective mass may signal that the contribution of higher state persists up to time-slice  $t = 6$  while their higher effective mass were observed up to time-slice  $t = 4$  in the subsample  $(C_a)$ . This may be an effect of the increased statistics, which may increase the number of configurations where the signal of higher states is relevant. Similar results are obtained when we considered all configurations of the subsamples  $(C_a)$  and  $(C_b)$  together (Fig. 4.11). A drop of the effective mass is observed from  $t = 9$  which may be caused by statistical fluctuations. Of interest is to find evidence of an isolate low-lying state. The estimation of the lowest mass is obtained by performing one mass fit in the interval  $[4, 7]$  which reads

$$am_{a-\eta'} \sim 0.5426(75) . \quad (4.11)$$

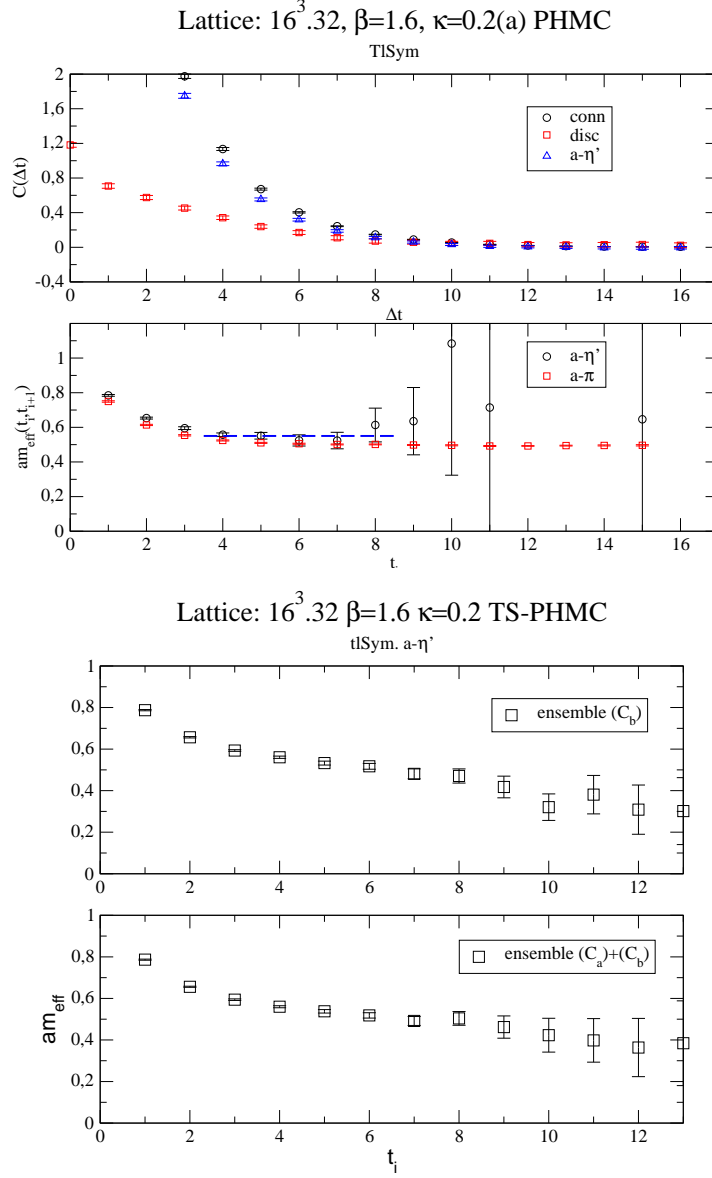


Figure 4.11: *Effective mass plots and correlators for ensemble (Ca) and (Cb).*

The mass gap  $\Delta m = am_{a-\eta'} - am_{a-\pi}$  increases slightly to about 0.04. The advantage of increasing the statistics is the optimization of the signal-to-noise ratio by decreasing the statistical error of the measured correlation functions. In addition to inevitably degrading the signal-to-noise ratio of the physical state, the disconnected contribution may introduce systematic errors from the noisy estimators methods. The total correlator and its connected are thought to be sum of falling exponentials, reducing to single exponential when the lowest state is dominating. In Fig. 4.12 the  $a-\eta'$  correlator and its components are plotted in a logarithmic scale to highlight the quality of the signal.



The connected part has a clear linear behavior in a long range of time-separations  $t$  which indicates the dominance of the lowest state (here the unphysical  $a$ - $\pi$ ) and hence the existing of one exponential. However, the log-plot of the disconnected correlator displays a non-linear character and its shape indicates that the disconnected correlator is no longer one exponential even not a sum of exponential. Only after building up the physical correlator as shown in Fig. 4.12 we can see again a linear behavior in the log-plot of the  $a$ - $\eta'$  correlation function in a reasonable range of the time-separation interval. We indeed not have a single exponential at large time-separation, but a sum of several exponentials which signals persistence of higher mass states.

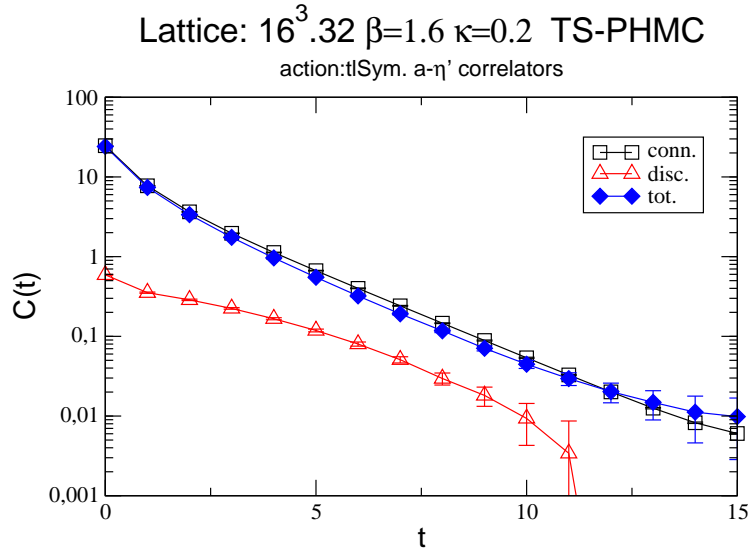


Figure 4.12: *Logarithmic scale plots of correlators components of  $a$ - $\eta'$  at  $\kappa = 0.2$ . The lines are drawn to guide the eye.*

The last ensemble analyzed on  $16^3 \cdot 32$  lattices is the ensemble (D). The reweighting procedure was necessary for extracting the lowest mass of the  $a$ - $\eta'$ . The effect of the correction factor on the  $a$ - $\eta'$  correlator is shown in Fig. 4.13. The reweighting of the statistical subsample has the effect of reproducing the correct exponential behavior of the  $a$ - $\eta'$ . Furthermore, the statistical error is also corrected and reduced allowing a reasonable signal. The effect of light gluino mass can be clearly seen on the effective mass of  $a$ - $\eta'$  in Fig. 4.14 where the signal provides a good fit, giving a plateau from  $t = 5$  to  $t = 10$  where the effective mass stabilizes. However, the error is relatively large comparing to previous estimations. This is in fact expected at sufficiently light

quark mass as in QCD. The correlators of the  $a\text{-}\eta'$  presented in Fig. 4.14 show that the disconnected part is positive for all time-separation, but it has larger error than the connected one. Furthermore, both contributions display a small offset in the correlators. This offset is suppressed and does not appear after constructing the physical correlator where the disconnected correlator is subtracted from the connected one,  $C_{conn} - \frac{1}{2}C_{disc}$ .

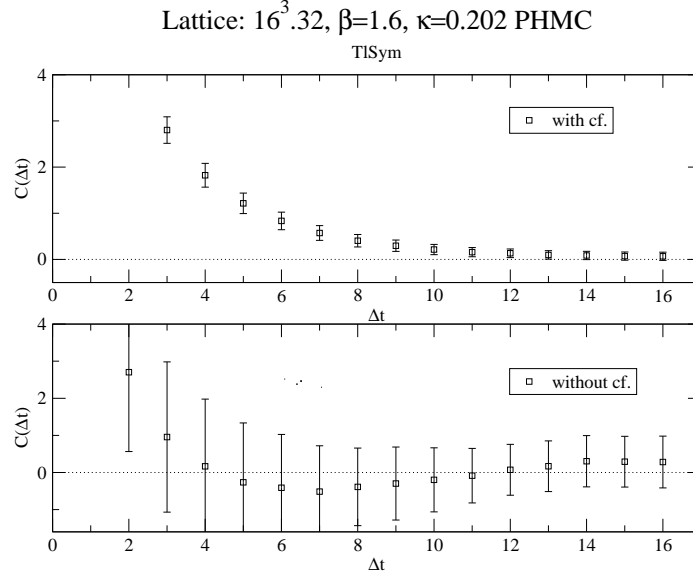
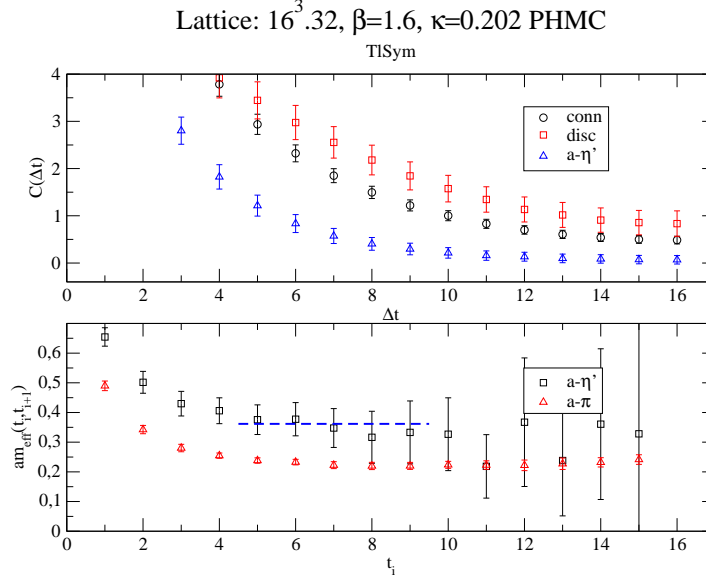


Figure 4.13: *Effect of the correction factor on the  $a\text{-}\eta'$  correlator.*

The  $a\text{-}\eta'$  mass at lightest gluino mass has a relatively large error and the value

$$am_{a\text{-}\eta'} \sim 0.361(60) \quad (4.12)$$

provides an estimate the  $a\text{-}\eta'$  mass on this ensemble from single exponential fit in the interval  $t = 5$  to  $t = 9$ . Recall that we have also simulated a point where the gluino mass is expected to be small, the ensemble ( $D_s$ ). It will be of interest to explore the effect of the stout smearing on the  $a\text{-}\eta$  mass at light gluino mass.

Figure 4.14: Correlators of  $a-\eta'$  and effective mass.

We also explored the behavior of the disconnected correlators as function of the gluino mass. The disconnected correlators of  $a-\eta'$  on the subsamples  $\kappa = 0.2$  and  $\kappa = 0.202$  are compared in Fig. 4.15. Compared to the disconnected correlator at  $\kappa = 0.2$ , the disconnected correlator at  $\kappa = 0.202$  is about five orders of magnitude greater. We also observe the increasing of the statistical error of the disconnected correlator at light gluino. Recall that this error is the cumulative error of the gauge noise and of the noisy estimators where the latter may dominate. One way to reduce this error is through the analysis of higher statistics which in turn increases the computation costs. The other way is to use more efficient variance reduction methods to estimate the all-to-all propagators while retaining the same set of gauge configurations.

We checked the signal of the disconnected contribution by observing the effective mass  $m_{\text{disc}}$  displayed in Fig. 4.15 (lower panel)<sup>2</sup>. The effective mass increases as function of the time separation up to time  $t = 8$  and starts to fluctuates within error afterward. This agrees with the observations in QCD (see Ref. [74]) where the disconnected contribution are only relevant for the ground states and not for the excited states. In other words, the signal of higher mass states in the  $a-\eta'$  are essentially encoded in its connected contribution.

<sup>2</sup>  $m_{\text{disc}}$  is defined as the parameter in the single exponential  $e^{-m_{\text{disc}}t}$  function used as an approximation the disconnected correlator decay.

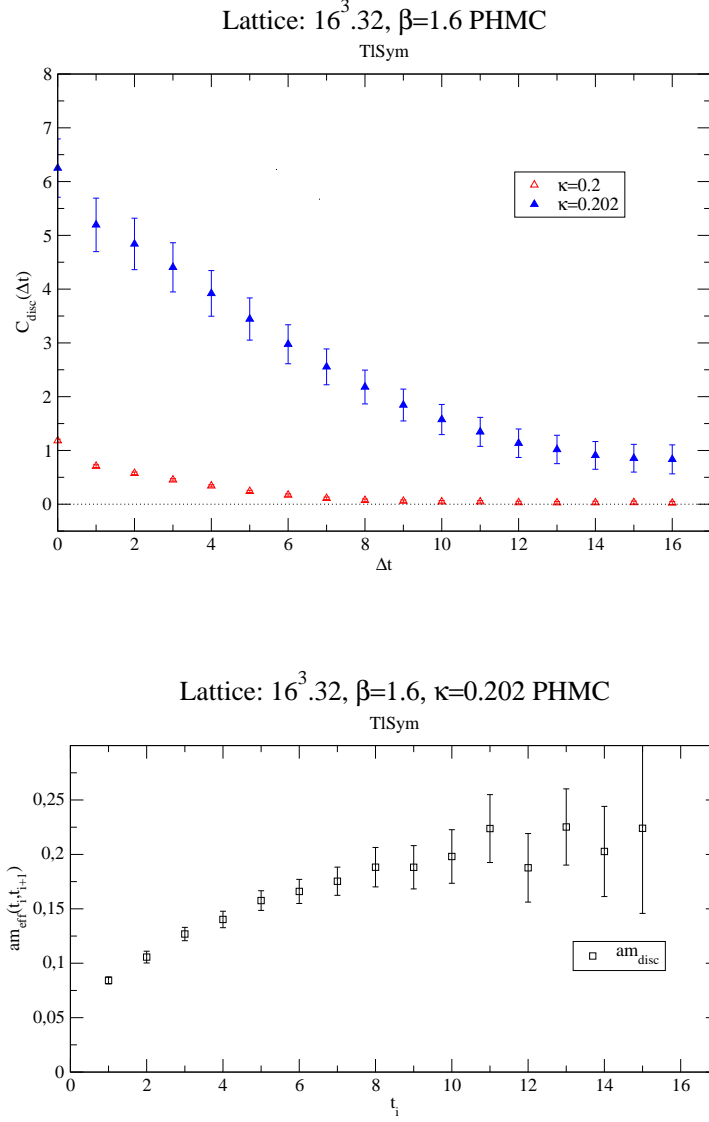


Figure 4.15: Comparison of the disconnected correlators at  $\kappa = 0.2$  and  $\kappa = 0.202$  (upper panel), and the effective mass  $m_{disc}$  at  $\kappa = 0.202$  (the disconnected correlator is fitted to single exponential).

Of interest here also, is the mass gap which continues to grow. On this subsample the value of the mass gap is

$$\Delta m \sim 0.14 . \quad (4.13)$$

From the analysis of all ensembles we observe that as the gluino mass is getting smaller, the  $a$ - $\eta'$  mass also does. Furthermore, the mass gap increases as function of  $1/\kappa$  as it is shown in Fig. 4.16. This splitting is expected to get greater towards smaller gluino masses. In the chiral limit at  $m_{\tilde{g}} = 0$  where the mass of connected part  $a$ - $\pi$  goes to zero

the  $a\text{-}\eta'$  remains massive due to the contribution of the disconnected graphs.

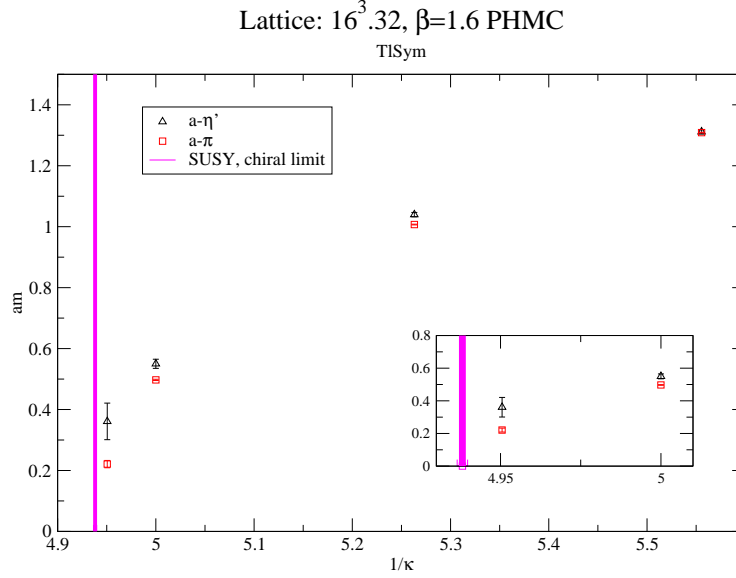


Figure 4.16: Measured  $a\text{-}\eta'$  masses and the masses of its connected part as function of  $1/\kappa$ . The vertical line is the expected chiral limit where  $m_{\tilde{g}} = 0$ .

### $24^3 \cdot 48$ ensembles

Going to larger lattices we can estimate the finite size effects with a larger temporal extent we can better separate the higher states from the lightest state. For the ensembles simulated with stout-smearing action, the starting point was  $\kappa_s = 0.15$  which is used as a guide for the tuning. The most relevant points from these ensembles are  $(C_s)$  and  $(D_s)$  where in the latter the measured adjoint pion indicates a sufficiently light gluino mass. The number of configurations selected for the adjoint mesons analysis, the corresponding integrated autocorrelation-times of mass and the number of the noise vectors for SET/SEM for all  $24^3 \cdot 48$  (stout/unstout) subsamples are summarized in Table 4.10.

We expected a smooth behavior of the  $a\text{-}\eta'$  mass on the  $24^3 \cdot 48$  ensembles simulated without stout-smearing *i.e.* the ensembles  $(\bar{A})$ ,  $(\bar{B})$  and  $(\bar{C})$ . Based on the observations of the analysis on  $16^3 \cdot 32$  lattices we conclude that the present points correspond to values of light gluino masses which are close to each other. The  $a\text{-}\eta'$  effective mass for these subsamples is displayed in Fig. 4.17. The signal is sufficiently good at all points allowing an isolation of the mass of the lowest-lying state. A small signal of higher states is observed up to few time-separations 3–4 before the effective mass stabilizes for several time-separations 4–9 where the lightest state dominates. As expected at larger time-separations the error grows which is caused by degradation of the signal as function

of time-separation. On the intervals where the effective mass emerges we selected the intervals for the single mass fits. At  $\kappa = 0.198$  the fit in the interval 5 – 7 leads to the mass

$$am_{a-\eta'} \sim 0.675(18) . \quad (4.14)$$

The signal of  $a-\eta'$  at  $\kappa = 0.199$  allows us to perform the fit to the correlator in the time-separation range 4 – 7. The fitted mass is

$$am_{a-\eta'} \sim 0.6215(86) . \quad (4.15)$$

The effective mass on the ensemble ( $\bar{C}$ ) displays a plateau for larger time-slices interval than in previous ensembles (lower panel of Fig. 4.17). We can thus use the data up to  $t = 11$  in the fits. The fit performed in the range 5 – 11 yields a mass estimate

$$am_{a-\eta'} \sim 0.536(24) . \quad (4.16)$$

We are most interested in the search of a systematical finite size effect on the  $a-\eta'$  mass. This obtained mass in (4.16) agrees with the estimated mass 0.543 at  $\kappa = 0.2$  on the  $16^3 \cdot 32$  lattice. In the effective mass we indeed see a larger plateau as the lattice volume increased. But, the estimated masses are almost equal. This agreement in the masses suggests that starting from the present simulated volume the  $a-\eta'$  exhibits negligible finite size effects. We also checked the effects of the size on the mass gap  $m_{\eta'} - m_\pi$  on larger lattice. The latter turns out to be of the same magnitude as the mass gap on smaller lattice. The estimated mass gap is

$$\Delta am \sim 0.03 - 0.04 . \quad (4.17)$$

Table 4.10: *Subsamples selected for adjoint mesons analysis. Lattice  $24^3 \cdot 48$  TS-PHMC.*

Run	$N_{conf}$	offset	$N_{SET}$	$\tau_{int}^{a-\eta'}$	$\tau_{int}^{a-f_0}$
$\bar{A}$	345	4	16	0.6	0.8
$\bar{B}$	600	2	16	0.7	0.8
$\bar{C}$	585	4	16	0.6	1.4
$A_s$	200	1	16	0.5	2.0
$B_s$	383	4	16	0.6	1.0
$C_s$	400	4	16	0.6	1.8
$D_s$	951	2	20	0.8	1.5

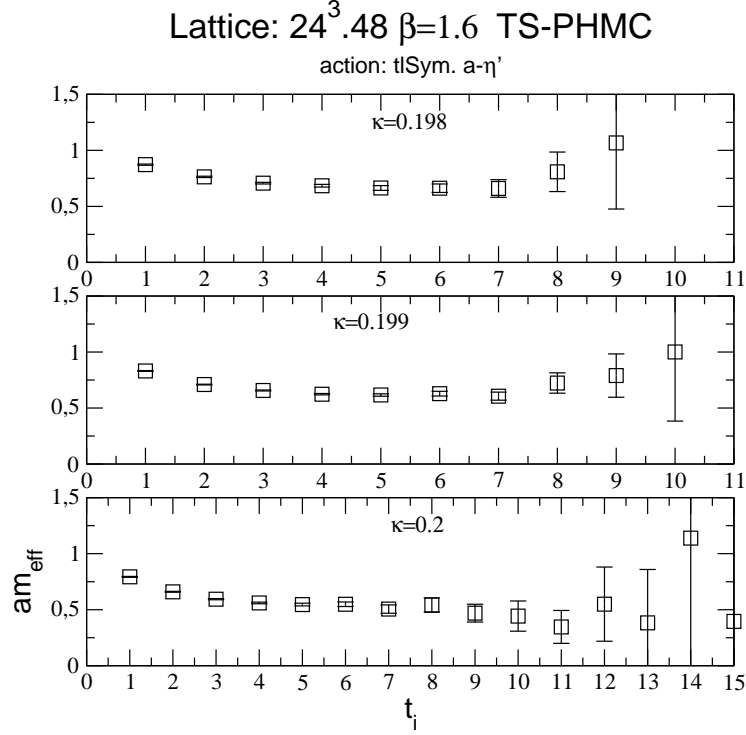


Figure 4.17: *Effective mass of  $a-\eta'$  for the ensembles  $(\bar{A})$ ,  $(\bar{B})$  and  $(\bar{C})$ .*

We turn now to the analysis of  $a-\eta'$  particle on the ensembles produced with stout-smearred Wilson action. Here again we have used the ensemble  $(A_s)$  as a guide to the tuning, and the analysis of this ensemble is less relevant. On the remaining ensembles, the best results were obtained for the ensemble  $(C_s)$  at  $\kappa = 0.157$  where the gluino mass is small enough for a reasonable mass of the adjoint pseudo-scalar. The lightest gluino mass, however, corresponds to the ensemble  $(D_s)$  at  $\kappa = 0.1575$ . As the gluino mass decreases the signal is getting better up to  $\kappa = 0.157$  allowing to see plateaus in the effective mass plots which are shown in Fig. 4.18. The onset of the plateaus is at most from time-separation  $t = 3$ . The intervals for the single mass fit are fixed to  $t = 3 - 5$ ,  $t = 5 - 9$  and  $t = 5 - 9$  for subsamples  $(A_s)$ ,  $(B_s)$  and  $(C_s)$  respectively. Therefore, the estimates of the  $a-\eta'$  on these subsamples are

$$(A_s) : am_{a-\eta'} \sim 1.0114(82) , \quad (4.18)$$

$$(B_s) : am_{a-\eta'} \sim 0.614(23) , \quad (4.19)$$

$$(C_s) : am_{a-\eta'} \sim 0.415(29) . \quad (4.20)$$

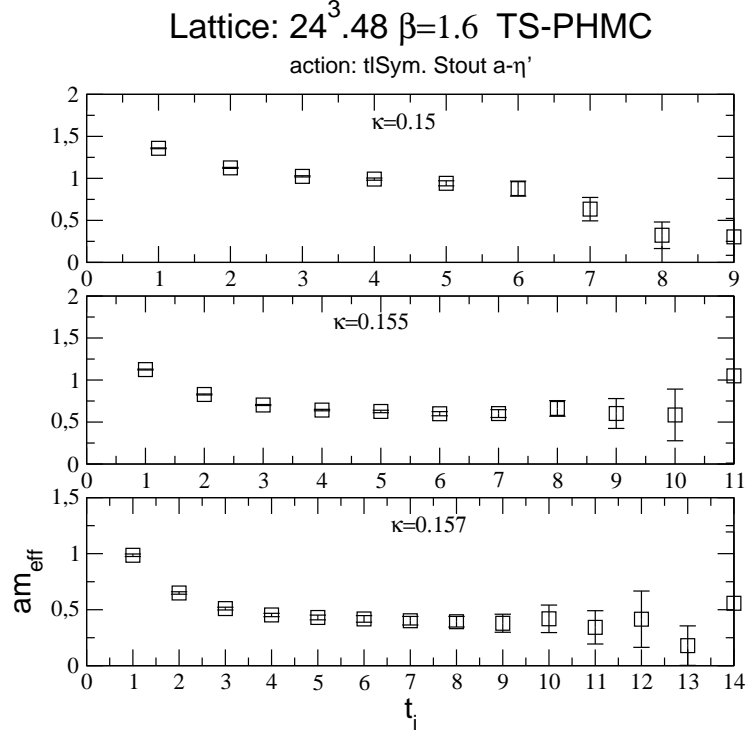


Figure 4.18: *Effective mass of  $a\text{-}\eta'$  for the ensembles  $A_s$ ,  $B_s$  and  $C_s$ .*

The number of stochastic estimators  $N_{SET} = 16$  was set at the same value for all the above stout subsamples. The tests performed on a small subsamples to fix this number showed that the error of the disconnected correlator does not become lower for larger number of  $N_{SET}$  than the above value. However, the error increases as we go towards lighter gluino mass rendering the signal lower. It is assumed that besides the systematic error of the noisy estimators method with a few estimations, the error is still dominated by the noise of the gauge sample. Therefore, one solution is the increasing of our statistics for lighter gluinos in order to lower the statistical error of the disconnected correlator (see Table 4.10).

As a side note, we remark that a significant mass gap  $\Delta m \sim 0.06 - 0.09$  is observed, larger than in the un-stout ensembles. This may tell us that the point ( $C_s$ ) is simulated at lighter gluino mass than the one at the point ( $\bar{C}$ ). A cross check can be obtained by comparing the adjoint pion mass given in lattice unit where the adjoint pion at  $\kappa = 0.2$  is roughly 34% heavier than at  $\kappa_s = 0.157$ , assuming here that the lattice spacings are the same. Nevertheless, this is only a qualitative comparison and it is not conclusive since, as we have seen in Section 4.2.2, the stout smearing increases the value of  $r_0/a$  and hence the masses are heavier in physical units. Let us consider the case ensemble ( $\bar{B}$ ) where the adjoint pion mass in lattice unit coincides with the one estimated on the ensemble ( $B_s$ );  $am_{a-\pi} \sim 0.58$ . Here, the mass of  $a\text{-}\eta'$  is almost of the same order



of magnitude on both ensembles. We are somewhat hesitant to conclude that the two above stout and un-stout points were simulated at equal gluino mass since we should also observe the case of other particles which may exhibit different  $\mathcal{O}(a)$  effects.

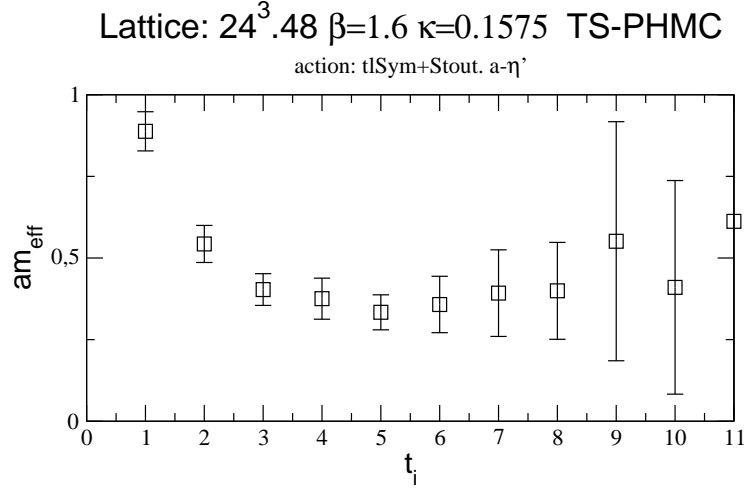


Figure 4.19: *Effective mass of  $a\text{-}\eta'$  at  $\kappa_s = 0.1575$ .*

The determination of the  $a\text{-}\eta'$  lowest mass at  $\kappa_s = 0.1575$  turned out to be the most challenging one in the series of these stout ensembles. On one hand, as we argued in Section 4.1.3 exceptional configurations appear frequently in the run ( $D_s$ ) where the computation of the correction factors (absolute correction factor + Pfaffian sign) is necessary for the reweighting of the statistical average. The reweighting procedure is relevant as we saw at the end of Section 4.4.2 for the subsample ( $D$ ). On the other hand, the expected grow of the error of the disconnected correlator, as observed in the case the ensemble ( $D$ ), renders the signal noisier leading to large error of the mass estimate.

We experienced that the strong increase of the disconnected correlator and its variance signals that the simulated point resides close to the chiral limit. A comparison of the disconnected correlators for the stout ensembles is presented in Fig. 4.21 where the highest statistic corresponds to the point  $\kappa_s = 0.1575$  with 450 configurations and  $N_{SET} = 20$  estimators were applied. The correction factors are taken into account in the statistical average of time-slice disconnected correlator at  $\kappa = 0.1575$ . The behavior is similar to that observed in Fig. 4.15 (upper panel) for the subsample ( $D$ ). Thus, the highest statistic was used for the analysis of the stout ensemble. Observe that the correlator error decreases slower than the inverse root  $1/\sqrt{N_{stat}}$  of the statistic as it is

shown in Fig. 4.20. As the statistic is increased by more than nine times from 100 to 951, the error is reduced by roughly 60%.

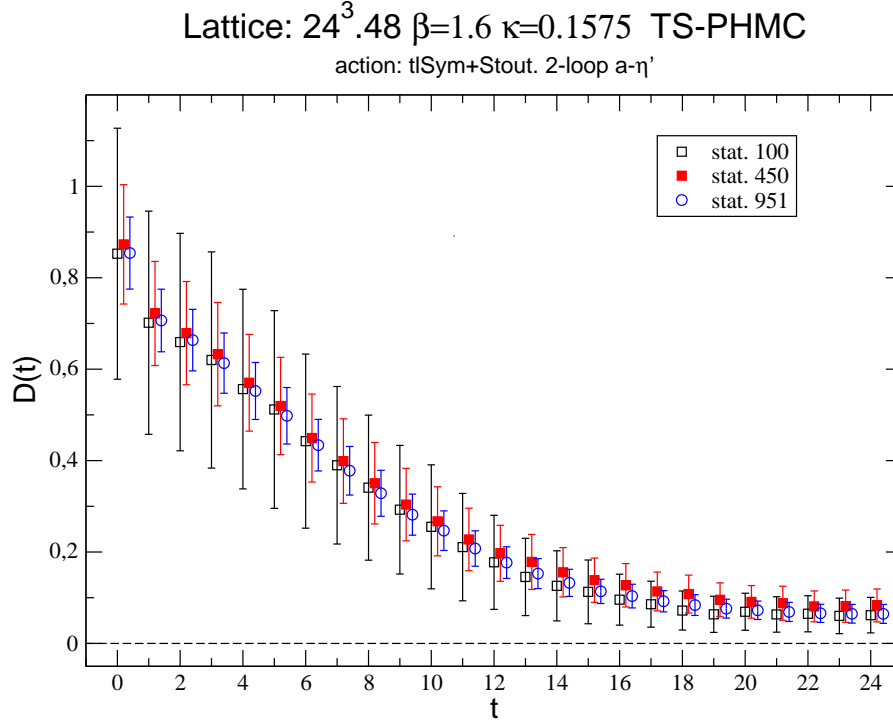


Figure 4.20: *The effect of increasing the statistic on the disconnected correlator error for the ensemble  $D_s$ .*

At the simulation point ( $D_s$ ) the subsample for the  $a-\eta'$  analysis constitutes about 50% of the thermalized configurations produced for the present study, which is the maximal decorrelated number of configurations with respect to the smallest eigenvalue (see Table 4.4). Therefore, we did not analyze more configurations since besides optimizing the error significantly, this would also require high computational costs. Nevertheless, the obtained signal in this channel generates a clear plateau in the effective mass starting from  $t = 4$ , continuing within error up to  $t = 11$  (Fig. 4.19). However, at  $t = 9$  and onward the error is larger indicating a low signal-to-noise ratio. Note here that no signal could be found when the correction factors are not included in the statistical average. After reweighting, our best estimate on this ensemble was obtained by performing one mass fit in the interval  $t = 4$  to  $t = 9$ , which is

$$(D_s) : am_{a-\eta'} \sim 0.364(70) . \quad (4.21)$$

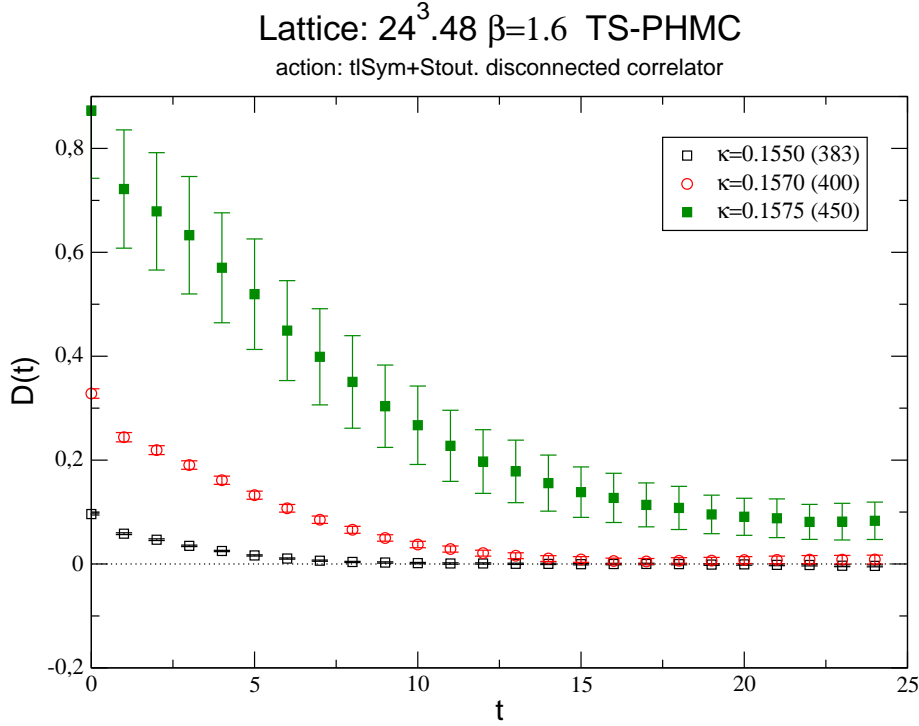


Figure 4.21: *Disconnected correlation function for ensembles ( $B_s$ ),  $C_s$  and  $D_s$ .*

Before closing this section, let us discuss the application of the improved volume source technique (IVST) for the estimation of the all-to-all correlator versus the SET/SEM method. During the course of the analysis of the adjoint mesons on the ensemble ( $D_s$ ) we performed some tests to study the error optimization by IVST. Therefore, we take the opportunity to compare both methods. Recall at first that from our experience on the TSMB samples and the previous results of the DESY-Münster collaboration we observed that both methods gave consistent results. Hence, we opted for the use of SET/SEM since it has advantage of allowing to compute each element of the inverse fermionic matrix (IVST only allows the determination of the diagonal terms). We selected 100 configurations from the subsample ( $D_s$ ) and we estimated the two-loop graphs by  $8 \times 2 \times 3 = 48$  IVST inversions and by  $20 \times 2 = 40$  SET/SEM inversions. As can be seen in Fig. 4.22 (in upper panel is the disconnected correlator and in lower panel is the effective mass  $am_{disc}$ ) the error of the disconnected correlator estimated by IVST is almost 25% smaller than of the one estimated by SET/SEM. Furthermore, even though the number of inversions for IVST is larger than for SET/SEM, from the computational costs point of view the 40 SET/SEM inversions are more expensive than 48 IVST inversions. This can be understood by the fast convergence of the iterations in the IVST comparing to SET/SEM inversion which converges slower. In fact, IVST uses source vectors which have (real numbers) 1 as entries; SET/SEM has complex  $Z_2$  numbers which renders the

source vector denser, and hence the solver converges slowly in this case.

Furthermore, recall that the SET/SEM is a stochastic method with spin dilution while IVST is equivalent to a stochastic method with dilution over spin and color spaces. As it is known in QCD, the greater is the number of dilutions the smaller are the error of the correlator. In SYM, we can attribute the reducing of the disconnected correlator error by IVST to: the increasing number of inversions on one hand, and to the effect of dilution. This provides a new idea for variance reduction methods at very small dynamical gluino. Here, we see that IVST at light gluino mass is computationally more economical than SET/SEM and provides better results for the variance reduction. However, this result is only preliminary and the question must be explored in detail in the future to see which method is the most efficient at light gluino mass.

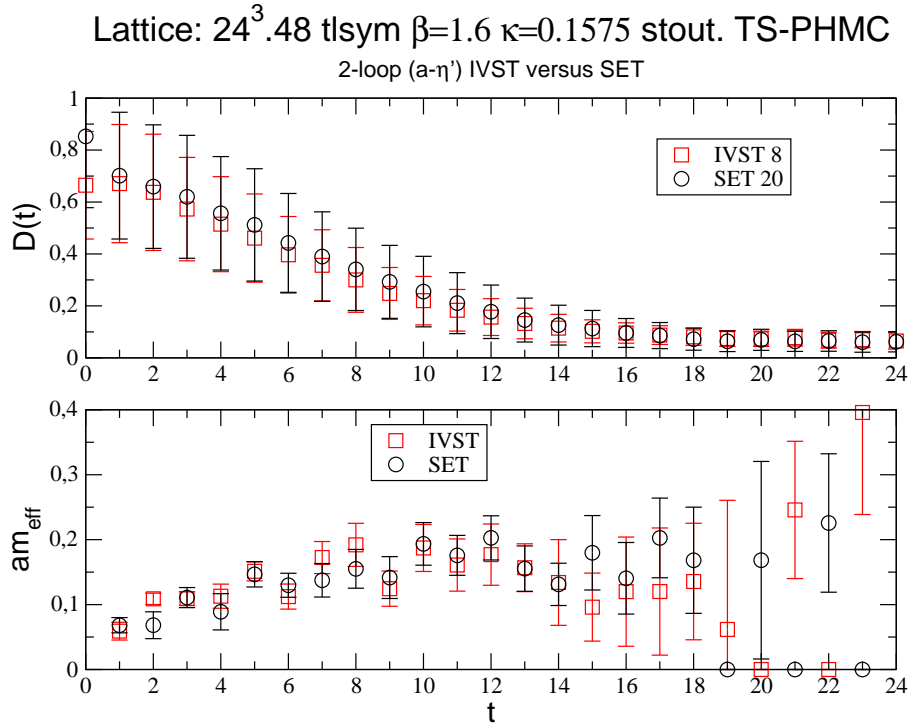


Figure 4.22: Comparison of the estimation of disconnected correlator using SET/SEM and IVST, and the effective mass  $am_{\text{disc}}$  on 100 configurations at  $\kappa_s = 0.1575$ .

#### 4.4.3 The adjoint scalar meson $a - f_0$ ( $J^{PC} = 0^{++}$ )

As we argued in the analysis of TSMB samples, the identification of the single flavor scalar meson is still one of the missing puzzles of QCD. Difficulties arise when trying to extract the mass of the ground state in the scalar channel using lattice techniques. In SYM, the low energy effective action [17] expected the adjoint scalar meson  $a\text{-}f_0$  to be

rearranged in the heavier supermultiplet together with  $a\text{-}\eta'$  and a gluino-gluon bound state. We used the gluino bilinear interpolating operator  $\mathcal{O} = \bar{\lambda}\lambda$  to create a  $J^{PC} = 0^{++}$  state on the lattice. Beside usual connected and disconnected contribution to the adjoint scalar correlator, a subtraction of an offset from the correlator must be performed since the vacuum expectation value  $\langle \bar{\lambda}\lambda \rangle$  does not vanish. The subtracted term does not involve additional computational expense and it is calculated using the  $Z_2$  SET/SEM noise method during the computation of disconnected graphs. The resulting correlator is fitted to the usual single exponential function. Both the disconnected term and the subtracted term are the order of  $10^5 - 10^6$ , and the difference  $C_{disc} - vev$  becomes less than  $10^{-1} - 10^{-3}$ . Therefore, to obtain the signals correctly as the difference between these terms, numerical simulations with high precision and careful analysis are necessary. We set the precision in our case for example to more than 10 decimal digits to avoid missing of the signal.

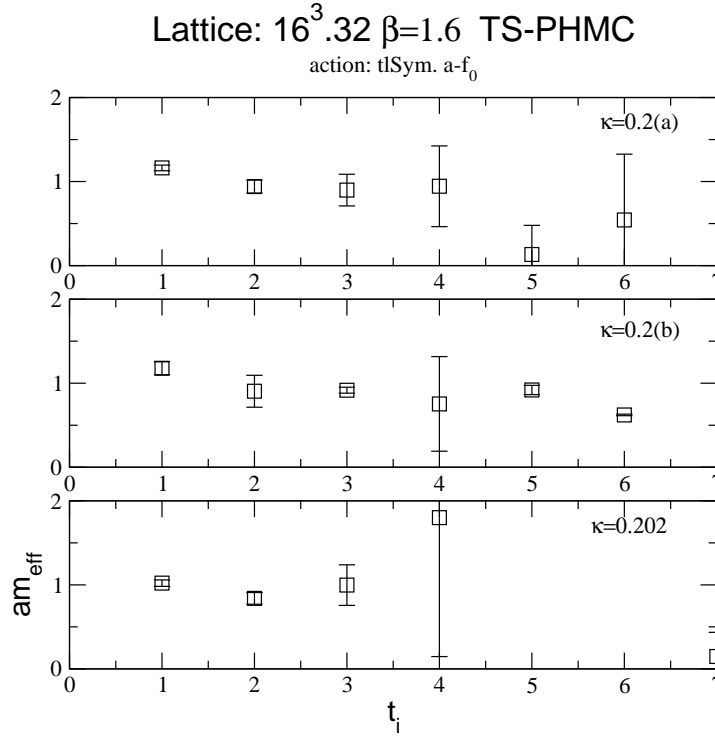


Figure 4.23: *Effective mass of  $a\text{-}f_0$  on the  $16^3 \cdot 32$  lattices.*

### $16^3 \cdot 32$ ensembles

The analyzed subsamples for  $a\text{-}f_0$  on the  $16^3 \cdot 32$  lattice are listed in Table 4.9. Differently from ensemble ( $D$ ), in the ensembles ( $C_a$ ) and ( $C_b$ ) we see in the effective mass an early stabilization at short time-separations before the signal is washed out (Fig. 4.23). We

assume from this stabilization of the effective mass and the small error that the lowest state is dominating in these times since for larger time-separations the drop of the mass is not smooth which would underline that a lowest state could be isolated. We then simply perform the fitting procedure in the interval 2 – 5, which leads to

$$(C_a) : am_{a-f_0} = 0.93(11) , \quad (4.22)$$

$$(C_b) : am_{a-f_0} = 0.931(60) . \quad (4.23)$$

The effect of higher statistic of the ensemble ( $C_b$ ) is clear from the small error of the effective mass. The analysis on the subsamples ( $A$ ) and ( $B$ ) are not presented here, we will however give the estimates of the masses at the end of this section.

At  $\kappa = 0.202$ , which corresponds to the lightest gluino on these ensembles, it was difficult to extract an estimate of the mass since we have only four data points up to  $t = 4$  at our disposal in the effective mass plot in Fig. 4.23 (lower panel). Beyond this time-separation the data are interpreted as noise. The effective mass reaches its minimum at  $t = 2$  than starts increasing as an effect of the noise. Therefore, for the estimation of the mass we use either the effective  $am(2, 3, T)$  or we fit the correlator data in the interval 2 – 4 to the single exponential form. The latter gives us

$$D : am_{a-f_0} = 0.87(10) . \quad (4.24)$$

This value is however to be considered as an upper limit of the mass estimate and the true mass may be located below this value.

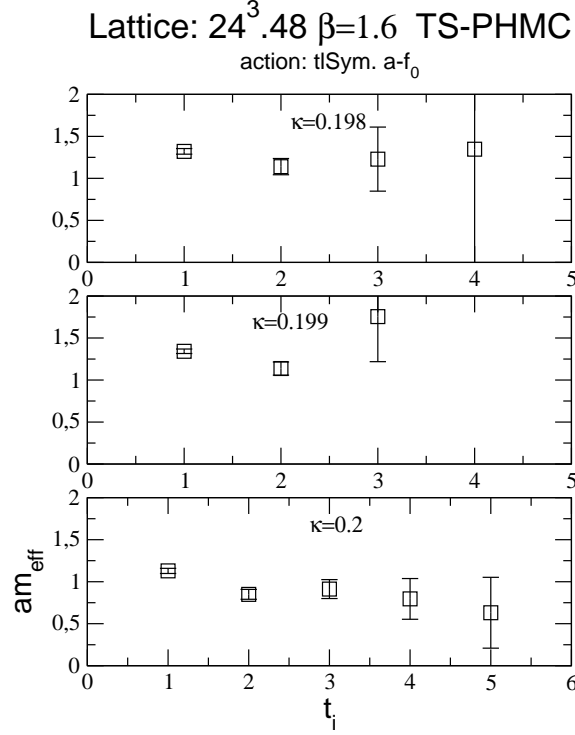


Figure 4.24: *Effective mass of  $a\text{-}f_0$  for the un-stout ensembles on  $24^3 \cdot 48$  lattices*

### $24^3 \cdot 48$ ensembles

The statistics analyzed on the  $24^3 \cdot 48$  lattices for  $a\text{-}f_0$  are summarized in Table 4.10. Here, for the un-stout ensembles we are confronted with somewhat similar problems to those we have met in the previous  $16^3 \cdot 32$  case, despite the fact that we selected reasonable decorrelated subsamples for the analysis. The scalar channel is still characterized by low signal-to-noise ratio as shown in Fig. 4.24 beyond few time-separations up to  $t = 5$  at the latest (at  $\kappa = 0.2$ ). Furthermore, larger lattices could also have the impact of lowering the signal due to the increasing of the global numerical sums for the disconnected terms and may lead to insufficient numerical accuracy. The simulated un-stout points are, as we argued in Section 4.4.2, close to each other and could give us a picture on the smoothness of the masses as function of the bare gluino mass. Despite the problems described above, we nevertheless attempted to extract mass estimates of  $a\text{-}f_0$ . At  $\kappa = 0.198$  and  $\kappa = 0.199$  the mass fit is performed in the intervals  $2 - 4$  and  $1 - 3$  respectively, which yields the estimates

$$\bar{A} : am_{f_0} = 1.15(12) , \quad (4.25)$$

$$\bar{B} : am_{f_0} = 1.314(32) , \quad (4.26)$$

where the small error in the estimations is due to the combination of higher statistics and early starting time in the fit.

We want to discuss the ensemble ( $\bar{C}$ ) separately since we are interested in the effect of the volume. In the last panel of Fig. 4.24 the effective mass stabilizes within error in the  $t$ -range  $[2, 5]$ , but beyond  $t = 5$  it seems to continue getting lower which suggest the influence of higher states in this interval. Nevertheless, the one mass fit in this range yields

$$\bar{C} : am_{a-f_0} = 0.863(81) . \quad (4.27)$$

When comparing to the value  $am_{a-f_0} = 0.931(60)$  obtained on  $16^3 \cdot 32$  lattice at the same point  $\kappa = 0.2$  the mass decreased about 8% as the volume is increased. The larger lattice is usually needed to obtain cleaner results and to identify the true particle. A quantity which is free from finite size effects suggest that is correctly identified. However, the 8% effect in the  $a$ - $f_0$  mass could not be only attributed to the volume effects since the early fitting range could also produce a systematic error.

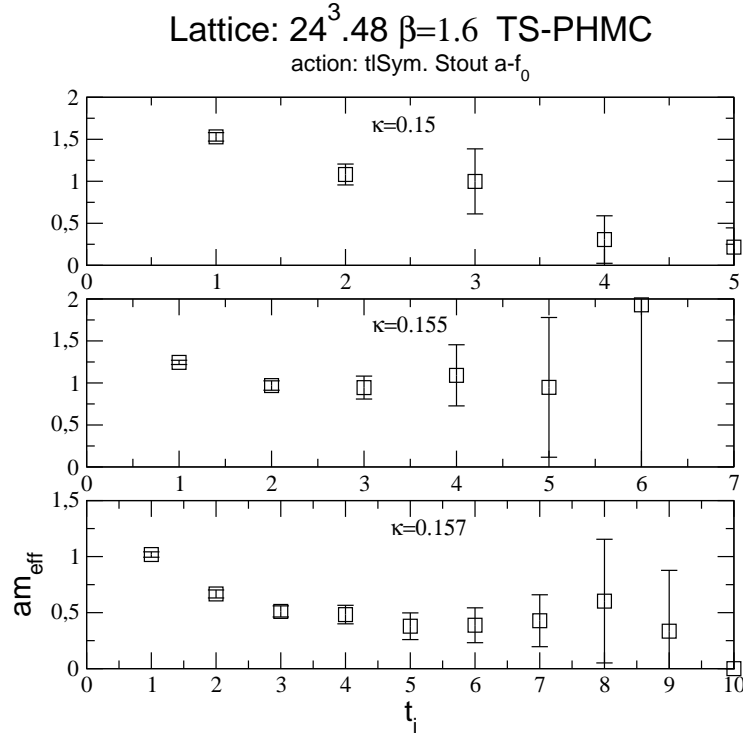


Figure 4.25: *Effective mass of  $a$ - $f_0$  for the un-stout ensembles on  $24^3 \cdot 48$  lattices*

The determination of the  $a$ - $f_0$  mass on the stout subsamples is, interestingly, more accurate than in the unsmearred ensembles. Unlike the un-stout subsamples, excellent



plateaus<sup>3</sup> can be clearly seen in the effective mass as we simulate towards lighter gluino (Fig. 4.25). The good quality of the data can be attributed to the effect of smearing where the  $a$ - $f_0$  signal is more sensitive to the stout smearing. We also observe small errors for the mass at lightest gluino. This is different from what observed for the  $a$ - $\eta'$  where we saw large errors at light gluino mass even with increased statistic. Except the subsample ( $A_s$ ) which is used as starting point for the simulations with stout action, a mass estimation from the effective mass can be obtained on the remaining stout subsamples. The stout smearing seems to increase the signal-to-noise ratio in the scalar channel  $0^{++}$  at the values of dynamical gluino masses closed to the chiral limit, where the effects of supersymmetry breaking are expected. At  $\kappa = 0.15$  and  $\kappa = 0.155$  the fitting ranges were fixed to  $2 - 4$  where the estimated mass may be influenced by higher states at these short time-separations. The effective mass plots are shown in Fig. 4.25 and the estimated masses from global fit are

$$A_s : am_{a-f_0} = 1.07(16) , \quad (4.28)$$

$$B_s : am_{a-f_0} = 0.964(70) . \quad (4.29)$$

At  $\kappa = 0.157$  where the simulation begins to approach the chiral limit as reflected by the smallness of the adjoint pion mass, here  $M_r = 3.4$ , the effective mass in Fig. 4.25 (lower panel) displays good signal allowing the extraction of the  $a$ - $f_0$  mass. We observe at the two starting times a die off of higher states in the signal up to  $t = 3$  where the mass begins to stabilize within small error.

As we mentioned above, this may be due to stout smearing effects at light gluino mass. Thus, we selected a range of time-separations beginning from  $t = 3$  up to  $t = 9$  to isolate the lowest state in this channel. The single mass fit in this range gives us

$$C_s : am_{a-f_0} = 0.467(93) . \quad (4.30)$$

The estimated mass is smaller by roughly 50% than the previous estimated mass at  $\kappa = 0.155$ , which follows a change to smaller value of  $M_r$  of about 70%. This shows a strong dependence of the  $a$ - $f_0$  mass on the light gluino mass.

---

<sup>3</sup>Having in mind here that it concerns the scalar meson known as one of the most noisy channels in lattice hadron spectroscopy and experiments.

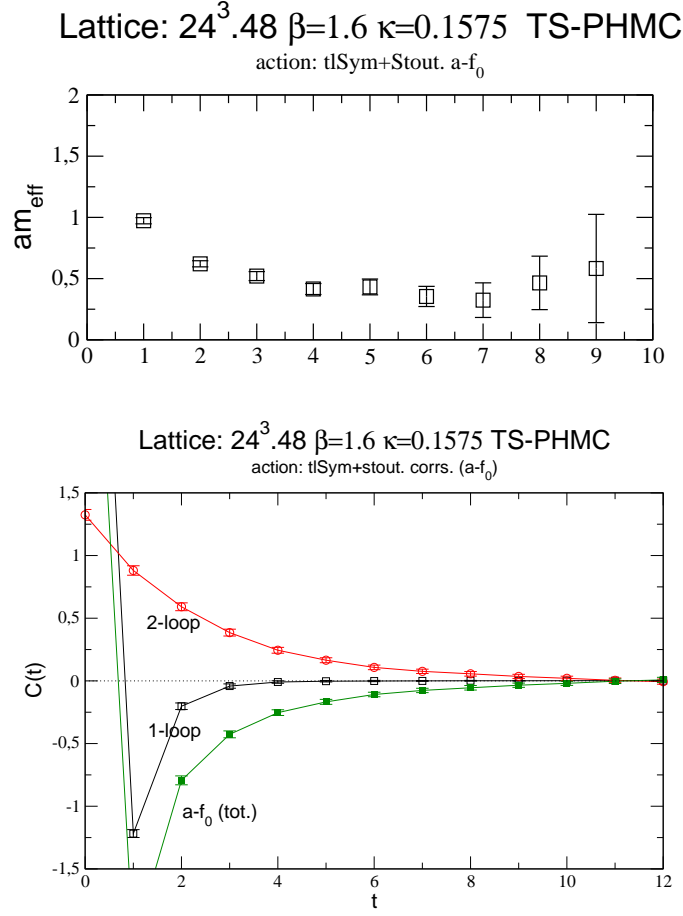


Figure 4.26: *Effective mass of  $a\text{-}f_0$  at  $\kappa_s = 0.1575$  (upper panel) and its correlator contributions (lower panel). The lines are to guide the eye.*

As we saw in the  $a\text{-}\eta'$  analysis, the ensemble ( $D_s$ ) is the most interesting one since it corresponds to the lightest gluino mass in our subsamples, where the smallness of the gluino mass signals that the actual simulation ( $D_s$ ) sits closely to the chiral limit. We tested the effect of the reweighting on the  $a\text{-}f_0$  correlator. The results show that it is not possible to extract the mass estimate without the inclusion of correction factors in the measurement step because the large fluctuation of the errors. The effect is important and the correction factors are necessary for the  $a\text{-}f_0$  mass. This is also expected since the correlator  $C^{a\text{-}f_0}(t)$  is a quantity depending on gluino propagators, and hence such quantity with fermionic degree of freedom is very sensitive to the correction factors. In Fig. 4.26 we show the effective mass plot (upper panel) and the correlator contributions

of the  $a$ - $f_0$  correlation function. As can be seen, the contribution of excited states is suppressed by time-separation  $t = 4$  and the effective mass is independent of time up to  $t = 9$  within error. We fit the  $a$ - $f_0$  correlator in the  $t$ -range  $[4, 8]$  to extract an estimate of the mass which is

$$D_s : am_{a-f_0} = 0.400(59) . \quad (4.31)$$

We observe that the quality of the plateau is better than in the case of  $16^3 \cdot 32$  lattices and  $24^3 \cdot 48$  un-stout lattices. This explains, in one hand, why the result on the  $a$ - $f_0$  mass has smaller error at  $\kappa_s = 0.1575$ . On the other hand, we should discuss why the errors are so small for  $a$ - $f_0$  mass comparing to  $a$ - $\eta'$  mass. In other words, why the disconnected  $a$ - $f_0$  correlator has such as small error as it can be seen in Fig. 4.26 (lower panel). In this figure the individual parts (connected and disconnected) which enter the  $a$ - $a_0$  correlator and the  $a$ - $f_0$  correlator itself are all displayed. The connected part shows clear signal of rapid damping with small error bars. We note that the connected part can be regarded as the adjoint  $a$ - $a_0$  meson in analogy to QCD. We tried during the analysis to extract a mass estimate of the connected correlator mass but the effective mass displays large errors. Note that in QCD  $a_0$  is a heavier state than the pion. The rapid damping of the connected correlator of  $a$ - $f_0$  is in accordance with the fact that the  $a$ - $a_0$  is a heavy mass state that is difficult to be extracted. Fig. 4.26 (lower panel) shows that the disconnected part dominates the  $a$ - $f_0$  correlator which is of order 10 times greater than the connected part. Therefore, we see that the  $a$ - $f_0$  as light adjoint meson results from the disconnected part of the  $a$ - $f_0$  correlator, where the vacuum expectation value (condensate) is subtracted. Moreover, the mass of  $a$ - $f_0$  exhibits strong dependence on the gluino mass, suggesting the relevance of the chiral symmetry breaking to the  $a$ - $f_0$  adjoint meson.

We observe that the fluctuation in the disconnected correlator (without subtraction) is balanced by the condensate subtraction which results in small error for the disconnected correlator  $C_{disc} - \langle f_0 \rangle^2$ . This has to be compared to the disconnected correlator in the  $0^{-+}$  channel for which we observed larger errors (see for example Fig. 4.21).

We also explored the behavior of the scalar disconnected correlator as function of the gluino mass. We choose for this study the subsamples  $(B_s)$ ,  $(C_s)$  and  $(D_s)$ . The disconnected correlators for these ensembles are presented in Fig. 4.27. Unlike the behavior of disconnected correlators in the case of the un-stout ensembles as shown in Fig. 4.21 the disconnected correlators varies slightly as we move from  $\kappa_s = 0.157$  to  $\kappa_s = 0.1575$ . At large time-separations the disconnected correlator is oscillating near zero indicating that the signal is no longer one exponential but sums of more exponentials. Thus, the behavior of the disconnected correlators indicates that the  $a$ - $f_0$  mass decreases considerably slower as function of the hopping parameter.

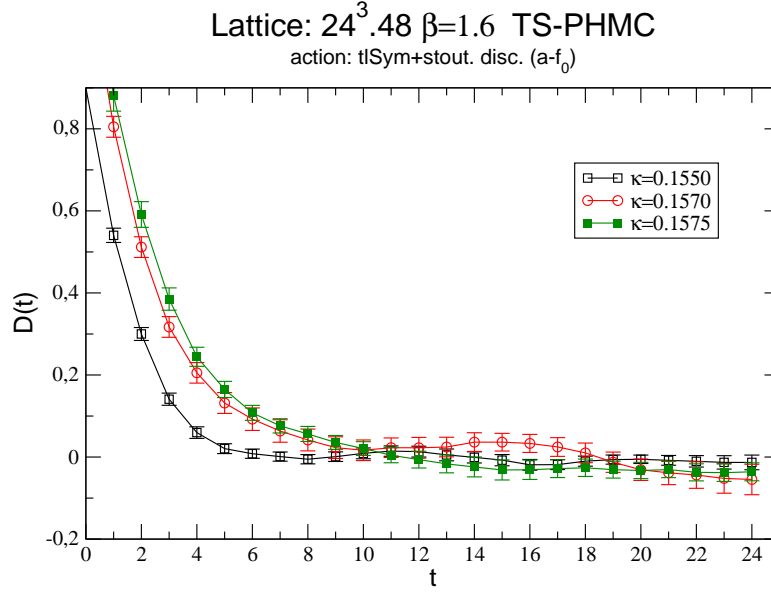


Figure 4.27: Comparison of disconnected correlators for the stout subsamples.

As a conclusion of the two previous sections we summarize the results of the  $a\text{-}\eta'$  and  $a\text{-}f_0$  adjoint mesons mass analysis on the TS-PHMC ensembles. The quoted masses are presented in Table 4.11.

Table 4.11: The results of the  $a\text{-}\eta'$  and  $a\text{-}f_0$  lowest masses for all TS-PHMC ensembles.

Ensemble	$[t_1, t_2]$	$am_{a\text{-}\eta'}$	$[t_1, t_2]$	$a\text{-}f_0$
$A$	[3, 5]	1.3115(67)	[1, 3]	2.229(80)
$B$	[3, 7]	1.0396(72)	[2, 4]	1.27(18)
$C_a$	[5, 7]	0.542(23)	[2, 5]	0.93(11)
$C_b$	[4, 7]	0.5426(75)	[2, 5]	0.931(60)
$D$	[5, 9]	0.361(60)	[2, 5]	0.87(10)
$\bar{A}$	[5, 7]	0.675(18)	[2, 4]	1.15(12)
$\bar{B}$	[4, 7]	0.6215(86)	[1, 3]	1.314(32)
$\bar{C}$	[5, 11]	0.536(24)	[2, 5]	0.863(81)
$A_s$	[3, 5]	1.0114(82)	[2, 4]	1.07(16)
$B_s$	[5, 9]	0.614(23)	[2, 4]	0.964(70)
$C_s$	[5, 9]	0.416(29)	[3, 9]	0.467(93)
$D_s$	[4, 9]	0.364(70)	[4, 8]	0.400(59)

#### 4.4.4 The Glueball $J^{PC} = 0^{++}$

We saw in the previous chapter that glueballs  $G$  mass determination presents challenges in SYM as it is the case also in lattice QCD. The problem lies in the fact that the zero-momentum glueball correlator function decreases rapidly, and is obtained as difference between two fluctuating quantities

$$\langle GG \rangle - \langle G \rangle \langle G \rangle, \quad (4.32)$$

of comparable magnitude, where the last term  $\langle G \rangle$  is present since the scalar glueball  $G$  has non-vanishing overlap with the vacuum. In the calculation of the glueballs, it is known that very large statistics are necessary for a precise determination of the correlation function of gluonic operators by Monte Carlo simulation and hence reduce the statistical error in the correlators. Note that in the case of the TSMB ensembles (previous chapter and Ref. [71]) we saw large fluctuations in the correlator as the lattice size increases, even if smearing techniques are used. There was indeed no argument for an increase in noise with larger lattice size. We would interpret this effect by the increase of the numerical sums in time-slices summations which could make the signal in the correlator more noisy. Therefore, a precise measurement prohibits the lattice size being too large. On the other hand, the physical size has to be maintained to at least 2 fm for reasonable spectrum explorations. A technique which is well known in QCD is the use of anisotropic lattices, where the lattice is finer in the temporal direction so that a reliable signal can be measured before it is spoiled by statistical fluctuations. Our SYM investigation does not consider (at least for the moment) such construction of actions for this purpose, since we are interested on a range of different particles and not only on glueballs.

In this study we analyzed glueballs on all TS-PHMC ensembles ( $16^3 \cdot 32$  and  $24^3 \cdot 48$  lattices), where we take the whole statistics at each value of the hopping parameter  $\kappa$ . The standard gauge invariant operator consisting in a sum of spacial plaquettes  $\mathcal{O} \equiv \mathcal{O}_G = U_{12} + U_{23} + U_{13}$  is used as interpolating field for the scalar glueball. We also applied smearing to the operator  $\mathcal{O}$  in combination with the variational method. The smearing (especially APE) is used to increase the overlap of the glueball ground state with the interpolating operator, while the variational method helps us to better separate the energy of the ground state.

The smearing procedure results in the cross correlation function  $C_{ij}(t) = \langle \mathcal{O}_i \mathcal{O}_j \rangle - \langle \mathcal{O}_i \rangle \langle \mathcal{O}_j \rangle$ . The cross correlator is variationally-optimized  $C_{ij}(t) \rightarrow \tilde{C}_{ij}(t)$ , where  $\tilde{C}_{ij}(t)$  is a diagonal matrix with respect to an optimized fixed time-separation  $t_0$  (see for details Section 2.11). The variational method requires fixing of two times  $t_b$  and  $t_0$  for the basis time and the optimization time respectively where the generalized eigenvalue problem is solved. In all our simulations we fixed the optimization time-separation to  $t_0 = 1$  and the basis time  $t_b = 0$ . Other values of  $t_0$  are used for consistency checks. This method is

known as “fixed-eigenvector method”. This method involves diagonalization on single time-slice  $t_0 = 1$  using the fixed time  $t_b = 0$ . The obtained solution of the eigenvectors is used then to rotate each time-slice correlator to this basis. The largest diagonal element of the each rotated time-slice correlator is used in the exponential fit to extract the lowest state mass.

The second method which has also tested in our study is called principal-correlator method also called  $t$ -eigenvector method in Section 2.11. The difference with respect to the method discussed above is that in the principal-correlator method the diagonalizations are performed on each time-slice  $t_0 = t$  instead of fixed  $t_0 = 1$ . We tested both methods which were consistent and we opted for the use of the fixed-eigenvector method.

In addition to the variational method, we also fit the original diagonal correlators  $C_{ii}(t)$ , where  $i$  refers to the level of APE-smearing, to the asymptotic behavior as it was done in the previous chapter to check our results.

We will discuss in the next the details of analysis at each point  $\kappa$  and lattice size present in this study and the results of the fitting procedures. Our aim was to find on each ensemble a possible fit region  $t_{min} - t_{max}$  in which the correlation function was well described by its asymptotic form. As we will see in the next very convincing plateaus were observed in the case of stout-smearred ensembles.

### **16<sup>3</sup> · 32 ensembles**

On the 16<sup>3</sup> · 32 ensembles we applied four level  $i$  of APE smearing parameters. Each level consists of four steps of APE smearing. At the end the total steps of smearing is equal to  $N_{APE} = 16$ . The APE smearing parameter  $\epsilon$  is fixed to 0.5. We observed short plateaus up to three or four time-separations starting at very early time  $\sim 1$ . Beyond time-separation  $t = 3$  or  $t = 4$  no possible signal is found.

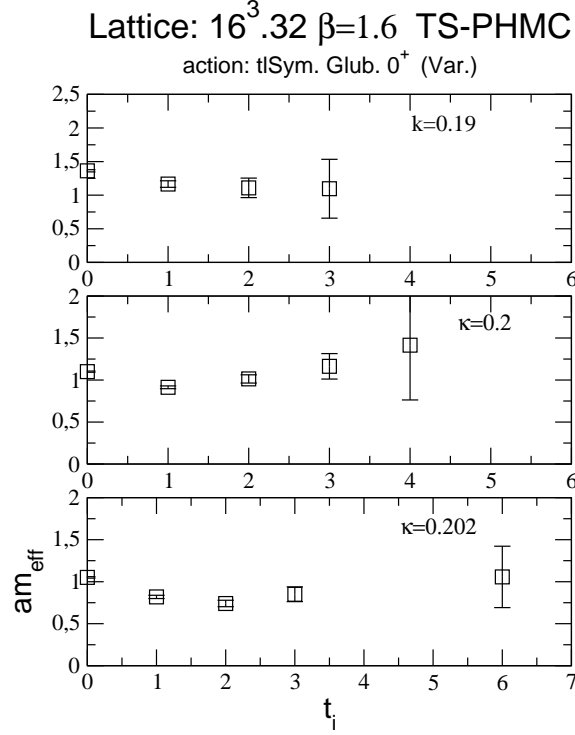


Figure 4.28: *Effective mass of scalar glueball analyzed on lattices  $16^3 \cdot 32$ .*

The effective mass plots for  $0^{++}$  glueball are shown in Fig. 4.28. The plotted mass is the ground state mass from variational method

$$am_{eff}(t) = \ln \frac{\lambda(t)}{\lambda(t+1)} , \quad (4.33)$$

where  $\lambda(t)$  is the largest eigenvalue of the diagonalized cross correlator  $\tilde{C}(t)$  at time-slice  $t$ . The possible reason for very low signal-to-noise ratio is that our lattices are coarse and hence for the glueball a few lattice spacings represent a large time-separation. The signal is dominated by the noise at early time-separations on a coarse lattice. The onset of the single fit was fixed to  $t = 1$  for all subsamples. We assume that the smearing procedure was sufficiently enough to wash out the higher states. We observed also that the error is small for these short plateaus. However, the signal is not enough good to make definite statements. The single mass fit was performed in intervals  $t = 1 - 3$  at  $\kappa = 0.19$  and  $\kappa = 0.2$ , however we take the mass  $am(1, 2, T)$  as estimate at  $\kappa = 0.202$ . The finale mass estimates read

$$(B) : am_{0^{++}} = 1.156(51) , \quad (4.34)$$

$$(C_b) : am_{0^{++}} = 0.945(20) , \quad (4.35)$$

$$(D) : am_{0^{++}} = 0.819(19) . \quad (4.36)$$

These values are consistent with the values of the fitting to the original cross-correlators at similar interval and after three levels of APE smearing. We should however note that the smearing procedure may be not sufficient and the correlator may contain contamination from higher states. Hence, these values are considered as upper limit of the scalar glueball mass.

### $24^3 \cdot 48$ ensembles

On larger lattices we analyzed among the un-stout ensembles the subsample  $\bar{C}$  at  $\kappa = 0.2$  to study finite size effects on the scalar glueball mass.

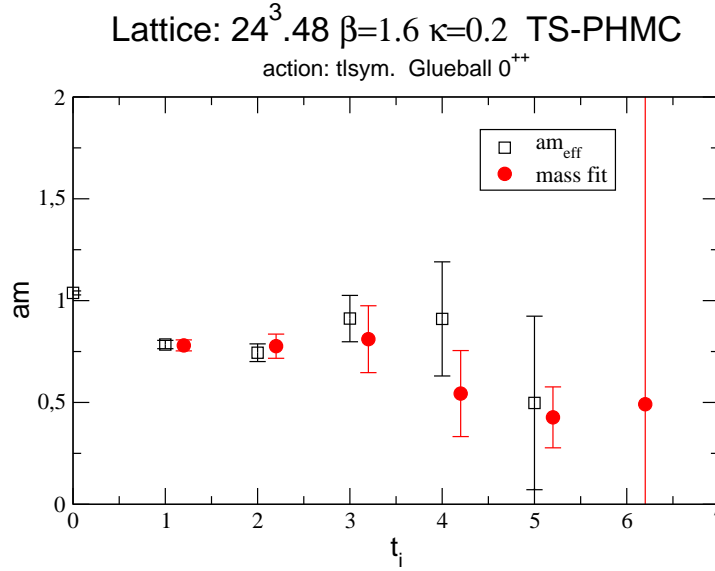


Figure 4.29: *Effective mass and mass fit for scalar glueball on the ensembles ( $\bar{C}$ ). The results are slightly displaced for improved readability.*

The effective mass and mass fit plots displayed in Fig. 4.29 show a signal up to time-separation  $t = 4$ . We applied the smearing parameters  $(\epsilon_{APE}, N_{APE}) = (0.5, 16)$ . Beyond  $t = 4$  the error becomes large indicating the noisiness of the data. The mass fit and the effective mass in this range are of the same order. We fitted the correlator to the single exponential form in the interval  $t = 1 - 4$  to obtain an estimate of the lowest assuming that the influence of higher states is reduced by applying the smearing steps. The mass estimate found on this subsample is

$$\bar{C} : am_{0^{++}} = 0.781(24) . \quad (4.37)$$



Of interest here is the comparison to the scalar glueball mass extracted at the same value of the hopping parameter  $\kappa = 0.2$  on smaller lattice. The mass at larger lattice ( $24^3 \cdot 48$ ) is 17% smaller than the one determined on small lattice ( $16^3 \cdot 32$ ). This difference of masses indicates important finite size effects on the scalar glueball mass. This was, however, not the case of the TSMB ensembles where one observed the increase of the mass as function of the lattice volume. But the TSMB algorithm has simulated smaller physical volumes up to  $\sim (1\text{fm})^3$  which are not suitable for mass spectrum exploration. In addition the TSMB ensembles were produced at smaller lattice spacing. Therefore, a direct comparison to TSMB results does not yield final statements.

We turn back the TS-PHMC ensembles and the scalar glueball mass determined on  $16^3 \cdot 32$  and  $48^3 \cdot 48$  at  $\kappa = 0.2$ . An indication of the effect of the volume on the scalar glueball mass can be also obtained from the behavior of the Sommer scale parameter  $r_0/a$  since the latter is a pure gluonic quantity. We saw from the extrapolated values of  $r_0/a$  that its value on the  $24^3 \cdot 48$  lattice is about 6% smaller than on the  $16^3 \cdot 32$  lattice. Qualitatively, we observe that the scalar glueball mass is more affected by finite lattice volume than other gluonic quantities like  $r_0/a$  or the plaquette.

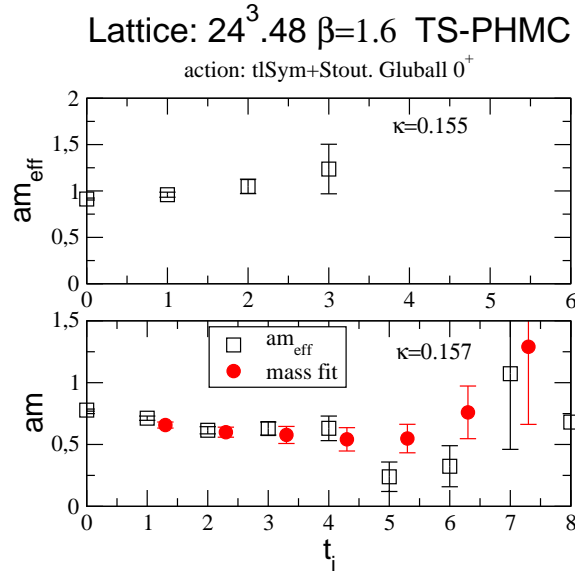


Figure 4.30: *Effective mass and mass fit for scalar glueball on the ensembles ( $B_s$ ) and ( $C_s$ ). The results are slightly displaced for improved readability.*

The stout smearing is used for the first time in the production of gauge configurations

for the SYM spectrum study. Besides reducing the fluctuation of the lowest eigenmodes of the Dirac-Wilson fermion matrix, the stout smearing has also the benefit in SYM of increasing the signal-to-noise ratio of the  $a$ - $f_0$  adjoint meson. It seems that the  $0^{++}$  channel is very sensitive to the stout smearing as we will see in the next. We analyzed the scalar glueball  $0^{++}$  on the stout smeared ensembles using the variational method applied to APE smearing with the same parameters as in the previous analysis,  $(\epsilon_{APE}, N_{APE}) = (0.5, 16)$ .

In Fig. 4.30 the effective mass plots are shown for the ensemble  $(B_s)$  and  $(C_s)$  in upper and lower panel respectively. Beside the effective mass we plotted the fitted mass in the lower panel, ensemble  $(C_s)$ . At  $\kappa_s = 0.155$  no signal beyond  $t = 4$  is found. The effective mass  $am(t, t+1, T)$  grows slowly as function of  $t$  in the  $t$ -range suggesting that effect of the smearing decreases with the time-separation for this ensemble and the applied smearing parameters may be not the optimal. Nevertheless, we take as estimate for the mass on this ensemble the following fitted mass in the  $t$ -range 2 – 4

$$B_s : am_{0^{++}} = 1.079(92) . \quad (4.38)$$

In the ensemble  $(C_s)$  the fitting of the largest eigenvalue data  $\lambda(t)$  to the one mass form shows the emergence of a clear plateau spanning five time-separations. The onset of the plateau occurred at time-separation  $t = 1$  (lower panel in Fig. 4.30). The effective mass calculations displays also consistent results. The mass fit has the advantage that it incorporates as much as possible informations in the fit differently from the effective mass which uses a pair of time-slices. This demonstrates indeed the effectiveness of APE smearing and variational technique in diminishing excited-state contamination. But also here the better signal-to-noise ratio can be attributed to the stout smearing which is expected to be efficient at light gluino mass for the  $0^{++}$  channel. This is compatible with what we saw in the analysis of  $a$ - $f_0$  at light gluino. As our best estimate for the scalar glueball  $0^{++}$  we take the fitted value in the interval 3 – 6 which reads

$$C_s : am_{0^{++}} = 0.582(61) . \quad (4.39)$$

As we expected in the analysis of the scalar glueball  $0^{++}$  on the  $(D_s)$  ensembles, similarly to the previous point the resulting good signal-to-noise ratio allows reliably extraction of lowest state mass. Unlike the scalar adjoint meson at this point  $\kappa_s = 0.1575$  the scalar glueball signal is independent of the reweighting procedure. The effective mass calculation and the mass fit plots is presented in Fig. 4.31 with and without the inclusion of the correction factors in the statistical average, lower and upper panel respectively. As can be seen the statistical averages are not affected by the inclusion of the correction factor as it is expected for the pure gluonic quantities. We observed consistent results from effective mass and mass fit which generates a clear plateau starting at  $t = 2$ , continuing within error up to  $t = 6$ . This suggests the isolation of the lowest state since

for large  $t$  the fitted mass grows again. A fit in the  $t$ -range 3 – 6 is performed to extract the best determination of lowest mass estimated to be

$$D_s : am_{0^{++}} = 0.449(38) . \quad (4.40)$$

Finally, we summarize the results of the scalar glueball  $0^{++}$  mass estimates on the TS-PHMC ensembles in Table 4.12. In column 2 the configuration range used in the analysis is given, where each configuration was analyzed. Column 3 and 5 give the mass estimate from variational technique and usual method respectively. We note that the best results were obtained for the stout-smearred ensembles at lighter gluino mass, *i.e.* ensemble ( $C_s$ ) and ( $D_s$ ).

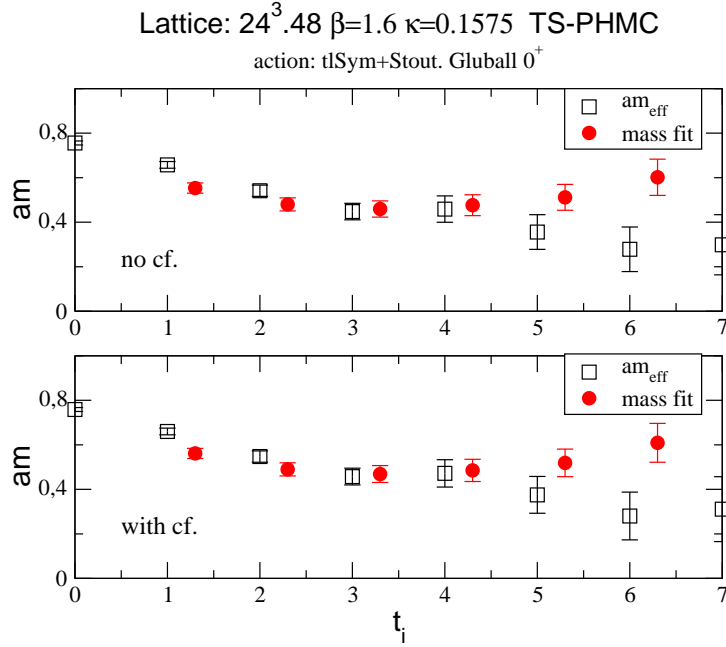


Figure 4.31: *Effective mass and mass fit for scalar glueball at  $\kappa_s = 0.1575$ . Correction factor included in lower panel and not included in upper panel. The results in the lower panel are slightly displaced for improved readability.*

#### 4.4.5 The Gluino-glueballs

From our analysis of the gluino-glueball Majorana fermion  $\chi \equiv \tilde{g}g$  on the TSMB ensembles we observed that no signal can be obtained when using local interpolating operators  $\chi(x) \sim \sigma \text{Tr}[P(x)\lambda(x)]$  at source and sinks (no smearing). A first source of noise is the

Table 4.12: *The results of the scalar glueball  $0^{++}$  lowest mass for all TS-PHMC ensembles.*

Run	$N_{conf}^{0^{++}}$	$am_{0^{++}}(\text{var})$	$[t_1, t_2]$	$am_{0^{++}}(\text{diag})$	$[t_1, t_2]$
<i>A</i>	300-2499	1.291(13)	1-3	1.21(17)	1-3
<i>B</i>	100-2699	1.156(51)	1-3	1.14(10)	1-3
<i>Ca</i>	400-1972	0.927(40)	1-3	0.952(84)	1-3
<i>Cb</i>	1800-10669	0.945(20)	1-4	0.961(80)	1-3
<i>D</i>	1700-6859	0.819(19)	1-2	0.84(12)	1-4
$\bar{C}$	4100-6443	0.781(24)	1-4		
$B_s$	200-1729	1.079(92)	2-4		
$C_s$	300-2110	0.582(61)	3-6	0.588(76)	2-4
$D_s$	100-2000	0.449(38)	3-6		

gluonic content of those operators. Furthermore, the interpolating field could have an important overlap with higher states which may have masses near the ground state mass. We used the same techniques as in the analysis of the TSMB subsamples.

The two periodic and anti-periodic components of the gluino-glueball correlator are used for independent determinations of the lowest mass. We performed tests on selected configurations to find the optimal smearing parameters on these ensembles at  $\beta = 1.6$ . Optimal smearing parameters yield an interpolating field having good projection onto the ground state. In addition, to preserve the signal from being totally washed out, we searched the Jacobi smearing parameters which give a Jacobi radius  $R_J$  defined in eq. (2.111) of about half the spatial lattice extent *i.e.*  $R_J \sim 8$  on a  $16^3 \cdot 32$  lattice. There are indeed several combinations of smearing parameters which satisfy  $R_J = 8$ , but taking into account the computing time which grows with  $N_{jac}$  we fixed  $N_{jac}$  to few values ranging in 4 – 8. After much exploratory testing and trials, we found that  $\epsilon_{jac} = 0.2$ , which was used in previous DESY-Münster collaboration, minimizes the contamination of higher states.

In all runs, the correlator is constructed from the smeared source operator and the smeared/local operator sink. In most cases the results of masses are obtained from correlators built up from both smeared source and sink. The correlator depends on the gluino propagator whose computation is the most demanding task. We were confronted with some problems in parallelizing the code into a MPI/C++ code in all directions of the lattice. For this part these problems occur for the Jacobi smearing routine. A serial version could not help here since we simulated larger lattices at light gluino masses and the computation would take too long time. We split the code into three part; generating the source vectors, performing inversions on these sources and finally building

up the time-slice correlation functions. This results in relatively fast running time and calculation of gluino-gluon correlators can be done for our TS-PHMC ensembles.

In the following, we will give details on the analysis of the gluino-gluon  $\chi$  on the TS-PHMC subsamples.

### $16^3 \cdot 32$ ensembles

On the  $16^3 \cdot 32$  lattices we analyzed all produced configurations at each value of  $\kappa$  except for the ensemble ( $C_b$ ) where we skipped one configuration in the measurement steps. The number of analyzed configurations and the smearing parameters are summarized in Table 4.13.

Table 4.13: *The number of configurations and the smearing parameters for the gluino-gluon for the lattices  $16^3 \cdot 32$ .*

Run	$N_{conf}$	$\epsilon_{APE}$	$N_{APE}$	$\kappa_{jac}$	$N_{jac}$
$A$	2200	0.15, 0.5	8	0.2	0, 6
$B$	2600	0.15	8	0.2	0, 4
$Ca$	1573	0.15	8	0.2	0, 4, 8
$Cb$	4435	0.15	8	0.2	6
$D$	5160	0.5	4	0.2	6

The data obtained from effective mass calculations are shown in Fig. 4.32 and Fig. 4.33 for  $C_{\parallel}$  and  $C_{\gamma_0}$  components respectively. At lighter gluino masses,  $\kappa = 0.2$  and  $\kappa = 0.202$  the effective mass develops plateaus with  $t$  from the beginning up to time-separation  $t = 7, 8$  for the anti-symmetric component. Shorter plateaus emerge in the corresponding effective mass for the  $C_{\gamma_0}$  component where the signal is polluted by higher states up to three time-separation. The error are large for large  $t$  values, and the data points are not shown if the error render them insignificant. For example at  $\kappa = 0.2$  the  $\chi$  mass using the  $C_{\parallel}$  and  $C_{\gamma_0}$  data is extracted from the one exponential fit in the  $t$ -range 3 – 7 and 4 – 7 respectively, and its estimate is

$$C_b : am_{\chi_1} = 0.979(17) , \quad (4.41)$$

$$C_b : am_{\chi_{\gamma_0}} = 1.023(30) . \quad (4.42)$$

It turns out that the two independent extractions of the  $\chi$  mass agree within error and give consistent estimates. In our case we focus on the results of  $C_{\parallel}$  since more data are available for the mass fit compared to the results of component  $C_{\gamma_0}$ . Note that in [18] it was found that the  $C_{\gamma_0}$  gives a better signal than the  $C_{\parallel}$  correlator, and the latter was considered for mass estimations. However, in Ref. [71] an extremely stable plateau

was found right from the starting time-separation using the  $C_{\mathbb{I}}$  component. This was considered as a rather intriguing result.

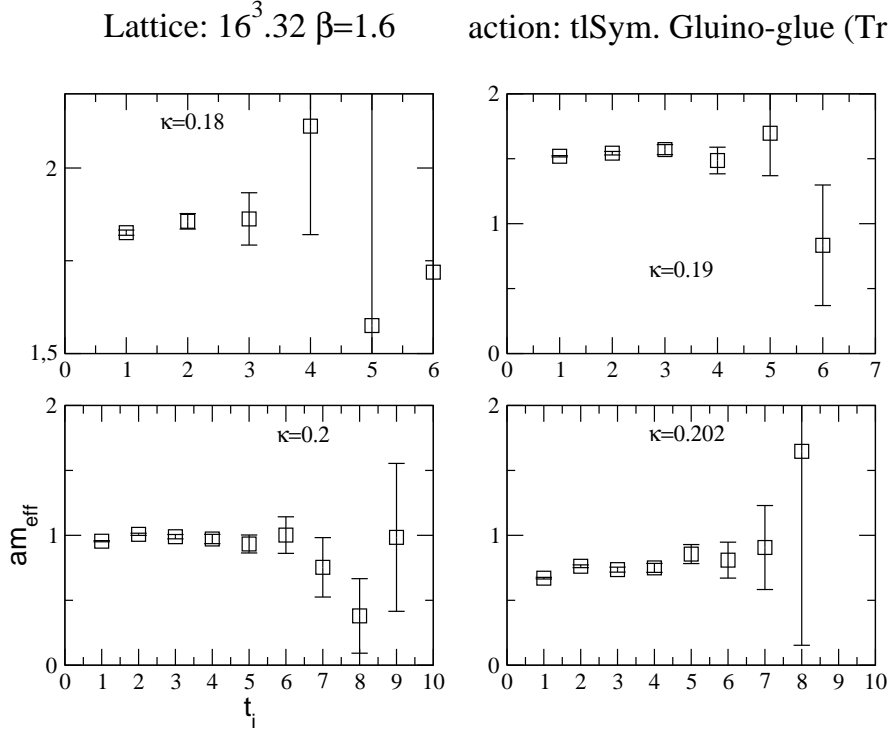


Figure 4.32: *Effective mass plots of the gluino-gluon bound state  $\chi$  from the anti-periodic component  $C_{\mathbb{I}}$ .*

Nevertheless, the plateaus from periodic and anti-periodic components refer to consistent fitted masses. At lightest gluino mass  $\kappa = 0.202$  no signal could be obtained without the inclusion of the correction factor. This is somehow expected since besides gluonic degrees of freedom the gluino-gluon contains also fermionic degrees of freedom. Therefore, the correlator depending on fermionic propagators is sensitive to the reweighting step. We observed also small errors at small time-separations. Note that besides the smearing procedure high statistics in the present work are considered which decrease the statistical error since the TS-PHMC ensembles are characterized by short autocorrelations with respect to many lattice observables. Furthermore, for the anti-periodic  $C_{\mathbb{I}}$  component the smearing procedure was sufficient to wash out the higher states from the first time-separation.

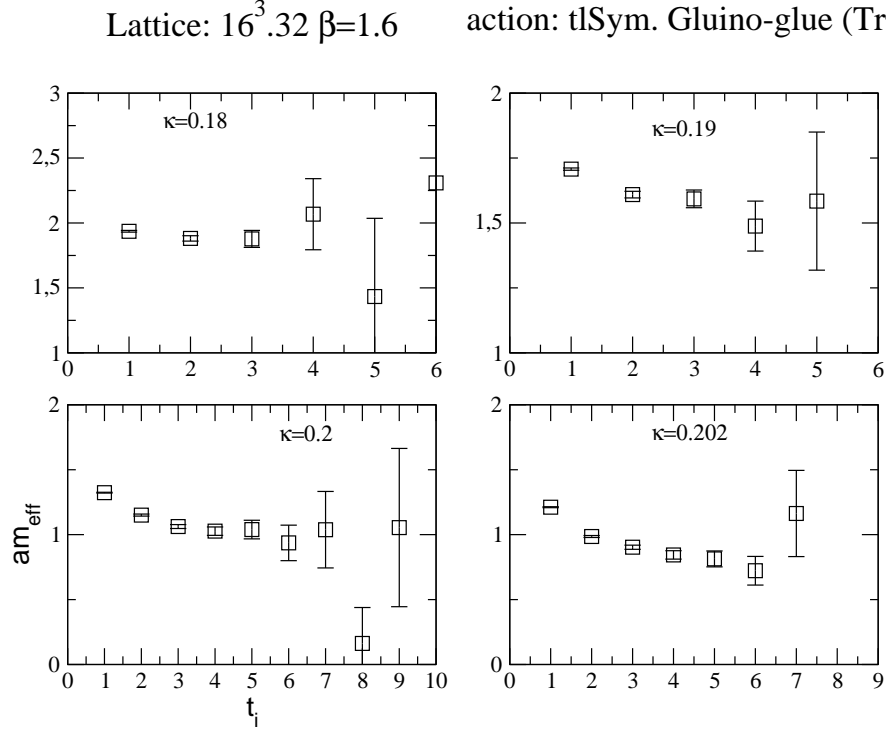


Figure 4.33: *Effective mass plots of the gluino-gluon bound state  $\chi$  from the periodic component  $C_{\gamma_0}$ .*

To check how the results depend on the light gluino mass we plotted the masses (extracted using the two correlator components  $C_{\parallel}$  and  $C_{\gamma_0}$ ) as function of the inverse hopping parameter,  $1/\kappa$ . As can be seen in Fig. 4.34 there is a clear dependence on the gluino mass, and the decrease of the  $M_r$  quantity of about 80% from  $\kappa = 0.2$  to  $\kappa = 0.202$  results in  $\chi$  mass which is  $\sim 23\%$  lower at  $\kappa = 0.202$  than that at  $\kappa = 0.2$ . We also compare the difference of mass estimates from both gluino-gluon components. It is seen that the difference is negligible in most estimations except at  $\kappa = 0.202$  where the estimate from  $C_{\gamma_0}$  component is about 8% heavier than the one from  $C_{\parallel}$ . However, this is still a small deviation. Furthermore, since we observed that the signal of  $C_{\gamma_0}$  is not as good as the signal of  $C_{\parallel}$ , the difference can be attributed to statistical uncertainties.

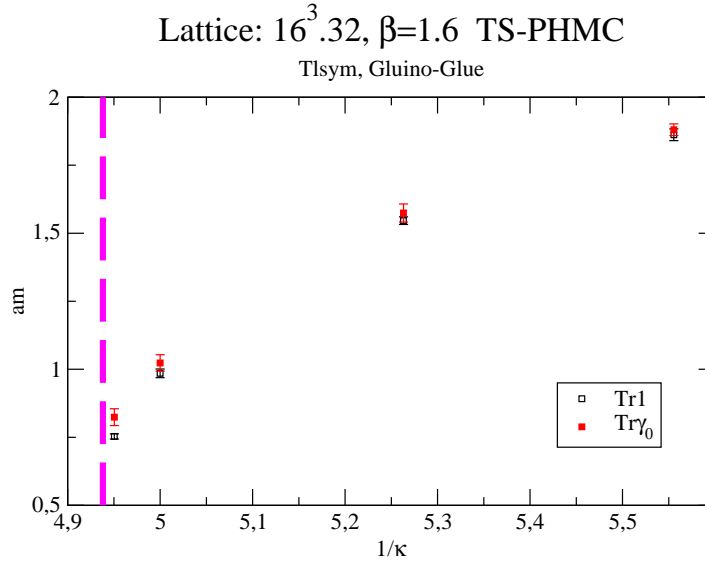


Figure 4.34: Results of gluino-glueball masses on  $16^3 \cdot 32$  lattices for periodic and anti-periodic components as function of the inverse hopping parameter.

### $24^3 \cdot 48$ ensembles

On finer lattices explored during several past years by the DESY-Münster collaboration, the results showed that passing to largest lattices resulted in better results for the gluino-glueball bound state. On our present coarse lattices we see clear signals in the effective mass in all  $24^3 \cdot 48$  ensembles. Particularly for the  $C_{\mathbb{I}}$  the mass is constant over a long  $t$ -range starting in most cases at  $t = 1$  and continuing up to time-separation  $t = 8, 9$ . For larger time-separation the noise dominates probably as an effect of the coarseness of the lattice. The number of configurations analyzed at  $24^3 \cdot 48$  and the smearing parameters applied on these ensembles are summarized in Table 4.14.

The results of effective mass agree nicely for the  $C_{\mathbb{I}}$  and  $C_{\gamma_0}$  components. This is valid for both un-stout and stout subsamples. The stabilization of the effective mass with small error and the absence of a smooth drop of the mass suggests that the spatially-extended smeared interpolating operators appear to be very useful for optimizing the signal-to-noise ratio of the gluino-glueball and the overlap with the lowest mass state. The combination of link smearing (APE) and gluino smearing (Jacobi) dramatically reduces the statistical error of the correlator and the excited state contamination. Hence, the single state is dominating the correlator in the  $t$ -window where the effective mass is  $t$  independent. A single exponential in most cases gives an accurate estimate of the gluino-glueball mass.



Table 4.14: *The number of configurations and the smearing parameters for the gluino-glueball for the lattices  $24^3 \cdot 48$ .*

Run	$N_{conf}$	$\epsilon_{APE}$	$N_{APE}$	$\kappa_{jac}$	$N_{jac}$
$\bar{A}$	1380	0.15	8	0.2	6
$\bar{B}$	1200	0.15	8	0.2	6
$\bar{C}$	1561	0.15	8	0.2	6
$B_s$	1530	0.15	8	0.2	6
$C_s$	1811	0.15	8	0.2	6
$D_s$	900	0.15	8	0.2	6

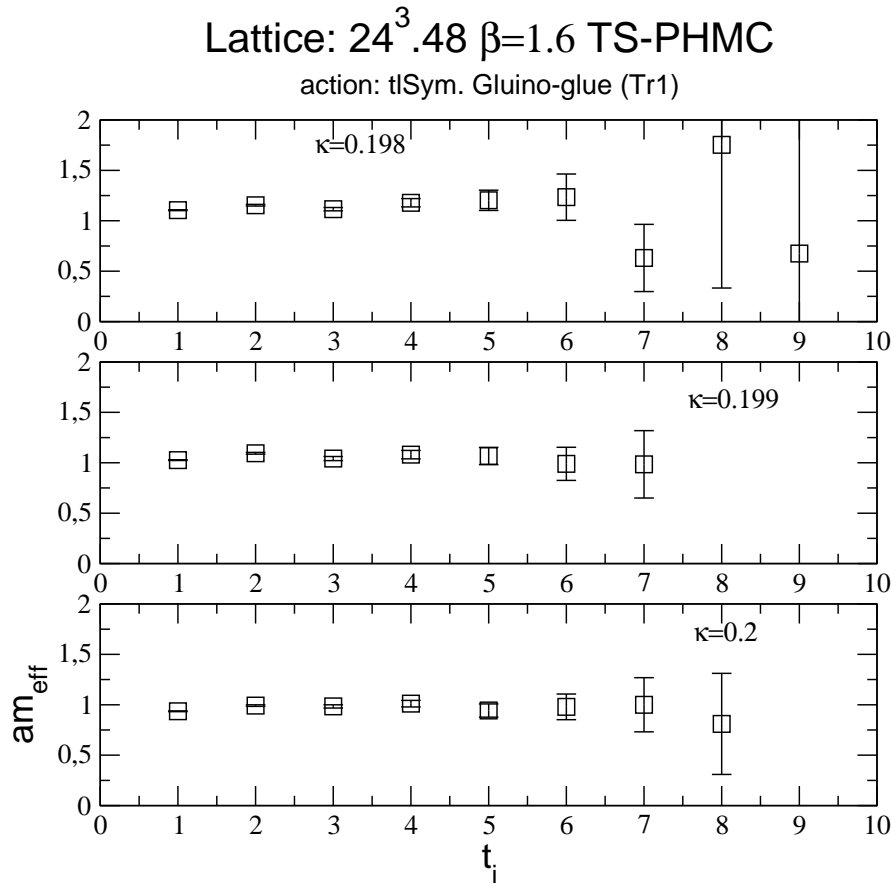


Figure 4.35: *Effective mass plots of the gluino-glueball bound state using the independent component  $C_{\mathbb{I}}$  for the un-stout subsamples.*

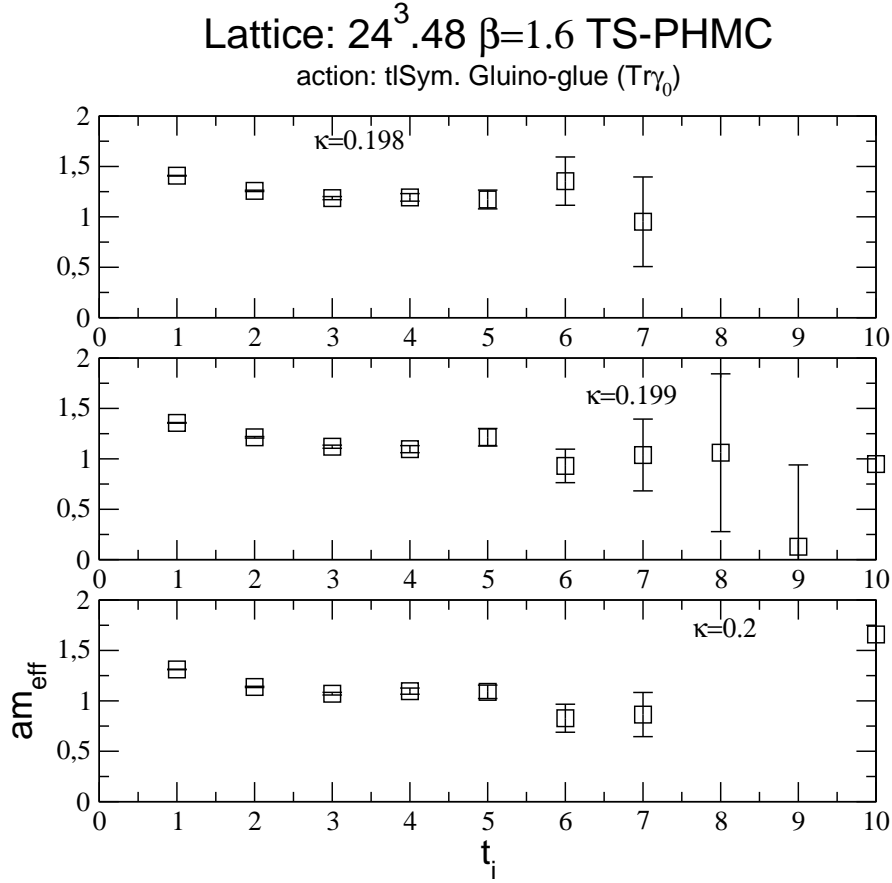


Figure 4.36: *Effective mass plots of the gluino-gluon bound state using the independent component  $C_{\gamma_0}$  for the un-stout subsamples.*

The effective mass calculations are presented in Fig. 4.35 , Fig. 4.36 for the unstout subsamples and Fig. 4.38, 4.37 for stout subsamples. On most subsamples one mass fits were performed in intervals starting at  $t = 2$  for the  $C_{\parallel}$  component and spanned 7 – 8 time-separations. Of interest is the estimation of the gluino-gluon mass at  $\kappa = 0.2$ . The fitted mass in  $t$ -range 2 – 8 reads

$$\bar{C} : am_{\chi_1} = 0.9895(70) . \quad (4.43)$$

When comparing to the results obtained on small lattice at the same gluino mass  $\kappa = 0.2$ , it is evident that the estimations are free of finite size effects starting at the lattice volume  $16^3 \cdot 32$ . The masses agree nicely, but our measurements could be affected by different systematic errors, in particular  $\mathcal{O}(a)$  effects, when extrapolating to chiral/SUSY limit. Nevertheless, we observed more stable and wide plateaus on larger lattices which renders the results more accurate. Accuracy is relevant in the spectrum investigations, where extrapolation to continuum limit must be eventually carried out. The signal-to-noise

ratio is also better on larger lattices. Improving the resolution in the temporal direction will result in more data for the fit in the region where the plateaus emerge.

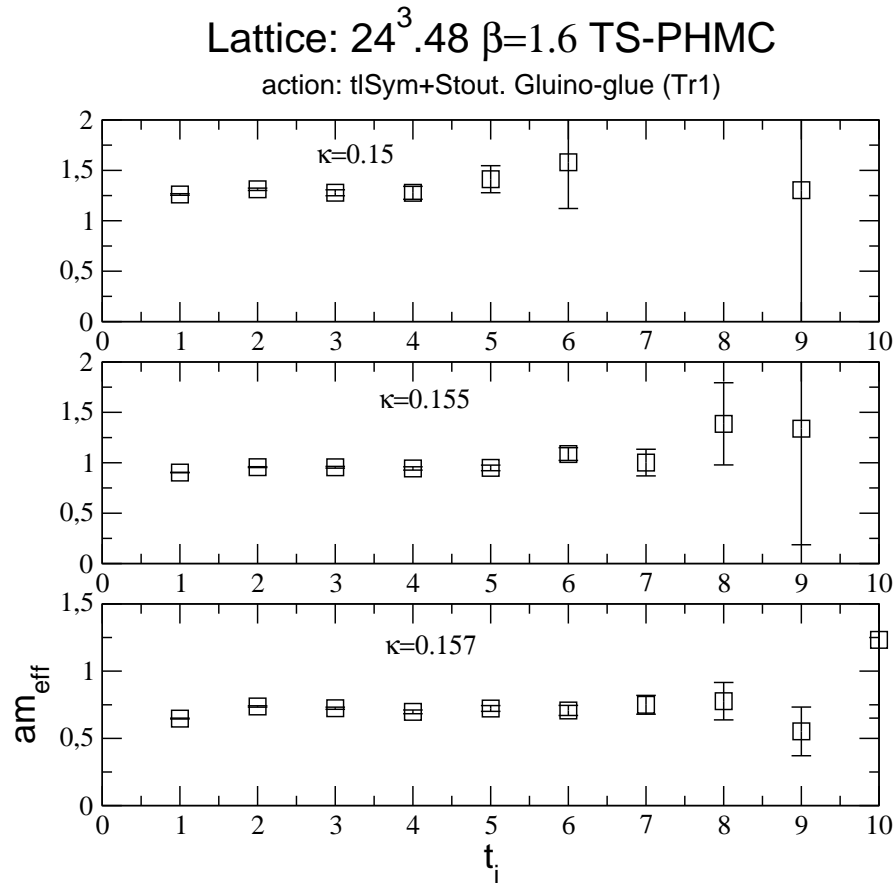


Figure 4.37: *Effective mass plots of the gluino-gluon bound state using the independent component  $C_{\perp}$  for the stout subsamples.*

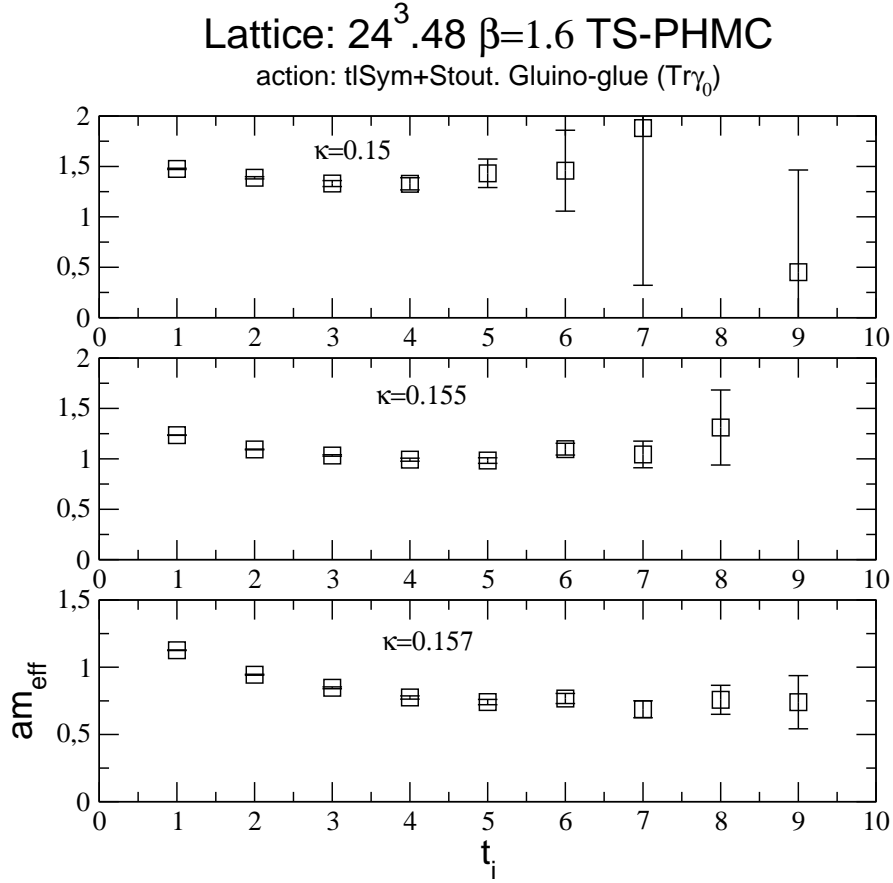


Figure 4.38: *Effective mass plots of the gluino-gluon bound state using the independent component  $C_{\gamma_0}$  for the stout subsamples.*

We turn now out to the analysis of the gluino-gluon on the stout subsample at  $\kappa_s = 0.1575$ . As argued in the sections above this point corresponds to the lightest gluino mass of our present runs and may show effects of a weak SUSY breaking. The analysis at this point must involve the correction factors: no reasonable signal can be obtained when the reweighting step is not carried out. We checked also the results by using local and smeared sinks, which give consistent results. In Fig. 4.39 the results show the effective mass from  $C_{\mathbb{1}}$  and  $C_{\gamma_0}$  components where only the source is smeared and the sink is local. In addition the mass fit plot in the upper panel ( $C_{\mathbb{1}}$  component) illustrates the consistency of the results.

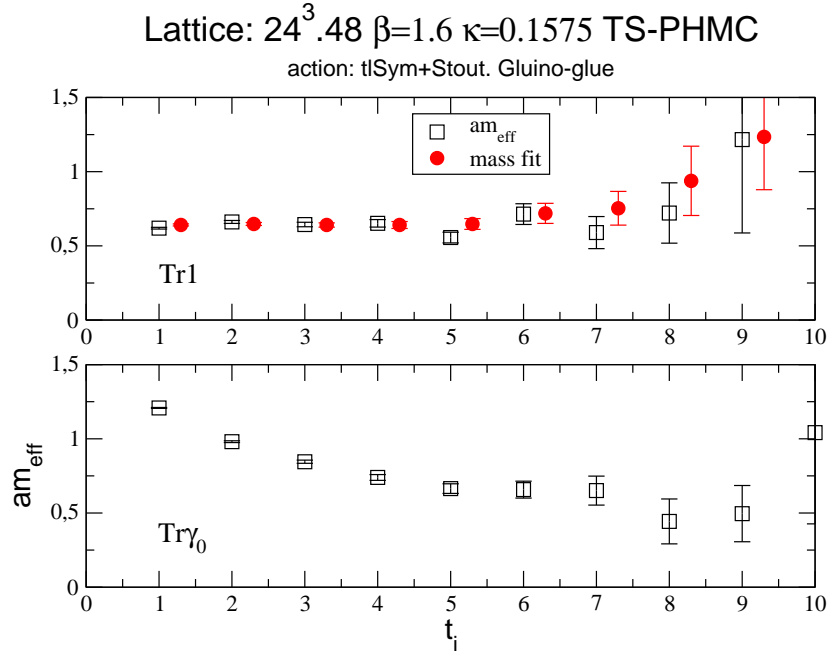


Figure 4.39: *Effective mass plots of the gluino-gluon bound state using the two independent components  $C_{\mathbb{I}}$  and  $C_{\gamma_0}$  at  $\kappa_s = 0.1575$ . In upper panel the fitted mass is plotted to show consistency, the data are slightly displace to improve readability.*

Our results of the gluino-gluon mass using the two independent Dirac structures  $C_{\mathbb{I}}$  and  $C_{\gamma_0}$  for all lattice are summarized in Table 4.15. It becomes now evident that larger lattices and the smeared operators are very suitable to obtain satisfactory signal for the gluino-gluon, and hence accurate mass determination. Furthermore, combining the smearing with variational techniques and the simulation of finer lattices, at larger gauge coupling  $\beta$ , could improve the estimations.

## 4.5 Lattice SUSY Ward-Identities

We have seen in previous chapter for TSMB that a complete investigation of the SYM in numerical simulations involves the exploration of the lattice supersymmetric Ward identities (SUSY WIs) which are used to verify the restoration of SUSY in the continuum limit. In our analysis we study the lattice SUSY WIs in numerical simulation along the line of Ref. [21].

We consider here again the lattice SUSY WIs as explored in the previous chapter. Our aim is the non-perturbative determination of the renormalization constants ratio

Table 4.15: *The results of the gluino-gluonball  $\chi$  lowest masses for all TS-PHMC ensembles.*

Ensemble	$[t_1, t_2]$	$am_{\chi_1}$	$[t_1, t_2]$	$am_{\chi_{70}}$
$A$	[2, 5]	1.862(21)	[2, 4]	1.883(22)
$B$	[2, 5]	1.546(14)	[3, 5]	1.574(33)
$C_a$	[2, 4]	0.984(12)	[3, 5]	1.049(25)
$C_b$	[3, 7]	0.979(17)	[4, 7]	1.023(30)
$D$	[2, 4]	0.7532(96)	[4, 7]	0.824(31)
$\bar{A}$	[2, 8]	1.1456(82)	[3, 6]	1.187(15)
$\bar{B}$	[2, 7]	1.0789(95)	[3, 7]	1.117(15)
$\bar{C}$	[2, 8]	0.9895(70)	[3, 7]	1.074(13)
$A_s$	[2, 6]	1.302(14)	[3, 5]	1.329(26)
$B_s$	[2, 7]	0.9559(48)	[4, 6]	0.989(14)
$C_s$	[2, 8]	0.7250(56)	[5, 9]	0.742(20)
$D_s$	[2, 8]	0.6454(96)	[5, 7]	0.66(30)

$Z_T/Z_S$  and the additively renormalized gluino mass  $am_S/Z_S$  for the bare gluino masses simulated within the TS-PHMC algorithm. For the numerical analysis of SUSY WIs we consider the version involving the local (point-like) SUSY current  $S_\mu^l(x)$  and mixing current  $T_\mu^l(x)$  at sink. As insertion operator is the spatial interpolating operator with the clover plaquette  $\chi^{(sp)}(x)$ .

We analyzed all the TS-PHMC subsamples where the statistics are as given in Table 4.13 and Table. 4.14. The smearing parameters listed in these tables are used for the source operators in the SUSY WIs correlators. The sink operators are however local.

The two approaches to solve the system of equations for unknown  $am_S/Z_S$  and  $Z_T/Z_S$  are carried out as explained in Section 2.9. The results for the subtracted gluino mass from solving the equations system on each time-slice (effective) and from the linear fit involving all data (fitted value) are summarized in Table 4.16. For the ratio of renormalization constants the results are given in Table 4.17.

Table 4.16: *The results for the renormalized gluino mass  $am_{\tilde{g}}/Z_S$  in lattice unit from effective mass calculation (column 3) and as function of  $t_{min}$  from the linear fit (column 5). (TS-PHMC ensembles).*

Ensemble	$t_i$	effective $am_{\tilde{g}}/Z_S$	$t_{min}$	fitted $am_{\tilde{g}}/Z_S$
$A$	3	1.210(52)	3	1.212(52)
	4	1.59(30)	4	1.59(30)
	5	1.5(12)	5	1.5(11)
$B$	3	0.710(22)	3	0.710(21)
	4	0.725(92)	4	0.727(92)
			5	0.99(50)
$C_a$	3	0.172(16)	3	0.171(15)
	4	0.187(60)	4	0.180(56)
$C_b$	3	0.1658(99)	3	0.1676(92)
	4	0.166(34)	4	0.163(31)
			5	0.133(93)
$D$			3	0.059(42)
			4	0.054(59)
			5	0.100(27)
$\bar{A}$	3	0.271(10)	3	0.2722(98)
	4	0.277(36)	4	0.279(34)
	5	0.28(12)	5	0.27(11)
$\bar{B}$	3	0.216(10)	3	0.2167(97)
	4	0.212(36)	4	0.213(34)
$\bar{C}$	3	0.1527(85)	3	0.1557(78)
	4	0.161(29)	4	0.166(27)
$B_s$			7	0.46(11)
			8	0.496(89)
			9	0.40(13)
$C_s$	7	0.22(12)	7	0.253(66)
			8	0.210(26)
			9	0.231(31)
			10	0.237(69)
			11	0.207(74)
$D_s$			6	0.113(47)
			7	0.192(55)
			8	0.172(43)
			9	0.118(53)

The results of the subtracted gluino mass were carried out by fitting the data from  $t_{min}$  to the maximum extent of the symmetrized correlation functions,  $T/2 - 1$ . A signal of contact terms indicates their presence up to time-separation  $t < 3$ . Therefore, in the case of un-stout subsamples we started the linear fit from  $t_{min} = 3$ . The effective data, when available, agree with the fitted values. From  $t_{min} = 3$  up to roughly three time-separations we observed a stable value resulting in a plateau behavior in most cases. For larger time-separations we observed huge statistical error indicating the noisiness of the data. At  $\kappa = 0.202$  the statistical reweighting was necessary to obtain reliable data. The effect of the correction factor is relevant in this case. The dependence of the renormalized gluino mass on the hopping parameter is clear from the results. As expected  $am_S/Z_S$  decreases when the hopping parameter approaches the critical point  $\kappa_{cr}$ . In this case we obtain for our lightest gluino  $m_{\tilde{g}} \approx 126$  MeV using the Sommer scale parameter discussed in Section 4.2.2. This value is of the order of the strange quark (70-130 MeV). Of interest also is the comparison of the gluino mass at  $\kappa = 0.2$  on  $16^3 \cdot 32$  and  $24^3 \cdot 48$  lattices to study the effect of the lattice volume. We find agreement for the obtained values, and hence the gluino mass does not undergo finite size effect on our coarse lattices  $\beta = 1.6$  starting from lattice extension  $L = 16$ . This agrees nicely with what is expected since as known the SUSY WIs hold for any lattice volume up to  $\mathcal{O}(a)$  effects.

Table 4.17: *The results for the renormalization ratio  $Z_T/Z_S$  as function of  $t_{min}$  from the linear fit (TS-PHMC ensembles).*

Ensemble	$t_{min} = 2$	$t_{min} = 3$	$t_{min} = 4$	$t_{min} = 5$
$C_a$	0.4469(82)	0.182(27)	0.14(11)	
$C_b$	0.4438(53)	0.193(16)	0.237(65)	0.27(20)
$D$	0.343(28)	0.119(80)		
$\bar{A}$	0.4540(45)	0.185(15)	0.203(60)	0.27(22)
$\bar{B}$	0.4496(50)	0.185(16)	0.201(65)	0.48(20)
$\bar{C}$	0.4333(44)	0.211(14)	0.243(54)	
$B_s$	1.5076(94)	0.458(11)	0.336(31)	0.282(93)
$C_s$	1.2210(77)	0.410(11)	0.379(30)	0.310(82)
$D_s$	1.116(12)	0.372(16)	0.351(51)	0.25(12)

For the stout smeared ensembles the contact terms seem to still present up to time-separation  $t = 5, 6$ . We observed stabilization of the extracted  $am_S/Z_S$  values at somewhat larger time-separations comparing to the un-stout case. Plateaus behavior begin at



time-separation  $t_{min} = 6, 7$  and sweep a  $t$ -range up to  $t = 11$  at  $\kappa_s = 0.157$  for example.

The results for the renormalization constants ration  $Z_T/Z_S$  presented in Table 4.17 as described above for  $am_S/Z_S$ . For the un-stout smeared subsamples our best results correspond to the points  $C$  and all the points on  $24^3 \cdot 48$  with un-stout fermion action. The presence of the contact terms is suspected up to  $t < 3$ . Therefore, starting the fitting from  $t_{min} = 3$  reveals no role played by contact terms. As the final result we take the estimation

$$\bar{B} : Z_S/Z_T \sim 0.185(16) . \quad (4.44)$$

The results are surprisingly in agreement with the ones found in the pioneering work of Ref. [21] for the local current where the value  $Z_S/Z_T \sim 0.185(7)$  was found. In Ref. [21] finer  $12^3 \cdot 24$  lattices at  $\beta = 2.3$  with plaquette gauge action and several values of  $\kappa$ . The improved gauge action (tlSym) provides a  $\mathcal{O}(a^2)$  in the gauge action but it still a  $\mathcal{O}(a)$  from the fermion action.

For the case of subsamples with stout smearing we observed indeed consistent values for the ratios, which are however not consistent with the determinations on the un-stout subsamples. This inconsistency could be interpreted as resulting from the stout smearing in the fermion action and not an  $\mathcal{O}(a)$  effect. Indeed the stout action is a totally different action and the results cannot be confronted directly to those of simple Wilson action.

## 4.6 The massless gluino limit

As we have seen in the chapter of TSMB analysis it is of interest in SYM simulation to know the critical value of the hopping parameter  $\kappa_{cr}$  where the renormalized gluino mass vanishes. The critical hopping parameter value provides us the information on how far are we from the massless gluino limit. As we have at our disposal the values of the adjoint pion masses at each simulated point and as we explored also the SUSY WIs, we are able to use two independent methods for the determination of  $\kappa_{cr}$ .

We had already an idea on the lightness of the bare gluino masses simulated with TS-PHMC algorithm as indicated by the values of the quantity  $M_r = (r_0 m_{a-\pi})^2$  calculated in Table 4.8. In the OZI arguments applied to SYM theory, the square pion mass is expected to be approximately linearly dependent of the inverse hopping parameter  $1/\kappa$  in a region where the gluino mass is sufficiently light and vanishes at  $\kappa_{cr}$ . The linear behavior is clear as it is shown in Fig. 4.40 and Fig. 4.41 (left panels) for  $16^3 \cdot 32$  and  $24^3 \cdot 32$  lattices respectively.

The subtracted gluino mass  $am_S/Z_S$  extracted from SUSY WIs is also expected to vanish linearly when  $\kappa \rightarrow \kappa_{cr}$  i.e. for sufficiently light gluino mass. We see the clear linear decrease of  $am_S/Z_S$  when  $\kappa$  is increased towards  $\kappa_{cr}$  in Fig. 4.40 and Fig. 4.41 (left panels) for  $16^3 \cdot 32$  and  $24^3 \cdot 32$  lattices respectively.

Table 4.18: Values of the critical hopping parameter  $\kappa_{cr}$  estimated from OZI arguments and SUSY WIs for  $16^3 \cdot 32$  and  $24^3 \cdot 48$  TS-PHMC ensembles. The last column gives a rough estimate of un-stout  $\kappa$  which corresponds to stout  $\kappa_s = 0.1575$ .

$L$	$\kappa_{cr}^{OZI}$	$\kappa_{cr}^{WIs}$	$\kappa(\kappa_s = 0.1575)$
$16^3 \cdot 32$	0.20330(3)	0.2032(2)	$\sim 0.2027$
$24^3 \cdot 48$	0.20300(5)	0.2027(4)	$\sim 0.2025$

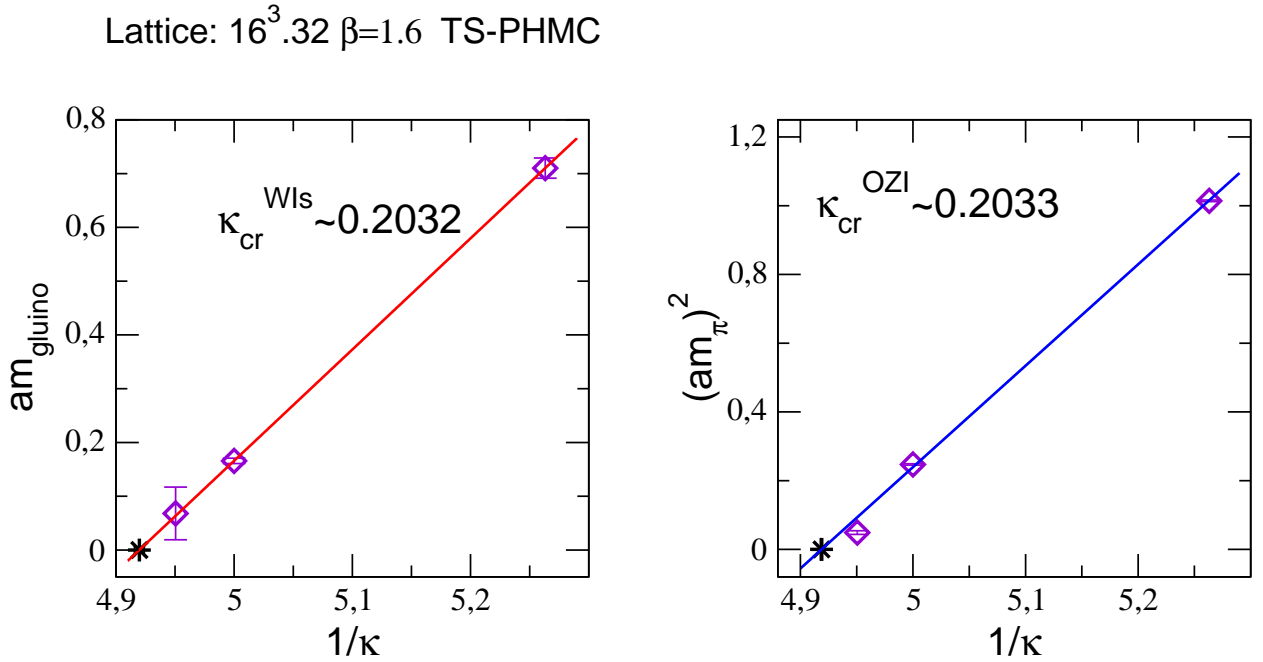


Figure 4.40: The gluino mass  $am_S/Z_S$  (left panel) and pion mass square  $(am_{a-\pi})^2$  (right panel) as function of the inverse hopping parameter for  $16^3 \cdot 32$  lattices.

We finally performed extrapolations to  $(am_{a-\pi})^2 = 0$  and to  $am_S/Z_S = 0$  to obtain a determination of  $\kappa_{cr}$ . Besides the illustration of extrapolations in Fig. 4.40 and Fig. 4.41 the results of extrapolations are summarized in Table 4.18 for  $16^3 \cdot 32$  and  $24^3 \cdot 48$  lattices. The high accuracy of the pion mass data results in estimations of  $\kappa_{cr}$  with small error using OZI arguments. The obtained results using both independent methods and on both  $16^3 \cdot 32$  and  $24^3 \cdot 48$  lattices agree nicely. The analogy to QCD through the OZI approach seems still to work impressively for SYM.

We also used the value of  $\kappa_{cr}$  obtained from OZI arguments and the pion mass at  $\kappa_s = 0.1575$  to find an estimate of what the corresponding un-stout value  $\kappa$  would be. We replace the values in the OZI relation

$$(am_{a-\pi})^2 = c \left( \frac{1}{\kappa} - \frac{1}{\kappa_{cr}} \right). \quad (4.45)$$

The corresponding  $\kappa$  value to  $\kappa_s = 0.1575$  are given in the last column of Table 4.18. We observe that the corresponding value  $\kappa = 0.2025 - 0.2027$  to  $\kappa_s = 0.1575$  is relatively larger than the value of the hopping parameter of the ensemble ( $D$ ) which is  $\kappa = 0.202$ . This was also indicated by the values of  $a-\pi$  mass in lattice unit. However, a more accurate comparison involves dimensionless quantities by multiplying with the Sommer scale  $r_0/a$ . When considering the values of  $M_r$  we conclude that the ensembles ( $D$ ) and ( $D_s$ ) were simulated at comparable bare gluino mass.

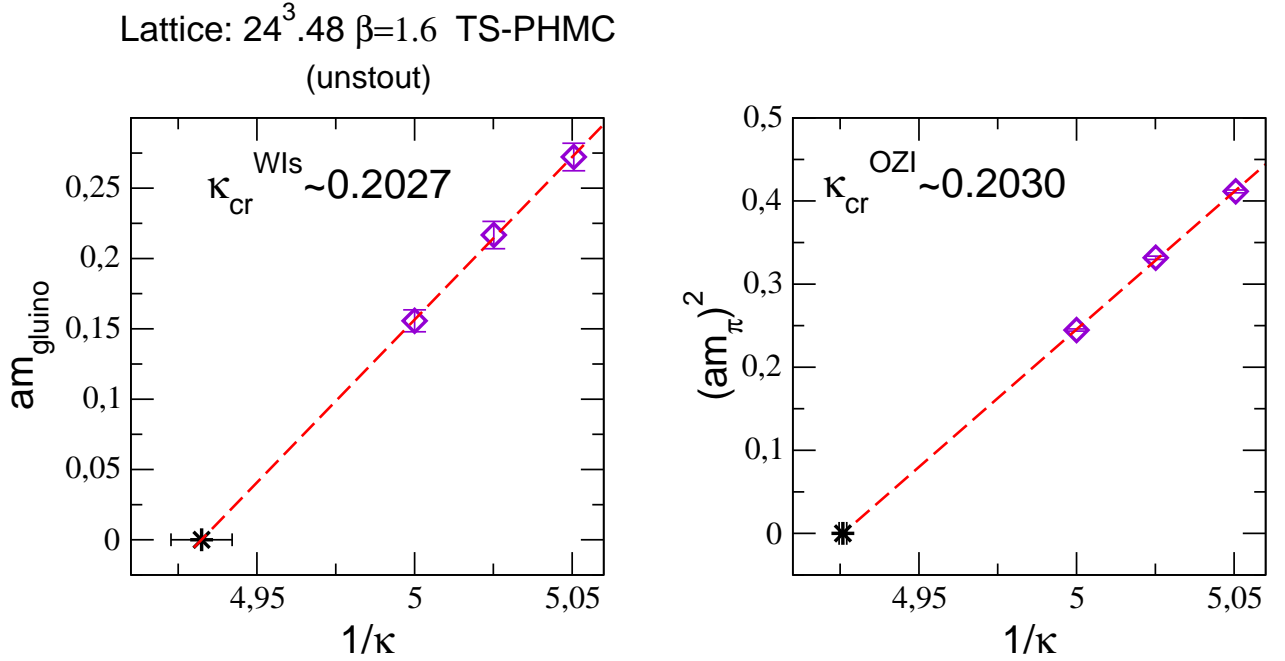


Figure 4.41: *The gluino mass  $am_S/Z_S$  (left panel) and pion mass square  $(am_{a-\pi})^2$  (right panel) as function of the inverse hopping parameter for  $24^3 \cdot 48$  lattices.*

### 4.6.1 Gluino condensate

In  $SU(2)$  SYM a first order phase transition is expected to occur at zero gluino mass. The spontaneous chiral symmetry breaking implies the existence of two ground states. The order parameter of the chiral transition is the gluino condensate  $\langle \bar{\lambda}\lambda \rangle$ . In the two degenerate vacua the gluino condensate has opposite signs:  $\langle \bar{\lambda}\lambda \rangle_+ > 0$  and  $\langle \bar{\lambda}\lambda \rangle_- < 0$ . The first large scale numerical Monte Carlo simulation with the aim to find numerical evidence for the existence of this phase transition are reported in Ref. [69].

In order to check the expected pattern of spontaneous chiral symmetry breaking, the expression of the renormalized gluino condensate is considered:

$$\langle \bar{\lambda}\lambda \rangle_{R(\mu)} = Z(a\mu)[\langle \bar{\lambda}\lambda \rangle - b_0(a\mu)] , \quad (4.46)$$

which is obtained by additive and multiplicative renormalizations in the Wilson fermionic formulation and  $\mu$  is the renormalization scale. The renormalization factor  $Z$  is expected to be of order  $\mathcal{O}(1)$ . The presence of the shift  $b_0(a\mu)$  implies that in numerical simulation, a first order phase transition should show up as a jump in the expectation value of the gluino condensate at  $m_{\tilde{g}} = 0$ . By tuning the hopping parameter  $\kappa$  to  $\kappa_{cr}$ , for fixed  $\beta$  value, the appearance of a two peak structure in the distribution of the bare gluino condensate is expected. We note that this two-phase structure can also be searched for in other variables such as pure gauge field variables. It turns out that their distributions are rather insensitive to chiral breaking. We have seen in the TSMB analysis an example of using the smallest eigenvalue  $\lambda_{min}$  for the exploration of the chiral phase (see Section 3.1.2). It is also important to note, that when increasing the volume the tunneling between the two ground states becomes less and less probable and may be come at some point practically impossible.

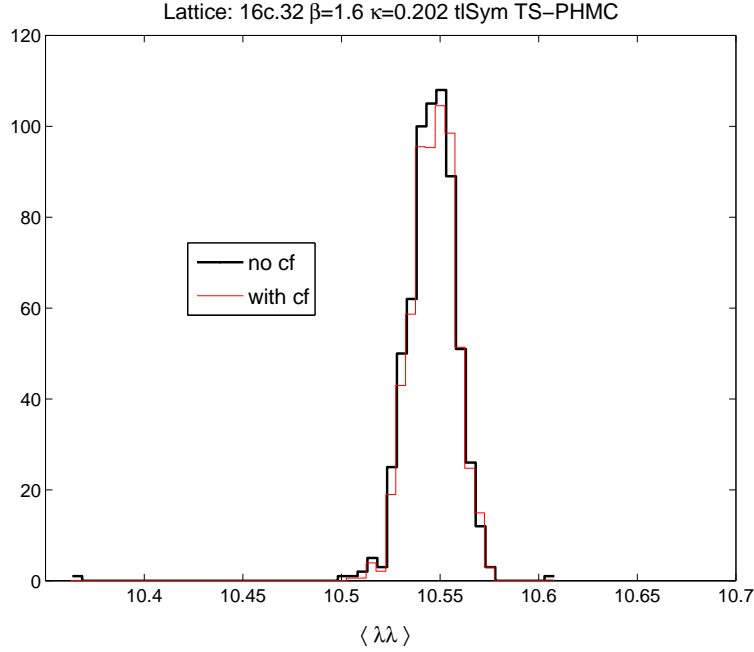


Figure 4.42: *The effect of the correction factor on the gluino condensate distribution for the run D (TS-PHMC).*

Our volume may indeed be relatively large for the chiral phase study. But we consider the opportunity of having calculated the (bare) gluino condensate during the adjoint meson analysis. The gluino condensate appears in the disconnected part of the adjoint scalar meson  $a$ - $f_0$  correlator as the vacuum expectation value to be subtracted. Therefore, the gluino condensate involves the all-to-all propagator which have been calculated by means of SET/SEM method. We concentrated here on the ensembles simulated at the lightest gluino masses, ensemble ( $D$ ) and ( $D_s$ ). Our investigation goes along the lines of Ref. [69] suitable for theories with Wilson fermions. Other formulations also allow the calculation of the bare gluino condensate in the chiral limit as in Domain Wall Fermion (DWF). The first use of DWF in SYM is reported in Ref. [14]. More recent results on larger lattices are given in Ref. [88]. However, in Ref. [88]  $r_0/a$  appears to be much smaller than with Wilson formulation. This is due to the fact that at non-zero lattice spacing DWF have more fermions because of the extra dimension. Furthermore, the dimensionless residual mass  $r_0 m_{res}$  is rather large, in most case above 0.5. Therefore, a strong chiral symmetry breaking occurs in the action.

The expectation value of the bare gluino condensate are collected in Table 4.19. We observe, as expected, the decrease of the gluino condensate as function of the hopping parameter, and its value is of order  $\mathcal{O}(10)$  at lightest gluino masses. However, we cannot extrapolate to  $\kappa_{cr}$  since the shift  $b_0$  in eq. (4.46) is unknown. Therefore, to check the

chiral phase transition we perform single and two gaussian fits to the distribution of the bare gluino condensate.

Table 4.19: *The expectation value of the bare gluino condensate  $\langle\bar{\lambda}\lambda\rangle$  for all TS-PHMC ensembles.*

Ensemble	$\langle\bar{\lambda}\lambda\rangle$
$A$	11.3853(3)
$B$	11.1333(3)
$Ca$	10.6949(11)
$Cb$	10.6970(10)
$D$	10.5440(19)
$\bar{A}$	10.8107(4)
$\bar{B}$	10.7559(3)
$\bar{C}$	10.6941(4)
$A_s$	11.0770(3)
$B_s$	10.8226(3)
$C_s$	10.6838(6)
$D_s$	10.64166(64)

We analyzed the data of the gluino condensate collected at  $\kappa = 0.202$  and  $\kappa_s = 0.1575$  for the analysis of  $a\text{-}f_0$  (see Tables 4.9 and 4.10). Recall that at these point we have seen the relevance of statistical reweighting by including the correction factors. Therefore, before studying the distribution of the gluino condensate at these points we checked the impact of the correction factors on the gluino condensate distribution which is shown in Fig. 4.42 at  $\kappa = 0.202$ . As can be seen the correction factors do not have sizable effect on the distribution, and the number of data in roughly  $\sim 50\%$  of bins is unchangeable.

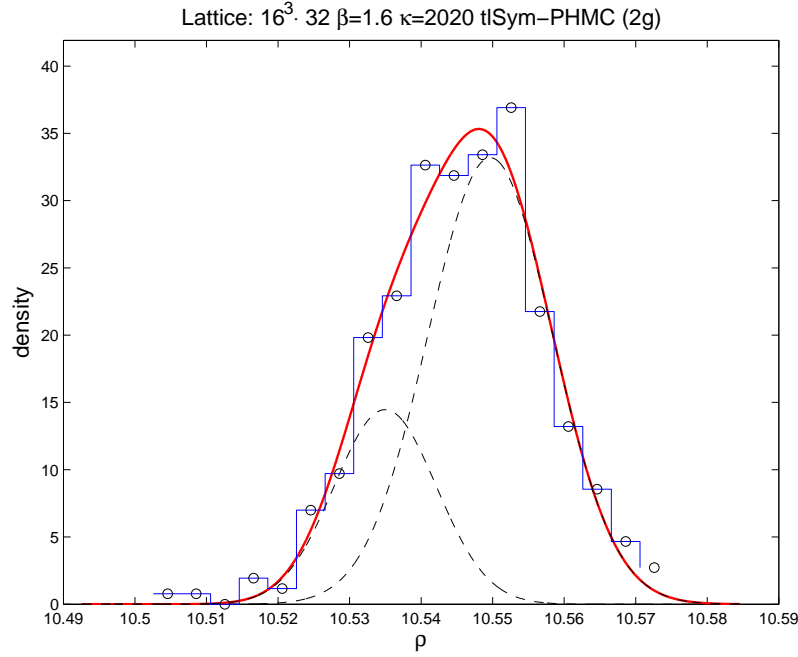


Figure 4.43: *The probability distribution of the bare gluino condensate at  $\kappa = 0.202$ . The dashed lines show the two components of the two-gaussian fit (solid smooth line).*

The results of fitting to two-gaussian model are shown in Fig. 4.43 and Fig. 4.44 at  $\kappa = 0.202$  and  $\kappa_s = 0.1575$  respectively. The two-gaussians represent the contributions of the chiral two phases on this lattice. We observed that the distribution can be well fitted by a two-gaussian model indicating a signal of chiral symmetry breaking and that the simulation points are close to the chiral limit. However, we note here that we have observed during the fitting that the results of the two-peak heights depend on the choice of the number of bins of data. After many tests and taking into account the statistics we have, the number of bins was tuned in the range 18 – 24 to find best fitting to the two-gaussian model.

Comparing to the results of Ref. [69] we find that as the volume increases the data become more compact *i.e.* the distribution width at large volumes is much narrower than that at smaller volumes which renders the appearance of the two-peak structure difficult. Furthermore, in the present work we have considered one subsample at each  $\kappa$  and the study may need more than one subsample such that we can define the error on the probability distribution and hence perform the fitting with weights of data *i.e.* their errors.

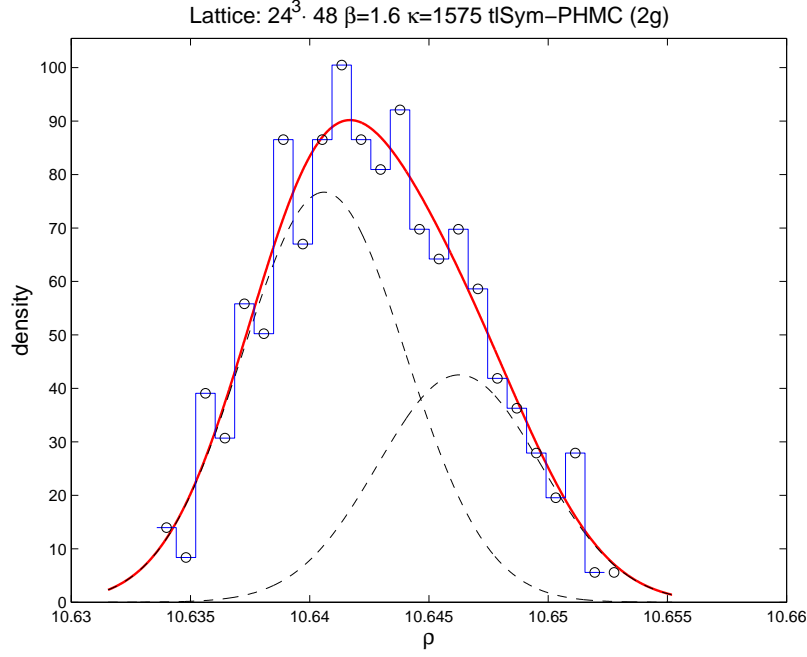


Figure 4.44: *The probability distribution of the bare gluino condensate at  $\kappa_s = 0.1575$ . The dashed lines show the two components of the two-gaussian fit (solid smooth line).*

This is a first exploration of the chiral phase structure in SYM theory on coarse and large lattices. More accurate numerical investigations would need more statistics to study the manifestation of the discrete chiral symmetry breaking at non-zero lattice spacing. Finally, it is interesting to see the dependence on the bare gauge coupling  $\beta$  since after all the spontaneous chiral symmetry breaking to the discrete subgroup  $Z_2$  refers the continuum limit  $\beta \rightarrow \infty$ .

## 4.7 Summary and discussion

In this chapter we presented the details and the results of the dynamical simulation of  $\mathcal{N} = 1$   $SU(2)$  SYM on the lattice with the TS-PHMC algorithm at  $\beta = 1.6$ . In this first study with this new algorithm, light dynamical gluino masses were simulated where we applied tree-level improved Symanzik gauge (tlSym) action and Wilson fermion action with/without stout-smear links. Our aim was to determine the mass spectrum of the low-lying bound states which is expected to be organized in two Wess-Zumino supermultiplets. For an improved analysis, a lighter gluino mass in a larger volume, and larger statistics was essential. Furthermore, we explored the lattice SUSY WIs to check their validity on one hand, and on the other hand the determination of the gluino



subtracted mass  $am_{\tilde{g}}/Z_S$  which is useful for the tuning of the hopping parameter towards its critical value where supersymmetry is expected. We also used the hypothesis of the OZI arguments in SYM to check independently the massless gluino limit. In addition the gluino condensate is also studied in order to find evidence for spontaneous chiral symmetry breaking in the massless gluino limit.

The results on the mass spectrum of  $\mathcal{N} = 1$   $SU(2)$  SYM studied in this chapter are collected and summarized in Table 4.20. A graphical representation of the masses and the possible scenarios towards the massless gluino limit is illustrated in Fig. 4.45. The vertical line indicates the massless gluino region where SUSY emerges up to  $\mathcal{O}(a)$  effects. We analyzed four bound states:  $a\text{-}\eta'$ ,  $a\text{-}f_0$ , gluino-glueball  $\chi$  and the scalar glueball  $0^{++}$ . We note here that we also analyzed the pseudo-scalar glueball, but the latter has a much noisier signal rendering the analysis difficult in this channel<sup>4</sup>. Recall that in the analysis the particle masses obtained with the highest confidence are the adjoint pseudo-scalar  $a\text{-}\eta'$  and the gluino-glueball  $\chi$ . The masses of the determined particles in units of the Sommer scale parameter are displayed as function of the quantity  $M_r = (r_0 m_{a-\pi})^2$  in Fig. 4.45. To improve readability of the spectrum results and for clarity in the discussion we displayed four panels in Fig. 4.45 which are discussed in the following:

- In the panel (P1) the masses of  $a\text{-}\eta'$  and the gluino-glueball  $\chi$  particles are presented. As can be seen, runs with and without stout smearing give consistent results for the  $a\text{-}\eta'$  and  $\chi$  masses. We have also seen small finite size effects of the results on  $16^3 \cdot 32$  and  $24^3 \cdot 48$  lattice volumes. Both bound state masses appear to be characterized by a linear dependence on the quantity  $M_r$ . The gluino-glueball turns out to be appreciably heavier ( $\sim 50\%$ ) than the  $a\text{-}\eta'$  at lightest gluino mass. This could be due to the fact that the gluino-glueball interpolating operator used in our study overlap with a member of a higher supermultiplet while  $a\text{-}\eta'$  belongs to lower supermultiplet. Therefore, in the weakly broken SUSY region the remainder bound states of the spectrum have masses either similar to the  $a\text{-}\eta'$  mass or to the  $\chi$  mass. Another possibility is that the gluino-glueball interpolating operator projects on the lowest state and the discrepancy is due to  $\mathcal{O}(a)$  SUSY breaking effects.
- In the panel (P2) besides the masses of  $a\text{-}\eta'$ , the results of masses of the  $0^{++}$  bound states,  $a\text{-}f_0$  and the scalar glueball, for only unstout runs are shown. We find that at lightest simulated gluino mass the scalar particles masses are near the  $\chi$  mass, and hence tend to be superpartners of the spin- $\frac{1}{2}$  gluino-glueball  $\chi$ . However, recall that we have seen during the analysis that especially for  $a\text{-}f_0$  and the scalar

---

<sup>4</sup> The pseudo-scalar glueball  $0^{-+}$  is also a predicted bound state of the  $\mathcal{N} = 1$  SYM spectrum. We have tried to extract an estimate of its mass on the stout subsamples. However, it reveals to be very difficult. It is probable that this bound state has higher mass which lies nearby excited states. The pseudo-scalar glueball requires more careful analysis.

glueball  $0^{++}$  we confronted various problems and this channel is characterized by low signal-to-noise ratios. Therefore, the determined mass estimates could lie higher than the true values since we extracted most masses in this channel at very short time-separations.

- In the panel (P3) the same particles are shown as in the previous panel (P2) but now only the results of masses of the  $0^{++}$  bound states for the stout ensembles. As we argued in the analysis of the particles with quantum numbers  $0^{++}$  the stout smearing improve substantially the signal-to-noise ratios of the particles in the  $0^{++}$  channel which are considered to belong to the most notorious hadrons to measure in lattice QCD, and here also in lattice SYM. Our measurements of the scalars on the stout ensembles were impressively good and are considered as solid for spectrum studies. On the contrary, see above, those performed on the ensembles without stout smearing are subject for systematic errors. We observed a drop of the masses of the scalars bound states shown in panel (P3) as we simulated towards light gluino mass. A rapid convergence of the masses of the  $a$ - $f_0$  and the scalar glueball  $0^{++}$  is clear towards a mass of the order of the  $a$ - $\eta'$ . Therefore, this picture suggests that the scalars  $0^{++}$  and the adjoint pseudo-scalar  $a$ - $\eta'$  belong to a lighter supermultiplet. Furthermore, a mass-splitting of the order of the SUSY soft breaking  $\mathcal{O}(m_{\tilde{g}})$  occurs within this possible supermultiplet. Of interest here is also the pair behavior of the scalars as function of the gluino mass. The masses of the  $a$ - $f_0$  and the glueball  $0^{++}$  are of the same order at each simulated  $\kappa_s$ . This could be a signal of a mixing of the  $a$ - $f_0$  and the scalar glueball  $0^{++}$  as expected by the low energy effective action of Farrar *et al.* in Ref. [17]. A check of the  $a$ - $f_0$ -glueball is planned as next step in our to-do list.
- In panel (P4) illustrates a final picture where all masses are shown except those of the scalar masses determined on un-stout subsamples.

According to the low-energy effective theory of [15] the  $a$ - $\eta'$ , the gluino-glueball  $\chi$  and the  $a$ - $f_0$  belong to the same supermultiplet and therefore should be degenerate in the SUSY limit. However our results show a gluino-glueball mass which is systematically heavier than the  $a$ - $\eta'$  and the  $a$ - $f_0$  until the lightest simulated gluino mass in the weakly broken SUSY region. Whether this outcome is a discretization artifact or a physical effect will become clear in future studies at finer lattice spacings. If the latter case applies, the interpolating gluino-glueball operator could have dominant overlap with a member of a higher supermultiplet. Besides the  $a$ - $\eta'$  and the  $a$ - $f_0$  the scalar glueball  $0^{++}$  indeed tends to be degenerate with the formers for light gluino masses. But since one scalar is allowed in the supermultiplet the  $a$ - $f_0$  and the scalar glueball  $0^{++}$  should mix in one bound state. The puzzle here is the fact that we did not find spin- $\frac{1}{2}$  gluino-glueball in the lower group of particles even if we carried out simulations at quite low gluino

masses where supersymmetry breaking should be weak. The lightness of the gluino was confirmed in this chapter by the investigation of the SUSY WIs, by OZI arguments and the gluino condensate.

The problem of the missing lower gluino-glueball has been also seen in early stages of the SYM project until the last investigation (see Refs. [63, 18, 71]). Results towards continuum limit  $\beta \rightarrow \infty$  will clarify this question. Furthermore, the design of new interpolating operators with spin- $\frac{1}{2}$  content is very recommended. A preliminary discussion on possible baryonic projecting operator can be found in Ref. [45, 89].

Finally, we conclude that the volumes in the series of simulations performed in this work by means of the TS-PHMC algorithm are appropriate for spectrum calculations as the systematic error of the finite size effects is under control. Nevertheless, a final statement requires the continuum extrapolation.

The spectrum of SYM is still challenging from the point of view of numerical analysis. From the point of view of spectroscopy investigations we still use simple projecting operators with only improvement given by smearing techniques for the interpolating operators involving gauge links variables. Within the use of these projecting operators the qualitative features of the bound state spectrum in SYM were visible in small volumes. The results of the present work on larger volumes are the most precise in the series of investigations of the DESY-Münster collaboration in the determination of the mass spectrum. However, in the future the spectroscopy investigations should involve new techniques and methods already applied in lattice QCD hadron spectroscopy with the goal of more clarifications and accuracy in the spectrum.

Table 4.20: *The spectrum of  $\mathcal{N} = 1$   $SU(2)$  SYM on  $16^3 \cdot 32$  and  $24^3 \cdot 48$  lattices at  $\beta = 1.6$  with tree-level Symanzik improved gauge action and Wilson fermions. The gluino dynamics is simulated by TS-PHMC algorithm. In the ensembles with subscript  $s$  the stout smearing of the gauge links in the Wilson-Dirac operator is used. The masses are given in lattice unit.*

Ensemble	$L$	$\kappa$	$a\text{-}\eta'$	$a\text{-}f_0$	$\tilde{g}g$	glub. $0^{++}$
$A$	16	0.1900	1.3115(67)	2.229(80)	1.862(21)	1.291(13)
$B$	16	0.1800	1.0396(72)	1.27(18)	1.546(14)	1.156(51)
$Ca$	16	0.2000	0.542(23)	0.93(11)	0.984(12)	0.927(40)
$Cb$	16	0.2000	0.5426(75)	0.931(60)	0.979(17)	0.945(20)
$D$	16	0.2000	0.361(60)	0.87(10)	0.7532(96)	0.819(19)
$\bar{A}$	24	0.1980	0.675(18)	1.15(12)	1.1456(82)	
$\bar{B}$	24	0.1990	0.6215(86)	1.314(32)	1.0789(95)	
$\bar{C}$	24	0.2000	0.536(24)	0.863(81)	0.9895(70)	0.781(24)
$A_s$	24	0.1500	1.0114(82)	1.07(16)	1.302(14)	
$B_s$	24	0.1550	0.614(23)	0.964(70)	0.9559(48)	1.079(92)
$C_s$	24	0.1570	0.416(29)	0.467(93)	0.7250(56)	0.582(61)
$D_s$	24	0.1575	0.364(70)	0.400(59)	0.6454(96)	0.449(38)

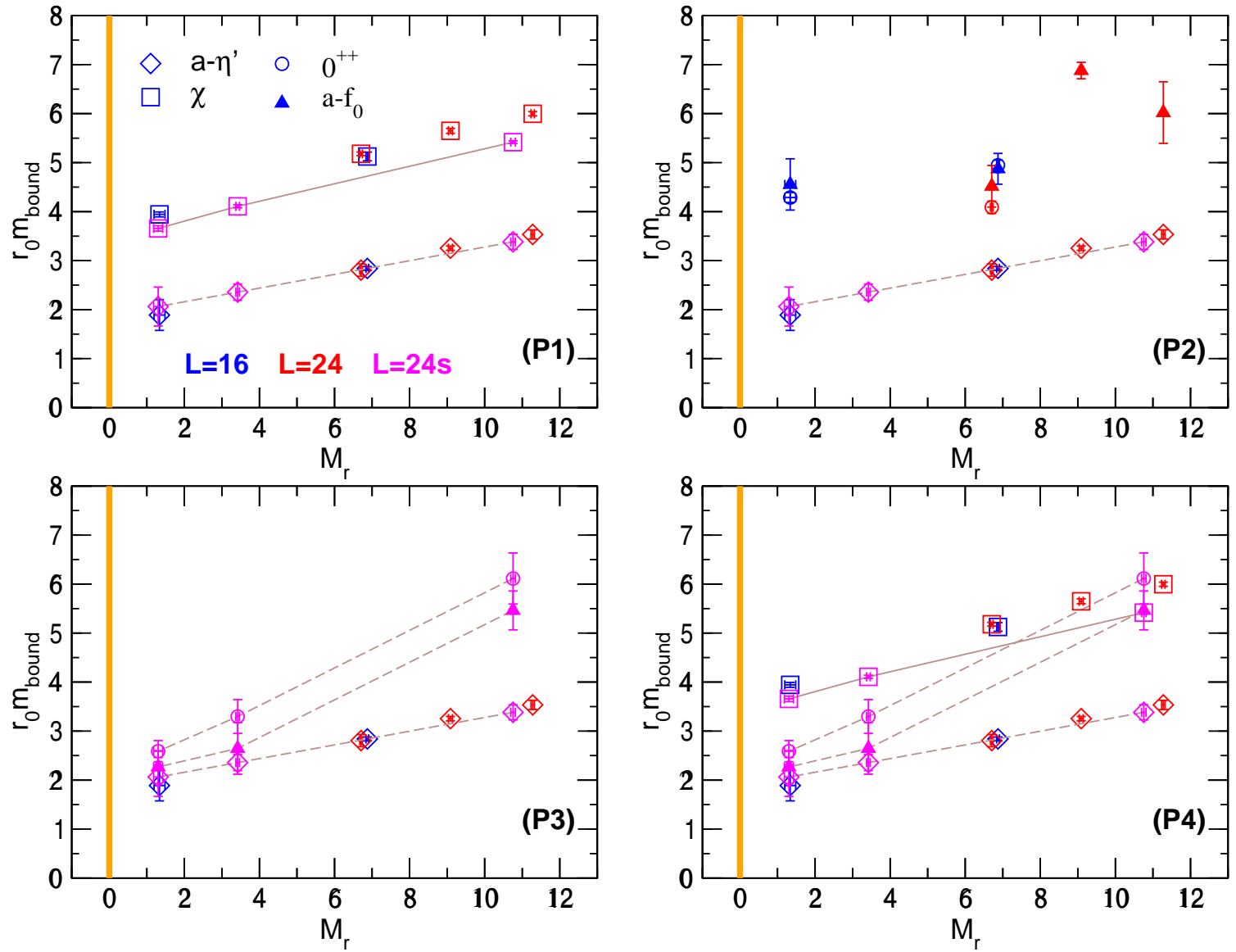


Figure 4.45: Spectrum of  $\mathcal{N} = 1$   $SU(2)$  SYM at  $\beta = 1.6$ . Action: *tlSym+Wilson(unstout/stout)*. Algorithm: *TS-PHMC*. The legend in panel 1 (P1) indicates the symbols for bound states in all panels. The lines are drawn on the stout data to guide the eye. Discussion and details are given in the text.

# Conclusions and Outlook

In this thesis we have performed Monte Carlo investigations of the  $4d \mathcal{N} = 1$  supersymmetric Yang-Mills (SYM) theory on the lattice with dynamical gluinos in the adjoint representation of the  $SU(2)$  color gauge group. This work represents a continuation of a long-standing project of the DESY-Münster-Roma collaboration (see Ref. [13] and references therein for a review). The lattice regularization provides a unique possibility and a powerful tool to non-perturbatively investigate the strongly coupled SYM theory. The general features of low energy dynamics of this theory have been summarized in term of low energy effective actions [15, 17] which predict a picture of low-lying bound states organized in Wess-Zumino supermultiplets.

We have concentrated on performing analysis of the masses of the bound states on two series of gauge ensembles at different values of the bare fermion hopping parameter  $\kappa$ . The first group of samples were prepared by the previously tuned Two-Step Multi-Boson algorithm (TSMB) on fairly small lattice volumes up to  $\sim (1 \text{ fm})^3$  at gauge coupling  $\beta = 2.3$  with the simple plaquette gauge action. The second group of samples were prepared by the new Two-Step Polynomial Hybrid Monte Carlo (TS-PHMC) updating algorithm on larger coarse lattices up to a volume  $\sim (2.3 \text{ fm})^3$  at gauge coupling  $\beta = 1.6$  with the tISym gauge action. In the TSMB algorithm the Wilson approach in the gauge and the gluino parts of the Curci-Veneziano lattice action was applied [12]. In the TS-PHMC runs we used the tree-level improved Symanzik gauge action, while we kept the Wilson formulation for the gluino where for some samples we applied stout-smearing of the gauge links in the Dirac-Wilson operator.

Besides the spectrum calculations, the breaking of supersymmetry of the lattice formulation was explored through the lattice SUSY Ward-Identities (WIs). This allows a non-perturbative determination of the ratio of renormalization coefficients and the renormalized gluino mass in numerical simulations. We used the SUSY WIs as an independent determination of the massless gluino limit besides the OZI arguments of the theory. The restoration of SUSY is expected at massless gluino up to  $\mathcal{O}(a)$  effects.

The predicted bound states entering the massive supermultiplets are color singlet composite states: two scalars ( $a$ - $f_0$ ,  $0^{++}$  glueball), two pseudo-scalar ( $a$ - $\eta'$ ,  $0^{-+}$  glueball) and two spin- $\frac{1}{2}$  gluino-glueballs. The masses of these bound states are extracted from the asymptotic behavior of time-slice correlation functions of projecting operators with the corresponding quantum number. At large time-separation the correlation functions are dominated by the lightest state. However, some projecting operators like the scalar

adjoint meson  $a$ - $f_0$  and the scalar glueball  $0^{++}$  develop large content of noise due to influence of higher states preventing a precise determination of the mass. A smearing procedure which can be combined with variational method could improve to some degree the signal-to-noise ratio by diminishing the contribution of higher states. Furthermore, the adjoint mesons correlation functions require the evaluation of disconnected diagrams. These are computed by techniques which are well-known in lattice QCD, especially, we have applied stochastic estimators technique in the spin explicit variant (SET/SEM) besides the variant of improved volume source technique (IVST) which was developed in Ref. [51] for adjoint color representations. As the experience showed the most accurate determination of masses could be obtained for the adjoint pseudo-scalar meson  $a$ - $\eta'$  and the spin- $\frac{1}{2}$  gluino-glueball. However, the latter receives noise from its gluonic part content, and hence smearing techniques are applied in order to improve its signal-to-noise ratio.

Chapter 3 and Chapter 4 covered the results of the numerical simulations with the TSMB and the TS-PHMC algorithms respectively. The study of the static quark potential on our samples supports the hypothesis of the confinement in SYM theory. Of interest is the conversion of the determined quantities into physical units. To this end we have computed the physical scale in QCD units by using the Sommer scale parameter  $r_0 \sim 0.5$  fm. We found the lattice spacings to be  $\sim 0.06$  fm and up to  $\sim 0.1$  fm for TSMB and TS-PHMC samples respectively. Using this scale the estimated gluino mass calculated by means of WIs at largest hopping parameter are  $\sim 115$  and  $\sim 126$  MeV for TSMB and TS-PHMC respectively, in QCD units. These masses are of the order of the strange quark mass.

In the case of TSMB ensembles the last simulated hopping parameter  $\kappa = 0.1965$  is close to its critical value estimated from both WIs and OZI arguments to be  $\sim 0.1969$ . At light gluino mass the TSMB algorithm develops large autocorrelation-times which result in low statistics and large error of the physical quantities and hence too long runs are required. Within the TSMB statistics available for the present work the results of the simulation at the lightest gluino mass indicate the degeneracy of the scalar glueball  $0^{++}$ ,  $\chi$  and  $a$ - $\eta'$  within large errors and these bound states may occur in a supermultiplet. Without consideration of the error, the mass of the pseudo-scalar  $a$ - $\eta'$  seems to be much smaller than the other bound states. On the other hand the scalar glueball  $0^{++}$  and the gluino-glueball have comparable masses and may occur in a supermultiplet. However, recalling the relatively small physical volume of  $(1 \text{ fm})^3$  this picture could be dominated by large finite size effect. But this still show qualitatively the feature of the bound state spectrum in softly broken SUSY. A next step should be then the determination of the spectrum on larger lattices while keeping the gluino mass light.

Within the TS-PHMC algorithm larger lattices were simulated with sufficiently light gluino mass. Furthermore, this algorithm is still efficient even at light gluino mass where short autocorrelation-times in the runs were observed. This resulted in larger statistics

suitable for precise spectrum determination. We attained two simulation points where the gluino mass is the lightest. The first point corresponds to  $\kappa = 0.2$  and the second one to  $\kappa_s = 0.1575$ , where in the latter stout smearing was applied in the updating process. In both points the reweighting in the statistical average was necessary for a reliable extraction of the physical quantities in the case of observable involving fermionic degree of freedom. However, the pure gluonic quantities were not affected by the reweighting. For the pseudo-scalar  $a\text{-}\eta'$  the statistical error of the disconnected correlation function increased impressively towards light gluino which results in a relatively large error for the mass comparing to previous studies at larger gluino mass. In QCD, similar observations were also made in light quark simulations. An improvement of the results would be the inclusion of the low eigen-modes of the fermion matrix in the correlation function. For the  $a\text{-}f_0$  the overlap with the vacuum plays the role of stabilizing the fluctuation in the error of the disconnected contribution. The obtained results of the gluino-glueball showed that its mass is systematically heavier than the  $a\text{-}\eta'$  until the lightest gluino mass in the weakly broken SUSY region. Whether this outcome is a discretization artifact or a physical effect will become clear in future studies at finer lattice spacings. If the latter case applies, the interpolating gluino-glueball operator could have dominant overlap with a member of a higher supermultiplet. For the scalar glueball  $0^{++}$  the combined smearing and variational method applied in the analysis did not allow a reliable determination of the glueball mass. The estimated values were extracted at early times and could be considered as upper bound. Results of the runs with and without stout smearing give consistent results for the  $a\text{-}\eta'$  and the gluino-glueball  $\chi$ .

The results of analysis of the stout smeared ensembles are the interesting in this study. The lower group of bound states is consisting of the pseudo-scalar  $a\text{-}\eta'$ , the scalar  $a\text{-}f_0$  and the scalar gluball  $0^{++}$  at a mass of  $\simeq 760$  MeV. Mixing of the  $a\text{-}f_0 - 0^{++}$  is strongly expected. However, the gluino-glueball is heavier about 50% than the previous bound states with a mass of  $\simeq 1580$  MeV.

The stout smearing produced an improvement of the signal-to-noise in the scalar channel though to be the hardest to measure in SYM. A direction one could pursue to improve the signal, proposed in previous works, is the use of anisotropic lattices which make the lattice finer in the time direction. Within the present results the stout smearing presents an alternative for the improvement of the results. The future production will be carried out with stout smeared actions. The next step is to pursue the analysis on finer lattices.



# A Dirac matrices, Majorana fermions and fermion matrix

The Euclidean  $\gamma$ -matrices  $\gamma_\mu$ ,  $\mu = 0, 1, 2, 3$  used in this work are given by

$$\begin{aligned}\gamma_0 &= \begin{pmatrix} 0 & 0 & 1 & 0 \\ 0 & 0 & 0 & 1 \\ 1 & 0 & 0 & 0 \\ 0 & 1 & 0 & 0 \end{pmatrix}, & \gamma_1 &= \begin{pmatrix} 0 & 0 & 0 & -i \\ 0 & 0 & -i & 0 \\ 0 & i & 0 & 0 \\ i & 0 & 0 & 0 \end{pmatrix}, \\ \gamma_2 &= \begin{pmatrix} 0 & 0 & 0 & -1 \\ 0 & 0 & 1 & 0 \\ 0 & 1 & 0 & 0 \\ -1 & 0 & 0 & 0 \end{pmatrix}, & \gamma_3 &= \begin{pmatrix} 0 & 0 & -i & 0 \\ 0 & 0 & 0 & i \\ i & 0 & 0 & 0 \\ 0 & -i & 0 & 0 \end{pmatrix}.\end{aligned}\tag{A.1}$$

Therefore,  $\gamma_5 = \gamma_1\gamma_2\gamma_3\gamma_0 = \gamma_5^\dagger$  is given by

$$\gamma_5 = \begin{pmatrix} 1 & 0 & 0 & 0 \\ 0 & 1 & 0 & 0 \\ 0 & 0 & -1 & 0 \\ 0 & 0 & 0 & -1 \end{pmatrix}.\tag{A.2}$$

The  $\gamma$ -matrices satisfy the following formulas

$$\gamma_\mu = \gamma_\mu^\dagger,\tag{A.3}$$

$$(\gamma_\mu)^2 = \mathbb{1},\tag{A.4}$$

$$\gamma_\mu\gamma_5 + \gamma_5\gamma_\mu = 0.\tag{A.5}$$

The charge conjugation matrix has the form

$$\mathcal{C} = -\gamma_2\gamma_0 = \begin{pmatrix} 0 & 1 & 0 & 0 \\ -1 & 0 & 0 & 0 \\ 0 & 0 & 0 & -1 \\ 0 & 0 & 1 & 0 \end{pmatrix}.\tag{A.6}$$

The Majorana spinor is a 4-component Dirac spinor

$$\Psi = \begin{pmatrix} \lambda_A \\ \bar{\lambda}^{\dot{A}} \end{pmatrix} \quad (\text{A.7})$$

satisfying the Majorana condition

$$\bar{\Psi}_\alpha = (\Psi^T \mathcal{C})_\alpha = \Psi_\beta \mathcal{C}_{\beta\alpha} . \quad (\text{A.8})$$

Using the anti-symmetry property of fermion matrix  $M = \mathcal{C}Q$  in the SYM action and the properties of the fermion matrix  $Q$  the following formulas can be derived

$$\mathcal{C}Q\mathcal{C}^{-1} = Q^{T_{xa\alpha}} , \quad (\text{A.9})$$

$$\mathcal{C}\gamma_5 Q \gamma_5 \mathcal{C}^{-1} = Q^* . \quad (\text{A.10})$$

Therefore, one obtains for the fermion propagator  $\Delta = Q^{-1}$

$$\mathcal{C}\Delta\mathcal{C}^{-1} = \Delta^{T_{xa\alpha}} , \quad (\text{A.11})$$

or writing the indices explicitly, the above formula can be written

$$\mathcal{C}_{\gamma\alpha} \Delta_{xa\alpha, yb\sigma} \mathcal{C}_{\sigma\beta}^{-1} = \Delta_{yb\beta, xa\gamma} . \quad (\text{A.12})$$

From the last relations we see that the propagator matrix  $\Delta$  for a fixed space-time and color in Dirac space has only two independent column instead of four in QCD. Therefore, this reduces the necessary inversions with conjugate gradient by a factor of 2.

## B Preconditioning

It turns out that the application of the conjugate gradient is more efficient on the Even-Odd preconditioned hermitian matrix  $\tilde{\tilde{Q}}$  than on  $\tilde{Q}$  itself. The preconditioned matrix is characterized by a condition number smaller by almost a factor two.

Observe that in the Wilson fermion action that the fermion matrix elements  $Q_{xy} = \delta_{xy} + \kappa M_{xy}$  contain only self interaction term and interaction with the next neighbor site. This motivates rearranging the Majorana field  $\Psi_x$  acting on  $N$  lattice sites in even and odd sites

$$\Psi \equiv \begin{pmatrix} \Psi_{even} \\ \Psi_{odd} \end{pmatrix}. \quad (\text{B.1})$$

In this basis, the hermitian fermion matrix has now the following form

$$\tilde{Q} = \begin{pmatrix} \gamma_5 & -\gamma_5 \kappa M_{even-odd} \\ -\gamma_5 \kappa M_{odd-even} & \gamma_5 \end{pmatrix}. \quad (\text{B.2})$$

Now, the  $LU$ -decomposition can be used and the resulting form is

$$\tilde{Q} = L \tilde{\tilde{Q}} U = \begin{pmatrix} \mathbb{1} & 0 \\ -\kappa M_{oe} & \mathbb{1} \end{pmatrix} \begin{pmatrix} \gamma_5 & 0 \\ 0 & \gamma_5 - \gamma_5 \kappa^2 M_{oe} M_{eo} \end{pmatrix} \begin{pmatrix} \mathbb{1} & -\kappa M_{eo} \\ 0 & \mathbb{1} \end{pmatrix}, \quad (\text{B.3})$$

where  $\tilde{\tilde{Q}}$  is the preconditioned hermitian matrix and  $L, U$  are easy invertible matrices given by

$$L^{-1} = \begin{pmatrix} \mathbb{1} & 0 \\ \kappa M_{oe} & \mathbb{1} \end{pmatrix}, \quad U^{-1} = \begin{pmatrix} \mathbb{1} & \kappa M_{eo} \\ 0 & \mathbb{1} \end{pmatrix}. \quad (\text{B.4})$$

# C Spin $J^{PC}$ on the lattice

## C.1 Irreps of the cubic group $O_h$

The symmetry group of the 3-dimensional lattice is called the cubic group  $O$  (or commonly  $O_h$  when parity and charge conjugation are included). It is a subgroup of the rotation group  $SO(3)$ . The cubic group is a finite group with 24 elements, enumerated in their five conjugacy classes [6, 7]. Recalling that for finite group the number of irreducible representations (irreps) equals the number of conjugacy classes, there are then five irreps of  $O$ . They are usually called  $A_1, A_2, E, T_1$  and  $T_2$  with respective dimensions 1, 1, 2, 3 and 3. Recall also the rule for finite groups  $G$  that the sum of squares of dimensions of irreps equals the number of group elements  $\sum_i d_i^2 = n_G$ . Among irreps of  $O$ ,  $A_1$  is the identity representation and  $T_1$  rotates the geometrical vector  $(x, y, z)$ .

Let us  $D_J$  be the spin  $J$  irreducible representation of  $SO(3)$  for integer  $J$ . Because  $O$  is subgroup of  $SO(3)$ , its elements are also represented by  $D_J$ . Viewed as a representation of  $O$  this yields the *subduced representation*  $D_J^O$ . It will be in general no longer irreducible and can be decomposed into the irreducible representations of  $O$ . Up to  $J = 4$  one finds [43]

$$\begin{aligned} D_0^O &= A_1 \\ D_1^O &= T_1 \\ D_2^O &= E \oplus T_2 \\ D_3^O &= A_2 \oplus T_1 \oplus T_2 \\ D_4^O &= A_1 \oplus E \oplus T_1 \oplus T_2 \end{aligned} \tag{C.1}$$

Each irreps  $\mathcal{R}$  of  $O$  can describe a range of integer spins  $J$  in the continuum. Nevertheless, the most important state is the one corresponding to the lowest spin in  $\mathcal{R}$ , since it is usually belongs to the lowest mass and will therefore dominates the correlation function. The irreps of  $O$ , their dimension and the spin content are summarized in Table C.1

In addition to the transformations of the cubic group there are two further discrete symmetries. The first one is total space reflection  $\mathcal{P}$ . Its eigenvalues are the parity  $\mathcal{P} = \pm 1$ . The second one is the "charge conjugation"  $\mathcal{C}$ , which is equivalent to complex conjugation of Wilson loops. Its eigenvalues are called  $\mathcal{C}$ -parity  $\mathcal{C} = \pm 1$ . For each

Table C.1: *Irreps of  $O$  and their spin content.*

Irreps $\mathcal{R}$ of cubic group	contribution to spin $j$ in the continuum
$A_1$	0, 4, 6, 8, ...
$A_2$	3, 6, 7, 9, ...
$E$	2, 4, 5, 6, ...
$T_1$	1, 3, 4, 5, ...
$T_2$	2, 3, 4, 5, ...

channel of  $\mathcal{C}$ -parity the resulting group is the full cubic group  $O_h = O \times Z_2$ , whose representations are labeled  $\mathcal{R}^{PC}$ .

Untill now, we have discussed construction of spin integer states, however, objects with half-integer spin states are also bluit on the lattice. The double group  ${}^2O$  is the *covering* group of  $O$  as the  $SU(2)$  is the covering group of  $SO(3)$  rotation group. The  ${}^2O$  is constructed by adding a negative identity, then two additional conjugacy classes come from the classes of  $O$ . Thus, the 48 elements of  ${}^2O$  divide into 8 conjugacy classes. In addition to the irreps of  $O$ ,  ${}^2O$  has further three irreps labelled  $G_1, G_2$  and  $H$  with dimensions 2,2 and 4 (see Ref. [6, 7]). The spin content of these additional irreps is summerized in Table C.2

Table C.2: *Half-integer spin irreps of  ${}^2O$ .*

Irreps $\mathcal{R}$ of cubic group	contribution to spin $j$ in the continuum
$G_1$	$\frac{1}{2}, \frac{7}{2}, \frac{9}{2}, \frac{11}{2}, \dots$
$G_2$	$\frac{5}{2}, \frac{7}{2}, \frac{11}{2}, \dots$
$H$	$\frac{3}{2}, \frac{5}{2}, \frac{7}{2}, \dots$

## C.2 Orthonormal basis ONB

For a given lattice operator like spacelike Wilson loops of fixed length  $L$ , the number of the prototypes of Wilson loops is the dimension of the representation  $\mathcal{R}$  which can be decomposed into direct sum of irreps. Let us consider the plaquette operators  $U_P$  in the three directions, hence  $\dim(\mathcal{R}) = 3$ . One constructs all irreps of  $O_h$  on Wilson loops. The irreducible contents of the representation  $\mathcal{R}$  are best explored by means of the character relation. In a given channel of  $\mathcal{C}$ -parity the multiplicity  $a_\mu^P$  of the irreducible representation  $\mathcal{R}_\mu^P$ , where  $\mu = A_1, A_2, E, T_1, T_2$ , in the decomposition of  $\mathcal{R}$  into irreps is given by

$$a_\mu^P = \frac{1}{48} \sum_i n_i \chi_i^{\mathcal{R}} \chi_i^{\mu^P}, \quad (\text{C.2})$$

where the sum goes over all classes of conjugate elements, and  $n_i$  is the number of elements in class  $C_i$ .  $\chi^{\mathcal{R}}$  are the character of the matrix representation  $\mathcal{M}$  of an element  $g$  of  $O_h$  given by

$$\chi^{\mathcal{R}}(g) = \text{Tr} \mathcal{M}^{\mathcal{R}}(g). \quad (\text{C.3})$$

For the choice of the operators, we have to calculate an orthonormal basis explicitly. The method relies on an elaboration of Schur's lemma: Let  $C$  be a matrix which commutes with  $\mathcal{R}$  (i.e. all the matrices of the representation  $\mathcal{R} = \{\mathcal{R}_g\}$ ) and let  $A$  be the matrix which diagonalizes  $C$  ( $ACA^{-1} = \text{diagonal}$ ), then  $A$  reduces the representation  $\mathcal{R}$ , and in the next step one may go on with the representation

$$A\mathcal{R}A^{-1} = \{A\mathcal{R}_gA^{-1} | \mathcal{R}_g \in \mathcal{R}\}. \quad (\text{C.4})$$

The matrix  $A$  diagonalizes each matrix  $\mathcal{R}_g$  in blocks. For example, in the case of the 3-dimensional basis (3.42) the matrix representation of the element  $C_{4y}$  (this is an element of  $O_h$  see [6, 7] for details) is written as

$$\mathcal{M}^{\mathcal{R}}(C_{4y}) = \begin{pmatrix} 0 & 1 & 0 \\ 0 & 1 & 0 \\ 1 & 0 & 0 \end{pmatrix}.$$

The character of the representation  $\mathcal{R}$  on the element  $C_{4y}$  is given by

$$\chi(C_{4y})^{\mathcal{R}} = 1. \quad (\text{C.5})$$

Using the transformation matrix  $A$  to the orthonormal basis shown in the table 3.28, the  $C_{4y}$  becomes then

$$A\mathcal{R}(C_{4y})A^{-1} = \begin{pmatrix} 1 & 0 & 0 \\ 0 & \frac{-1}{2} & \frac{1}{2} \\ 0 & \frac{3}{2} & \frac{1}{2} \end{pmatrix},$$

where we see that it decomposes into two diagonal blocks corresponding to  $A_1$  and  $E$  respectively. The matrix  $A$  is the basis change matrix. Note here also that the matrices  $C$  which commute with  $\mathcal{R}$  can be constructed by summing the matrices of conjugacy class of  $\mathcal{R}$ .

Finally, we summarize the steps for the determination of the irreducible representation on the lattice.

**How to Construct irreducible lattice operators and determine their spin  $j^{PC}$  content ?**

- Create gauge invariant product of links and fermions.
- Determine the basis of  $\mathcal{R}$ : the set in different directions.
- Combine to construct  $PC$  invariant basis.
- Perform all possible rotations separately for each sector (link, fermion).
- Compute the characters of  $\mathcal{R}$ .
- Decomposition of  $\mathcal{R}$  into irreps.
- Diagonalize and find the wave functions (ONB).

## D Scaling and $\beta$ -function

A lattice formulation is realized by introducing the lattice spacing  $a$  which is the cutoff of the theory. The extrapolation process to the continuum limit  $a \rightarrow 0$  is an important issue and has to be kept under control. The only parameters at our hands are the bare parameters appearing in the lattice action in eq.(2.2). If we know the functional dependence of the bare coupling  $g_0$  on the cutoff  $a$ , in other word solving the renormalization group equation, the variation variation of the bare coupling of our theory becomes clear in order to reach the continuum limit.

A guidance for large-scale simulations, as in the SYM project, can be provided by the perturbative study of the space of bare couplings. These are useful to understand the behavior of lattice gauge theory as the continuum limit is approached. This is called *scaling*. The existence of the continuum limit requires that for  $a \rightarrow 0$  the measured physical quantities become independent of the lattice spacing  $a$ . The  $\beta$ -function encodes the dependence of the lattice spacing  $a$  on the bare gauge coupling  $g_0^2 = 2N_c/\beta$ . The lattice spacing is determined by the bare coupling according to the renormalization group equation

$$\beta_{\text{lat}}(g_0) = -a \left. \frac{\partial g_0}{\partial a} \right|_{g_R \text{ fixed}}. \quad (\text{D.1})$$

For a the SYM theory with gauge group  $SU(N_c)$  and  $N_f$  flavors, the two-loop computation of the  $\beta$ -function in perturbation theory yields the familiar expression

$$\beta_{\text{lat}}(g_0) = -\beta_0 g_0^3 - \beta_1 g_0^5 + O(g_0^7) \quad (\text{D.2})$$

$$\beta_0 = \frac{1}{(4\pi)^2} \left[ \frac{11}{3} N_c - \frac{4}{3} N_c N_f \right] \quad (\text{D.3})$$

$$\beta_1 = \frac{1}{(4\pi)^2} \left[ \frac{34}{3} N_c^2 - \frac{20}{3} N_c^2 N_f - 4 N_c^2 N_f \right], \quad (\text{D.4})$$

where in the case of  $SU(2)$  SYM with one flavor  $N_f = 1/2$  this gives for the universal coefficients  $\beta_0$  and  $\beta_1$

$$\beta_0 = 0.0379954 \quad (\text{D.5})$$

$$\beta_1 = 0.000962435 \quad (\text{D.6})$$

The asymptotic behavior of  $a(g_0)$  is obtained by integrating eq.(D.1), and invariant renormalization group mass parameter  $\Lambda_{\text{lat}}$  appears in this procedure. Following the



notation in Ref. [90] the solution is

$$a(g_0)\Lambda_{\text{lat}} = \exp \left[ -1/(2\beta_0 g_0^2) \right] (\beta_0 g_0^2)^{-\beta_1/(2\beta_0^2)} \left[ 1 + O(g_0^2) \right]. \quad (\text{D.7})$$

$\Lambda_{\text{lat}}$  provides us with a scale, which survives the continuum limit. Its connection to the popular  $\Lambda_{\overline{MS}}$  for the Curci-Veneziano lattice action [90, 91] is given by the ratio

$$\Lambda_{\overline{MS}}/\Lambda_{\text{lat}} = 32.27. \quad (\text{D.8})$$

In turn, solving eq.(D.7) for  $g_0$  yields

$$g_0^2 = -\frac{1}{\beta_0 \ln(a^2)\Lambda_{\text{lat}}^2} + \dots, \quad (\text{D.9})$$

which reveals that  $g_0 \rightarrow 0$  as  $a \rightarrow 0$ .

## E Majorana-Link-Majorana correlators

In this appendix we compute explicitly the correlation function or the vacuum expectation value of the two point Majorana-Link-Majorana operator defined in Section 3.8.5. The symbol of  $\mathcal{T}$  product is omitted.

$$\begin{aligned}
\langle O_\mu(x) O_\nu(y) \rangle_S &= \langle \text{Tr} \{ \bar{\lambda}(x) U_\mu^\dagger(x) \gamma_\mu \lambda(x + a\hat{\mu}) U_\mu(x) \} \\
&\quad \text{Tr} \{ \bar{\lambda}(y) U_\nu^\dagger(y) \gamma_\nu \lambda(y + a\hat{\nu}) U_\nu(y) \} \rangle_S \\
&= \frac{1}{4} \langle \bar{\lambda}_\alpha^a(x) V_\mu^{ba}(x) \lambda_\alpha^b(x + a\hat{\mu}) \bar{\lambda}_\beta^c(y) V_\nu^{dc}(y) \lambda_\beta^d(y + a\hat{\nu}) \rangle_S \\
&= \frac{1}{4} \langle \lambda_{\alpha'}^a(x) \mathcal{C}_{\alpha'\alpha} \lambda_\alpha^b(x + a\hat{\mu}) \lambda_{\beta'}^c(y) \mathcal{C}_{\beta'\beta} \lambda_\beta^d(y + a\hat{\nu}) \rangle_S \\
&\quad V_\mu^{ba}(x) V_\nu^{dc}(y) \\
&= \frac{1}{4} \{ \langle \Delta_{\alpha'\rho}^{ab}(x, x + a\hat{\mu}) \mathcal{C}_{\rho\alpha}^{-1} \mathcal{C}_{\alpha'\alpha} \Delta_{\beta'\rho'}^{cd}(y, y + a\hat{\nu}) \mathcal{C}_{\rho'\beta}^{-1} \mathcal{C}_{\beta'\beta} \rangle_U \\
&\quad - \langle \Delta_{\alpha'\rho}^{ac}(x, y) \mathcal{C}_{\rho\beta'}^{-1} \mathcal{C}_{\alpha'\alpha} \Delta_{\alpha\rho'}^{bd}(x + a\hat{\mu}, y + a\hat{\nu}) \mathcal{C}_{\rho'\beta}^{-1} \mathcal{C}_{\beta'\beta} \rangle_U \\
&\quad + \langle \Delta_{\alpha'\rho}^{ad}(x, y + a\hat{\nu}) \mathcal{C}_{\rho\beta}^{-1} \mathcal{C}_{\alpha'\alpha} \Delta_{\alpha\rho'}^{bc}(x + a\hat{\mu}, y) \mathcal{C}_{\rho'\beta'}^{-1} \mathcal{C}_{\beta'\beta} \rangle_U \} \\
&\quad V_\mu^{ba}(x) V_\nu^{dc}(y) \\
&= \frac{1}{4} \{ \langle \mathcal{C}_{\alpha\alpha'} \Delta_{\alpha'\rho}^{ab}(x, x + a\hat{\mu}) \mathcal{C}_{\rho\alpha}^{-1} \mathcal{C}_{\beta\beta'} \Delta_{\beta'\rho'}^{cd}(y, y + a\hat{\nu}) \mathcal{C}_{\rho'\beta}^{-1} \rangle_U \\
&\quad - \langle \mathcal{C}_{\alpha\alpha'} \Delta_{\alpha'\rho}^{ac}(x, y) \mathcal{C}_{\rho\beta'}^{-1} \underbrace{\mathcal{C}_\beta \mathcal{C}_{\beta'}^{-1}}_{\delta_{\beta'\rho'}} \Delta_{\alpha\rho'}^{bd}(x + a\hat{\mu}, y + a\hat{\nu}) \rangle_U \\
&\quad - \langle \mathcal{C}_{\alpha\alpha'} \Delta_{\alpha'\rho}^{ad}(x, y + a\hat{\nu}) \mathcal{C}_{\rho\beta}^{-1} \underbrace{\mathcal{C}_{\beta'\beta} \mathcal{C}_{\rho'\beta'}^{-1}}_{\delta_{\beta\rho'}} \Delta_{\alpha\rho'}^{bc}(x + a\hat{\mu}, y) \rangle_U \} \\
&\quad V_\mu^{ba}(x) V_\nu^{dc}(y)
\end{aligned} \tag{E.1}$$

Using the relation in eq.(A.12) this yields

$$\begin{aligned}
\langle O_\mu(x) O_\nu(y) \rangle_S &= \frac{1}{4} \{ \langle Tr_s [\Delta^{ab}(x, x + a\hat{\mu})] Tr_s [\Delta^{cd}(y, y + a\hat{\nu})] \rangle_U \\
&\quad - \langle Tr_s [\Delta^{ca}(y, x) \Delta^{bd}(x + a\hat{\mu}, y + a\hat{\nu})] \rangle_U \\
&\quad + \langle Tr_s [\Delta^{da}(y + a\hat{\nu}, x) \Delta^{bc}(x + a\hat{\mu}, y)] \rangle_U \} V_\mu^{ba}(x) V_\nu^{dc}(y) \\
&= \frac{1}{4} \{ \langle Tr_s [\Delta^{ab}(x, x + a\hat{\mu}) V_\mu^{ba}(x)] Tr_s [\Delta^{cd}(y, y + a\hat{\nu}) V_\nu^{dc}(y)] \rangle_U \\
&\quad - \langle Tr_s [\Delta^{ca}(y, x) V_\mu^{ba}(x) \Delta^{bd}(x + a\hat{\mu}, y + a\hat{\nu}) V_\nu^{dc}(y)] \rangle_U \\
&\quad - \langle Tr_s [\Delta^{da}(y + a\hat{\nu}, x) V_\mu^{ba}(x) \Delta^{bc}(x + a\hat{\mu}, y) V_\nu^{dc}(y)] \rangle_U \} \\
&= \frac{1}{4} \langle Tr_{sc} \{ \Delta(x, x + a\hat{\mu}) V_\mu(x) \} Tr_{sc} \{ \Delta(y, y + a\hat{\nu}) V_\nu(y) \} \rangle_U \\
&\quad - \frac{1}{4} \langle Tr_{sc} \{ \Delta(y, x) V_\mu^T(x) \Delta(x + a\hat{\mu}, y + a\hat{\nu}) V_\nu(y) \} \rangle_U \\
&\quad - \frac{1}{4} \langle Tr_{sc} \{ \Delta(y + a\hat{\nu}, x) V_\mu^T(x) \Delta(x + a\hat{\mu}, y) V_\nu^T(y) \} \rangle_U .
\end{aligned} \tag{E.2}$$

# Bibliography

- [1] LHC Homepage, “CERN,”. [www.cern.ch/lhc](http://www.cern.ch/lhc).
- [2] **Particle Data Group** Collaboration, W. M. Yao *et al.*, “Review of particle physics,” *J. Phys.* **G33** (2006) 1–1232.
- [3] K. G. Wilson, “Confinement of quarks,” *Phys. Rev.* **D10** (1974) 2445–2459.
- [4] M. Creutz, L. Jacobs, and C. Rebbi, “Monte Carlo Study of Abelian Lattice Gauge Theories,” *Phys. Rev.* **D20** (1979) 1915.
- [5] P. H. Dondi and H. Nicolai, “Lattice Supersymmetry,” *Nuovo Cim.* **A41** (1977) 1.
- [6] J. F. Cornwell, “Group theory in physics. vol. 1,”. London, Uk: Academic ( 1984) 399 P. ( Techniques Of Physics, 7).
- [7] J. F. Cornwell, “Group theory in physics. vol. 2,”. London, Uk: Academic ( 1984) 589 P. ( Techniques Of Physics, 7).
- [8] S. Catterall and S. Karamov, “Exact lattice supersymmetry: the two-dimensional  $N = 2$  Wess-Zumino model,” *Phys. Rev.* **D65** (2002) 094501, [arXiv:hep-lat/0108024](https://arxiv.org/abs/hep-lat/0108024).
- [9] M. F. L. Golterman and D. N. Petcher, “A local interactive lattice model with supersymmetry,” *Nucl. Phys.* **B319** (1989) 307–341.
- [10] D. B. Kaplan, E. Katz, and M. Unsal, “Supersymmetry on a spatial lattice,” *JHEP* **05** (2003) 037, [arXiv:hep-lat/0206019](https://arxiv.org/abs/hep-lat/0206019).
- [11] J. Giedt, “Deconstruction and other approaches to supersymmetric lattice field theories,” *Int. J. Mod. Phys.* **A21** (2006) 3039–3094, [arXiv:hep-lat/0602007](https://arxiv.org/abs/hep-lat/0602007).
- [12] G. Curci and G. Veneziano, “Supersymmetry and the Lattice: A Reconciliation?,” *Nucl. Phys.* **B292** (1987) 555.
- [13] I. Montvay, “Supersymmetric Yang-Mills theory on the lattice,” *Int. J. Mod. Phys.* **A17** (2002) 2377–2412, [arXiv:hep-lat/0112007](https://arxiv.org/abs/hep-lat/0112007).

- [14] G. T. Fleming, J. B. Kogut, and P. M. Vranas, “Super Yang-Mills on the lattice with domain wall fermions,” *Phys. Rev.* **D64** (2001) 034510, [arXiv:hep-lat/0008009](#).
- [15] G. Veneziano and S. Yankielowicz, “An Effective Lagrangian for the Pure N=1 Supersymmetric Yang-Mills Theory,” *Phys. Lett.* **B113** (1982) 231.
- [16] G. R. Farrar, G. Gabadadze, and M. Schwetz, “On the effective action of N = 1 supersymmetric Yang-Mills theory,” *Phys. Rev.* **D58** (1998) 015009, [arXiv:hep-th/9711166](#).
- [17] G. R. Farrar, G. Gabadadze, and M. Schwetz, “The spectrum of softly broken N = 1 supersymmetric Yang- Mills theory,” *Phys. Rev.* **D60** (1999) 035002, [arXiv:hep-th/9806204](#).
- [18] F. Farchioni and R. Peetz, “The low-lying mass spectrum of the N = 1 SU(2) SUSY Yang- Mills theory with Wilson fermions,” *Eur. Phys. J.* **C39** (2005) 87–94, [arXiv:hep-lat/0407036](#).
- [19] K. Demmouche *et al.*, “Dynamical simulation of lattice 4d N=1 SYM,” *PoS(Confinement 2008)* (2008) 136, [arXiv:0811.1964 \[hep-lat\]](#).
- [20] K. Demmouche *et al.*, “Spectrum of 4d N=1 SYM on the lattice with light dynamical Wilson gluinos,” *PoS(LATTICE 2008)* (2008) 061, [arXiv:0810.0144 \[hep-lat\]](#).
- [21] **DESY-Münster-Roma** Collaboration, F. Farchioni *et al.*, “The supersymmetric Ward identities on the lattice,” *Eur. Phys. J.* **C23** (2002) 719–734, [arXiv:hep-lat/0111008](#).
- [22] I. Montvay, “An Algorithm for Gluinos on the Lattice,” *Nucl. Phys.* **B466** (1996) 259–284, [arXiv:hep-lat/9510042](#).
- [23] I. Montvay and E. Scholz, “Updating algorithms with multi-step stochastic correction,” *Phys. Lett.* **B623** (2005) 73–79, [arXiv:hep-lat/0506006](#).
- [24] F. Farchioni *et al.*, “Hadron masses in QCD with one quark flavour,” *Eur. Phys. J.* **C52** (2007) 305–314, [arXiv:0706.1131 \[hep-lat\]](#).
- [25] S. R. Coleman and J. Mandula, “All possible symmetries of the s matrix,” *Phys. Rev.* **159** (1967) 1251–1256.
- [26] S. Weinberg, “The quantum theory of fields. Vol. 3: Supersymmetry,” Cambridge, UK: Univ. Pr. (2000) 419 p.

- [27] J. Wess and B. Zumino, “Supergauge Transformations in Four-Dimensions,” *Nucl. Phys.* **B70** (1974) 39–50.
- [28] R. Haag, J. T. Lopuszanski, and M. Sohnius, “All Possible Generators of Supersymmetries of the s Matrix,” *Nucl. Phys.* **B88** (1975) 257.
- [29] F. Farchioni *et al.*, “Hadron spectrum of QCD with one quark flavor,” *PoS LAT2007* (2007) 135, [arXiv:0710.4454 \[hep-lat\]](#).
- [30] A. Donini, M. Guagnelli, P. Hernandez, and A. Vladikas, “Towards  $N = 1$  Super-Yang-Mills on the lattice,” *Nucl. Phys.* **B523** (1998) 529–552, [arXiv:hep-lat/9710065](#).
- [31] C. Morningstar and M. J. Peardon, “Analytic smearing of SU(3) link variables in lattice QCD,” *Phys. Rev.* **D69** (2004) 054501, [arXiv:hep-lat/0311018](#).
- [32] M. Lüscher, “A New approach to the problem of dynamical quarks in numerical simulations of lattice QCD,” *Nucl. Phys.* **B418** (1994) 637–648, [arXiv:hep-lat/9311007](#).
- [33] R. Frezzotti and K. Jansen, “A polynomial hybrid Monte Carlo algorithm,” *Phys. Lett.* **B402** (1997) 328–334, [arXiv:hep-lat/9702016](#).
- [34] R. Frezzotti and K. Jansen, “The PHMC algorithm for simulations of dynamical fermions. I: Description and properties,” *Nucl. Phys.* **B555** (1999) 395–431, [arXiv:hep-lat/9808011](#).
- [35] R. Frezzotti and K. Jansen, “The PHMC algorithm for simulations of dynamical fermions. II: Performance analysis,” *Nucl. Phys.* **B555** (1999) 432–453, [arXiv:hep-lat/9808038](#).
- [36] J. C. Sexton and D. H. Weingarten, “Hamiltonian evolution for the hybrid Monte Carlo algorithm,” *Nucl. Phys.* **B380** (1992) 665–678.
- [37] C. Gebert and I. Montvay, “A recurrence scheme for least-square optimized polynomials,” [arXiv:hep-lat/0302025](#).
- [38] I. Montvay, “Quadratically optimized polynomials for fermion simulations,” *Comput. Phys. Commun.* **109** (1998) 144–160, [arXiv:hep-lat/9707005](#).
- [39] K. Spanderen., “Monte Carlo Simulationen einer SU(2) Yang-Mills Theorie mit dynamischen Gluinos,”. PhD thesis (in german), University of Münster, 1998.
- [40] M. Hasenbusch, “Speeding up finite step-size updating of full QCD on the lattice,” *Phys. Rev.* **D59** (1999) 054505, [arXiv:hep-lat/9807031](#).

- [41] A. Alexandru and A. Hasenfratz, “Partial-global stochastic Metropolis update for dynamical smeared link fermions,” *Phys. Rev.* **D66** (2002) 094502, [arXiv:hep-lat/0207014](#).
- [42] N. Madras and A. D. Sokal, “The Pivot algorithm: a highly efficient Monte Carlo method for selfavoiding walk,” *J. Statist. Phys.* **50** (1988) 109–186.
- [43] I. Montvay and G. Münster, “Quantum fields on a lattice,”. Cambridge, UK: Univ. Pr. (1994) 491 p. (Cambridge monographs on mathematical physics).
- [44] **ALPHA** Collaboration, U. Wolff, “Monte Carlo errors with less errors,” *Comput. Phys. Commun.* **156** (2004) 143–153, [arXiv:hep-lat/0306017](#).
- [45] R. Kirchner., “Ward Identities and Mass Spectrum of  $N = 1$  Super Yang Mills Theory on the Lattice,”. PhD thesis, University of Hamburg, 2000.
- [46] **DESY-Münster** Collaboration, R. Kirchner, S. Luckmann, I. Montvay, K. Spanderen, and J. Westphalen, “Numerical simulation of dynamical gluinos: Experience with a multi-bosonic algorithm and first results,” *Nucl. Phys. Proc. Suppl.* **73** (1999) 828–833, [arXiv:hep-lat/9808024](#).
- [47] M. J. Teper, “Glueball masses and other physical properties of  $SU(N)$  gauge theories in  $D = 3+1$ : A review of lattice results for theorists,” [arXiv:hep-th/9812187](#).
- [48] C. J. Morningstar and M. J. Peardon, “The glueball spectrum from an anisotropic lattice study,” *Phys. Rev.* **D60** (1999) 034509, [arXiv:hep-lat/9901004](#).
- [49] B. Berg and A. Billoire, “Glueball Spectroscopy in Four-Dimensional  $SU(3)$  Lattice Gauge Theory. 1,” *Nucl. Phys.* **B221** (1983) 109.
- [50] **UKQCD** Collaboration, C. R. Allton *et al.*, “Gauge invariant smearing and matrix correlators using Wilson fermions at  $\text{Beta} = 6.2$ ,” *Phys. Rev.* **D47** (1993) 5128–5137, [arXiv:hep-lat/9303009](#).
- [51] F. Farchioni, G. Münster, and R. Peetz, “The volume source technique for flavor singlets: A second look,” *Eur. Phys. J.* **C38** (2004) 329–334, [arXiv:hep-lat/0404004](#).
- [52] Y. Kuramashi, M. Fukugita, H. Mino, M. Okawa, and A. Ukawa, “eta-prime meson mass in lattice QCD,” *Phys. Rev. Lett.* **72** (1994) 3448–3451.
- [53] **TXL** Collaboration, J. Viehoff *et al.*, “Improving stochastic estimator techniques for disconnected diagrams,” *Nucl. Phys. Proc. Suppl.* **63** (1998) 269–271, [arXiv:hep-lat/9710050](#).

- [54] K. Schilling, H. Neff, and T. Lippert, “Computing the eta and eta’ mesons in lattice QCD,” *Lect. Notes Phys.* **663** (2005) 147–176, [arXiv:hep-lat/0401005](#).
- [55] H. Neff, N. Eicker, T. Lippert, J. W. Negele, and K. Schilling, “On the low fermionic eigenmode dominance in QCD on the lattice,” *Phys. Rev.* **D64** (2001) 114509, [arXiv:hep-lat/0106016](#).
- [56] J. Foley *et al.*, “Practical all-to-all propagators for lattice QCD,” *Comput. Phys. Commun.* **172** (2005) 145–162, [arXiv:hep-lat/0505023](#).
- [57] T. Burch and C. Hagen, “Domain decomposition improvement of quark propagator estimation,” *Comput. Phys. Commun.* **176** (2007) 137–145, [arXiv:hep-lat/0607029](#).
- [58] S. Collins, G. Bali, and A. Schafer, “Disconnected contributions to hadronic structure: a new method for stochastic noise reduction,” *PoS LAT2007* (2007) 141, [arXiv:0709.3217 \[hep-lat\]](#).
- [59] R. B. Morgan and W. Wilcox, “Deflated Iterative Methods for Linear Equations with Multiple Right-Hand Sides,” [arXiv:0707.0505 \[math-ph\]](#).
- [60] A. Stathopoulos and K. Orginos, “Computing and deflating eigenvalues while solving multiple right hand side linear systems in Quantum Chromodynamics,” [arXiv:0707.0131 \[hep-lat\]](#).
- [61] **APE** Collaboration, M. Albanese *et al.*, “Glueball Masses and String Tension in Lattice QCD,” *Phys. Lett.* **B192** (1987) 163.
- [62] M. Lüscher and U. Wolff, “How to calculate the elastic scattering matrix in two-dimensional quantum field theories by numerical simulation,” *Nucl. Phys.* **B339** (1990) 222–252.
- [63] **DESY-Münster** Collaboration, I. Campos *et al.*, “Monte Carlo simulation of SU(2) Yang-Mills theory with light gluinos,” *Eur. Phys. J.* **C11** (1999) 507–527, [arXiv:hep-lat/9903014](#).
- [64] R. Sommer, “A New way to set the energy scale in lattice gauge theories and its applications to the static force and alpha-s in SU(2) Yang-Mills theory,” *Nucl. Phys.* **B411** (1994) 839–854, [arXiv:hep-lat/9310022](#).
- [65] M. Creutz, “Monte Carlo Study of Quantized SU(2) Gauge Theory,” *Phys. Rev.* **D21** (1980) 2308–2315.
- [66] M. Creutz, “Asymptotic Freedom Scales,” *Phys. Rev. Lett.* **45** (1980) 313.



- [67] S. Luckmann., “Supersymmetrische Feldtheorien auf dem Gitter,”. PhD thesis (in german), University of Münster, 2001.
- [68] F. Farchioni, C. Gebert, I. Montvay, and L. Scorzato, “Numerical simulation tests with light dynamical quarks,” *Eur. Phys. J.* **C26** (2002) 237–251, [arXiv:hep-lat/0206008](#).
- [69] **DESY-Münster** Collaboration, R. Kirchner, I. Montvay, J. Westphalen, S. Luckmann, and K. Spanderen, “Evidence for discrete chiral symmetry breaking in  $N = 1$  supersymmetric Yang-Mills theory,” *Phys. Lett.* **B446** (1999) 209–215, [arXiv:hep-lat/9810062](#).
- [70] D. J. Gross, I. R. Klebanov, A. V. Matytsin, and A. V. Smilga, “Screening vs. Confinement in 1+1 Dimensions,” *Nucl. Phys.* **B461** (1996) 109–130, [arXiv:hep-th/9511104](#).
- [71] R. Peetz., “Spectrum of  $N = 1$  Super Yang Mills Theory on the Lattice with a Light Gluino,”. PhD thesis, University of Münster, 2004.
- [72] H. Wada *et al.*, “Lattice study of low-lying nonet scalar mesons in quenched approximation,” *Phys. Lett.* **B652** (2007) 250–254, [arXiv:hep-lat/0702023](#).
- [73] H. Jürgens., “Methoden der Spektrumanalyse,”. Diploma thesis, University of Münster, 2004. (in German).
- [74] K. Jansen, C. Michael, and C. Urbach, “The eta-prime meson from lattice QCD,” *Eur. Phys. J.* **C58** (2008) 261–269.
- [75] S. Prelovsek, C. Dawson, T. Izubuchi, K. Orginos, and A. Soni, “Scalar meson in dynamical and partially quenched two- flavor QCD: Lattice results and chiral loops,” *Phys. Rev.* **D70** (2004) 094503, [arXiv:hep-lat/0407037](#).
- [76] N. Mathur *et al.*, “Scalar mesons  $a_0(1450)$  and  $\sigma(600)$  from lattice QCD,” *Phys. Rev.* **D76** (2007) 114505, [arXiv:hep-ph/0607110](#).
- [77] G. Koutsoumbas and I. Montvay, “Gluinos on the lattice: Quenched calculations,” *Phys. Lett.* **B398** (1997) 130–134, [arXiv:hep-lat/9612003](#).
- [78] H. Schmalle., “Spin-1 Zustände der  $N=1$   $SU(2)$  Super-Yang-Mills Theorie auf dem Gitter,”. Diploma thesis (in german), University of Münster, 2004.
- [79] **TXL** Collaboration, T. Struckmann *et al.*, “Flavor singlet pseudoscalar masses in  $N(f) = 2$  QCD,” *Phys. Rev.* **D63** (2001) 074503, [arXiv:hep-lat/0010005](#).

- [80] **CP-PACS** Collaboration, V. I. Lesk *et al.*, “Flavor Singlet Meson Mass in the Continuum Limit in Two- Flavor Lattice QCD,” *Phys. Rev.* **D67** (2003) 074503, [arXiv:hep-lat/0211040](#).
- [81] K. Johnson., “Darstellungstheorie der Ueberlagerung der kubischen Gruppe in Anwendung auf Operatoren der N=1 SUSY-Yang-Mills-Theorie auf dem Gitter,”. Diploma thesis (in german), University of Münster, 2002.
- [82] F. Heitger., “Darstellungstheorie der kubischen Gruppe in Anwendung auf Operatoren der N=1 SYM Theorie auf dem Gitter,”. Diploma thesis (in german), University of Münster, 2000.
- [83] E. E. Scholz and I. Montvay, “Multi-step stochastic correction in dynamical fermion updating algorithms,” *PoS LAT2006* (2006) 037, [arXiv:hep-lat/0609042](#).
- [84] T. Kalkreuter and H. Simma, “An Accelerated conjugate gradient algorithm to compute low lying eigenvalues: A Study for the Dirac operator in SU(2) lattice QCD,” *Comput. Phys. Commun.* **93** (1996) 33–47, [arXiv:hep-lat/9507023](#).
- [85] **ALPHA** Collaboration, R. Frezzotti, M. Hasenbusch, U. Wolff, J. Heitger, and K. Jansen, “Comparative benchmarks of full QCD algorithms,” *Comput. Phys. Commun.* **136** (2001) 1–13, [arXiv:hep-lat/0009027](#).
- [86] A. K. De, A. Harindranath, and J. Maiti, “On Scale Determination in Lattice QCD with Dynamical Quarks,” [arXiv:0803.1281 \[hep-lat\]](#).
- [87] S. R. Sharpe and N. Shores, “Physical results from unphysical simulations,” *Phys. Rev.* **D62** (2000) 094503, [arXiv:hep-lat/0006017](#).
- [88] J. Giedt, R. Brower, S. Catterall, G. T. Fleming, and P. Vranas, “Lattice super-Yang-Mills using domain wall fermions in the chiral limit,” [arXiv:0810.5746 \[hep-lat\]](#).
- [89] **DESY-Münster** Collaboration, A. Feo, R. Kirchner, I. Montvay, and A. Vladikas, “Low-energy features of SU(2) Yang-Mills theory with light gluinos,” *Nucl. Phys. Proc. Suppl.* **83** (2000) 670–672, [arXiv:hep-lat/9909071](#).
- [90] P. Weisz, “On the connection between the lambda parameters of euclidean lattice and continuum qcd,” *Phys. Lett.* **B100** (1981) 331.
- [91] I. Montvay, “SYM on the lattice,” [arXiv:hep-lat/9801023](#).

# Curriculum Vitae

<i>Name:</i>	Kamel Demmouche	
<i>Date of birth:</i>	December, 15 <sup>th</sup> 1977	
<i>Place of birth:</i>	Oran (Algeria)	
<i>Family status:</i>	married (one child)	
<i>Education:</i>	9/1983-7/1989	Primary school "Ennasr", Oran
	9/1989-7/1992	Middle school "Belahcen El Houari", Oran
	9/1992-7/1995	Secondary school "Al Khawarizmi", Oran
	6/1995	High school exam
<i>Higher Education:</i>	9/1995-7/2000	Diploma of high studies: Physics Oran's university
	9/2000-12/2003	Magister degree: Physics Oran's university
		Thesis: <i>Structure constants of the <math>(D_4, A_6)</math> conformal model</i>
<i>Ph.D. Studies:</i>	10/2005	Beginning of Ph.D. Studies at Institute for theoretical physics Münster's university (Germany) Under Supervision of Prof. Dr. G. Münster
<i>Professional Occupation:</i>	9/2001-7/2002	Instructor, secondary school "Med Herrache", Oran
	9/2002-6/2003	Teaching assistant, Oran's university
	9/2004-7/2005	Teaching assistant, Tiaret's university (Algeria)
	since 10/2005	Institute member, Institute for theoretical physics, Münster's university (Germany)